TESIS DE LA UNIVERSIDAD DE ZARAGOZA

2013

59

Jorge Monforte García

Study of the critical and low temperature properties of finite dimensional spin glasses

Departamento
Física Teórica

Director/es
Tarancón Lafita, Alfonso
Ruiz Lorenzo, Juan Jesús

ISSN 2254-7606

Prensas de la Universidad
Universidad Zaragoza

Universidad Zaragoza
1542

Tesis Doctoral

STUDY OF THE CRITICAL AND LOW TEMPERATURE PROPERTIES OF FINITE DIMENSIONAL SPIN GLASSES

Autor

Jorge Monforte García

Director/es

Tarancón Lafita, Alfonso
Ruiz Lorenzo, Juan Jesús

UNIVERSIDAD DE ZARAGOZA

Física Teórica

2013

Study of the critical and low temperature properties of finite dimensional spin glasses

Memoria de tesis doctoral presentada por
Jorge Monforte García

Directores
Alfonso Tarancón Lafita
Juan Jesús Ruiz Lorenzo

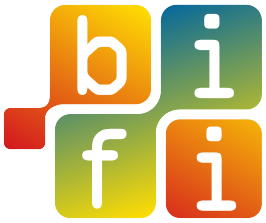

Departamento de Física Teórica, Facultad de Ciencias
Universidad de Zaragoza
Instituto de Biocomputación y Física de Sistemas Complejos

Zaragoza, 29 de abril de 2013

D. Alfonso Tarancón Lafita, Catedrático en el Departamento de Física Teórica de la Universidad de Zaragoza
y
D. Juan Jesús Ruiz Lorenzo, Profesor Titular del área de Física Teórica del Departamento de Física de la Universidad de Extremadura

HACEN CONSTAR

que la presente memoria de Tesis Doctoral presentada por Jorge Monforte García y titulada *"Study of the critical and low temperature properties of finite dimensional spin glasses"* ha sido realizada bajo su dirección en el Departamento de Física Teórica de la Universidad de Zaragoza y en el Instituto de Biocomputación y Física de Sistemas Complejos, BIFI. El trabajo recogido en esta memoria se corresponde con lo planteado en el proyecto de tesis doctoral aprobado en su día por el órgano responsable del programa de doctorado.

Y para que conste, cumplimiento de la legislación vigente, informan favorablemente sobre la referida Tesis Doctoral y autorizan su presentación para su admisión a trámite.

Zaragoza, a 29 de abril de 2013
Los directores de la Tesis

Fdo: Alfonso Tarancón Lafita Fdo:Juan Jesús Ruiz Lorenzo

A mi familia

Contents

Agradecimientos

Tras tantos meses de duro trabajo y esfuerzo dedicados, por fin veo mi trabajo terminado y consigo divisar el final de este camino que, por supuesto, no he recorrido solo. Durante todo este camino he recibido el apoyo de muchas personas, algunas de ellas siendo un importante pilar de apoyo en momentos de angustia o desesperación.

Es por ello que considero igual de importante, tanto mi investigación plasmada en estas páginas, como dejar impresos mis más sinceros sentimientos para con aquellas personas que me han tendido la mano y arropado con sus consejos.

Agradecer a mis familiares, que desde pequeño me han sabido transmitir esos valores de perseverancia, esfuerzo y humildad que me han convertido en la persona que soy ahora, pero sobre todo agradecerles su amor. A mi madre, quien siempre me ha ofrecido palabras de aliento para seguir adelante y me ha dado motivación constante para no rendirme en los momentos difíciles. A mi padre, por transmitirme el valor necesario para enfrentarme a los pequeños y grandes retos que la vida plantea día a día y ayudarme a superarlos.

A Elena, mi compañera y pareja, por su apoyo y comprensión durante estos cuatro años que he estado trabajando con esta tesis. Ella ha sabido sobrellevar mis estados de ánimo siendo un importante apoyo moral a lo largo de todo el proceso.

A mis amistades, por apoyarnos mutuamente en nuestro recorrido universitario y profesional. Y por que siguen estando ahí.

También tener en cuenta a todos aquellos profesores que desde mi infancia hasta mi adolescencia, no sólo me han brindado sus conocimientos en varios campos de la enseñanza y ofrecido sus consejos para afrontar el camino de la vida de la mejor forma, sino que también me han enseñado a reflexionar y tener una mirada crítica de lo que me rodea.

Gracias, también, a aquellos profesionales del terreno de la investigación científica, como son mis directores de tesis Alfonso Tarancón Lafita y Juan Jesús Ruiz Lorenzo, que han sabido darme consejos y guía en esta empresa, ayudándome a tomar las decisiones más correctas y aportándome conocimien-

tos tales como aquel curso sobre vidrios de espín de Badajoz. Agradecerles también, por darme la oportunidad de tener una visión más amplia del mundo de la investigación y ayudarme a descubrir cuánto me motiva.

A Luis Antonio Fernández y Victor Martín Mayor, los cuales me han ayudado a enriquecerme con sus saberes e interesantes charlas en las numerosas reuniones que he compartido con ellos.

A mi compañero Sergio Pérez Gaviro por ser un apoyo y modelo a seguir, le agradezco sus siempre atentas y rápidas respuestas a las diferentes inquietudes que me iban surgiendo, ayudándome en todos aquellos problemas que se me presentaban.

A Antonio Gordillo Guerrero y David Yllanes, con los que también he tenido la oportunidad de compartir y aprender de sus conocimientos en temas de investigación; y conocer Roma desde otro punto de vista de la mano de David.

También tengo muy presentes a todas aquellas personas que he conocido durante todo este tiempo y con las que he tenido la oportunidad, no sólo de aprender nuevos conceptos en el terreno de la investigación, sino de conocer y de enriquecerme con sus culturas, como: Marco Guidetti, quien me ha aportado su gran experiencia profesional; Andrea Maiorano, por sus siempre interesantes comentarios sobre física, programación y Janus, y su amabilidad y disponibilidad durante mi estancia en Roma; Giorgio Parisi, Enzo Marinari y Federico Ricci-Tersenghi, los cuales no solo me ayudaron con su profundo conocimiento de los vidrios de espín sino que además me proporcionaron y mostraron curiosidades de la cultura italiana; Giuglia Loguercio, por su ayuda y guía, la cual me facilitó sobremanera mi estancia en Roma, proporcionándome todo tipo de información que me fuera útil; Denis Navarro, responsable de las nociones que tengo de VHDL; Rafaelle Tripiccione, Fabio Schifano y Marcello, que me aportaron un punto de vista diferente sobre las FPGA y me ayudaron a conocer mejor Ferrara durante mi estancia.

A José Miguel Gil y Raquel Álvarez Baños, darles las gracias por los buenos momentos que hemos compartido. Todos hemos tenido la oportunidad de aprender de todos y cada uno de nosotros, tanto en lo profesional como en el terreno personal. Espero que sus tesis les resulten igual de enriquecedoras que a mí la mía y les deseo suerte en su carrera investigadora.

A mis compañeros del BIFI, por el gran ambiente de trabajo y el compañerismo existente entre todos nosotros. Más en concreto: Isabel Vidal y Beatriz por la ayuda en los trámites, burocracia, papeleo, etc. A Guillermo Losilla, Arturo, Patricia y Pedro por la ayuda en temas informáticos.

A la *Janus Collaboration*, por poder trabajar en una colaboración internacional tan dinámica, agradable, edificante y productiva. Muchas gracias por permitirme vivir una experiencia tan importante para mi formación como

investigador.

Agradecer a su vez a Jesús Clemente Gallardo, Pierpaolo Bruscolini y José Luis Alonso por enseñarme y guiarme en las que han sido las primeras clases que he impartido en la universidad. Gracias también a Joaquín Sanz, por compartir tan buenos momentos preparándolas.

En general y para concluir, quiero agradecer a todas aquellas personas que han vivido conmigo la realización de esta tesis doctoral. Desde lo más profundo de mi corazón os agradezco todo el apoyo, ánimo y colaboración que me habéis dado, pero sobre todo, todo vuestro cariño, amor y amistad.

Jorge Monforte García ha realizado esta Tesis Doctoral gracias a una beca del BIFI, una beca Predoctoral de Formación de Personal Investigador del Gobierno de Aragón, a los proyectos "Complejidad en materiales y fenómenos de transporte" FIS2006-08533-C03-02 y FIS2009-12648-C03-02 del MICINN, "Grupo de excelencia de biocomputación" del Gobierno de Aragón E24/3 y "SCC Computing" del VII proyecto Marco de la UE.

Resumen

Esta memoria ha sido dedicada al estudio de modelos de vidrios de espín con interacciones a corto alcance, en concreto el modelo de Potts de vidrios de espín y el de Edwards-Anderson. El objetivo principal de esta Tesis Doctoral ha sido el estudio de las transiciones de fase que estos modelos presentan así como la caracterización de su fase de vidrio de espín a bajas temperaturas. La complejidad que presentan los vidrios de espín exigen el desarrollo de sofisticadas herramientas para su estudio, las cuales pueden ser aplicadas en otras ramas de la ciencia como el plegamiento de proteínas. Para el desarrollo de esta tesis se han utilizado programas propios escritos en lenguaje C y la máquina dedicada *Janus* del BIFI, así como en menor medida otras infraestructuras como el Cluster del BIFI.

Un vidrio de espín es una colección de momentos magnéticos, espines, que a baja temperatura presenta un estado congelado desordenado, la fase de vidrio de espín. En esta fase, el sistema posee características muy interesantes. Los tiempos de relajación son extremadamente largos debido a un paisaje de energía muy complicado. Una de las principales causas de ello es la frustración, que consiste en que los espines no son capaces de encontrar un estado estable debido a que hay competencia entre distintas interacciones con los espines vecinos.

Los primeros vidrios de espín que se estudiaron, en la década de 1970, fueron los vidrios de espín metálicos o canónicos, compuestos por una base metálica en la que se añaden impurezas magnéticas. Desde entonces se han dedicado muchos trabajos al estudio tanto experimental como teórico de los vidrios de espín, aunque aún quedan muchas incógnitas abiertas. Esta tesis intenta realizar una pequeña aportación a este vasto campo de investigación.

El Capítulo 1 es una introducción a los vidrios de espín donde se explican qué son estos materiales, sus características y se dan algunos ejemplos de materiales reales que presentan el comportamiento de un vidrio de espín. Además, se presentan varios modelos realistas de vidrios de espín así como aproximaciones que tienen solución analíticas que nos permiten lanzar hipótesis sobre el comportamiento de los modelos más realistas.

En el Capítulo 2 se estudia el comportamiento crítico del modelo de Potts de vidrios de espín en tres dimensiones con 5 y 6 estados. Este modelo presenta un diagrama de fases muy rico y por eso recibe bastante atención. En este caso, nosotros caracterizamos la transición a la fase de vidrio de espín y estudiamos su dependencia con el número de estados, así como buscamos la posible existencia de otra transición de fase, esta vez a una ferromagnética.

Uno de los objetivos principales del Capítulo 3 es el estudio de ciertas características de la fase de vidrio de espín de sistemas finitos con interacciones de rango finito, como por ejemplo estabilidad estocástica, *Replica Equivalence* (equivalencia de réplicas), *Overlap Equivalence* (equivalencia de *overlap*) y ultrametricidad. Para ello se estudian las fluctuaciones entre muestras del modelo de Edwards-Anderson en tres dimensiones.

En el Capítulo 4 se investiga, utilizando técnicas fuera del equilibrio, si existe transición de fase en un vidrio de espín en tres dimensiones en presencia de un campo magnético externo, ya que los dos principales escenarios teóricos predicen comportamientos antagónicos.

En el Capítulo 5 aplicamos una técnica alternativa para estudiar transiciones de fase en vidrios de espín, el análisis de las singularidades complejas de la función de partición. Esta técnica, fue desarrollada en 1952 por Lee y Yand y desde entonces se ha aplicado a multitud de sistemas físicos, por lo que queremos estudiar su aplicación a vidrios de espín.

En el Capítulo 6 se estudian los fenómenos de rejuvenecimiento y memoria que presentan los vidrios de espín cuando son sometidos a cambios de temperaturas en su fase de vidrio de espín fuera del equilibrio. Se intentará reproducir el impresionante experimento *dip* en el que estos fenómenos se evidencian claramente.

En el Capítulo 7 se recoge un resumen de los trabajos de investigación en los que he trabajados dentro de la *Janus Collaboration* pero que no forman la parte principal de investigación de esta Tesis Doctoral.

Finalmente, el Capítulo 8 está dedicado a las conclusiones.

Como resultado de todo este trabajo han sido realizadas las siguientes publicaciones

- R. Alvarez Baños, A. Cruz, L. A. Fernandez, A. Gordillo-Guerrero, J. M. Gil-Narvion, M. Guidetti, A. Maiorano, F. Mantovani, E. Marinari, V. Martin-Mayor, J. Monforte-Garcia, A. Muñoz Sudupe, D. Navarro, G. Parisi, S. Perez-Gaviro, J. J. Ruiz-Lorenzo, B. Seoane, S. F. Schifano, A. Tarancon, R. Tripiccione and D. Yllanes, *J. Stat. Mech. P05002* (2010). *"Critical Behavior of Three-Dimensional Disordered Potts Models with Many States"*.

- R. A. Baños, A. Cruz, L. A. Fernandez, J. M. Gil-Narvion, A. Gordillo-

Guerrero, M. Guidetti, D. Iñiguez, A. Maiorano, F. Mantovani, E. Marinari, V. Martin-Mayor, J. Monforte-Garcia, A. Muñoz-Sudupe, D. Navarro, G. Parisi, S. Perez-Gaviro, F. Ricci-Tersenghi, J. J. Ruiz-Lorenzo, S. F. Schifano, B. Seoane, A. Tarancón, R. Tripiccione and D. Yllanes, *Phys. Rev. B* **84**, 174209 (2011). *"Sample-to-sample fluctuations of the overlap distributions in the three-dimensional Edwards-Anderson spin glass"*.

- R. A. Baños, J. M. Gil-Narvion, J. Monforte-Garcia, J. J. Ruiz-Lorenzo and D. Yllanes, *J. Stat. Mech.* P02031 (2013). *"Numerical Study of the Overlap Lee-Yang Singularities in the Three-Dimensional Edwards-Anderson Model"*.

- F. Belletti, A. Cruz, L. A. Fernandez, A. Gordillo-Guerrero, M. Guidetti, A. Maiorano, F. Mantovani, E. Marinari, V. Martin-Mayor, J. Monforte, A. Muñoz Sudupe, D. Navarro, G. Parisi, S. Perez-Gaviro, J. J. Ruiz-Lorenzo, S. F. Schifano, D. Sciretti, A. Tarancon, R. Tripiccione and D. Yllanes, *J. Stat. Phys.* **135**, 1121 (2009). Eprint: arXiv:0811.2864. *"An in-depth look at the microscopic dynamics of Ising spin glasses at fixed temperature"*.

- R. Álvarez Baños, A. Cruz, L. A. Fernandez, J. M. Gil-Narvion, A. Gordillo-Guerrero, M. Guidetti, A. Maiorano, F. Mantovani, E. Marinari, V. Martin-Mayor, J. Monforte-Garcia, A. Muñoz Sudupe, D. Navarro, G. Parisi, S. Perez-Gaviro, J. J. Ruiz-Lorenzo, S. F. Schifano, B. Seoane, A. Tarancon, R. Tripiccione and D. Yllanes, *J. Stat. Mech.* P06026 (2010). Eprint: arXiv:1003.2569. *"Nature of the spin-glass phase at experimental length scales"*.

- R. Álvarez Baños, A. Cruz, L. A. Fernandez, J. M. Gil-Narvion, A. Gordillo-Guerrero, M. Guidetti, A. Maiorano, F. Mantovani, E. Marinari, V. Martin-Mayor, J. Monforte-Garcia, A. Muñoz Sudupe, D. Navarro, G. Parisi, S. Perez-Gaviro, J. J. Ruiz-Lorenzo, S. F. Schifano, B. Seoane, A. Tarancon, R. Tripiccione and D. Yllanes, *Phys. Rev. Lett.* **105**, 177202 (2010). Eprint: arXiv:1003.2943. *"Static versus dynamic heterogeneities in the $D = 3$ Edwards-Anderson-Ising spin glass"*.

- R. Álvarez Baños, A. Cruz, L. A. Fernandez, J. M. Gil-Narvion, A. Gordillo-Guerrero, M. Guidetti, D. Iñiguez, A. Maiorano, E. Marinari, V. Martin-Mayor, J. Monforte-Garcia, A. Muñoz Sudupe, D. Navarro, G. Parisi, S. Perez-Gaviro, J. J. Ruiz-Lorenzo, S. F. Schifano, B. Seoane, A. Tarancon, P. Tellez, R. Tripiccione and D. Yllanes,

PNAS **109** 6452 (2012). Eprint: arxiv:1202.5593. *"Thermodynamic glass transition in a spin glass without time-reversal symmetry"*.

- M. Baity-Jesi, R. A. Baños, A. Cruz, L. A. Fernandez, J. M. Gil-Narvion, A. Gordillo-Guerrero, M. Guidetti, D. Iñiguez, A. Maiorano, F. Mantovani, E. Marinari, V. Martin-Mayor, J. Monforte-Garcia, A. Muñoz Sudupe, D. Navarro, G. Parisi, M. Pivanti, S. Perez-Gaviro, F. Ricci-Tersenghi, J. J. Ruiz-Lorenzo, S. F. Schifano, B. Seoane, A. Tarancon, P. Tellez, R. Tripiccione and D. Yllanes, *Eur. Phys. J. Special Topics* **210**, 33 (2012). *"Reconfigurable computing for Monte Carlo simulations: Results and prospects of the Janus project"*.

Nota filológica

El resumen, el primer capítulo y el capítulo de las conclusiones han sido escritos en español. El resto de la tesis, incluidas las traducciones del primer capítulo y del capítulo de las conclusiones, ha sido escrito en inglés con el objetivo de permitir su lectura a un grupo más amplio de personas.

Capítulo 1

Introducción

Los vidrios de espín[1] son sistemas magnéticos (es decir, una colección de espines) que presentan una transición de fase a una fase congelada de baja temperatura desde una paramagnética. Sin embargo, esta fase no exhibe orden de largo alcance (mientras que los materiales ferromagnéticos y antiferromagnéticos sí), por lo que esta fase es una especie de desorden congelado. Por tanto, la magnetización local m_i es no nula mientras que la magnetización media

$$M = \frac{\sum_i m_i}{N} \tag{1.1}$$

donde N es el número total de espines, y la magnetización a momento $\mathbf{k}$

$$M_{\mathbf{k}} = \frac{\sum_i e^{-i\mathbf{k}\cdot\mathbf{r}_i} m_i}{N} \tag{1.2}$$

se anulan para todos los momentos $\mathbf{k}$. La ausencia de un orden de largo alcance (a diferencia de los materiales antiferromagnéticos) se puede comprobar con experimentos de *scattering* de neutrones.

Los vidrios de espín metálicos o canónicos fueron el primer tipo de vidrios de espín estudiado. Estos materiales son aleaciones metálicas creadas añadiendo impurezas magnéticas a una base metálica, por ejemplo, CuMn. Es bien conocido que en un ferromagneto (como Fe), la interacción magnética es calculada con la interacción de canje, por lo que se obtiene que

$$H = -J\mathbf{S}_1\mathbf{S}_2 \tag{1.3}$$

donde $\mathbf{S}_1$ y $\mathbf{S}_2$ son los espines (es decir, los momentos magnéticos) de los átomos magnéticos. Sin embargo, en un vidrio de espín metálico, los átomos

[1] Se han publicado muchas *reviews*, nos centraremos en las Refs. [2, 3, 5].

magnéticos son impurezas por lo que se tiene una especie de interacción de canje indirecta, una impureza magnética interacciona con un electrón de conducción quien, después, interacciona con otra impureza magnética. Esta interacción es la llamada interacción RKKY (debido a que fue estudiada por Runderman y Kittel en 1954 [6], Kasuya en 1956 [7] y Yosida en 1957 [8]) y la expresión de la interacción es

$$J(r) = J_0 \frac{\cos(2k_F r + \varphi_0)}{(k_F r)^3} \tag{1.4}$$

donde J_0 y φ_0 son constantes y k_F es el número de ondas de Fermi del metal anfitrión (en nuestro ejemplo, Cu).

Los tiempos de relajación en la fase congelada de vidrio de espín son extremadamente largos, por lo que el estudio de la dinámica fuera del equilibrio es muy útil para comparar con experimentos. Además, algunos fenómenos típicos de los vidrios de espín aparecen en este régimen. El comportamiento del sistema depende del proceso de enfriamiento y el tiempo, t_w, que el sistema haya estado en la fase de vidrio de espín, es decir, los vidrios de espín exhiben *aging* (ver, por ejemplo, Ref. [9]). Si el sistema evoluciona un tiempo t_w en una temperatura fija, T, en la fase de vidrio de espín, aparecen dos ejemplos de fenómenos de *aging*: la magnetización termorremanente (el sistema evoluciona en presencia de un campo magnético externo que luego se retira) y la magnetización de un enfriamiento a campo cero, ZFC (el campo magnético externo se enciende tras haber pasado el sistema un tiempo t_w en la fase de vidrio de espín). Un par de ejemplos de este tipo de experimentos se muestra en las Figuras 1.1 y 1.2. Además, si la temperatura en la fase de vidrio de espín no se mantiene constante aparece otros fenómenos, como el rejuvenecimiento y la memoria (ver Capítulo 6).

En resumen, las principales características de un vidrio de espín en su fase de vidrio de espín son que los momento magnéticos están congelados, ausencia de orden de largo alcance ($M_{\mathbf{k}} = 0$ y $M = 0$), tiempo de relajación muy largos y dependencia del protocolo de enfriamiento.

Finalmente, en el resto de este trabajo, $\langle(\cdots)\rangle$ denotará el promedio termal típico y $\overline{(\cdots)}$ denotará el promedio sobre el desorden (congelado).

1.1 Modelos de vidrios de espín

Se han desarrollado muchos modelos de vidrios de espín para modelizar los sistemas reales, con diferentes formas de afrontar el problema. Vamos a describir brevemente aquí algunos de ellos. El primer tipo de modelo que uno puede estudiar es un sistema que reproduzca el vidrio de espín experimental

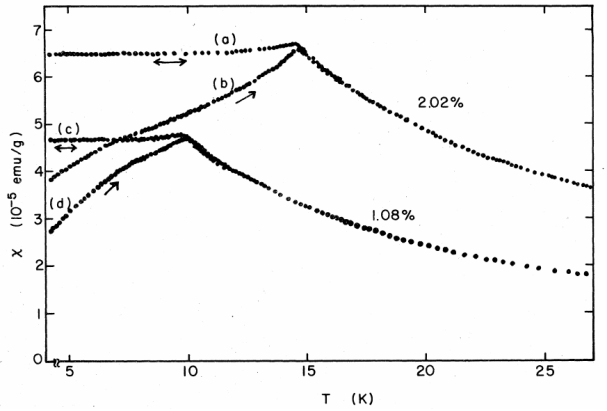

Figure 1.1: Susceptibilidad de dos muestras de CuMn, con un 1.08% y un 2.02% de Mn, respectivamente, al ser recalentadas. Líneas (b) y (d) son los experimentos de enfriamiento a campo cero, mientras que en las líneas (a) y (c) el sistema había sido enfriado en presencia de un campo magnético de $h = 5.90$ Oe. Por encima de la temperatura crítica, T_c, la susceptibilidad de ambos protocolos coincide pero no por debajo de T_c. Figura de la Ref. [10].

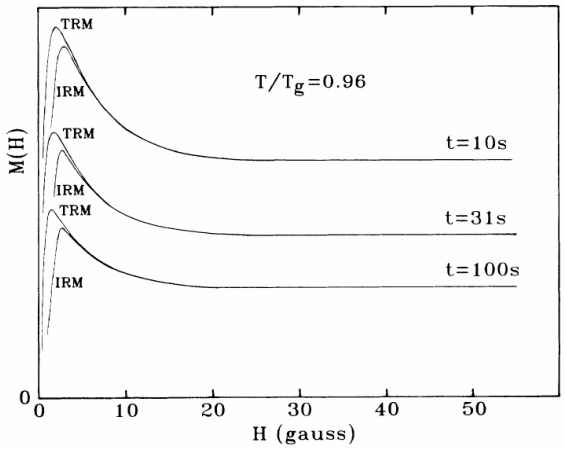

Figure 1.2: Magnetización remanente del $(Fe_{0.15}Ni_{0.85})_{75}P_{16}B_6Al_3$ a una temperatura T con $T/T_g = 0.96$ (donde T_g es la temperatura crítica) tras quitar el campo magnético H. TRM significa que el sistema había sido enfriado en un campo magnético H, mientras que IRM significa que el sistema había sido enfriado en ausencia de campo magnético y en la temperatura T se aplicó un pulso de 30 s del campo magnético H. Las medidas se han realizado un tiempo t tras retirar el campo H. Figura de la Ref. [11].

descrito en la sección anterior. Por ejemplo, en el modelo RKKY, uno tiene impurezas que producen una interacción como la de la Ec. (1.4). Este tipo

de modelos con impurezas son los modelos con aleatoriedad en los sitios. Sin embargo, se ha desarrollado otro tipo de vidrios de espín, los modelos con enlaces aleatorios. Edwards y Anderson [13] propusieron el primero de este tipo de modelos

$$\mathcal{H} = -\sum_{\langle i,j\rangle} J_{ij}\mathbf{S}_i\mathbf{S}_j - \sum_i h_i S_{iz} \tag{1.5}$$

donde $\langle i,j\rangle$ significa que la suma corre sobre los vecinos más próximos, h_i es el campo magnético en el sitio i, $\mathbf{S}_i$ es un vector unitario de una dimensión (Ising, que habitualmente se le llama modelo de Edwards-Anderson, EA), dos dimensiones (modelo XY) o tres dimensiones (modelo de Heisenberg), y, obviamente, S_{iz} es la componente z del vector $\mathbf{S}_i$. A partir de ahora, en el resto de este trabajo, denotaremos las variables de Ising de una dimensión como σ_i. Finalmente, J_{ij} son los acoplamientos, que son variables aleatorias congeladas: es decir, $\mathbf{S}_i$ son variables dinámicas (cambian con el tiempo) mientras que J_{ij} son estáticas (son constantes en el tiempo). El hecho de que sólo interactúen los vecinos más próximos (dependiendo del modelo primeros, segundos vecinos, etc.) es una forma de modelar el decaimiento con la distancia de la interacción en sistemas reales. Sea D la dimensión del espacio en el que vive el sistema y asumiendo interacción sólo con los primeros vecinos, cada espín interacciona con $6D$ vecinos. Las dos principales distribuciones de probabilidad de los acoplamientos son la distribución gaussiana

$$P(J_{ij}) = \frac{1}{\sqrt{2\pi\Delta J_{ij}}} \exp\left[-\frac{\left(J_{ij} - \overline{J_{ij}}\right)}{2\left(\Delta J_{ij}\right)^2}\right] \tag{1.6}$$

y la distribución bimodal $\pm J$

$$P(J_{ij}) = p_1\delta(J_{ij} - J) + (1 - p_1)\delta(J_{ij} + J) \tag{1.7}$$

Otro modelo de enlaces aleatorios es el modelo de Potts de vidrios de espín de p estados [14, 15] definido como

$$\mathcal{H} \equiv -\sum_{\langle i,j\rangle} J_{ij}\,\delta_{s_i,s_j} \tag{1.8}$$

donde s_i puede tomar p valores distintos $\{0, 1, \ldots, p-1\}$. La distribución de probabilidad de los acoplamientos puede ser o bien Ec.(1.6) o bien Ec. (1.7).

En este trabajo nos vamos a centrar en el modelo de Potts de vidrios de espín y en el modelo de Edwards-Anderson de vidrios de espín de tipo Ising.

1.2 El método de las réplicas

Para hacer un análisis en física estadística primero se ha de calcular la función de partición en una realización dada del desorden congelado, una muestra (etiquetada con J)

$$Z_J = \sum_{\{\sigma_i\}} e^{-\beta H_J(\{\sigma_i\})} \tag{1.9}$$

donde la suma corre sobre todas las configuraciones posibles. Un ejemplo de realización del desorden congelado es un conjunto fijo de acoplamientos en el modelo de vidrio de espín de Edwards-Anderson (ver Sección 1.1). El observable más importante es la energía libre, que puede ser calculada como

$$F_J = -K_B T \log Z_J \tag{1.10}$$

Sin embargo, hay que promediar sobre todas las muestras, por lo que

$$F = \overline{F_J} = -K_B T \overline{\log Z_J} \tag{1.11}$$

La desventaja de esta relación es que promedia un logaritmo es bastante difícil. La solución es el método de las réplicas, basado en

$$\log Z = \lim_{n \to 0} \frac{Z^n - 1}{n} \tag{1.12}$$

Por tanto, tenemos n réplicas del sistema y el promedio sobre el desorden se puede calcular como

$$Z_n \equiv \overline{Z_J^n} = \overline{\prod_{a=1}^{n} Z_J^{(a)}} = \overline{\sum_{\{\sigma_i^a\}} \exp\left(-\beta \sum_{a=1}^{n} H_J(\{\sigma_i^a\})\right)} \tag{1.13}$$

En el caso del modelo de Edwards-Anderson esta relación se convierte en

$$\overline{Z_J^n} = \sum_{\{\sigma_i^a\}} \exp\left(\frac{1}{4}\beta^2 \sum_{ij} J \sum_{ab} \sigma_i^a \sigma_i^b \sigma_j^a \sigma_j^b\right) \tag{1.14}$$

por lo que el problema inicial de promediar sobre el desorden se ha convertido en un problema de calcular n réplicas distintas. Entonces, se debe extender a valores no enteros de n y tomar el límite cuando $n \to 0$. De la Ec. (1.14) se deduce que se puede definir un Hamiltoniano efectivo, H_{eff}, que depende de los espines de dos réplicas distintas. De hecho, todo observable que dependa de un conjunto de k promedios termales de espines puede ser reescrito usando k réplicas distintas.

1.3 Aproximaciones de los modelos de vidrios de espín con solución exacta

En la Sección 1.1, se han presentado algunos modelos realistas de vidrios de espín. Sin embargo, la solución analítica de estos modeles es bastante complicada por lo que se deben realizar algunas aproximaciones. En esta sección presentaremos dos aproximaciones que permiten cálculo analítico: la aproximación de campo medio y el modelo de droplet.

1.3.1 El modelo de Sherrington-Kirkpatrick

En 1975, Sherrington y Kirkpatrick [16] propusieron una teoría de campo medio basada en un modelo con un rango de interacciones infinito. El Hamiltoniano del modelo de Sherrington-Kirkpatrick (SK) es

$$\mathcal{H} = -\frac{1}{2}\sum_{i\neq j} J_{ij}\sigma_i\sigma_j + \sum_i h_i\sigma_i \tag{1.15}$$

donde la distribución de los acoplamientos, $P(J_{ij})$, es gaussiana (la misma para cada pajera de espines) con

$$\overline{J_{ij}} = J_0 \tag{1.16}$$

$$\overline{J_{ij}^2} = \frac{J^2}{N} \tag{1.17}$$

Nótese que, comparando este modelo con el de Edwards-Anderson, Ec. (1.5), el modelo de SK es una especie de modelo de EA en el que cada espín interacciona con un número infinito de vecinos, por lo que el modelo SK se suele interpretar a menudo como un modelo de EA con infinitas dimensiones.

Solución simétrica (fase paramagnética)

Utilizando el método de las réplicas explicado en la Sección 1.2, calcularemos en primer lugar la función de partición

$$\begin{aligned}\overline{Z^n} &= \sum_{[\sigma^a]} \exp\left\{-J_0\beta + \frac{J^2\beta^2}{2}\left[\frac{n}{2}\left(N-1\right)\right) - \frac{n\left(n-1\right)}{2}\right] \\ &+ \frac{J_0\beta}{2N}\sum_a\left(\sum_i \sigma_i^a\right)^2 + \frac{J^2\beta^2}{2N}\sum_{a<b}\left(\sum_i \sigma_i^a\sigma_i^b\right)^2\Bigg\}\end{aligned} \tag{1.18}$$

donde los índices a y b corren sobre las réplicas del sistema. Se necesita evitar lo términos cuadráticos, lo que se puede lograr usando la identidad de Hubbard-Stratonovich.

Ahora cambiamos nuestras variables por unas nuevas, Q_{ab} y m_a, definidas como

$$Q_{ab} = \frac{1}{N}\sum_{i}^{N}\langle\sigma_i^a\sigma_i^b\rangle \tag{1.19}$$

$$m_a = \frac{1}{N}\sum_{i}^{N}\langle\sigma_i^a\rangle \tag{1.20}$$

Como consecuencia, se puede definir una función de partición efectiva

$$Z_{\text{eff}} \equiv \sum_{[\sigma^a]}\exp\left[(J\beta)^2\sum_{a<b}Q_{ab}^2\sigma^a\sigma^b + J_0\beta\sum_a m_a\sigma^a\right] \tag{1.21}$$

por lo que finalmente se obtiene

$$\begin{aligned}\overline{Z^a} &\propto \int[dm]\,[dQ]\exp\left[-\frac{1}{2}NJ_0\beta\sum m_a^2 - \frac{1}{2}N\left(J\beta\right)^2\sum_{a<b}Q_{ab}^2 + N\log Z_{\text{eff}}\right] \\ &\equiv \int[dm]\,[dQ]\exp\left[-NG(m,Q)\right]\end{aligned} \tag{1.22}$$

donde

$$[dm] \equiv \prod_a dm_a \tag{1.23}$$

$$[dQ] \equiv \prod_{ab} dQ_{ab} \tag{1.24}$$

La Ec. (1.22) define una nueva función $G(m,Q)$. Sean (m_a^0, Q_{ab}^0) los puntos silla y asumamos el *Ansatz* de la solución simétrica: $m_a^0 \equiv m$ y $Q_{ab}^0 \equiv q$, es decir, todas las réplicas tienen los mismos parámetros. Por tanto, uno puede calcular la energía libre (por espín), $f(m,q)$ que es la función $G(m,Q)$ de la Ec. (1.22)

$$\begin{aligned}f(m,q) &= -\frac{J^2\beta}{4}\left(1-q^2\right) + \frac{J_0}{2}m^2 \\ &- \frac{1}{\beta}\int\frac{dz}{\sqrt{2\pi}}e^{-\frac{1}{2}z^2}\log\left[2\cosh\left(J\beta\sqrt{q}z + \beta h + J_0 m\beta\right)\right]\end{aligned} \tag{1.25}$$

y los valores en el equilibrio

$$m = \int \frac{dz}{\sqrt{2\pi}} e^{-\frac{1}{2}z^2} \tanh\left(J\beta\sqrt{q}z + \beta h + J_0 m\beta\right) \tag{1.26}$$

$$q = \int \frac{dz}{\sqrt{2\pi}} e^{-\frac{1}{2}z^2} \tanh^2\left(J\beta\sqrt{q}z + \beta h + J_0 m\beta\right) \tag{1.27}$$

Es bastante fácil calcular que si $h = 0$ cuando $T > T_f$, la única solución es $q = 0$, pero cuando $T < T_f$, el observable $q(T) \neq 0$ (de hecho cuando $T \to 0$, $q \to 1$), donde T_f es una temperatura crítica. Por tanto, se tiene un parámetro de orden. En la Figura 1.3, se representa la distribución de probabilidad de este parámetro de orden q cuando $T > T_f$ (la fase de alta temperatura, la fase paramagnética).

Sin embargo, esta solución simétrica no es correcta, al menos a bajas temperaturas, mientras que se puede asumir que sí lo es en la fase paramagnética. El fallo de la solución simétrica para $T < T_f$ es identificado por un valor negativo de la entropía a $T = 0$ y por la aparición de autovalores negativos en la matriz Hessiana. Por tanto, se ha de buscar una nueva solución a bajas temperaturas que evite estos problemas, y esta solución será la *Replica Symmetry Breaking* (Rotura de Simetría de las Réplicas) de Parisi (RSB) [17, 18, 19, 20].

Replica Symmetry Breaking de Parisi

En primer lugar, vamos a expandir el argumento de la exponencial en la Ec. (1.22), por lo que, asumiendo que $J_0 = 0$, se puede llegar a

$$\begin{aligned} G(\hat{Q}) &= \lim_{n\to 0} \frac{1}{n} \left[\frac{-1}{2}\tau \mathrm{tr}(Q^2) - \frac{1}{6}\mathrm{tr}(Q^3) - \frac{1}{12}\sum_{a,b} Q_{ab}^4 + \frac{1}{4}\sum_{a\neq b\neq c} Q_{ab}^2 Q_{ac}^2 \right. \\ &- \left. \frac{1}{8}\mathrm{tr}(\hat{Q}^4) \right] + \mathcal{O}(Q^5) \end{aligned} \tag{1.28}$$

donde $\tau = (T_c - T)/T_c$ y $\theta = -\tau$. Se pueden despreciar los dos últimos términos, $\frac{1}{4}\sum_{a\neq b\neq c} Q_{ab}^2 Q_{ac}^2$ y $-\frac{1}{8}\mathrm{tr}(\hat{Q}^4)$ porque acaban dando lugar a términos $\mathcal{O}(\tau^5)$ o $\mathcal{O}(\tau^6)$ que pueden ser ignorados.

Una vez que se ha definido la energía libre en función de la matriz $\hat{Q}$, discutiremos ahora el *Ansatz* que elegiremos para esta matriz. El primer *Ansatz* que se puede imaginar es el que usamos en la solución simétrica en las réplicas, llamémosle la matriz del paso 0 (0-step). Recordemos que la

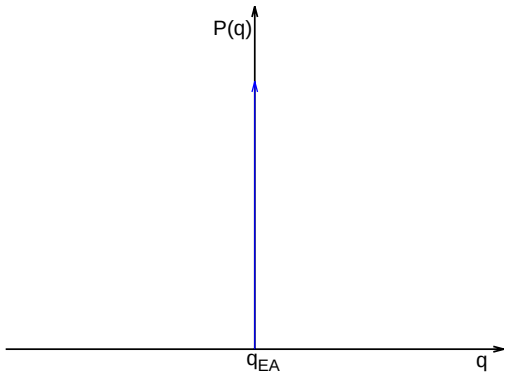

Figure 1.3: Representación esquemática de la distribución del *overlap* en la fase paramagnética.

matriz era de la forma de la Ec. (1.29)

$$\hat{Q}_{0-\text{step}} = \begin{pmatrix} 0 & & q_0 \\ & \ddots & \\ q_0 & & 0 \end{pmatrix} \tag{1.29}$$

Sin embargo, vimos que esta solución es incorrecta porque, en concreto, la entropía era negativa, por lo que debemos proponer un nuevo *Anzatz*. El primer paso consiste en crear n/m grupos de m_1 réplicas cada uno, y tome Q_{ab} el valor q_1 si a y b pertenecen al mismo grupo y q_0 si pertenecen a diferentes grupos. Ahora, la matriz se ha roto en $n/m_1 \times n/m_1$ bloques, cada uno de tamaño $m_1 \times m_1$. Llamemos a esta matriz la matriz de paso 1 (1-step), y en la Ec. (1.30) se muestra un ejemplo de una $\hat{Q}_{1-\text{step}}$ típica.

$$\hat{Q}_{1-\text{step}} = \begin{pmatrix} \overbrace{\begin{matrix} 0 & & q_1 \\ & \ddots & \\ q_1 & & 0 \end{matrix}}^{m_1} & & & & & & \\ & \begin{matrix} 0 & & q_1 \\ & \ddots & \\ q_1 & & 0 \end{matrix} & & & & & \\ & & \begin{matrix} 0 & & q_1 \\ & \ddots & \\ q_1 & & 0 \end{matrix} & & & & \\ & & & \ddots & & & \\ & & & & \begin{matrix} 0 & & q_1 \\ & \ddots & \\ q_1 & & 0 \end{matrix} & & \\ & & & & & \ddots & \\ & & & & & & \begin{matrix} 0 & & q_1 \\ & \ddots & \\ q_1 & & 0 \end{matrix} \end{pmatrix} \tag{1.30}$$

Con este *Ansatz* el resultado es mejor que en la solución simétrica pero sigue siendo incorrecta (la entropía sigue siendo negativa pero menor), por lo que se ha de probar un nuevo *Ansatz*, el segundo paso. Ahora, dividiremos cada grupo en $m_1/m_2 \times m_1/m_2$ bloques, cada uno de tamaño $m_2 \times m_2$, donde m_1 y m_2 son aún números enteros. Esta matriz de paso 2 (2-steps) tiene la forma de la Ec. (1.31).

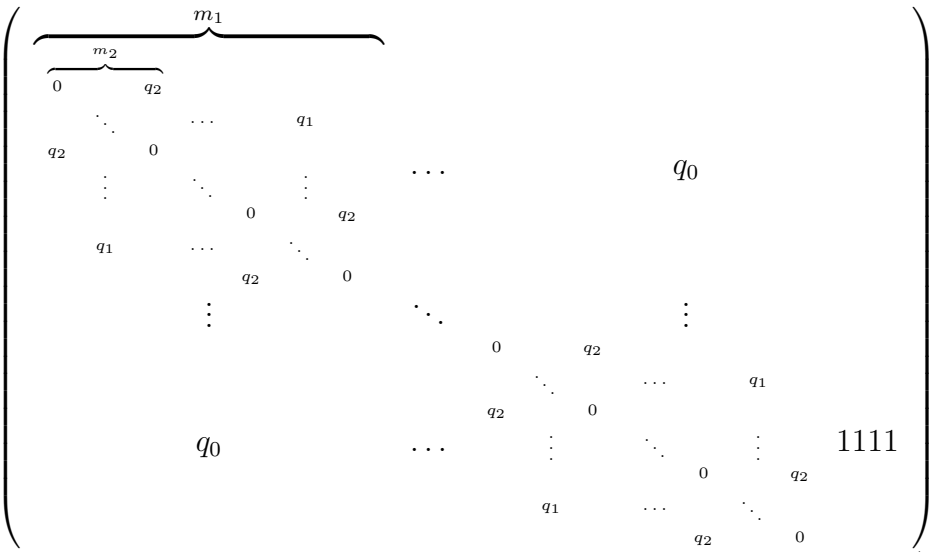

(1.31)

pero la solución sigue siendo incorrecta. Sin embargo, cuanto más pasos realizamos mejor es la solución, por lo que si se repite estos pasos infinitas veces, se hallará la solución correcta. En este caso los números enteros m_i se convierten en una variable continua $x \in (0,1)$ y todos los q_m se convierten en una función continua $q(x)$. Por tanto, una matriz de Parisi se pude escribir como $Q = (0, q(x))$, donde el primer término es el valor de la diagonal de la matriz (en los ejemplos anteriores era siempre cero porque estábamos trabajando en ausencia de campo magnético externo) y el segundo término es el valor del resto de elementos de la matriz. En presencia de un campo magnético externo el valor de los sitios de la diagonal deja de ser cero, por lo que una matriz de Parisi general es $Q = (\overline{q}, q(x))$. Antes de calcular la solución con este *Ansatz*, vamos a demostrar cómo trabajar con este tipo de matrices. La traza de la matriz es bastante fácil de calcular

$$\mathrm{tr}Q = n\overline{q} \tag{1.32}$$

Para calcular las siguientes cantidades, las calcularemos primero en un paso finito y después en el límite de infinitos pasos (∞-step).

$$\sum_{a,b}^{n} Q_{ab} = n\left[\overline{q} + \sum (m_i - m_{i+1}) q_i\right] \to n\overline{q} - \int_n^1 q(x)dx \tag{1.33}$$

$$\sum_{a,b}^{n} Q_{ab}^{l} = n\left[\overline{q}^{l} + \sum (m_i - m_{i+1}) q_i^{l}\right] \rightarrow n\overline{q}^{l} - \int_n^1 q^{l}(x)dx \tag{1.34}$$

Finalmente, calcularemos el producto de dos matrices de Parisi, $A = (\overline{a}, a(x))$ y $B = \left(\overline{b}, b(x)\right)$. El resultado es la matriz $AB = C = (\overline{c}, c(x))$ donde

$$\overline{c} = \overline{a}\overline{b} - \langle ab \rangle \tag{1.35}$$

$$\begin{aligned} c(x) &= n a(x)b(x) + \left[\overline{a} - \langle a \rangle\right] b(x) + \left[\overline{b} - \langle b \rangle\right] a(x) \\ &- \int_n^x \left[a(x) - a(y)\right]\left[b(x) - b(y)\right] dy \end{aligned} \tag{1.36}$$

y con

$$\langle a \rangle = \int_n^1 a(x)dx \tag{1.37}$$

Ahora, ya podemos calcular los términos relevantes de la energía libre, Ec. (1.28), cerca del punto crítico sin campo magnético externo, que se expresa como $G(q)$.

$$G(q) = \lim_{n \to 0} \frac{1}{2n}\left[\theta \mathrm{tr} Q^2 - \frac{1}{3}\mathrm{tr} Q^3 - \frac{1}{6}\sum_{a,b}(Q_{ab})^4\right] \tag{1.38}$$

El término cuadrático se calcula usando las Ecs. (1.35) y (1.32)

$$\mathrm{tr} Q^2 = -n \int_n^1 q^2(x)dx \tag{1.39}$$

El término cuártico se calcula usando la Ec. (1.34)

$$\sum_{a,b} Q_{ab}^4 = -n \int_n^1 q^4(x)dx \tag{1.40}$$

Finalmente el término cúbico, que es el más complicado, se calcula utilizando las Ecs. (1.35), (1.36) y (1.32)

$$\mathrm{tr} Q^3 = n\left[\int_n^1 x q^3(x)dx + 3\int_n^1 dx q(x)\int_n^x q^2(y)dy\right] \tag{1.41}$$

Substituyendo las Ecs. (1.39), (1.40) y (1.41) en la Ec. (1.38) y tomando el límite $n \rightarrow 0$, se encuentra que la energía libre

$$G(q) = \frac{1}{2}\int_0^1 dx\left[|\theta| q^2(x) + \frac{1}{6}q^4(x) - \frac{1}{3}x q^3(x) - q(x)\int_0^x q(y)dy\right] \tag{1.42}$$

Ahora, la ecuación de punto silla se puede escribir como

$$\frac{\delta G}{\delta q(x)} = 0 \tag{1.43}$$

y haciendo la derivada funciona, se halla

$$2|\theta|q(x) + \frac{2}{3}q^3(x) - xq(x) - 2q\int_x^1 q(y)dy - \int_0^x xq(x)dx \tag{1.44}$$

y derivando con respecto a x se encuentra

$$|\theta| + q^2(x) - xq(x) - \int_x^1 q(y)dy = 0 \tag{1.45}$$

y derivando de nuevo se obtiene finalmente

$$q(x) = \frac{x}{2} \qquad \text{or} \qquad \frac{dq}{dx} = 0 \tag{1.46}$$

La solución es $q(x) = x/2$ para valores pequeños de x y $q(x) = q_{\max}$ constante para valores grandes de x (nótese que si la solución fuera $q(x) = q_0$ en todo el rango de $x \in (0, 1)$, se recobraría la solución simétrica en las réplicas). Sea x_1 el punto en el que cambia el comportamiento de la solución. Como la solución tiene que ser continua, $2q_{\max} = x_1$ y substituyendo en la Ec. (1.45) se halla que

$$q_{\max} = |\theta| + \mathcal{O}(\theta^2) \tag{1.47}$$

En la Figura 1.4 se puede observar esta solución. Nótese que si existe un campo magnético externo no nulo, de acuerdo a la Ref. [21], existe otra zona plana para valores pequeños de x con valor

$$q_{\min}(h) = \frac{3}{4}\left[\frac{h^2}{J^2}\right]^{\frac{2}{3}} \tag{1.48}$$

Estudiaremos ahora la función de distribución del *overlap*. En general, se puede escribir que

$$P(q) = \frac{1}{n(n-1)}\sum_{a\neq b}\delta(Q_{ab} - q) \tag{1.49}$$

Substituyendo Q_{ab} con una matriz de Parisi, se halla que

$$\begin{aligned} P(q) &= \frac{1}{n(n-1)} n\left[(n-m_1)\delta(q-q_0) + (m_1-m_2)\delta(q-q_2) + \dots\right] \\ &\to \frac{-1}{n-1}\int_n^1 \delta[q-q(x)]dx \end{aligned} \tag{1.50}$$

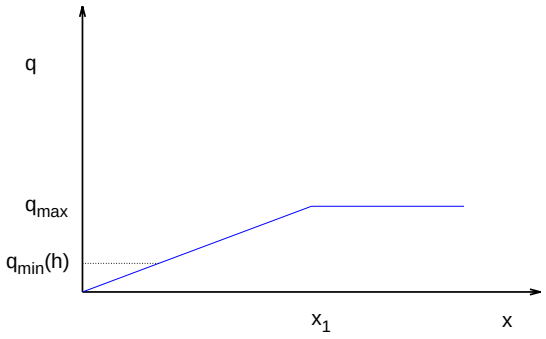

Figure 1.4: Representación esquemática de la solución hallada para RSB. La línea de puntos es la zona plana a bajas temperaturas en presencia de un campo magnético externo.

Finalmente, tomando el límite se llega a

$$P(q) = \frac{dx(q)}{dq} \tag{1.51}$$

donde $x(q)$ es la función inversa de $q(x)$. Nótese que en esta solución, $P(q)$ tiene una función delta de Dirac en $q = q_{\max}$ y no es nula en $(0, q_{\max})$. En la Figura 1.5, se puede observar una representación esquemática de este resultado.

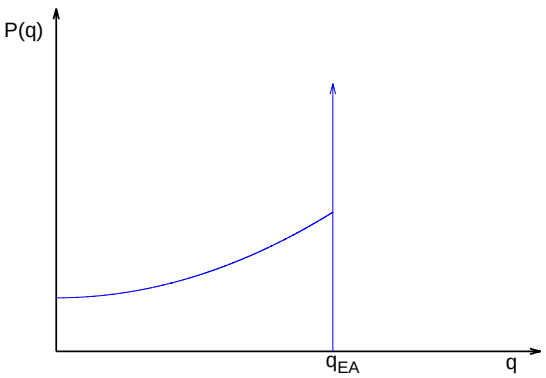

Figure 1.5: Representación esquemática de la distribución del *overlap* de la solución RSB.

Finalmente, como corolario, si se calcula la distribución del *overlap* de

tres réplicas, se halla que

$$\begin{aligned} P(q_1,q_2,q_3) &= \frac{1}{2}P(q_1)x(q_1)\delta(q_1-q_2)\delta(q_1-q_3) \\ &+ \frac{1}{2}\left[P(q_1)P(q_2)\theta(q_1-q_2)\delta(q_2-q_3)\right. \\ &+ P(q_1)P(q_3)\theta(q_3-q_1)\delta(q_1-q_2) \\ &+ \left.P(q_2)P(q_3)\theta(q_2-q_3)\delta(q_3-q_1)\right] \end{aligned} \tag{1.52}$$

$P(q_1,q_2,q_3)$ únicamente no se anula cuando los tres *overlaps* son iguales o cuando lo son dos y el tercero es mayor que ambos. Por tanto, los *overlaps* se organizan siguiendo las normas de un espacio ultramétrico.

1.3.2 Modelo de droplet

La teoría de los *droplets* fue desarrollada por Bray y Moore [22, 23] usando el grupo de renormalización de Migdal-Kadanoff [24, 25], y desde un punto de vista fenomenológico por Fisher y Huse [26, 27, 28]. En este caso se trabaja con un Hamiltoniano con interacciones de corto alcance. Un *droplet* es una región compacta en la que los espines están invertidos. La distribución de probabilidad de la energía libre de un *droplet* es

$$P\left[\Delta F(L)\right] = \frac{1}{L^y} f\left(\frac{\Delta F}{L^y}\right) \tag{1.53}$$

Calculemos ahora la función de correlación [28]

$$G(r_{ij}) = \overline{\left[\langle\sigma_i\sigma_j\rangle - \langle\sigma_i\rangle\langle\sigma_j\rangle\right]^2} \tag{1.54}$$

A $T=0$, esta función de correlación tiende a cero. Sin embargo, a temperatura $T \ll 1$

$$G(r_{ij}) \propto P\left[\Delta F(r_{ij}\right] \simeq P[0] \tag{1.55}$$

por lo que

$$G(r_{ij}) \propto \frac{1}{r^y} \qquad \text{and} \qquad \xi \to \infty \tag{1.56}$$

Ahora, si se elige una función de correlación un poco diferente, se puede calcular que

$$G_1(r_{ij}) = \overline{\langle\sigma_i\sigma_j\rangle^2} - \overline{\langle\sigma_i\rangle^2} - \overline{\langle\sigma_j\rangle^2} \sim (\overline{q^2} - \overline{q}^2) \sim \frac{1}{r^y} \to 0 \tag{1.57}$$

por lo que la distribución del *overlap* es bastante simple, como se muestra en la Figura 1.6.

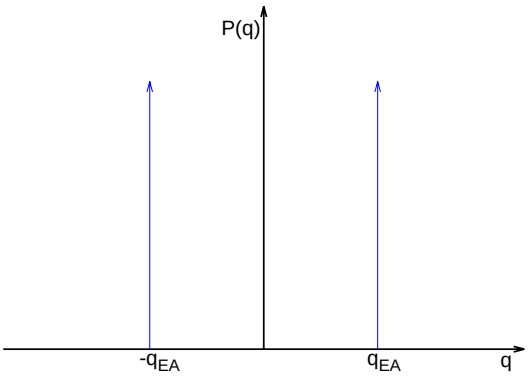

Figure 1.6: Representación esquemática de la distribución del *overlap* en un *droplet*.

Finalmente, estudiaremos el comportamiento de un *droplet* en presencia de un campo magnético externo, comparando cómo escalan la energía de la pared de un *droplet* y el campo [2]. En primer lugar, la energía de la pared de un dominio escala como L^y, donde y debe satisfacer la desigualdad

$$y \leq \frac{D-1}{2} \tag{1.58}$$

donde D es la dimensión del sistema. Por otra parte, el campo externo escala como $L^{D/2}$. De acuerdo con la Ec. (1.58), $y < D/2$ para todas las dimensiones, por lo que el campo crece más rápidamente que la energía de la pared del dominio, por lo que el orden magnético no es estable a largas distancias.

1.3.3 Consecuencias

La solución RSB en campo medio (interpretándolo como un modelo con interacciones de corto alcance en dimensión infinita) es la solución exacta por encima y en la dimensión crítica superior, $D_U = 6$, mientras que el modelo *droplet* es la solución exacta en bajas dimensiones. Sin embargo, no se conoce el comportamiento de un sistema realista en tres dimensiones. Afortunadamente, como hemos comprobado en esta sección, el comportamiento esperado en cada escenario es completamente diferente. RSB predice una transición de fase a un fase de vidrio de espín en presencia de campo magnético mientras que el modelo *droplet* no. Además, la distribución de probabilidad del *overlap* es bastante diferente en estos escenarios: en RSB, hemos hallado una función

delta de Dirac en q_{EA} y una probabilidad no nula $P(q) > 0$ para $0 < q < q_{\mathrm{EA}}$, Figura 1.5; mientras que en el modelo *droplet* hemos hallado sólo una función delta de Dirac en q_{EA}, Figura 1.6. Esta diferencia en $P(q)$ será bastante útil para distinguir si el escenario RSB o el *droplet* es el correcto. De hecho, hay otro escenario intermedio, TNT (trivial-no trivial) pero nos centraremos en los dos primeros.

1.4 Características de la fase de vidrio de espín

En las secciones anteriores hemos explicado varios modelos de vidrios de espín y la transición de fase de algunos de ellos. Ahora, presentaremos algunas características de los vidrios de espín, especialmente de su fase de vidrio de espín. La frustración es una de las principales causas de los tiempos de relajación largos que exhiben estos sistemas en su fase de vidrio de espín, y como consecuencia, la hipótesis de ergodicidad deja de cumplirse. Además, una herramienta útil para detectar transiciones de fase, el parámetro de orden de los vidrios de espín, será presentado.

1.4.1 Broken ergodicity

Si se quiere medir un observable en un experimento, se debería probar con un tiempo de observación mayor que el tiempo de relajación más largo del sistema. De esta forma, el sistema puede explorar todo el espacio de fase, y esta medida es equivalente a un promedio estadístico en equilibrio. Este fenómeno se conoce como ergodicidad. Sin embargo, en algunos sistemas, estos no ocurren, por ejemplo si el tiempo de relajación diverge en el límite termodinámico ($N \to \infty$). Estos sistemas se suelen conocer como no ergódicos.

De acuerdo con la solución RSB de Parisi del modelo SK (Sección 1.3.1 y Refs. [17, 18, 19, 20]), éste es el caso de los vidrios de espín y su fase de vidrio de espín en la que existen varios estados puros (fases). En el límite termodinámico, estos estados (también llamados valles porque son los mínimos de la energía libre) tienden a tener la misma energía libre, pero las barreras entre ellos tienden a infinito. Por tanto, el sistema no puede explorar todo el rango de microestados y el sistema se convierte en no ergódico. Sin embargo, no está claro si este es el comportamiento de un vidrio de espín con interacciones de alcance finito.

1.4.2 Parámetro de orden

Un parámetro de orden, si existe, es una herramienta común y útil para estudiar las transiciones de fase. Se trata de un observable cuyo comportamiento en cada fase es diferente. Un ejemplo de parámetro de orden es el *overlap* definido en la Sección 1.3. Su distribución de probabilidad tiene sólo una delta de Dirac en $q = 0$ en la fase paramagnética (Figura 1.3), pero en la fase de vidrio de espín tiene dos deltas de Dirac en el escenario *droplet* (Figura 1.6) o dos deltas de Dirac y una parte continua en el escenario RSB de Parisi (Figura 1.5).

Respecto a los vidrios de espín, el primer parámetro de orden fue propuesto por Edwards y Anderson [13], definido como

$$q_{\mathrm{EA}} = \lim_{t\to\infty} \lim_{N\to\infty} \overline{\langle \sigma_i(t_0)\sigma_i t_0 + t)\rangle} \tag{1.59}$$

donde el promedio térmico corre sobre un conjunto de distintos valores de t_0. Como comentamos más arriba, en el límite termodinámico, las barreras entre las diferentes fases tienden a infinito, por lo que el sistema no es capaz de cambiarse del valle en el que está. Como consecuencia, esta cantidad es una medida de la magnetización local media, promediada sobre todos los valles. Puede también escribirse como

$$q_{\mathrm{EA}} = \overline{\sum_a P_a \langle \sigma_i \rangle_a^2} \tag{1.60}$$

donde el índice a corre sobre todas las fases y P_a es la probabilidad térmica

$$P_a = \frac{e^{-\beta F_a}}{\sum_b e^{-\beta F_b}} \tag{1.61}$$

Definamos ahora la magnetización cuadrática local media en equilibrio

$$q = \overline{\langle \sigma_i \rangle^2} \tag{1.62}$$

Calculándola sólo sobre una muestra, se puede escribir como

$$q_J = \frac{1}{N}\sum_i \langle \sigma_i \rangle^2 = \frac{1}{N}\sum_i \sum_{ab} P_a P_b \langle \sigma_i \rangle_a \langle \sigma_i \rangle_b \tag{1.63}$$

Es también bastante útil calcular la correlación entre distintas fases, por lo que definimos el *overlap* para una sola muestra como

$$q_{ab} = \frac{1}{N}\sum_i \langle \sigma_i^a \rangle \langle \sigma_i^b \rangle \tag{1.64}$$

que tiene la propiedad de $|q_{ab}| \leq 1$. Estudiando la distribución de probabilidad de esta cantidad [29], se halla que

$$P(q) = \overline{\langle \delta(q - q_{ab}) \rangle} = \overline{\sum_{ab} P_a P_b \delta(q - q_{ab})} \tag{1.65}$$

Si solo hay dos fases, como en el modelo *droplet*, $P(q)$ sería la suma de dos funciones delta de Dirac (una en $-q_{\mathrm{EA}}$ y la otra en q_{EA}), como encontramos antes (Figura 1.6). Por otra parte, si el sistema presenta una rotura de ergodicidad no trivial, como RSB, $P(q)$ tendría también una parte continua, como encontramos anteriormente (Figura 1.5).

Finalmente, vamos a aplicar el método de las réplicas (Sección 1.2) para calcular estas cantidades en el contexto en el que trabajaremos en esta tesis. De acuerdo con Ref. [2], se puede definir

$$q^{\alpha\beta} = \langle \sigma_i^\alpha \sigma_i^\beta \rangle \tag{1.66}$$

donde los índices α y β indican un par de réplicas distintas ($\alpha \neq \beta$). Por tanto, se puede identificar

$$q = \lim_{n \to 0} \frac{1}{n(n-1)} \sum_{\alpha \neq \beta} q^{\alpha\beta} \tag{1.67}$$

donde n indica el número de réplicas. Finalmente, también se puede identificar el parámetro de orden de Edwards-Anderson como

$$q_{\mathrm{EA}} = \max_{\alpha\beta} q^{\alpha\beta} \tag{1.68}$$

1.4.3 Frustración

La Frustración es una de las mayores contribuciones al tremendamente complicado paisaje de energía libre que provoca la típica lenta dinámica de los vidrios de espín. Como ejemplo, vamos a trabajar con un vidrio de espín de tipo Ising de Edwards-Anderson sin campo magnético externo. Como se puede observar en la Figura 1.7, como los acoplamientos son aleatorios, ciertas configuraciones de ellos provocan que algunos espines (en la figura el de la esquina inferior derecha) no sean capaces de encontrar la posición más estable. En nuestro ejemplo, el espín de la esquina inferior derecha tiende a estar apuntando hacia arriba para estar en paralelo con el espín de la esquina inferior izquierda, debido al acoplamiento que hay entre ellos. Sin embargo, también tiende a estar apuntando hacia abajo para estar antiparalelo al espín de la esquina superior derecha, debido al acoplamiento entre ambos.

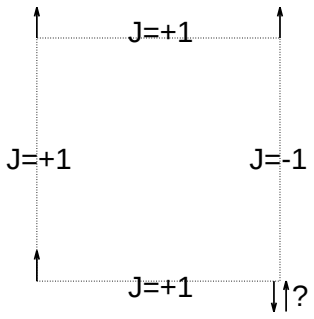

Figure 1.7: Un ejemplo de una plaqueta 2×2 frustrada. El espín de la esquina inferior derecha no tiene un estado estable.

En el modelo de Edwards-Anderson (como demuestra este ejemplo) y en el modelo de Potts, los dos principales modelos en este trabajo, la frustración es una consecuencia del desorden. Sin embargo, en general, la frustración es un fenómeno independiente y ciertos modelos la presentan sin tener desorden.

Chapter 1

Introduction

Spin glasses[1] are magnetic systems (that is, a collection of spins) which show a phase transition to a low temperature frozen phase from a paramagnetic one. However, this phase does not exhibit long range order (whereas ferromagnetic and antiferromagnetic materials do), so this phase is a kind of frozen disordered. Therefore, the local magnetization m_i is not zero whereas the mean magnetization

$$M = \frac{\sum_i m_i}{N} \tag{1.1}$$

where N is the number of total spins, and the magnetization at moment $\mathbf{k}$

$$M_{\mathbf{k}} = \frac{\sum_i e^{-i\mathbf{k}\cdot\mathbf{r}_i} m_i}{N} \tag{1.2}$$

do vanish for all moments $\mathbf{k}$. The absence of long range order (unlike antiferromagnetic materials) can be checked with neutron scattering experiments.

The metallic or canonical spin glasses were the first type of spin glasses studied. These materials are metallic alloys created by adding magnetic impurities to a metallic base, for example, CuMn. It is well known that in a ferromagnet (like Fe), the magnetic interaction is calculated by the exchange interaction, so one gets that

$$H = -J\mathbf{S}_1\mathbf{S}_2 \tag{1.3}$$

where $\mathbf{S}_1$ and $\mathbf{S}_2$ are the spins (that is, the magnetic moments) of the magnetic atoms. However, in a metallic spin glass, magnetic atoms are impurities so one has a kind of indirect exchange interaction, a magnetic impurity interacts with a conduction electron which, later, interacts with another magnetic

[1] Many reviews have been published, we will focus on Refs. [2, 3, 5].

impurity. This interaction is the so-called RKKY interaction (due to the fact that it was studied by Runderman and Kittel in 1954 [6], Kasuya in 1956 [7] and Yosida in 1957 [8]) and the coupling expression is

$$J(r) = J_0 \frac{\cos(2k_F r + \varphi_0)}{(k_F r)^3} \tag{1.4}$$

where J_0 and φ_0 are constants and k_F is the Fermi wave number of the host metal (in our example, Cu).

The relaxation times in the frozen spin glass phase are extremely long, so the study of the dynamic out of the equilibrium is quite useful to compare with experiments. Moreover, several phenomena arise in this regime. The behaviour of the system depends on the process of cooling and the time, t_w, spent in the spin glass phase, that is, spin glasses exhibit *aging* (see for example Ref. [9]). If the system evolves a time t_w at a fixed temperature, T, in the spin glass phase, two examples of aging phenomena emerge: the thermoremanent magnetization (the system evolves in presence of an external magnetic field and then it is switched off) and the zero-field cooled magnetization (the external magnetic field is switched on after the system spent a time t_w in the spin glass phase). Examples of this kind of experiments is shown in Figures 1.1 and 1.2. Besides, if the temperature in the spin glass phase is not constant, more phenomena arise, like rejuvenation and memory (see Chapter 6).

To sum up, the main characteristics of a spin glass in its spin glass phase are that the magnetic moments are frozen, absence of long range order ($M_{\mathbf{k}} = 0$ and $M = 0$), long relaxation times and the dependence on the cooling protocol.

Finally, in the rest of this work, $\langle(\cdots)\rangle$ will denote the usual thermal average and $\overline{(\cdots)}$ will denote the average over the (quench) disorder.

1.1 Models of spin glasses

Many spin glass models have been developed to modelize real systems, with different ways to deal with the problem. We will describe here some of them briefly. The first kind of models one can study is a system that reproduces the experimental spin glass described in the previous section. For example, in the RKKY model one has impurities that produce an interaction like Eq. (1.4). This kind of models with impurities are random-site models. However, another kind of spin glass models have been developed, the random-bond

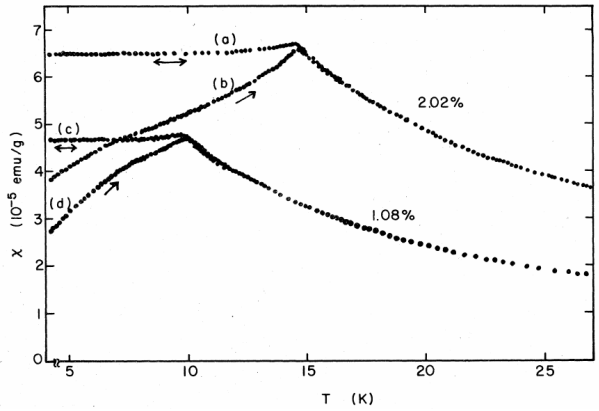

Figure 1.1: Susceptibility of two different samples of CuMn, with 1.08% and 2.02% of Mn, when they are reheated. Lines (b) and (d) are the zero field cooled experiment, whereas in lines (a) and (c) the system had been cooled in presence of a magnetic field $h = 5.90$ Oe. Above the critical temperature. T_c, the susceptibility of both protocols coincides but it do not below T_c. Figure from Ref. [10].

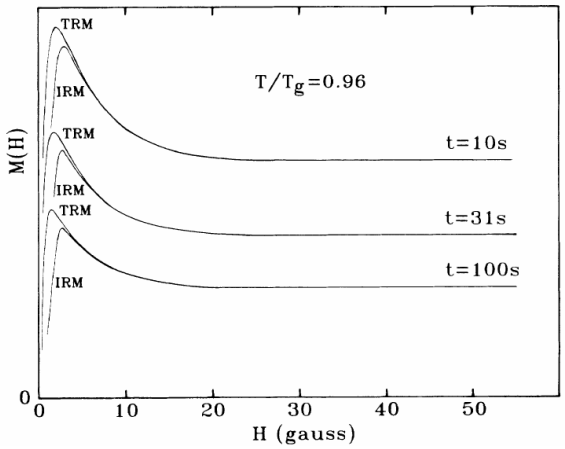

Figure 1.2: Remanent magnetization of $(Fe_{0.15}Ni_{0.85})_{75}P_{16}B_6Al_3$ at a temperature T with $T/T_g = 0.96$ where T_g is the critical temperature after removing the magnetic field H. TRM means that the system was cooled in a magnetic field H, whereas IRM means that the system was cooled in absence of a magnetic field and at temperature T a pulse of 30 s of a magnetic field H was applied. The measurements were performed at a time t after removing the field H. Figure from Ref. [11].

models. Edwards and Anderson [13] proposed the first of this kind of models

$$\mathcal{H} = -\sum_{\langle i,j \rangle} J_{ij} \mathbf{S}_i \mathbf{S}_j - \sum_i h_i S_{iz} \tag{1.5}$$

where $\langle i,j \rangle$ means the sum runs over the nearest neighbours, h_i is the magnetic field in the site i, $\mathbf{S}_i$ is a unitary vector of one dimension (Ising, which is the usual so-called Edwards-Anderson, EA, model), two dimensions (XY model) or three dimensions (Heisenberg model), and, obviously, S_{iz} is the z component of the vector $\mathbf{S}_i$. Following, in the rest of this work, we will denote the Ising one dimensional variable as σ_i. Finally, J_{ij} are the couplings, which are random quench variables: that is, $\mathbf{S}_i$ are dynamical variables (that changes with the time) whereas J_{ij} are static ones (they are constant in time). The fact that only nearest neighbours (first, second or so on nearest neighbours, depending on the model) interact is way of modelize the decay with space of the interaction in real systems. Let D be the dimensionality of the space where the system lives and assuming only interaction with first nearest neighbours, every spin interacts with $6D$ neighbours.The two main probability distribution of the couplings are the Gaussian distribution

$$P(J_{ij}) = \frac{1}{\sqrt{2\pi\Delta J_{ij}}} \exp\left[-\frac{\left(J_{ij} - \overline{J_{ij}}\right)}{2\left(\Delta J_{ij}\right)^2}\right] \tag{1.6}$$

and the $\pm J$ bimodal distribution

$$P(J_{ij}) = p_1\delta(J_{ij} - J) + (1 - p_1)\delta(J_{ij} + J) \tag{1.7}$$

Another random-bond model is the p-states Potts spin glass model [14, 15] defined as

$$\mathcal{H} \equiv -\sum_{\langle i,j \rangle} J_{ij}\, \delta_{s_i,s_j} \tag{1.8}$$

where s_i can take p different values $\{0, 1, \ldots, p-1\}$. The probability distribution of the couplings could be either Eqs. (1.6) or (1.7).

In this work, we will focus on Potts spin glass model and Edwards-Anderson Ising spin glass model.

1.2 The replica method

To perform an analysis in statistical physics, one must firstly compute the partition function in a given realization of the quench disorder, a sample, (labeled by J)

$$Z_J = \sum_{\{\sigma_i\}} e^{-\beta H_J(\{\sigma_i\})} \tag{1.9}$$

where the sum runs over all the possible configurations. An example of realization of the quench disorder is a fixed set of couplings Edwards-Anderson

spin glass model (see Section 1.1). The main quantity is the free energy, that can be computed as

$$F_J = -K_B T \log Z_J \tag{1.10}$$

However, one must average over the samples, so

$$F = \overline{F_J} = -K_B T \overline{\log Z_J} \tag{1.11}$$

The disadvantage of this relation is that averaging a logarithm is quite difficult. The solution is the replica method, based on

$$\log Z = \lim_{n \to 0} \frac{Z^n - 1}{n} \tag{1.12}$$

Therefore, we have n replicas of the system and the average over the disorder can be computed as

$$Z_n \equiv \overline{Z_J^n} = \overline{\prod_{a=1}^{n} Z_J^{(a)}} = \overline{\sum_{\{\sigma_i^a\}} \exp\left(-\beta \sum_{a=1}^{n} H_J(\{\sigma_i^a\})\right)} \tag{1.13}$$

In the case of the Edwards-Anderson model this relation becomes in

$$\overline{Z_J^n} = \sum_{\{\sigma_i^a\}} \exp\left(\frac{1}{4}\beta^2 \sum_{ij} J \sum_{ab} \sigma_i^a \sigma_i^b \sigma_j^a \sigma_j^b\right) \tag{1.14}$$

so the initial problem of averaging over the disorder have become in a problem of computing n different replicas. Then, one must extend it to a non-integer value of n and take the limit when $n \to 0$. From Eq. (1.14) one notices that an effective Hamiltonian, H_{eff}, which depends on the spins of two different replicas can be defined. In fact, every observable that depends on a set of k thermal averages of spins, this observable can be rewritten using k different replicas.

1.3 Approximations of spin glass models with exact solution

In Section 1.1, several realistic spin glasses models have been presented. However, the analytic solution of these models is quite difficult, so some approximation should be performed. In this section, we will present two approaches which allow us an analytical computation: the mean field approximation and the droplet model.

1.3.1 Sherrington-Kirkpatrick model

In 1975, Sherrington and Kirkpatrick [16] propounded a mean field theory based on a model with infinite range interactions. The Hamiltonian of Sherrington-Kirkpatrick (SK) model is

$$\mathcal{H} = -\frac{1}{2}\sum_{i\neq j} J_{ij}\sigma_i\sigma_j + \sum_i h_i\sigma_i \tag{1.15}$$

where the distribution of the couplings, $P(J_{ij})$ is Gaussian (the same for every pair of spins) with

$$\overline{J_{ij}} = J_0 \tag{1.16}$$

$$\overline{J_{ij}^2} = \frac{J^2}{N} \tag{1.17}$$

Notice that, comparing this model with the Edwards-Anderson one, Eq. (1.5), SK model is a kind of EA model where every spin interacts with an infinite number of neighbours, thus SK model is usually interpreted as an EA model in infinite dimensions.

Symmetric solution (paramagnetic phase)

Using the replica method explained in Section 1.2, we will firstly compute the partition function

$$\begin{aligned}\overline{Z^n} &= \sum_{[\sigma^a]} \exp\left\{-J_0\beta + \frac{J^2\beta^2}{2}\left[\frac{n}{2}\left(N-1\right)\right) - \frac{n\left(n-1\right)}{2}\right] \\ &+ \frac{J_0\beta}{2N}\sum_a\left(\sum_i \sigma_i^a\right)^2 + \frac{J^2\beta^2}{2N}\sum_{a<b}\left(\sum_i \sigma_i^a\sigma_i^b\right)^2\right\}\end{aligned} \tag{1.18}$$

where the indices a and b runs over the replicas of the system. One needs to avoid quadratic terms, which can be achieved by using the Hubbard-Stratonovich identity.

Now, we will change our variables to new ones, Q_{ab} and m_a, defined as

$$Q_{ab} = \frac{1}{N}\sum_i^N \langle\sigma_i^a\sigma_i^b\rangle \tag{1.19}$$

$$m_a = \frac{1}{N}\sum_i^N \langle\sigma_i^a\rangle \tag{1.20}$$

As a consequence, an effective partition function can be defined

$$Z_{\text{eff}} \equiv \sum_{[\sigma^a]} \exp\left[(J\beta)^2 \sum_{a<b} Q_{ab}^2 \sigma^a \sigma^b + J_0 \beta \sum_a m_a \sigma^a\right] \tag{1.21}$$

thus one finally gets

$$\begin{aligned}\overline{Z^a} &\propto \int [dm]\,[dQ] \exp\left[-\frac{1}{2} N J_0 \beta \sum m_a^2 - \frac{1}{2} N (J\beta)^2 \sum_{a<b} Q_{ab}^2 + N \log Z_{\text{eff}}\right] \\ &\equiv \int [dm]\,[dQ] \exp\left[-NG(m,Q)\right] \end{aligned} \tag{1.22}$$

where

$$[dm] \equiv \prod_a dm_a \tag{1.23}$$

$$[dQ] \equiv \prod_{ab} dQ_{ab} \tag{1.24}$$

Eq. (1.22) defines a new function $G(m,Q)$. Let (m_a^0, Q_{ab}^0) be the saddle point and let us assume the symmetric solution Ansatz: $m_a^0 \equiv m$ and $Q_{ab}^0 \equiv q$, that is, all the replicas have the same parameters. Therefore, one can compute the free energy (per spin), $f(m,q)$ which is the function $G(m,Q)$ in the previous Eq. (1.22)

$$\begin{aligned} f(m,q) &= -\frac{J^2\beta}{4}\left(1-q^2\right) + \frac{J_0}{2} m^2 \\ &- \frac{1}{\beta} \int \frac{dz}{\sqrt{2\pi}} e^{-\frac{1}{2}z^2} \log\left[2\cosh\left(J\beta\sqrt{q}z + \beta h + J_0 m \beta\right)\right] \end{aligned} \tag{1.25}$$

and the equilibrium values

$$m = \int \frac{dz}{\sqrt{2\pi}} e^{-\frac{1}{2}z^2} \tanh\left(J\beta\sqrt{q}z + \beta h + J_0 m\beta\right) \tag{1.26}$$

$$q = \int \frac{dz}{\sqrt{2\pi}} e^{-\frac{1}{2}z^2} \tanh^2\left(J\beta\sqrt{q}z + \beta h + J_0 m\beta\right) \tag{1.27}$$

It is quite easy to compute that if $h = 0$, when $T > T_f$ the only solution is $q = 0$, but when $T < T_f$, the observable $q(T) \neq 0$ (in fact when $T \to 0$, $q \to 1$), where T_f is a critical temperature. Thus one has an order parameter. In Figure 1.3, the probability distribution of this order parameter q is represented when $T > T_f$ (the high temperature phase, the paramagnetic one).

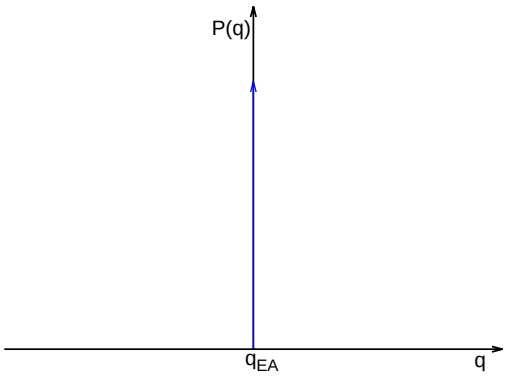

Figure 1.3: Schematic representation of the distribution of the overlap in the paramagnetic phase.

However, this symmetric solution is not correct, at least at low temperatures, whereas one can assume that it does hold in the paramagnetic phase. The breakdown of the symmetric solution for $T < T_f$ is signaled by a negative value of the entropy at $T = 0$ and for the appearance of negative eigenvalues in the Hessian matrix. Therefore, one has to compute a new solution at low temperatures that avoids these problems, and this solution will be the Parisi's Replica Symmetry Breaking (RSB) [17, 18, 19, 20].

Parisi's Replica Symmetry Breaking

Firstly, we will expand the argument of the exponential in Eq. (1.22), so, assuming $J_0 = 0$, we can get that

$$\begin{aligned} G(\hat{Q}) &= \lim_{n\to 0}\frac{1}{n}\left[\frac{-1}{2}\tau\mathrm{tr}(Q^2) - \frac{1}{6}\mathrm{tr}(Q^3) - \frac{1}{12}\sum_{a,b}Q_{ab}^4 + \frac{1}{4}\sum_{a\neq b\neq c}Q_{ab}^2Q_{ac}^2\right. \\ &- \left.\frac{1}{8}\mathrm{tr}(\hat{Q}^4)\right] + \mathcal{O}(Q^5) \end{aligned} \tag{1.28}$$

where $\tau = (T_c - T)/T_c$ and $\theta = -\tau$. One can ignore the two last terms, $\frac{1}{4}\sum_{a\neq b\neq c}Q_{ab}^2Q_{ac}^2$ and $-\frac{1}{8}\mathrm{tr}(\hat{Q}^4)$ because they finally get terms $\mathcal{O}(\tau^5)$ or $\mathcal{O}(\tau^6)$ which can be ignored.

Once one has defined the free energy in function of the matrix $\hat{Q}$, we will now discuss the Ansatz for this matrix. The first Ansatz one could imagine is the one that we have used in the replica symmetric solution, let us name

it the 0-step matrix. Remind that the matrix was like in Eq. (1.29)

$$\hat{Q}_{0-\text{step}} = \begin{pmatrix} 0 & & q_0 \\ & \ddots & \\ q_0 & & 0 \end{pmatrix} \tag{1.29}$$

However, we saw that this solution is incorrect because, in particular, the entropy was negative, so one can deal with a new Ansatz. The first step consists of creating n/m groups of m_1 replicas every one, and let Q_{ab} be q_1 if a and b belong to the same group and q_0 if they belong to different groups. Now, the matrix has been broken into $n/m_1 \times n/m_1$ blocks, every one of size $m_1 \times m_1$. Let us name it the 1-step matrix and in Eq. (1.30), an example of a typical $\hat{Q}_{1-\text{step}}$ is shown.

$$\hat{Q}_{1-\text{step}} = \begin{pmatrix} \overbrace{0 & & q_1}^{m_1} & & & & & & \\ & \ddots & & q_0 & & \cdots & & q_0 & \\ q_1 & & 0 & & & & & & \\ & & & 0 & & q_1 & & & \\ & q_0 & & & \ddots & & \cdots & & q_0 \\ & & & q_1 & & 0 & & & \\ & \vdots & & & \vdots & & \ddots & & \vdots \\ & & & & & & 0 & & q_1 \\ & q_0 & & & q_0 & & \cdots & \ddots & \\ & & & & & & & q_1 & & 0 \end{pmatrix} \tag{1.30}$$

With this Ansatz the result is better than in the replica symmetric solution but it is still incorrect (the entropy is also negative but smaller), so a new Ansatz can be tested, the second step. Now one divide every group in $m_1/m_2 \times m_1/m_2$ blocks, every one of size $m_2 \times m_2$, where m_1 and m_2 are

still integers. This 2-steps matrix reads like in Eq. (1.31).

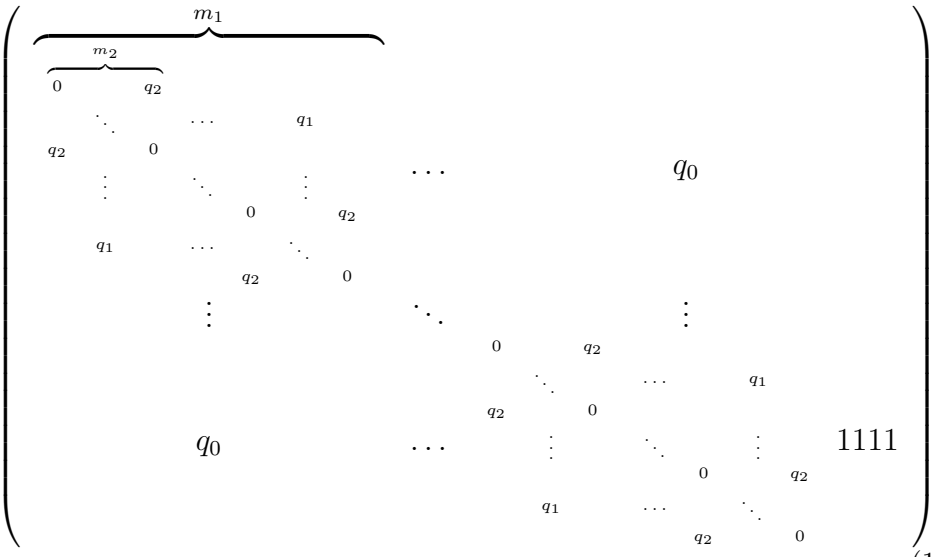

(1.31)

but the solution is also incorrect. However, the more steps one makes, the better the solution is, so if one repeats these steps infinitely times, one will find a correct solution. Then, the integers m_i tend to a continuous variable $x \in (0,1)$ and all the q_m become in the continuous function $q(x)$. Therefore, a Parisi's matrix can be written as $Q = (0, q(x))$, where the first term is the value in the diagonal of the matrix (in the previous examples it was always zero because we were working in no external magnetic field) and the second term is the value of the rest of the matrix elements. In presence of an external magnetic field, the value of the diagonal sites is not zero, so the general Parisi's matrix is $Q = (\overline{q}, q(x))$. Before computing the solution with this Ansatz, we will show how to work with this kind of matrices. The trace of the matrix is quite easy to compute

$$\mathrm{tr}Q = n\overline{q} \tag{1.32}$$

In order to compute the following quantities, we will firstly calculate them in a finite step and later in the limit ∞-step.

$$\sum_{a,b}^{n} Q_{ab} = n\left[\overline{q} + \sum (m_i - m_{i+1}) q_i\right] \to n\overline{q} - \int_n^1 q(x)dx \tag{1.33}$$

$$\sum_{a,b}^{n} Q_{ab}^l = n\left[\overline{q}^l + \sum (m_i - m_{i+1}) q_i^l\right] \to n\overline{q}^l - \int_n^1 q^l(x)dx \tag{1.34}$$

Finally, we will compute the product of two Parisi's matrices, $A = (\overline{a}, a(x))$ and $B = \left(\overline{b}, b(x)\right)$. The result is the matrix $AB = C = (\overline{c}, c(x))$ where

$$\overline{c} = \overline{a}\overline{b} - \langle ab \rangle \tag{1.35}$$

$$\begin{aligned} c(x) &= na(x)b(x) + \left[\overline{a} - \langle a \rangle\right] b(x) + \left[\overline{b} - \langle b \rangle\right] a(x) \\ &- \int_n^x \left[a(x) - a(y)\right] \left[b(x) - b(y)\right] dy \end{aligned} \tag{1.36}$$

and with

$$\langle a \rangle = \int_n^1 a(x) dx \tag{1.37}$$

Now, we can compute the relevant terms of the free energy, Eq. (1.28), near the critical point without an external magnetic field, which is denoted as $G(q)$.

$$G(q) = \lim_{n \to 0} \frac{1}{2n} \left[\theta \mathrm{tr} Q^2 - \frac{1}{3} \mathrm{tr} Q^3 - \frac{1}{6} \sum_{a,b} (Q_{ab})^4 \right] \tag{1.38}$$

The quadratic term is computed using Eqs. (1.35) and (1.32)

$$\mathrm{tr} Q^2 = -n \int_n^1 q^2(x) dx \tag{1.39}$$

The quartic term is computed using Eq. (1.34)

$$\sum_{a,b} Q_{ab}^4 = -n \int_n^1 q^4(x) dx \tag{1.40}$$

Finally the cubic term, which is the most complicated one, is computed using Eqs. (1.35), (1.36) and (1.32)

$$\mathrm{tr} Q^3 = n \left[\int_n^1 x q^3(x) dx + 3 \int_n^1 dx q(x) \int_n^x q^2(y) dy \right] \tag{1.41}$$

Substituting Eqs. (1.39), (1.40) and (1.41) in Eq. (1.38) and evaluating the limit $n \to 0$, the free energy reads

$$G(q) = \frac{1}{2} \int_0^1 dx \left[|\theta| q^2(x) + \frac{1}{6} q^4(x) - \frac{1}{3} x q^3(x) - q(x) \int_0^x q(y) dy \right] \tag{1.42}$$

Now, the saddle point equation can be written as

$$\frac{\delta G}{\delta q(x)} = 0 \tag{1.43}$$

and performing the functional derivative, one obtains

$$2|\theta|q(x) + \frac{2}{3}q^3(x) - xq(x) - 2q\int_x^1 q(y)dy - \int_0^x xq(x)dx \tag{1.44}$$

and differentiating it with respect to x one finds

$$|\theta| + q^2(x) - xq(x) - \int_x^1 q(y)dy = 0 \tag{1.45}$$

and differentiating again one finally obtains

$$q(x) = \frac{x}{2} \qquad \text{or} \qquad \frac{dq}{dx} = 0 \tag{1.46}$$

The solution is $q(x) = x/2$ for small x and $q(x) = q_{\max}$ constant for large x (notice that if the solution was $q(x) = q_0$ in the whole range of $x \in (0, 1)$, the replica symmetric solution would be recovered). Let x_1 be the point where the change of the behavior of the solutions takes place. As the solution must be continuous, $2q_{\max} = x_1$ and substituting in Eq. (1.45) one finds that

$$q_{\max} = |\theta| + \mathcal{O}(\theta^2) \tag{1.47}$$

In Figure 1.4 one can see this solution. Notice that if the external magnetic field does not vanish, according to Ref. [21], there is another plateau at small values x with value

$$q_{\min}(h) = \frac{3}{4}\left[\frac{h^2}{J^2}\right]^{\frac{2}{3}} \tag{1.48}$$

We will now study the overlap distribution function. In general, one can write that

$$P(q) = \frac{1}{n(n-1)}\sum_{a\neq b}\delta(Q_{ab} - q) \tag{1.49}$$

Substituting Q_{ab} with a Parisi's matrix one finds that

$$\begin{aligned} P(q) &= \frac{1}{n(n-1)} n\left[(n-m_1)\delta(q-q_0) + (m_1-m_2)\delta(q-q_2) + \dots\right] \\ &\to \frac{-1}{n-1}\int_n^1 \delta[q - q(x)]dx \end{aligned} \tag{1.50}$$

Finally, evaluating the limit one gets

$$P(q) = \frac{dx(q)}{dq} \tag{1.51}$$

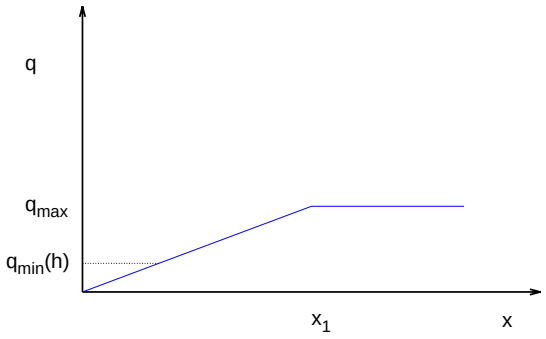

Figure 1.4: Schematic representation of the solution found to RSB. Dotted line is the plateau at low temperatures in presence of an external magnetic field.

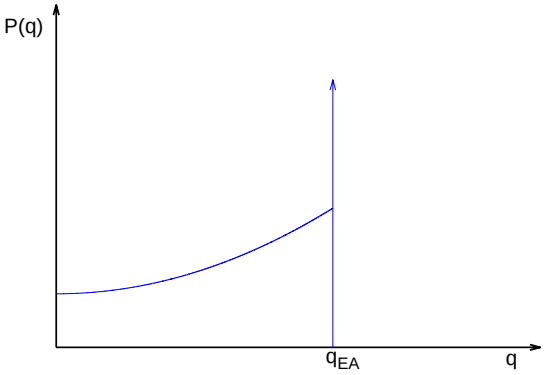

Figure 1.5: Schematic representation of the distribution of the overlap the RSB solution.

where $x(q)$ is the inverse function of $q(x)$. Notice that in this solution, $P(q)$ has a Dirac's delta function at $q = q_{\max}$ and it does not vanish in $(0, q_{\max})$. In Figure 1.5, one can see a schematic representation of this result.

Finally, as a corollary, if one computes the distribution of the overlap of

three replicas one finds that

$$\begin{aligned} P(q_1,q_2,q_3) &= \frac{1}{2}P(q_1)x(q_1)\delta(q_1-q_2)\delta(q_1-q_3) \\ &+ \frac{1}{2}\left[P(q_1)P(q_2)\theta(q_1-q_2)\delta(q_2-q_3)\right. \\ &+ P(q_1)P(q_3)\theta(q_3-q_1)\delta(q_1-q_2) \\ &+ \left.P(q_2)P(q_3)\theta(q_2-q_3)\delta(q_3-q_1)\right] \end{aligned} \tag{1.52}$$

$P(q_1,q_2,q_3)$ does not vanish only when the three overlaps are equal or when two of them are equal and the third one is bigger than them. Hence, the overlaps organize with the rules of an ultrametric space.

1.3.2 Droplet Model

The theory of the droplets was developed by Bray and Moore [22, 23] using Migdal-Kadanoff renormalization group [24, 25], and from a phenomenological point of view by Fisher and Huse [26, 27, 28]. In this case one works with a Hamiltonian with short range interactions. A droplet is a compact region of reversed spins. The probability distribution of the free energy of a droplet is

$$P\left[\Delta F(L)\right] = \frac{1}{L^y} f\left(\frac{\Delta F}{L^y}\right) \tag{1.53}$$

We will now compute the correlation function [28]

$$G(r_{ij}) = \overline{\left[\langle\sigma_i\sigma_j\rangle - \langle\sigma_i\rangle\langle\sigma_j\rangle\right]^2} \tag{1.54}$$

At $T=0$, this correlation function tends to zero. However at a temperature $T \ll 1$

$$G(r_{ij}) \propto P\left[\Delta F(r_{ij}\right] \simeq P[0] \tag{1.55}$$

hence,

$$G(r_{ij}) \propto \frac{1}{r^y} \qquad \text{and} \qquad \xi \to \infty \tag{1.56}$$

Now, if one chooses a bit different correlation function, one can compute that

$$G_1(r_{ij}) = \overline{\langle\sigma_i\sigma_j\rangle^2} - \overline{\langle\sigma_i\rangle^2} - \overline{\langle\sigma_j\rangle^2} \sim (\overline{q^2} - \overline{q}^2) \sim \frac{1}{r^y} \to 0 \tag{1.57}$$

so the distribution of the overlap is quite simple, as it is shown in Figure 1.6.

Finally, we will study the behaviour of a droplet in presence of an external magnetic field, comparing how the energy of the wall of a droplet and the

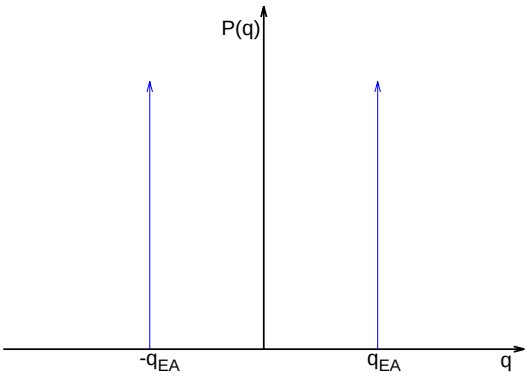

Figure 1.6: Schematic representation of the distribution of the overlap in a droplet.

field scale [2]. Firstly, the energy of the wall of a domain scales as L^y, where y must satisfy the inequality

$$y \leq \frac{D-1}{2} \tag{1.58}$$

where D is the dimensionality of the system. Whereas, the external field scales as $L^{D/2}$. According to Eq. (1.58), $y < D/2$ in every dimensionality, so the field grows faster than the energy of the wall of the domain, so the magnetic order is not stable at long distances.

1.3.3 Consequences

The RSB solution in mean field (interpreting it as a short range interaction model in infinite dimensions) is the exact solution above and at the upper critical dimension, $D_U = 6$, whereas the droplet model is the exact solution in low dimensions. However it is unknown the behavior one must expect in a realistic system living in three dimensions. Fortunately, as we have shown in this section, the behavior expected in each scenario is extremely different. RSB predicts phase transition to a spin glass phase in presence of magnetic field whereas droplet model does not. Moreover, the probability distribution of the overlap is quite different in these scenarios: in RSB, we found a Dirac's function at $q_{\rm EA}$ and a $P(q) > 0$ for $0 < q < q_{\rm EA}$, Figure 1.5; whereas in droplet model we just found a Dirac's function at $q_{\rm EA}$, Figure 1.6. This difference in $P(q)$ will be quite useful to distinguish whether RSB or droplet scenario holds. In fact, there is another intermediate scenario, TNT (trivial-not trivial) but we will focus on the two first ones.

1.4 Characteristics of the spin glass phase

In previous sections, we have explained several models of spin glasses and the phase transition of some of them. Now, we will present several characteristics of spin glasses, specially their spin glass phase. Frustration is one of the main causes of the long relaxation times that these systems exhibit in their spin glass phase, and as a consequence, ergodicity hypothesis does not hold. Besides, a useful tool to detect the phase transition, the spin glass order parameter, will be presented.

1.4.1 Broken ergodicity

If one wants to measure an observable in an experiment, one should try with an observation time larger than the largest relaxation time of the system. Then, the system can explore the whole phase space, and this measure is equivalent to an equilibrium statistical average. This phenomenon is the so-called ergodicity. However, in some systems, this does not happen, for example if the relaxation time diverges in the thermodynamic limit ($N \to \infty$). These systems are usually called non-ergodic.

According to the Parisi's RSB solution of the SK model (Section 1.3.1 and Refs. [17, 18, 19, 20]), this is the case of spin glasses at their spin glass phase where several pure states (phases) exist. In the thermodynamic limit, these states (also called valleys because they are minima of the free energy) tend to have the same free energy, but the energy barriers between them tend to infinity. Therefore, the system is not able to explore the whole range of microstates and the system becomes non-ergodic. However, it is not clear whether this behaviour also holds in a finite range spin glass.

1.4.2 Order parameter

An order parameter, if exists, is a common and useful tool to study phase transitions. It is an observable whose behavior in each phase is different. An example of an order parameter is the overlap defined in Section 1.3. Its probability distribution has only one Dirac's delta at $q = 0$ in the paramagnetic phase (Figure 1.3), but in the spin glass phase it has two Dirac's deltas in the droplet scenario (Figure 1.6) or two Dirac's deltas and a continuous part in the Parisi's RSB scenario (Figure 1.5).

Regarding spin glasses, the first order parameter was propound by Edwards and Anderson [13], defined as

$$q_{\mathrm{EA}} = \lim_{t\to\infty} \lim_{N\to\infty} \overline{\langle \sigma_i(t_0)\sigma_i t_0 + t)\rangle} \tag{1.59}$$

where the thermal average runs over a set of different t_0. As we commented above, in thermodynamic limit, the barriers between the different phases tend to infinite, so the system is not able to change the valley where it stays. As a consequence, this quantity is a measure of the mean square local magnetization averaged over all the valleys. It can also be written as

$$q_{\mathrm{EA}} = \overline{\sum_a P_a \langle \sigma_i \rangle_a^2} \tag{1.60}$$

where the index a runs over all the phases and P_a is the thermal probability

$$P_a = \frac{e^{-\beta F_a}}{\sum_b e^{-\beta F_b}} \tag{1.61}$$

We will now define the mean square local equilibrium magnetization

$$q = \overline{\langle \sigma_i \rangle^2} \tag{1.62}$$

Computing it only over one sample, it can be written as

$$q_J = \frac{1}{N} \sum_i \langle \sigma_i \rangle^2 = \frac{1}{N} \sum_i \sum_{ab} P_a P_b \langle \sigma_i \rangle_a \langle \sigma_i \rangle_b \tag{1.63}$$

It is also quite useful compute the correlations between different phases, so we define the overlap for a single sample as

$$q_{ab} = \frac{1}{N} \sum_i \langle \sigma_i^a \rangle \langle \sigma_i^b \rangle \tag{1.64}$$

which has the property of $|q_{ab}| \leq 1$. Studying the probability distribution of this quantity [29], one finds that

$$P(q) = \overline{\langle \delta(q - q_{ab}) \rangle} = \overline{\sum_{ab} P_a P_b \delta(q - q_{ab})} \tag{1.65}$$

In case there are only two phases, like in the droplet model, $P(q)$ would be the sum of two Dirac's delta functions (one in $-q_{\mathrm{EA}}$ and another in q_{EA}), as we found above (Figure 1.6). Whereas, if the system exhibits a nontrivial broken ergodicity, like RSB, $P(q)$ would also have a continuous part, as we also found above (Figure 1.5).

Finally, we will apply the replica method (Section 1.2) to compute this quantities in the context we will work in this thesis. According to Ref. [2], one can define

$$q^{\alpha\beta} = \langle \sigma_i^\alpha \sigma_i^\beta \rangle \tag{1.66}$$

where the indices α and β mean a pair of two different replicas ($\alpha \neq \beta$). Therefore, one can identify

$$q = \lim_{n \to 0} \frac{1}{n(n-1)} \sum_{\alpha \neq \beta} q^{\alpha\beta} \tag{1.67}$$

where, as usual, n means the number of replicas. Finally, one can also identify the Edwards-Anderson order parameter as

$$q_{\mathrm{EA}} = \max_{\alpha\beta} q^{\alpha\beta} \tag{1.68}$$

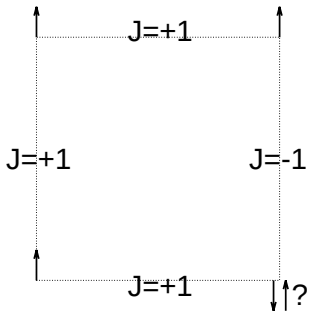

Figure 1.7: An example of a 2×2 frustrated plaquette. The spin at the bottom right corner does not have a stable state.

1.4.3 Frustration

Frustration is one of the main contribution to the extremely complicated free energy landscape which produce the typical slow dynamic of spin glasses. As an example, we will work with Edwards-Anderson Ising spin glass model without external magnetic field. As one can see in the Figure 1.7, due to the fact that couplings are random, some configurations of them produce that some spins (in the figure the one at the bottom right corner) are not able to find the most stable position. In our example, the spin at the bottom right corner tends to be up to be parallel with the spin at the bottom left corner, according to the coupling between them. However, it also tends to be down to be antiparallel to the spin at the top right corner, according to the coupling between them.

In the Edwards-Anderson model (as this examples shows) and in Potts model, the two main models in this work, frustration is a consequence of the disorder. However, in general frustration is an independent phenomenon and several models exhibit it without disorder.

Chapter 2

Potts

2.1 Preliminary study

The Disordered Potts Glass Model (DPM) has been extremely studied because of its interesting characteristics. In particular, mean field model exhibits a dynamic phase transition for a given number of states p, which makes this model quite useful to study supercooled liquids and glasses.

Besides, this model does not have any inversion symmetry ($\sigma_i \rightarrow \sigma_i$) whereas Ising-like models in absence of a magnetic field do, so DPM has been used to modelize systems without inversion symmetry, for example orientational (or quadrupolar) glasses [30, 31], like ortho-hydrogen, and mixed crystals [32, 33], like $(\mathrm{KCN})_x\,(\mathrm{KBr})_{1-x}$.

Finally, DPM plays a similar role as the pure Potts model does in the study of ferromagnets, it allows us to study several kinds of phase transitions, a first and second order thermodynamic phase transition and a dynamic one, just varying the value of the number of states (p) in our simulations.

2.1.1 Mean field analysis

In 1985, Gross, Kanter and Sompolinsky [34] studied the mean field theory of the DPM (see also Refs. [2, 35, 36] for a more detailed explanation). The mean field Hamiltonian of DPM is

$$\mathcal{H} = -\frac{1}{2}\sum_{i\neq j} J_{ij}\delta_{\sigma_i\sigma_j} \tag{2.1}$$

where p is the number of states that a given Potts spin σ_i can take. The (quenched) couplings, J_{ij}, are Gaussian-distributed random variables with

mean J_0/N. The order parameter can be defined as

$$q_{rr'} = \overline{\left(\langle\delta_{\sigma_i r}\rangle - \frac{1}{p}\right)\left(\langle\delta_{\sigma_i r'}\rangle - \frac{1}{p}\right)} \tag{2.2}$$

which has the symmetry [2]

$$q_{rr'} = q\left(\delta_{rr'} - \frac{1}{p}\right) \tag{2.3}$$

In the replica method (Section 1.2), q becomes a matrix and can be expressed as

$$Q_{\alpha\beta} = \langle\delta_{\sigma_\alpha\sigma_\beta}\rangle - \frac{1}{p} \tag{2.4}$$

where α and β are replica indices and the thermal average is computed with the replicated Hamiltonian. Now, we can compute the free energy (similarly to what we did in Section 1.3.1) near the critical temperature

$$\begin{aligned} f(Q) &= \lim_{n\to 0}\frac{p-1}{2n}\left[\theta\mathrm{tr}\left(Q^2\right) - \frac{1}{3}\mathrm{tr}\left(Q^3\right) - \frac{p-2}{6}\sum_{\alpha\beta}Q^3_{\alpha\beta}\right. \\ &+ \left.\frac{y\,(p)}{6}\sum_{\alpha\beta}Q^4_{\alpha\beta}\right] \end{aligned} \tag{2.5}$$

where, remind, $\theta = (T - T_c)/T_c$. If we compare this result with the analogous Eq. (1.38) found in Section 1.3.1 to the Sherrington-Kirkpatrick (SK) model, we notice two main differences. In Eq. (2.5) we have two cubic terms instead only one: $\sum_{\alpha\beta} Q^3_{\alpha\beta}$ does not vanish because in DPM the symmetry under inversion of the spins does not hold. The other main difference is that in Eq. (2.5) the coefficient of the quartic term is not constant but depends on p. Let p^* the value of p where $y(p)$ changes its sign. It is negative for $p < p^*$ and positive for $p > p^*$ with $p^* \sim 2.8$ (see Ref. [34]). In fact $y(2) = -1$, so if $p = 2$, the SK model is recovered.

Firstly, we will study this model in the region $p < p^*$ where $y(p)$ is negative. If we assume that a continuous Parisi's solution $q(x)$ holds, the solution would be

$$q(x) = -\frac{1}{4y(p)}\left[2x - (p-2)\right] \qquad \text{or} \qquad \frac{dq}{dx} = 0 \tag{2.6}$$

Due to the fact that $0 \le q(x) \le 1$, the solution presents two plateaus joint by a straight line of slope $1/[2y(p)]$ (see Figure 2.1a). Therefore, the probability

distribution of the order parameter q has two Dirac's deltas, one at $q_0 = 0$ and the another one at q_1, and it does not vanish in the $(0, q_1)$ region (see Figure 2.1b for more details). Notice that if $p = 2$, we have the same solution as in the SK model. Since $q(x)$ must also be a non-decreasing function, this solution is only correct if $y(p) < 0$, which agrees with our assumption, and it is incorrect for $p > p^*$.

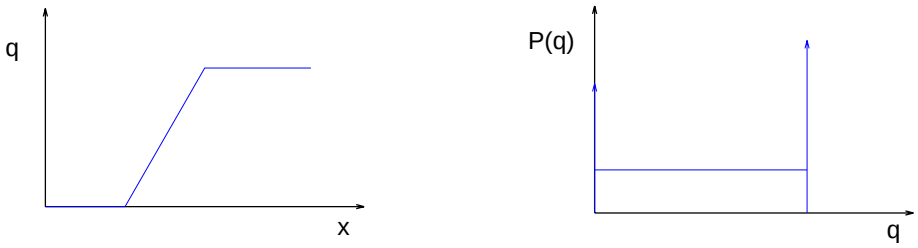

(a) $q(x)$ (b) $P(q)$

Figure 2.1: Schematic representation of the solution found for $p < p^*$.

Secondly, we will study the region where $p > p^*$. We will use the one step Replica Symmetry Breaking (RSB) Ansatz, Eq. (1.30), which is enough to solve the system. Let n be the total number of replicas and m_1 the number of replicas of every of the n/m_1 groups. The expression of the Eq. (1.34) in the one step Ansatz becomes (we assume that the terms of the diagonal of the matrix $\hat{Q}$ are 0)

$$\sum_{\alpha,\beta} Q^l_{\alpha,\beta} = n\left[(m_1 - 1)\, q_1^l + (n - m_1)\, q_0^l\right] \tag{2.7}$$

Computing $\mathrm{tr}\,(Q^3)$ is a bit more tricky, but after some algebra, it can be expressed as

$$\begin{aligned} \mathrm{tr}\left(Q^3\right) &= n\left\{(m_1 - 1)\,(m_1 - 2)\, q_1^3 + \left(\frac{n}{m_1} - 1\right)\left[3m_1\,(m_1 - 1)\, q_0^2 q_1\right.\right. \\ &+ \left.\left.\left(\frac{n}{m_1} - 2\right) m_1^2 q_0^3\right]\right\} \end{aligned} \tag{2.8}$$

Substituting Eqs. (2.7) and (2.8) in Eq. (2.5) and evaluating the limit, one

gets

$$\begin{aligned} f(q) &= \frac{p-1}{2}\left\{\theta\left[(m_1-1)\,q_1^2 - m_1 q_0^2\right] - \frac{1}{3}\left[(m_1-1)\,(m_1-2)\,q_1^3\right.\right. \\ &- 3m_1\,(m_1-1)\,q_0^2 q_1 + 2m_1^2 q_0^3\Big] - \frac{p-2}{6}\left[(m_1-1)\,q_1^3 - m_1 q_0^3\right] \\ &+ \left.\frac{y(p)}{6}\left[(m_1-1)\,q_1^4 - m_1 q_0^4\right]\right\} \end{aligned} \tag{2.9}$$

The saddle point equations can be expressed as

$$\begin{aligned} 0 = \frac{\partial f}{\partial q_0} &= \frac{p-1}{2}\left\{-2\theta m_1 q_0 + 2m_1\,(m_1-1)\,q_0 q_1 - 2m_1^2 q_0^2\right. \\ &+ \left.\frac{p-2}{2} m_1 q_0^2 - \frac{2y(p)}{3} m_1 q_0^3\right\} \end{aligned} \tag{2.10}$$

$$\begin{aligned} 0 = \frac{\partial f}{\partial q_1} &= \frac{p-1}{2}\left\{2\theta\,(m_1-1)\,q_1 - (m_1-1)\,(m_1-2)\,q_1^2\right. \\ &+ \left.m_1\,(m_1-1)\,q_0^2 - \frac{p-2}{2}\,(m_1-1)\,q_1^2 + \frac{2y(p)}{3}\,(m_1-1)\,q_1^3\right\} \end{aligned} \tag{2.11}$$

$$\begin{aligned} 0 = \frac{\partial f}{\partial m_1} &= \frac{p-1}{2}\left\{\theta\left(q_1^2 - q_0^2\right) - \frac{1}{3}\left[(m_1-1)\,(m_1-2)\,q_1^3 - 3m_1 q_0^2 q_1\right.\right. \\ &- \left.\left.3m_1\,(m_1-1)\,q_0^2 q_1 + 2m_1 q_0^3\right] - \frac{p-2}{6}\left(q_1^3 - q_0^3\right) + \frac{y(p)}{6}\left(q_1^4 - q_0^4\right)\right\} \end{aligned} \tag{2.12}$$

Taken into account that $q_0 \leq q_1$ and neglecting the quartic term, the solution of these equations, q, is a step function

$$q = \begin{cases} 0 & \text{if} \quad x < x_0 \\ \frac{2\theta}{p-4} & \text{if} \quad x > x_0 \end{cases} \tag{2.13}$$

where x_0 is the parameter m

$$x_0 \equiv m_1 = \frac{p-2}{2} \tag{2.14}$$

In Figure 2.2a one can see a schematic representation of this function. The probability distribution of the order parameter q can be observed in Figure 2.2b.

Nevertheless, this solution also becomes incorrect in the region $p > 4$, where a discontinuous transitions appears. Therefore, the approximation

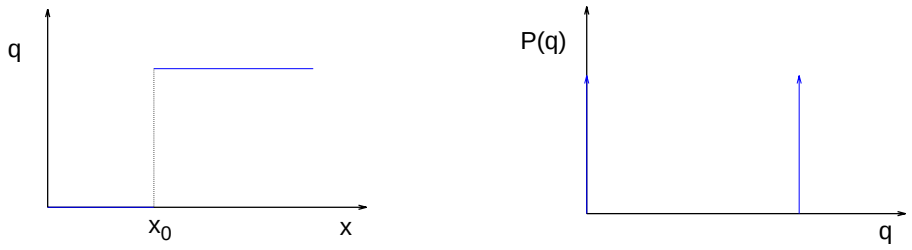

(a) $q(x)$ (b) $P(q)$

Figure 2.2: Schematic representation of the solution found for $p > p^*$ and $T_2 < T < T_c$.

used to compute Eq. (2.5) is not valid and the previous demonstration does not hold. However, Eq. (2.5) can still be used in the limit $\epsilon \equiv p - 4 \to 0$ because the discontinuity is small enough. In this situation one finds that at the critical temperature, T_c, the value of the order parameter above the discontinuous jump is $q(1) \propto p - 4$ and the position of the jump as temperature tends to the critical one is $x_0 \left(T \to T_c^-\right) \to 1$. Whereas, if one solves the full problem when $p \to \infty$, the value of q above the discontinuous jump is $q(1) = 1$ and the position of the jump is $x_0 = T/T_c$.

Finally, Gross, Kanter and Sompolinsky [34] also demonstrated that the system undergoes a second phase transition at a temperature $T_2 < T_c$, because the previous solution has a negative entropy at $T = 0$ for every finite $p > p^*$. Using an expansion of the free energy up to fifth order terms in $\hat{Q}$, they demonstrated that this phase transition is a continuous one, so $q(x)$ has a continuous part in a range of x, as can be observed in Figure 2.3a. In Figure 2.3b the probability distribution of the order parameter is plotted.

2.1.2 Glass phase transition

The glass phase transition was firstly studied in the framework of the supercooled liquids. This area deal with amorphous solids like the glass of windows. Many reviews of this topic have been written, but we will focused on Refs. [37, 38].

If one cools fast enough a liquid, it would not become solid at its melting temperature, T_m, and it would remain liquid even at temperatures below that temperature T_m: this is a supercooled liquid. However, the lower the temperature, the slower the dynamic of the system, that is, the relaxation time exhibits an extremely growth (several orders of magnitude) in a short

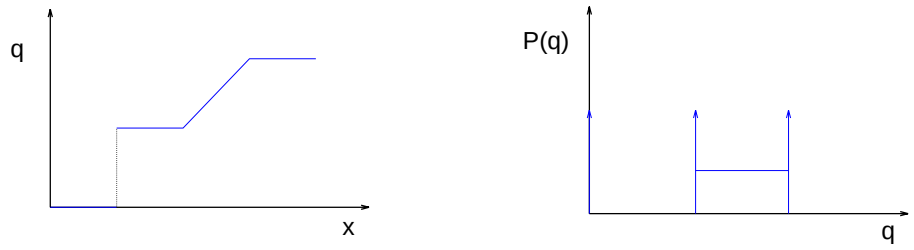

(a) $q(x)$ (b) $P(q)$

Figure 2.3: Schematic representation of the solution found for $p > p^*$ and $T < T_2 < T_c$.

range of temperature. In fact, at a temperature low enough the relaxation time is so long that the system is not able to explore the whole phase space in the time that a typical experiment spend, so the system becomes non-ergodic. This behavior defines a kind of dynamical phase transition, where the phase at low temperature is the so-called glass phase. To compute the temperature at which the phase transition takes place, T_g, one needs to establish a criterion to determine whether an experimental time is long enough to characterize a glass phase. This maximum experimental time is usually fixed at $10^2 - 10^3$ s. With this definition, the viscosity where the glass phase transition happens can be computed [38]:

$$\eta\left(T_g\right) = 10^{13} \quad \text{Poise.} \tag{2.15}$$

Different liquids have not the same evolution of the viscosity. Some of them, *strong liquids*, have a fast evolution, linear versus T_g/T, for example SiO_2. Other liquids, *fragile liquids*, have a far slower evolution at high temperatures, for example o-terphenyl. In Figure 2.4, this behaviour can be observed. Notice that, where $T_g/T = 1$, all liquids have the same evolution due to the definition of T_g, Eq. (2.15).

This definition of the phase transition and T_g seems to be a mathematical trick without any physical meaning. In fact T_g depends (weakly) on the cooling protocol of the experiment. However, this is not the case thanks to some characteristics of these systems, like the so-called two steps relaxation. Let $C(t_1, t_2)$ be a general defined two times correlation function

$$C(t_1, t_2) = \frac{1}{N} \sum_i \langle \phi_i(t_1) \phi_i(t_2) \rangle \tag{2.16}$$

where ϕ is an observable that depends on the particle (in liquids) or on the spin (in spin glasses) which stays in the position i. An example of this kind

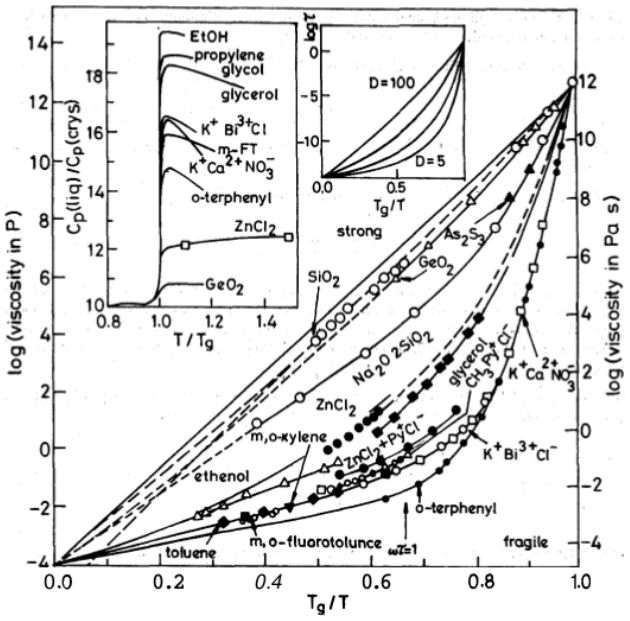

Figure 2.4: Evolution of the viscosity of several liquids. Notice that, although the evolution is different, all of them reach the same value of the viscosity. This figure is the famous Angell plot, from Ref. [45]

of two times correlation function in spin glasses is the one defined in Eq. (6.2), where the observable is the spin itself. At equilibrium, the two times correlation function, Eq. (2.16), does just depend on the difference of these times $t = t_2 - t_1$, so Eq. (2.16) can be rewritten as

$$C(t) = \frac{1}{N}\sum_i \langle \phi_i(t)\phi_i(0)\rangle \tag{2.17}$$

At high temperature, $C(t)$ decrease as an exponential function

$$C(t) = A\exp(-t/\tau) \tag{2.18}$$

However, this behaviour does not hold at temperatures near T_g, where a plateau in the relaxation of $C(t)$ appears, that is, $C(t)$ decreases and reaches a first plateau and later it resumes the decreasing. The length of this plateau depends on the temperature and appears continuously as T decreases, so this phase transition is usually called a continuous transition. Nevertheless, if one focuses on the value of $C(t)$ on the plateau, one has a discontinuous behaviour as T decreases.

Some characteristics of these supercooled liquids and their glass transition seems to be quite similar to properties of spin glasses in their spin

glass phase, such as the extremely long relaxation time. Besides, spin glasses without reversal spins symmetry, like DPM or p-spin model [39], undergo a discontinuous phase transition (in fact, several phase transitions actually happens, some of them continuous), as it is shown in the previous section (Section 2.1.1) for DPM. However, this phase transition seems to be a first order one, at least in mean field analysis. Kirkpatrick, Wolynes and Thirumalai [40, 41, 42, 43, 44] performed an in-depth study of this relation between spin glasses (they specially worked with Potts glass model) and the glass transition of the supercooled liquids. For example, they found [41] that the correlation function exhibit a plateau, a behaviour similar to the two steps relaxation.

2.1.3 Previous results

Brangian, Kob and Binder [46, 47, 48] performed a complete study of the ten-state infinite range DPM and Gaussian couplings with a negative mean. They checked whether this model presents the dynamical and static phase transitions that mean field theory predicts in the thermodynamic limit. Therefore they performed simulations of several system sizes, up to $N = 2560$ spins. They simulated 500 samples for the smallest system and between 20 and 50 for the largest one. They found strong finite size effects, although their simulations suggest the existence of both static and dynamical transition. Therefore a finite system behaves, at least qualitatively, similarly as in the thermodynamic limit.

Regarding the more realistic short range models, Brangian, Kob and Binder [49, 50] also studied the three dimensional ten-state short range model, although they focused on a bit different model from the one we will study in this chapter

$$\mathcal{H} = -\sum_{\langle i,j \rangle} J_{ij} \left(p\delta_{\sigma_i \sigma_j} - 1 \right) \tag{2.19}$$

where Gaussian and bimodal couplings were studied, both with a negative mean ($J_0 < 0$). Systems sizes up to $L = 16$ have been simulated, with up to 100 samples and 10^8 Monte Carlo steps (MCS). For both probability distributions of the quenched couplings, they did not find any sign of the existence neither the static nor the dynamical transition predicted in mean field theory, so the behavior of the short range systems would be extremely different to the infinite range ones.

Lee, Katzgraber and Young [55] also studied the short range DPM (in fact they studied the same model we will study in this chapter). They performed simulations of the four dimensional three-state DPM and the three

dimensional three- and ten-state DPM, all of them with Gaussian couplings. Besides, the three dimensional three-state model was also studied with bimodal couplings. In all of the three-state models, the probability distribution of the couplings was chosen with a vanishing mean, $J_0 = 0$, but in the ten-state model the mean was chosen negative, $J_0 = -1$. They simulated in the three dimensional three-state systems of size up to $L = 12$ performing $\sim 10^7$ MCS and 352 samples in the Gaussian probability distribution and 550 samples in the bimodal one (in both cases, more samples were simulated in smaller lattice sizes). They found a clear phase transition with both probability distributions. However, in the three dimensional ten-state Gaussian DPM[1], they did not find any sign of phase transition, which supports the previous result of Brangian, Kob and Binder [49, 50].

Finally, the *Janus Collaboration* [63] studied the three dimensional four states DPM with binary quenched couplings (with vanishing mean $J_0 = 0$). They used a prototype board of Janus (see Section 7.6, Appendix A and Refs. [224, 225, 226]) to perform their simulations. The simulations performed were far longer than in previous works. The statistic achieved was astonishing: the largest lattice size simulated was $L = 16$ with 1000 samples and 8×10^9 MCS every one. Therefore, they were more confident that the system was completely thermalized. They found a clear phase transition to a spin glass phase. Moreover, no sign of a ferromagnetic phase transition was found.

Therefore, an in-depth study of the three dimensional DPM with $p > 4$ states is quite interesting. In this work, we have used the full Janus machine which allows us to perform long simulations with far more statistic than previous works, so we are far more confident that our simulations are completely thermalized. Therefore, it seems that the results obtained in this study are more reliable, although some of them do not agree with previous works, which performed shorter simulations. However we did not manage to thermalize systems of $L = 16$ lattice size for $p \geq 5$ nor even relevant lattice sizes for $p = 8$. There are several open questions in this model that we will try to understand better with this work. For example whether a phase transition to a ferromagnetic transition exists or characterize the spin glass transition, its order and the behavior of β_c with p.

[1]The largest lattice size simulated was $L = 12$ with 343 samples and $\sim 10^4$ MCS (in smaller sizes, 1000 samples were simulated with up to $\sim 10^5$ MCS).

Critical Behavior of Three-Dimensional Disordered Potts Models with Many States

R. Alvarez Baños, A. Cruz, L. A. Fernandez, A. Gordillo-Guerrero, J. M. Gil-Narvion, M. Guidetti, A. Maiorano, F. Mantovani, E. Marinari, V. Martin-Mayor, J. Monforte-Garcia, A. Muñoz Sudupe, D. Navarro, G. Parisi, S. Perez-Gaviro, J. J. Ruiz-Lorenzo, B. Seoane, S. F. Schifano, A. Tarancon, R. Tripiccione and D. Yllanes.

Published in *J. Stat. Mech.* P05002 (2010).

2.2 Introduction

The three dimensional ($3D$) disordered Potts model (DPM) is an important system, that could help in clarifying a number of open and crucial questions. The first issue that comes to the mind is the possibility of understanding the glass transition, since this is a very challenging problem. On more general grounds, it is very interesting to try and qualify the behavior of the system when the number of states p becomes large: here we should see the paradigm of a "hard", first order like transition but, as we will discuss in the following, only sometimes this turns out to be clear (see for example the set of large scale, very accurate numerical simulations of Ref. [51], dealing with a model slightly different from the one defined here).

In such a difficult situation extensive numerical simulations are more than welcome, and the Janus supercomputer [52, 53], optimized for studying spin glasses, reaches its peak performances when analyzing lattice regular systems based on variables that can take a finite, small number of values: disordered Potts models fit very well these requirements. Using the computational power of Janus we have been able to consistently thermalize the DPM with $p = 5$ and 6 on $3D$ (simple cubic) lattice systems with periodic boundary conditions and size up to $L = 12$. Bringing these systems to thermal equilibrium becomes increasingly harder with increasing number of states: it has been impossible for us, even by using a large amount of time of Janus (that for these problems performs, as we discuss better in the following, as thousands of PC processors), to get a significant, unbiased number of samples thermalized, and reliable measurements of physical quantities, for $p \geq 5$ on a $L = 16$ lattice.

Our results lead us to the claim that the critical behavior of the DPM with a large number of states p is very subtle, and if p is larger than, say, 5, numerical simulations could easily give misleading hints. The numerical results that we will discuss in the following lead us to believe that the spin glass transition gets stronger with increasing number of states p: a theoretical

analysis of these results suggests that the transition could eventually become of first order for p large enough. We do not observe, for both $p = 5$ and $p = 6$, any sign of the presence of a spontaneous magnetization.

2.3 Model and observables

We have performed numerical simulations of the DPM on a simple cubic lattice of linear size L with periodic boundary conditions. The Hamiltonian of the DPM is

$$\mathcal{H} \equiv -\sum_{\langle i,j \rangle} J_{ij}\, \delta_{s_i,s_j}\,, \tag{2.20}$$

where the sum is taken over all pairs of first neighboring sites. In the p-states model spins s_i can take p different values $\{0, 1, \ldots, p-1\}$. In this work we analyze the $p = 5$ and 6 cases. The couplings J_{ij} are independent random variables taken from a bimodal probability distribution ($J_{ij} = \pm 1$ with probability $\frac{1}{2}$). For a different definition of a disordered Potts model see Ref. [54].

It is convenient to rewrite the variables of the Potts model using the *simplex* representation, where the p Potts states are described as vectors pointing to the corners of a $(p-1)$ dimensional hyper-tetrahedron. The Potts scalar spins s_i are thus written as $(p-1)$-dimensional unit vectors $\boldsymbol{S}_i$ satisfying the relations

$$\boldsymbol{S}_a \cdot \boldsymbol{S}_b = \frac{p\,\delta_{ab} - 1}{p-1}\,, \tag{2.21}$$

where a and $b \in [1, p]$. We use this vector representation to define the observables required to investigate the critical behavior of the system. In the simplex representation we have that:

$$H = -\sum_{\langle i,j \rangle} J'_{ij}\, \boldsymbol{S}_i \cdot \boldsymbol{S}_j\,. \tag{2.22}$$

The couplings in the simplex representation have the form

$$J'_{ij} = \frac{p-1}{p} J_{ij}\,. \tag{2.23}$$

The spin glass behavior is studied via a properly defined tensorial overlap between two *replicas* (independent copies of the system characterized by the same quenched disorder variables J_{ij}). Its Fourier transform (with wave vector $\boldsymbol{k}$) is given by [55]

$$q^{\mu\nu}(\boldsymbol{k}) = \frac{1}{V} \sum_i S_i^{(1)\mu} S_i^{(2)\nu} \mathrm{e}^{i\boldsymbol{k}\cdot\boldsymbol{R}_i}\,, \tag{2.24}$$

where $S_i^{(1)\mu}$ is the μ component of the spin at site i of the first replica in the simplex representation, $S_i^{(2)\nu}$ the ν component of the spin at site i in the second replica, and $V = L^3$ is the volume of the system.

This spin glass order parameter is then used to define the spin glass susceptibility in Fourier space.

$$\chi_q(\boldsymbol{k}) \equiv V \sum_{\mu,\nu} \overline{\langle |q^{\mu\nu}(\boldsymbol{k})|^2 \rangle}\,, \tag{2.25}$$

where $\langle(\cdots)\rangle$ indicates a thermal average and $\overline{(\cdots)}$ denotes the average over different realizations of the disorder (*samples* in the following). With the above definition, $\chi_q(0)$ is the usual spin glass susceptibility.

We are interested in studying the value of the dimensionless correlation length ξ/L, since at the transition temperature it does not depend on L, and is therefore extremely helpful to estimate the critical temperature value T_c: in fact one can usually simulate different lattice sizes, and look for the crossing point in the plot of the different ξ/L values. One can derive [56] the value of the correlation length ξ from the Fourier transforms of the susceptibility with

$$\xi = \frac{1}{2\sin\left(\boldsymbol{k}_{\mathrm{m}}/2\right)} \left(\frac{\chi_q(0)}{\chi_q(\boldsymbol{k}_{\mathrm{m}})} - 1 \right)^{1/2}, \tag{2.26}$$

where $\boldsymbol{k}_{\mathrm{m}}$ is the minimum wave vector allowed in the lattice. With the periodic boundary conditions used in this work we have $\boldsymbol{k}_{\mathrm{m}} = (2\pi/L, 0, 0)$ or any of the two vectors obtained permuting the indexes.

We also study the ferromagnetic properties of the model by monitoring the usual magnetization

$$\boldsymbol{m} = \frac{1}{V} \sum_i \boldsymbol{S}_i\,, \tag{2.27}$$

and correspondingly the magnetic susceptibility

$$\chi_m \equiv V\, \overline{\langle |\boldsymbol{m}|^2 \rangle}\,. \tag{2.28}$$

These two observables are crucial to check the possible existence of a ferromagnetic phase, as predicted by the mean field approximation of this model [57].

2.4 Numerical methods

We have analyzed the DPM with 5 and with 6 states, on a number of lattice sizes ($L = 4$, 6, 8, and 12). All the numerical simulations have been run using

a standard Metropolis algorithm combined with the Parallel Tempering (PT) optimized algorithm, in order to improve performances and allow to reach thermalization despite the very large relaxation times typical of spin glass models.

We define a Monte Carlo sweep (MCS) as a set of V trial updates of lattice spins. Each simulation consists on a thermalization phase, during which the system is brought to equilibrium, and a phase of equilibrium dynamics in which relevant physical observables are measured. As we require high quality random numbers, we use a 32-bit Parisi-Rapuano shift register [58] pseudo-random number generator. [2]

In order to improve the simulation performance and to speed up thermalization we apply a step of the PT algorithm [59] every few MCS's of the Metropolis algorithm. The PT algorithm is based on the parallel simulation of various copies of the system, that are governed by different values of temperature, and on the exchange of their temperatures according to the algorithm's rules. In practice we let the different configurations evolve independently for a few MCS, and then we attempt a temperature swap between all pairs of neighboring temperatures: the aim is to let each configuration wander in the allowed temperature range (that goes from low T values, smaller than T_c, to high T values, larger than T_c), and to use the decorrelation due to the high T part of the landscape to achieve a substantial speed up.

In order to check the time scales of the dynamical process, so as to assess the thermalization and the statistical significance of our statistical samples, we have computed a number of dynamical observables that characterize the PT dynamics.

One of them is the temperature-temperature time correlation function, introduced in Ref. [60], that we briefly recall. Let $\beta^{(i)}(t)$ be the inverse temperature of the system i at time t ($i = 0, \ldots, N_T - 1$), where N_T is the total number of systems evolving in parallel in the PT. [3] We consider an arbitrary function of the system temperature, $f(\beta)$, changing sign at $\beta_{\rm c}$. We shall name $f_t^{(i)} = f(\beta^{(i)}(t))$. In equilibrium, system i can be found at any of the N_T with uniform probability, hence $\langle f_t^{(i)} \rangle = \sum_{k=0}^{N_T-1} f(\beta_k)/N_T$, for all i and all t. We must choose a function f as simple as possible, such that

[2] Our FPGA did not have components to accomodate the L=12 code with a 48 bits generator (that could instead be used for L=8). We have performed additional numerical simulations in the smaller lattices, on PC, using 64 bits random numbers and in the $L = 8$, on Janus, using 48 bits random numbers. We have reproduced in all cases, within statistical errors, the results obtained with the 32 bits generator.

[3] We have used β's not uniformly distributed in order to have a PT acceptance of order 30-40% in the whole β-interval. In addition, we have include additional β's in the critical region to have clearer crossing points of the correlation length.

$\sum_{k=0}^{N_T-1} f(\beta_k) = 0$. [4] Next, we can define the correlation functions

$$C_f^{(i)}(t) = \frac{1}{N-|t|} \sum_{s=1}^{N-|t|} f_s^{(i)} f_{s+|t|}^{(i)} \,, \tag{2.29}$$

$$\rho_f^{(i)}(t) = \frac{C_f^{(i)}(t)}{C_f^{(i)}(0)} \,, \tag{2.30}$$

where N is the total simulation time. To gain statistics we consider the sum over all the systems

$$\rho_f(t) = \frac{1}{N_T} \sum_{i=0}^{N_T-1} \rho_f^{(i)}(t) \,. \tag{2.31}$$

Notice that this correlation function measures correlations for a given copy of the system, that is characterized, during the dynamics, by different temperature values.

We have characterized the correlation function $\rho_f(t)$ through its integrated autocorrelation time [56, 61]:

$$\tau_{\rm int} = \int_0^{\Lambda_{\rm int}} dt \; \rho_f(t) \,, \tag{2.32}$$

where $\Lambda_{\rm int} = \omega \, \tau_{\rm int}$ and we have used $\omega = 10$ (we have always used a total simulation time larger than 15 or 20 times $\tau_{\rm int}$).

We have studied the systems defined on the smaller lattices ($L = 4$ and 6) on standard PCs, while for the larger lattice sizes we have used the Janus computer [52, 53], an FPGA-based machine specifically designed to handle simulations of spin glass models. The performance improvement offered by Janus allowed us to thermalize lattices of size up to $L = 12$. While the thermalization of lattices with $L = 8$ was relatively fast, the bigger lattice sizes proved to be rather difficult to equilibrate, even within Janus, things getting worse as the number of Potts states increases.

Tables 2.1 and 2.2 summarize the details about the numerical simulations respectively for the $p = 5$ and the $p = 6$ case. We were able to thermalize a large number of samples for L up to 12. The thermalization of $L = 16$ is possible, but it requires a dramatically large investment in computer resources, since the time required by each sample is very large. Because of that, and given the resources we could count upon, we have only been able to analyze

[4] Our choice of $f(\cdot)$ is slightly different from that of Ref. [60]; $f(\beta) = a(\beta - \beta_{\rm c})$ for $\beta < \beta_{\rm c}$, and $f(\beta) = b(\beta - \beta_{\rm c})$ for $\beta > \beta_{\rm c}$. The ratio of the slopes a/b is fixed by the condition $\sum_{k=0}^{N_T-1} f(\beta_k) = 0$. The overall normalization being irrelevant, we choose $a = 1$.

a few samples: the results for the few samples that we have studied in this case are consistent with the ones obtained from the smaller sizes. In addition, for some samples with $L = 8$ and $L = 12$, which were especially difficult to thermalize, we had to use larger numbers of MCS's: see section 2.5.1.

L	N_{samples}	MCS_{min}	$[\beta_{\text{min}}, \beta_{\text{max}}]$	N_β	$N_{\text{Metropolis}}$	N_m
4	2400	10^7	[1.6, 9.5]	18	5	10^3
6	2400	2×10^7	[1.6, 9.5]	22	5	10^3
8	2448	4×10^8	[1.7, 6.5]	24	10	2×10^5
12	2451	6×10^9	[1.8, 5.5]	20	10	2×10^5

Table 2.1: Details of the simulations for $p = 5$. N_{samples} is the number of samples (i.e. of the disorder realizations that we have analyzed), MCS_{min} is the minimum number of MCSs that we have performed, $[\beta_{\text{min}}, \beta_{\text{max}}]$ is the range of inverse temperatures simulated in the PT, N_β is the number of temperatures inside this interval, $N_{\text{Metropolis}}$ is the frequency of the Metropolis sweeps per PT step, and N_{m} is the total number of measurements performed within each sample.

L	N_{samples}	MCS_{min}	$[\beta_{\text{min}}, \beta_{\text{max}}]$	N_β	$N_{\text{Metropolis}}$	N_m
4	2400	10^7	[2.1, 9.8]	10	5	10^3
6	2400	2×10^7	[2.0, 9.65]	16	5	10^3
8	1280	10^9	[1.7, 7.5]	30	10	2×10^5
12	1196	6×10^{10}	[1.6, 6.5]	22	10	2×10^5

Table 2.2: As in table 2.1, but for $p = 6$.

The number of Metropolis sweeps per PT step is 10 on Janus and 5 on the PC, and there is an important reason for that: in a standard computer the time needed for a step of the PT algorithm is small compared with a complete Metropolis MCS. This is not true on Janus, where it takes longer to perform a PT step than an Metropolis MCS: because of that, after a careful test of the overall simulation performance, we decided to lower the PT to Metropolis MCS ratio in order to increase Janus efficiency.

In the $p = 5$ case a numerical simulation of a single sample (thermalization plus measurements) on Janus takes 39 minutes for $L = 8$ and 10 hours on $L = 12$. The same simulations would require 7.4 days of an Intel$^{(R)}$ Core2Duo$^{(TM)}$ 2.4 GHz processor for $L = 8$ and 315 days for $L = 12$. These

values grow when $p = 6$: here the equilibration takes 120 minutes for an $L = 8$ sample and 110 hours for $L = 12$ (on the PC they would take 24 days for $L = 8$ and 10 years for $L = 12$).

The results shown in this paper for the $p = 5$ model would have required approximately 2150 equivalent years of an Intel$^{(R)}$ Core2Duo$^{(TM)}$ 2.4 GHz processor: the ones for $p = 6$ would have required 12000 years.

2.5 Results

2.5.1 Thermalization Tests

Thermalization tests are a crucial component of spin glass simulations. Before starting to collect relevant results from the data we have to be sure that they are actually taken from a properly thermalized system, and are not biased from spurious effects.

A standard analysis scheme consists in evaluating the average value of an observable on geometrically increasing time intervals. The whole set of measurements is divided in subsets, each of which covers only part of the system's history (the last *bin* covers the last half of the measurements, the previous bin takes the preceding quarter, the previous bin the previous eighth and so on), and observables are averaged within each bin. The convergence to equilibrium is checked comparing the results over different bins: stability in the last three bins within error bars (that need to be estimated in an accurate way) is a good indicator of thermalization.

We show in figures 2.5 and 2.6 the logarithmic binning of ξ, as defined in equation (2.26), in the $p = 5$ and $p = 6$ cases. The compatible (and stable) values for the three last points satisfy the thermalization test explained above. The data in the plots are for the lowest temperature used on each lattice size: this is expected to be the slowest mode of the system, and its thermalization guarantees that also data at higher temperature values are thermalized. The plateau in the last part of each plot is a clear signal of proper thermalization: only data from the last bin are eventually used to compute thermal averages.

We have also investigated how thermalization is reached in the individual samples (as opposed to the information on averages obtained from figures 2.5 and 2.6): to do that we have studied the correlation function for the temperature random walk defined in (2.31) and its associated integrated autocorrelation time, $\tau_{\rm int}$, defined in (2.32). As an example we plot in figure 2.7 the autocorrelation function (2.31) for a given sample as a function of the Monte Carlo time (here $L = 8$ and $p = 6$): one can see a fast, exponential decay in the left part of the figure, and (large) fluctuations around zero at

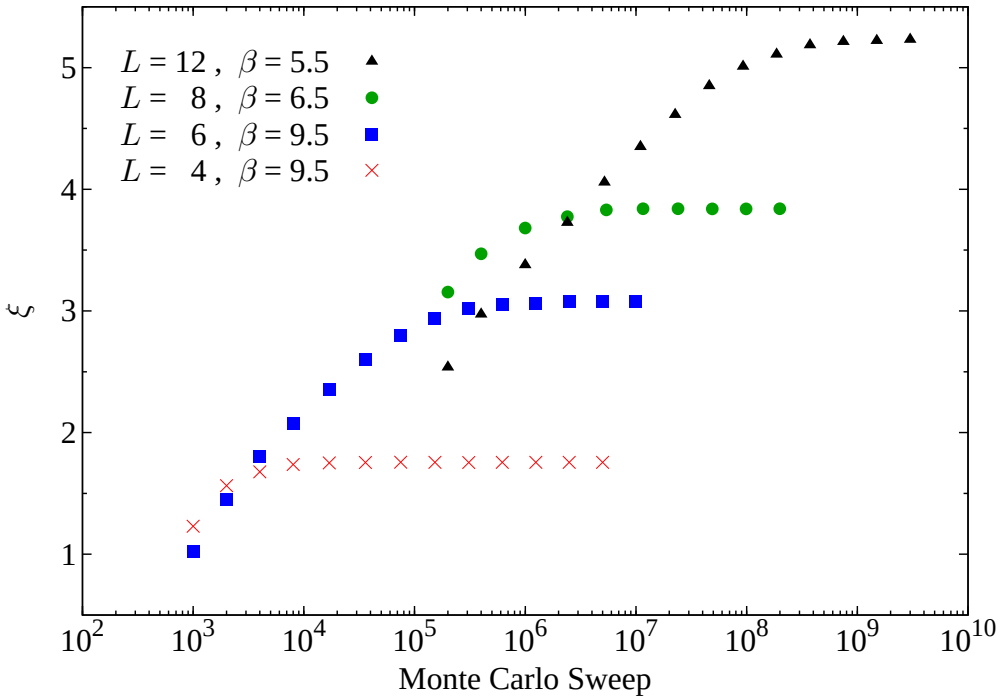

Figure 2.5: Log-binning thermalization test for $p = 5$. For all data points the point size is bigger than the corresponding error bar.

later times.

Sample to sample fluctuations of $\tau_{\rm int}$ are very large: in figure 2.8 we plot $\tau_{\rm int}$ for all our samples with $p = 5$, $L = 8$. In order to be on the safe side we have increased the number of MCS, by continuing the numerical simulation for a further extent, in all samples where our estimate of $\tau_{\rm int}$ was bigger than the length of the simulation divided by a constant c ($c = 20$ for $L = 8$ and $c = 15$ for $L = 12$, where achieving thermalization is much more difficult). [5]

[5] In the $p = 5$, $L = 8$ case for 2442 samples we have run a simulation of total extent $\eta = 4 \times 10^8$ MCSs, while for 5 samples $\eta = 8 \times 10^8$ MCSs, and for 1 sample $\eta = 1.6 \times 10^9$ MCS. In the $p = 5$, $L = 12$ case for 2382 samples $\eta = 6 \times 10^9$ MCSs, for 54 samples $\eta = 1.2 \times 10^{10}$, for 8 samples $\eta = 2.4 \times 10^{10}$, and for 7 samples $\eta = 4.8 \times 10^{10}$ MCS. In the $p = 6$, $L = 8$ case: for 1263 samples $\eta = 10^9$ MCSs, for 8 samples $\eta = 2 \times 10^9$ and for 9 samples $\eta = 4 \times 10^9$. In the $p = 6$, $L = 12$ case for 1173 samples $\eta = 6 \times 10^{10}$ MCSs, for 17 samples $\eta = 1.2 \times 10^{11}$ MCSs and for 6 samples $\eta = 2.4 \times 10^{11}$ MCSs.

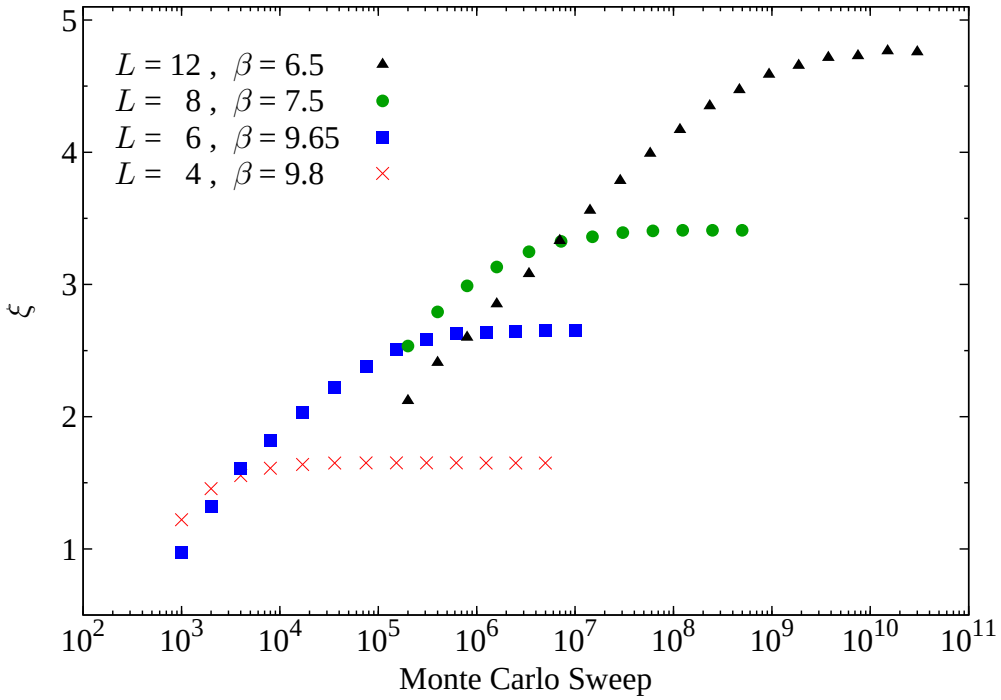

Figure 2.6: As in figure 2.5, but $p = 6$.

2.5.2 Critical temperature and critical exponents

Our analysis of the critical exponents of the system has been based on the quotient method [56, 62]: by using the averaged value of a given observable O measured in lattices of different sizes, we can estimate its leading critical exponent x_O,

$$\overline{\langle O(\beta)\rangle} \approx |\beta - \beta_c|^{-x_O} \,. \tag{2.33}$$

By considering two systems on lattices of linear sizes L and sL respectively one has that [56, 62]

$$\frac{\overline{\langle O(\beta, sL)\rangle}}{\overline{\langle O(\beta, L)\rangle}} = s^{x_O/\nu} + O(L^{-\omega}) \,, \tag{2.34}$$

where ν is the critical exponent of the correlation length and ω is the exponent of the leading-order scaling-corrections [56].

We use the operators $\partial_\beta \xi$, from (2.26), and χ_q, from (2.25) in equation (2.34) to obtain respectively the critical exponents $1 + 1/\nu$ and $2 - \eta_q$. The exponent $2 - \eta_m$ is obtained applying eq. (2.34) to the magnetic susceptibility χ_m, from (2.28).

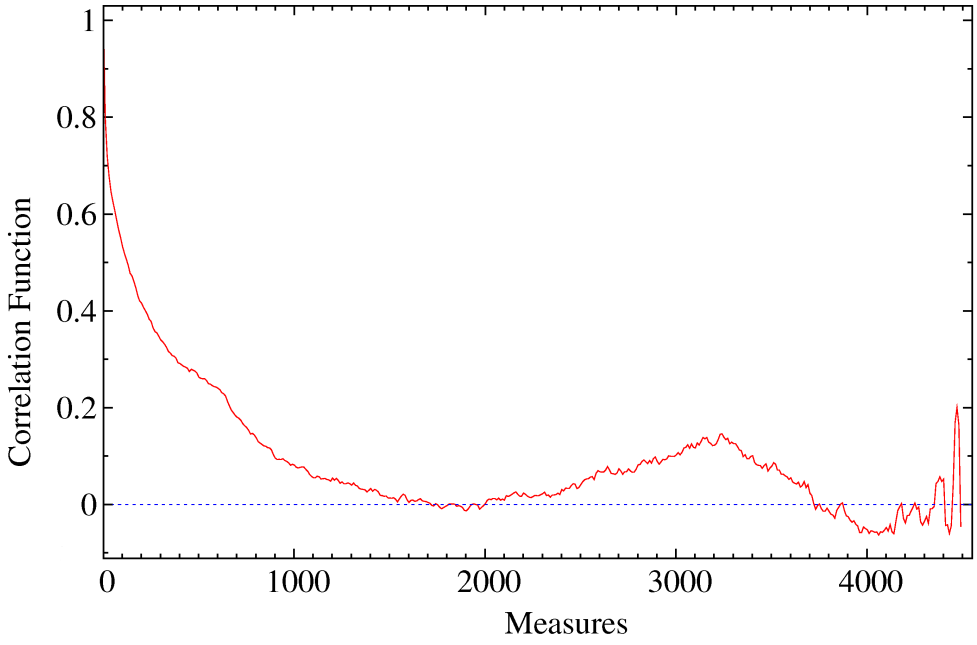

Figure 2.7: The autocorrelation function (2.31) for one generic sample ($p = 6$, $L = 8$).

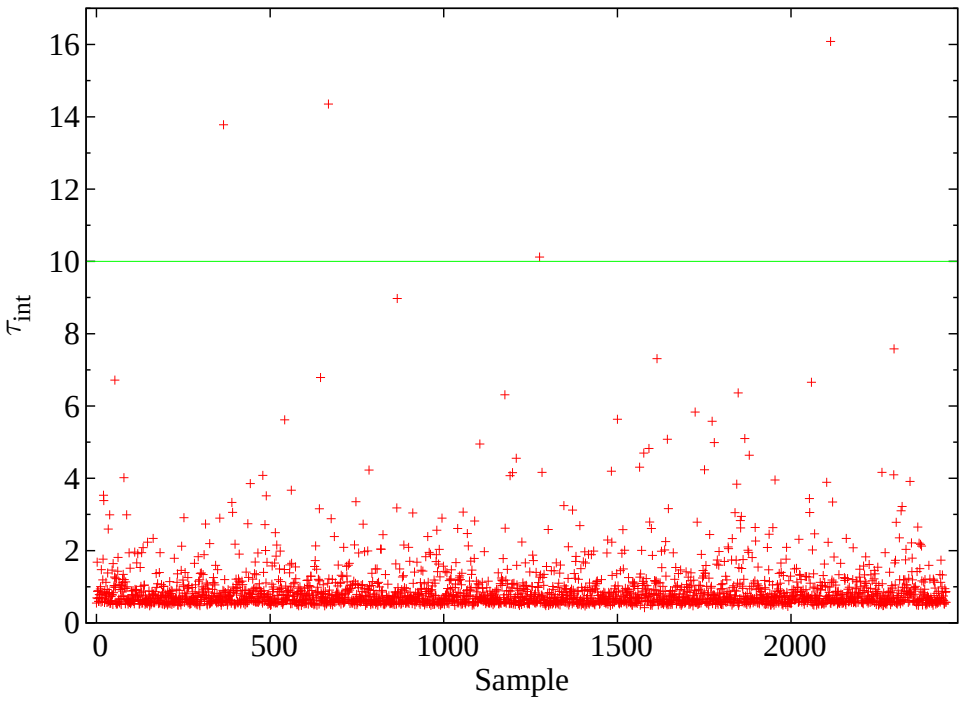

Figure 2.8: Integrated autocorrelation time, $\tau_{\rm int}$, for all $p = 5$, $L = 8$ samples. $\tau_{\rm int}$ is in units of blocks of ten measurements, i.e. of 2010^3 MCS. Samples above the green line have been "extended" (see the text for a discussion of this issue).

To use the quotient method we start estimating the finite-size transition temperature: we do this by looking at the crossing points of the correlation length in lattice units (ξ/L) for various lattice sizes. We have used a cubic spline interpolating procedure to compute both the crossings of ξ/L and its β-derivative (we have followed the approach described in detail in Ref. [63]).

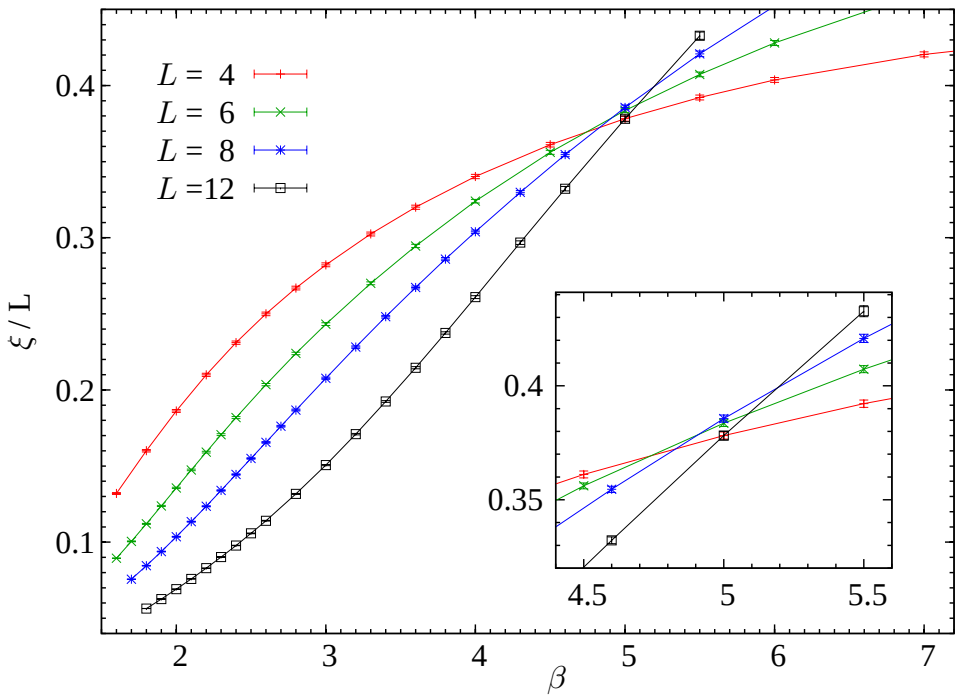

Figure 2.9: Overlap correlation length in lattice size units as a function of the inverse temperature β for $L = 4$, 6, 8 and 12. Here $p = 5$.

We show in figures 2.9 and 2.10 the behavior of ξ/L as a function of β. The different curves are for different lattice sizes. The crossing points are rather clear in both cases, giving a strong hint of the occurrence of a second order phase transition. At least for $p = 5$ scaling corrections play a visible role, and the crossing points undergo a small but clear drift towards lower temperatures for increasing lattice sizes. We summarize in tables 2.3 and 2.4 the β values of the crossing points for two different pairs of lattice sizes, together with the estimated values of the critical exponents ν and η_q that we obtain using relation (2.34).

Since we can only get reliable results on small and medium size lattice we cannot control in full scaling corrections, and a systematic extrapolation to the infinite volume limit is impossible. It is clear however that the effective critical exponents summarized in tables 2.3 and 2.4 do not suggest that

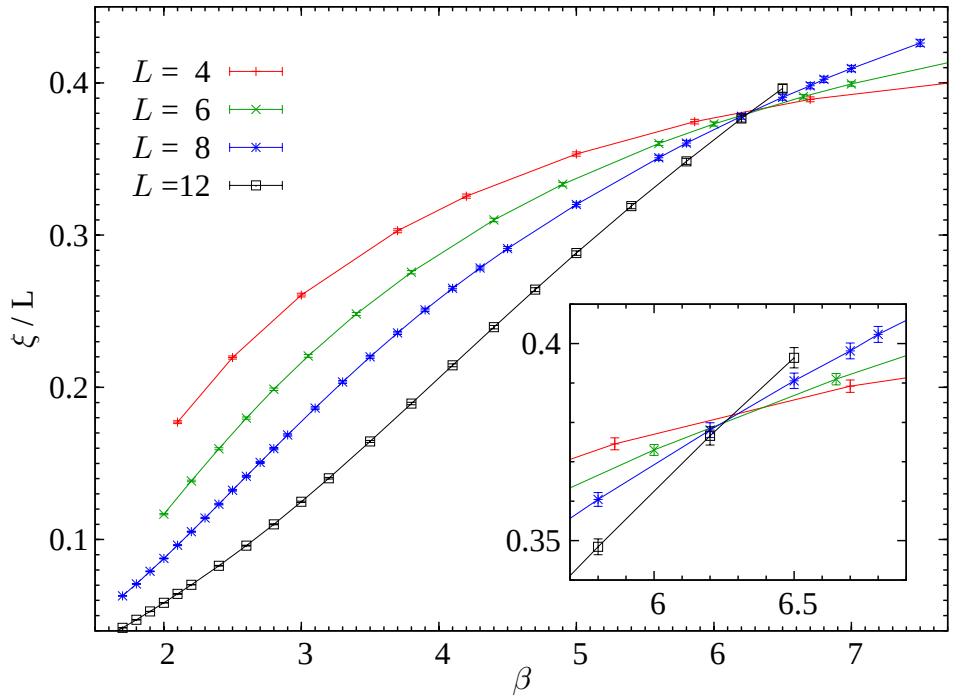

Figure 2.10: As in figure 2.9, but $p = 6$.

asymptotically for large volume the system will not be critical (in this case, for example, η_q should be asymptotically equal to 2): our numerical data clearly support the existence of a finite temperature phase transition.

(L_1, L_2)	$\beta_{\rm cross}(L_1, L_2)$	$\nu(L_1, L_2)$	$\eta_q(L_1, L_2)$	$\eta_m(L_1, L_2)$
$(4, 8)$	4.83(5)	0.82(3)	0.13(2)	1.72(2)
$(6, 12)$	5.01(4)	0.81(2)	0.16(2)	1.94(2)

Table 2.3: Numerical values of our estimates for the crossing point of the curves ξ/L. We give $\beta_{\rm cross}$, the thermal critical exponent ν, the anomalous dimension of the overlap η_q, and the anomalous dimension of the magnetization η_m.

We take as our best estimates for the critical exponents the one obtained from the lattices with sizes $L = 6$ and $L = 12$. For $p = 5$

$$\beta_c = 5.01(4)\,,\ \ \nu = 0.81(2)\,,\ \ \eta_q = 0.16(2)\,, \tag{2.35}$$

(L_1, L_2)	$\beta_{\rm cross}(L_1, L_2)$	$\nu(L_1, L_2)$	$\eta_q(L_1, L_2)$	$\eta_m(L_1, L_2)$
$(4, 8)$	6.30(9)	0.80(2)	0.10(2)	1.453(19)
$(6, 12)$	6.26(7)	0.80(4)	0.16(2)	1.971(19)

Table 2.4: As in table 2.3, but $p = 6$.

while for $p = 6$.

$$\beta_c = 6.26(7)\,,\ \nu = 0.80(4)\,,\ \eta_q = 0.16(2)\,. \tag{2.36}$$

It is interesting to compare these values with those of other Potts models with a different number of states. In particular we are interested in the value of the critical exponents as a function of the number of states, since we want to characterize the critical behavior of the various models and attempt a prediction of the model's behavior when the number of states is large. In our particular model and with the (low) values of the temperature that are interesting for us (since we need to get below the critical point) even with the large computational power available to us thanks to Janus the simulation for $p = 8$, say, on a $L = 12$ lattice, would require an unavailable amount of CPU time. What is found in the very interesting work of Refs. [51] and [55] is different, since there one is able to thermalize a $p = 10$ model on a large lattice, and no transition is observed. The model analyzed in these two references [51, 55] is indeed slightly (or maybe, it will turn out, not so slightly) different from the present one, since there $\overline{J}$ is negative. It is not clear to us if this difference could explain a quite dramatic discrepancy of the observed behavior, or if, for example, a different (very low) temperature regime should be analyzed to observe relevant phenomena: this is surely an interesting question to clarify, and the fact that the coupling have a negative expectation value, reducing in this way frustration, could turn out to make a difference.

2.5.3 Absence of ferromagnetic ordering in the critical region

Our DPM is in principle allowed to undergo a ferromagnetic phase transition (since no symmetry protects it), and at low temperatures could present a spontaneous magnetization, as discussed in Ref. [[63]]. Because of that we have carefully studied the magnetic behavior of the model at low temperatures. We have analyzed both the magnetization and the magnetic susceptibility below the spin glass critical point.

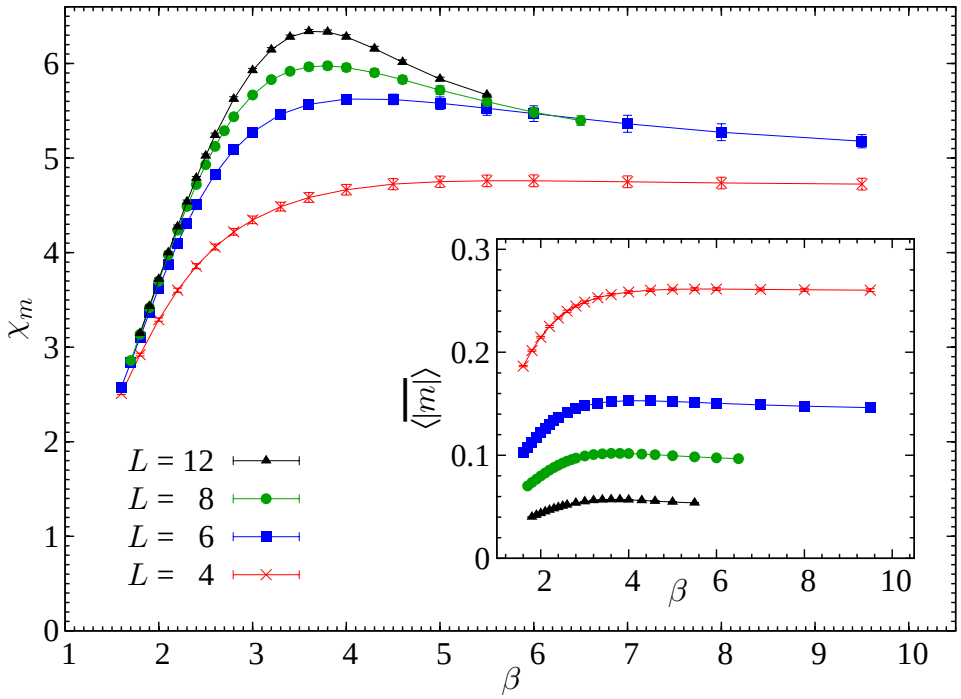

Figure 2.11: Magnetic susceptibility as a function of β for $L = 4$, 6, 8 and 12. Here $p = 5$.

In the paramagnetic phase the magnetization is random in sign, and its absolute value is expected to be proportional to $1/\sqrt{V}$. In Figs. 2.11 and 2.12 we check whether $\overline{\langle |\boldsymbol{m}| \rangle}$ around the spin glass critical region tends to an asymptotic value for larger lattice size, or not. From the figures we see $\overline{\langle |\boldsymbol{m}| \rangle}$ goes to zero in the critical region. Also, we studied the magnetic susceptibility $\chi_m = V\overline{\langle |\boldsymbol{m}|^2 \rangle}$ which is independent of size. Again in Figs. 2.11 and 2.12 we check that, and we see a non-divergent behavior. This behavior is extremely different from a ferromagnetic phase in which χ_m diverges as the volume.

Besides, as reported in Sec. 2.5.2 the exponent η_m is close to 2, so we could say that a ferromagnetic-paramagnetic phase transition does not happen in the range of temperatures that we have studied.

2.6 Evolution of critical exponents with p

In table 2.5 we summarize the values of the inverse critical temperature and of the thermal and overlap critical exponents for DPM from $p = 2$ (the Ising,

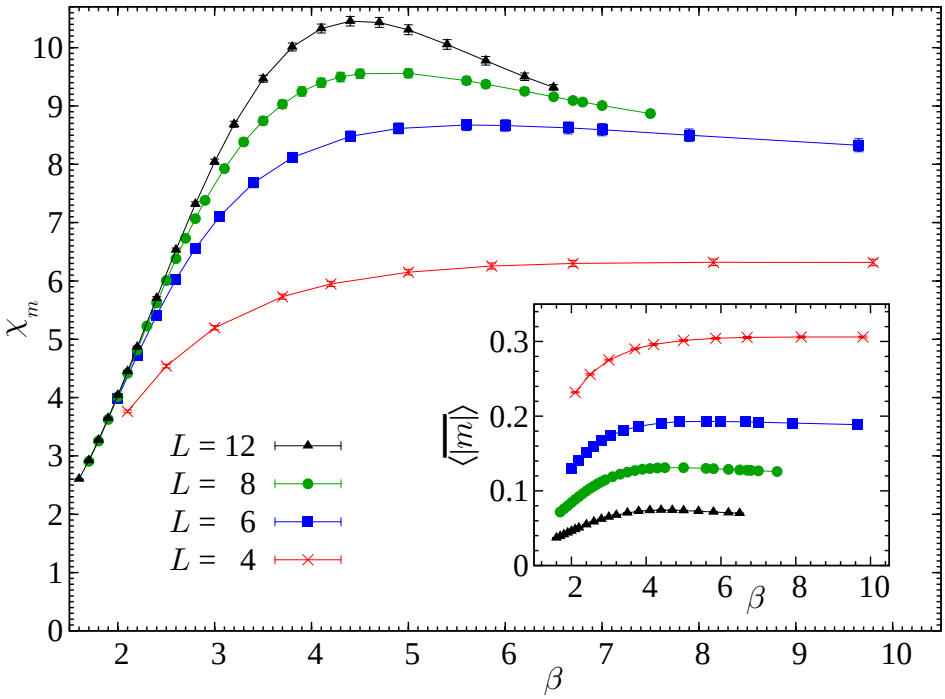

Figure 2.12: As in figure 2.11, but $p = 6$.

Edwards-Anderson spin glass) up to $p = 6$. We also plot these data items in figure 2.13.

From table 2.5 and figure 2.13 some results emerge very clearly. First, the inverse critical temperature roughly follows a linear behavior in p, with a slope very close to one. We have added in table 2.5 the ratio (R) between the numerical determinations (in $3d$) of $\beta_c(p)$ and their values in the Mean Field (MF) approximation. One can see that the large deviations from the MF prediction occur for large values of p (notice that $R > 1$ since MF suppresses fluctuations). [6]

[6] In the MF approximation was obtained, using the Hamiltonian [57, 67],

$$\mathcal{H} \equiv -\frac{p}{2} \sum_{i \neq j} J_{ij}\, \delta_{s_i, s_j} \,,$$

that $T_c/J = 1$ for $p \leq 4$ and $(T_c/J)^2 = 1 + (p-4)^2/42 + O((p-4)^4)$ for $p > 4$. In addition for very large p, $T_c/J \simeq \frac{1}{2}\,(p/\log p)^{1/2}$. Taking into account the extra p factor in the Hamiltonian used in the Mean Field and the fact that $J = \sqrt{2d}$ ($\overline{J_{ij}^2} = J^2/N$, being N the number of spins in the MF computation) since we are working in finite dimension (d), we obtain the finite dimension version of the critical β using the Mean Field approximation: $\beta_c = p/\sqrt{2d}$ for $p \leq 4$ and $\beta_c = \frac{p}{\sqrt{2d}}\left(1 - (p-4)^2/84 + O((p-4)^4)\right)$

Second, ν decreases monotonically and η_q grows monotonically with the number of states p. To discuss this behavior it is useful to keep in mind that when using finite size scaling to study a disordered first order phase transition one expects to find [64] $\nu = 2/D$ and $2 - \eta_q = D/2$, i.e., in our $D = 3$ case, $\nu = 2/3$ and $\eta_q = 1/2$. These are "effective" exponents, that are a bound to the ones allowed for second order phase transitions.

Both sets of values for ν and η_q are indeed completely compatible with tending, as p increases, to those limit values that characterize a first order phase transition. If this turns out, as our numerical data make very plausible to be true, two different scenarios open. The first possibility is that the p-states DPM undergoes a disordered first order phase transition for large enough values of p (just as in the ordered Potts model, that for $p \geq 3$ undergoes a first order phase transition), while the second possibility is that the DPM will show a standard second order phase transition for all finite values of p. This is the typical issue that is very difficult to settle with numerical work: an analytical solution of the model with infinite number of states would be very useful as a starting point in order to discriminate between these two possible scenarios.

p	β_c	ν	η_q	R
2 (Ref.[[65]])	1.786(6)	2.39(5) [7]	$-0.366(16)$[8]	2.187(8)
2 (Ref.[[66]])	1.804(16)	2.45(15)	$-0.375(10)$	2.209(20)
3 (Ref.[[55]])	2.653(35)	0.91(2)	0.02(2)	2.17(3)
4 (Ref.[[63]])	4.000(48)	0.96(8)	0.12(6)	2.45(3)
5 (this paper)	5.010(40)	0.81(2)	0.16(2)	2.51(2)
6 (this paper)	6.262(71)	0.80(4)	0.16(2)	2.69(3)

Table 2.5: Critical parameters as a function of p. All data are for binary couplings, with zero expectation value. By R we denote the ratio between the critical β in three dimensions and that computed in Mean Field.

2.7 Conclusions

In this note we have characterized the critical behavior of the $3D$ DPM with $p = 5$ and $p = 6$, i.e. with a reasonably large number of states. Our numerical

for $p > 4$ (notice the minus signum of the $(p-4)^2$ correction); in addition, for large p, one obtains $\beta_c \simeq \sqrt{\frac{2}{d}}\,(p \log p)^{1/2}$. Note that in our case $\sqrt{2d} \simeq 2.45$.

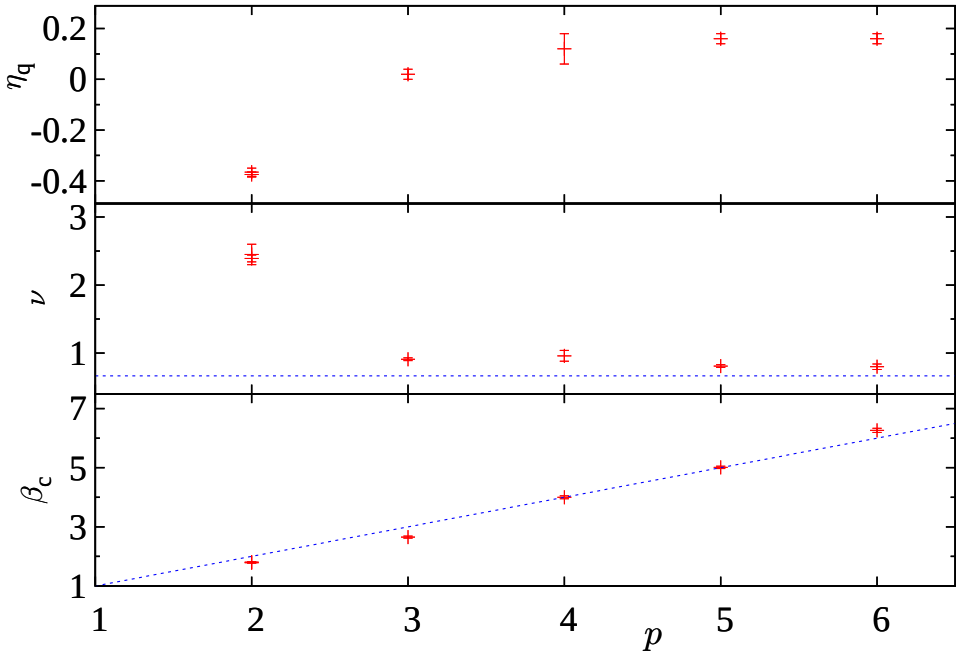

Figure 2.13: In the bottom plot: β_c versus p, and the straight line $f(p) = p$. Middle plot: ν as a function of p. We also show (dashed line) the value which marks the onset of a disordered first order phase transition ($\nu_{\rm first} = 2/3$). Upper plot: η_q as a function of p.

simulations have allowed us to reach some clear evidences, and to stress some difficult issues that will require further analysis.

We first stress that in both cases the spin glass transition is very clear, and we have been able to obtain a reliable estimate of the critical temperature and of the critical exponents ν and η_q. We have discussed what happens when p increases; we have found that β_c increases like p. A similar result was conjectured in Ref. [68] (for all values of p) analyzing high temperature series and found in Mean Field for $p \leq 4$ (although, of course, the slope is wrong). In addition, the behavior of ν and η_q is compatible with going to the large p limit value that characterizes a first order phase transition.

In the low temperature regime we do not see any sign of a transition to a ferromagnetic regime, that would be in principle allowed by the structure of our model. We cannot exclude that at very low T values something would happen, but in all the range we can explore the system stays in the spin glass phase.

A last piece of important evidence is that low temperature simulations of this model look difficult, and that they slow down severely for increasing p. In our particular model, where the expectation of the coupling is zero, it would be impossible to study reliably a $p = 8$ model with the computational resources available today.

This last observations opens indeed a last point that it will be interesting to analyze in the future. When couplings have a negative expectation value the simulation of a $p = 10$ model [51, 55] is possibly easier than it would be in our case, and the results are very different: in that case one does not see any sign of a phase transition. Analyzing how the DPM depends on the expectation value of the couplings is indeed at this point a crucial issue, since it could turn out that the reduction in frustration due to a negative net value of the couplings could completely change the critical behavior of the model.

Chapter 3

Sample to sample fluctuations

3.1 Preliminary study

Studying spin glasses, specially its spin glass phase, is a complex task. In Section 1.3.1, a brief analysis of the infinite range Sherrington-Kirkpatrick model was presented. This model has an exact solution which in the spin glass phase corresponds to the Parisi's Replica Symmetry Breaking (RSB). In fact, Guerra [70, 71] demonstrated the existence and uniqueness of the thermodynamic limit ($N \to \infty$) of all observables and also demonstrated that the thermodynamic limit of the free energy (without using the replica method) is bounded by the expression computed using Parisi's RSB Ansatz. Besides, Talagrand [72] demonstrated that the free energy asymptotically is that of the Parisi's Ansatz.

Several concepts have been developed to study the properties of the spin glass phase, such as stochastic stability, replica equivalence or overlap equivalence. These concepts will be described in detail are in following sections. In Section 3.1.1 it is shown that replica equivalence is equivalent to stochastic stability.

However, the application of these properties in short range models (like Edwards-Anderson model for instance), which are more realistic, is still controversial. Stochastic stability is thought to be a quite general property, so it should hold even in short range models, thus if one demonstrates that it is equivalent to replica equivalence, the last one would also hold. Besides, ultrametricity appears in mean field but demonstrating whether it also holds n short range models is quite complicated. In Section 3.1.2 it is shown that, in short range models, if overlap equivalence (which is an easier property to check) and replica equivalence hold, then ultrametricity appears.

In this context, the aim of the work presented in this chapter is to check

if these properties hold in a short range model: the Edwards-Anderson Ising spin glass. We focused on verifying the validity of the stochastic stability and ultrametricity, so our results complement analysis of overlap equivalence performed in Ref. [73, 88, 89, 100].

3.1.1 Stochastic stability and replica equivalence

In 1995, Guerra [82] demonstrated that[1]

$$\overline{\langle q_{12}^2 q_{23}^2 \rangle} = \frac{1}{2}\overline{\langle q_{12}^4 \rangle} + \frac{1}{2}\overline{\langle q_{12}^2 \rangle}^2 \tag{3.1}$$

$$\overline{\langle q_{12}^2 q_{34}^2 \rangle} = \frac{1}{3}\overline{\langle q_{12}^4 \rangle} + \frac{2}{3}\overline{\langle q_{12}^2 \rangle}^2 \tag{3.2}$$

His proof is based on the study of the average over the disorder of the internal energy and its fluctuations, and the properties of positivity and convexity of them. Moreover, they are stable under the addition of a stochastical perturbation

$$\lambda \sum_i \hat{J}_i \sigma_i \tag{3.3}$$

where $\hat{J}_i$ are independent random (Gaussian) variables. Guerra stated that

$$\overline{u_N} = -\frac{1}{2}\beta\left(1 - \overline{\langle q_{12}^2 \rangle}\right) \tag{3.4}$$

$$\begin{aligned} \frac{\partial \overline{u_N}}{\partial \beta} &= -\frac{1}{2}\left(1 - \overline{\langle q_{12}^2 \rangle}\right) \\ &+ \frac{\beta^2}{2} N \left(\overline{\langle q_{12}^4 \rangle} - 4\overline{\langle q_{12}^2 q_{23}^2 \rangle} + 3\overline{\langle q_{12}^2 q_{34}^3 \rangle}\right) \end{aligned} \tag{3.5}$$

$$\begin{aligned} \overline{u_N^2} - \overline{u_N}^2 &= -\frac{1}{2N}\overline{\langle q_{12}^2 \rangle} - \frac{1}{2N^2} + \frac{3}{2}\beta^2\left(\overline{\langle q_{12}^2 q_{34}^2 \rangle} - \overline{\langle q_{12}^2 q_{23}^2 \rangle}\right) \\ &+ \frac{1}{4}\beta^2\left(\overline{\langle q_{12}^4 \rangle} - \overline{\langle q_{12}^2 \rangle}^2\right) \end{aligned} \tag{3.6}$$

Using the property of the convexity of the free energy

$$\lim_{N\to\infty} N^{-1}\overline{\log Z_N} \tag{3.7}$$

and the fact that Eq. (3.6) is non-negative, he found that

$$\overline{\langle q_{12}^2 q_{34}^2 \rangle} - \overline{\langle q_{12}^2 q_{23}^2 \rangle} = \frac{1}{6}\left(\overline{\langle q_{12}^4 \rangle} - \overline{\langle q_{12}^2 \rangle}^2\right) \tag{3.8}$$

[1] Parisi in () using Replica Symmetry Breaking (RSB) obtained for first time these equations [102]

Besides, differentiating the right hand term of Eq. (3.4) with respect to β and using Eq. (3.5), he found, after a little algebra, that

$$\overline{\langle q_{12}^4 \rangle} - 4\overline{\langle q_{12}^2 q_{23}^2 \rangle} + 3\overline{\langle q_{12}^2 q_{34}^2 \rangle} = 0 \tag{3.9}$$

Now, using Eqs. (3.8) and (3.9), it is evident that Eqs. (3.1) and (3.2) hold. Moreover, it can also be demonstrated in a similar way that

$$\overline{\langle q_{12} q_{23} \rangle} = \frac{1}{2}\overline{\langle q_{12}^2 \rangle} + \frac{1}{2}\overline{\langle q_{12} \rangle}^2 \tag{3.10}$$

$$\overline{\langle q_{12} q_{34} \rangle} = \frac{1}{3}\overline{\langle q_{12}^2 \rangle} + \frac{2}{3}\overline{\langle q_{12} \rangle}^2 \tag{3.11}$$

In the last part of this section, we will show the derivation of the previous equations, Eqs. (3.10) and (3.11), for the moment of the overlap using replica equivalence concepts.

In 1998, Parisi [85] demonstrated these relations using the replica equivalence assumption, which means that

$$\sum_c f\left(Q_{ac}\right) = \sum_c f\left(Q_{bc}\right) \tag{3.12}$$

holds[2] for every function, f, and replica indices, a and b. We will report here the Parisi's derivation.

Replica equivalence implies:

$$\begin{aligned} \sum_{c,d} Q_{ac}^{k_1} Q_{bd}^{k_2} &= \left(\sum_c Q_{ac}^{k_1}\right)\left(\sum_d Q_{bd}^{k_2}\right) \\ &= \int dq_1 P(q_1) q_1^{k_1} \int d1_2 P(q_2) q_2^{k_2} \end{aligned} \tag{3.13}$$

The first term can be written as

$$\sum_{c,d} Q_{ac}^{k_1} Q_{bd}^{k_2} = \sum_{c,d;c\neq d} Q_{ac}^{k_1} Q_{bd}^{k_2} + \sum_{c,d;c=d} Q_{ac}^{k_1} Q_{bd}^{k_2} \tag{3.14}$$

The Eq. (3.13) holds both for $a \neq b$ and $a = b$. Firstly, we will solve the case $a = b$. Then the sum, where $c \neq d$, has $(n-2)(n-1)$ non-vanishing terms, so we can write it as

$$(n-2)(n-1) \int dq_{12} dq_{13} P^{12,13}(q_{12}, q_{13}) q_{12}^{k_1} q_{13}^{k_2} \tag{3.15}$$

[2] In the mean field framework this implies to have a well defined free energy in the limit $n \to 0$.

The second sum, where $c = d$, has $(n-1)$ non zero terms, so it is possible to be expressed as

$$(n-1)\int dq_{12}P(q_{12})q_{12}^{k_1+k_2} \tag{3.16}$$

Rewriting Eq. (3.13) taking into account Eqs. (3.14), (3.15) and (3.16) and evaluating the limit $n \to 0$, Parisi found that

$$P^{12,13}(q_{12},q_{13}) = \frac{1}{2}P(q_{12})P(q_{13}) + \frac{1}{2}P(q_{12})\delta(q_{12}-q_{13}) \tag{3.17}$$

Now, we will deal with the case $a \neq b$. Then the sum, where $c \neq d$, has $(n-2)(n-1)+1$ non vanishing terms, so its result is

$$[(n-2)(n-1)+1]\int dq_{12}dq_{34}P^{12,34}(q_{12},q_{34})q_{12}^{k_1}q_{34}^{k_2} \tag{3.18}$$

The second sum, where $c = d$, has $(n-2)$ non zero terms, so its result is

$$(n-2)\int dq_{12}dq_{13}P^{12,13}(q_{12},q_{13})q_{12}^{k_1}q_{13}^{k_2} \tag{3.19}$$

Substituting Eq. (3.17) in Eq. (3.19) and evaluating the limit $n \to 0$, one can rewrite Eq. (3.13) as

$$P^{12,34}(q_{12},q_{34}) = \frac{2}{3}P(q_{12})P(q_{34}) + \frac{1}{3}P(q_{12})\delta(q_{12}-q_{34}) \tag{3.20}$$

A similar method is used to deal with three or more overlaps. Eqs. (3.20) and (3.17) can also be written in terms of the averages. Assuming $k_1 = k_2 \equiv k$, then one finds that

$$\overline{\langle q_{12}^k q_{13}^k\rangle} = \frac{1}{2}\overline{\langle q_{12}^{2k}\rangle} + \frac{1}{2}\overline{\langle q_{12}^k\rangle}^2 \tag{3.21}$$

$$\overline{\langle q_{12}^k q_{34}^k\rangle} = \frac{1}{3}\overline{\langle q_{12}^{2k}\rangle} + \frac{2}{3}\overline{\langle q_{12}^k\rangle}^2 \tag{3.22}$$

Obviously, when $k = 2$ one recovers Eqs. (3.1) and (3.2) and when $k = 1$ one recovers Eqs. (3.10) and (3.11). According Parisi [85], every equation from replica equivalence, like the ones demonstrated here, can be also built using the general techniques of Guerra [82] or that of Aizenman and Contucci's method [83].

3.1.2 Overlap equivalence

The overlap equivalence is the property of a system when every generalized overlap that one can define, using an arbitrary observable, O,

$$q_O = \frac{1}{N}\sum_i O_i(\sigma^a)O_j(\sigma^b) \tag{3.23}$$

depends on the usual overlap q. That is, although they both do fluctuate when $N \to \infty$, q_O restricted to pairs of replicas with a given q do not fluctuate. Therefore, the usual overlap q contains all the useful information and, thus, is the complete order parameter[3]. Separability is a similar property, but using equilibrium configurations instead of real replicas. These two properties are equivalent[4].

Let M_{ab} be matrices that belong to the set of all matrices computed from the matrix Q (for example $\sum_c Q_{ac}Q_{cb}$). In 2000, Parisi and Ricci-Tersenghi [74] demonstrated that the overlap equivalence (or separability) implies that

$$\sum_b Q_{ab}^k M_{ab} = \sum_b \int dq\delta(q - Q_{ab})Q_{ab}^k M_{ab} = \int dqP(q)M(q)q^k \tag{3.24}$$

where $M(q)$ is the value that the matrix M_{ab} takes when $Q_{ab} = q$ and

$$P(q) = \sum_b \delta(q - Q_{ab}) \tag{3.25}$$

They setted that

$$\sum_b Q_{ab}^k M_{ab} = \int dqP(q)M(q)q^k \tag{3.26}$$

$$\sum_b Q_{ab}^k M'_{ab} = \int dqP(q)M'(q)q^k \tag{3.27}$$

$$\sum_b Q_{ab}^k M_{ab}M'_{ab} = \int dqP(q)M(q)M'(q)q^k \tag{3.28}$$

$$\tag{3.29}$$

Notice that the probability of the last equation can be written in function of the probabilities of the other two relations

$$P(q)M(q)M'(q) = \frac{[P(q)M(q)]\,[P(q)M'(q)]}{P(q)} \tag{3.30}$$

[3]For example, in mean field, the energy overlap satisfies $q_e = q^2$.

[4]See Ref. [74] for more details of this property. Moreover, a detailed analysis of the overlap equivalence is performed in this reference.

Choosing two matrices like

$$M_{ab} = \sum_c Q_{ac}^{k_1} Q_{cb}^{k_2} \tag{3.31}$$

$$M'_{ab} = \sum_c Q_{ac}^{k_3} Q_{cb}^{k_4} \tag{3.32}$$

and considering all possible values of k, they found that the joint probability $P^{(5)} \equiv P^{12,13,32,24,41}$ can be computed as

$$\begin{aligned} 3P^{(5)}(q, q_1, q_2, q_3, q_4) &= \delta(q_1 - q_4)\delta(q_2 - q_3)P^{(3)}(q, q_1, q_2) \\ &+ 2\frac{P^{(3)}(q, q_1, q_2)P^{(3)}(q, q_3, q_4)}{P(q)} \end{aligned} \tag{3.33}$$

where $P^{(3)}$ is defined as

$$P^{(3)} \equiv P^{12,23,31} \tag{3.34}$$

Now, integrating Eq. (3.33) over q, the joint probability $P^{(4)} \equiv P^{13,32,24,41}$ is computed

$$\begin{aligned} 3P^{(4)}(q_1, q_2, q_3, q_4) &= \frac{1}{2}\delta(q_1 - q_4)\delta(q_2 - q_3)\left[P(q_1)P(q_2) + \delta(q_1 - q_2)P(q_2)\right] \\ &+ 2\int dq \frac{P^{(3)}(q, q_1, q_2)P^{(3)}(q, q_3, q_4)}{P(q)} \end{aligned} \tag{3.35}$$

This relation is quite useful because $P^{(4)}(q_1, q_2, q_3, q_4)$ is, by construction, invariant under permutations of the overlaps, but the right hand term of Eq. (3.35) is not for a generic $P^{(3)}$ function. Therefore this equation enforces hard constrains in $P^{(3)}$. Impose equations like

$$P^{(4)}(q_i, q_j, q_j, q_i) - P^{(4)}(q_i, q_i, q_j, q_j) = 0 \tag{3.36}$$

$$P^{(4)}(q_i, q_i, q_j, q_l) - P^{(4)}(q_i, q_j, q_l, q_i) = 0 \tag{3.37}$$

One can compute admissible $P^{(3)}$.

3.1.3 Replica equivalence and overlap equivalence imply ultrametricity

Once we have explained the concepts of replica equivalence and overlap equivalence, we will now demonstrate that if this two concepts hold, then ultrametricity also hold.

In order to compute $P(q)$ and $P^{(3)}$, we assume that overlap can take only a few values, k (we suppose that our results also hold in the continuous case), so these probabilities are just a sum of delta functions

$$P(q) = \sum_{i=1}^{k} p_i \delta(q - q_i) \tag{3.38}$$

$$P^{(3)}(q_i, q_j, q_l) = \sum_{i,j,l} p_{ijl} \delta(q - q_i)\delta(q - q_j)\delta(q - q_l) \tag{3.39}$$

where p_i and p_{ijl} are weights, the last one is invariant under permutations of the indices. Obviously all the weights belong to the interval $[0, 1]$. Besides, relations like Eqs. (3.17) and (3.20) (from stochastic stability or replica equivalence) generate new relations between these p_{ijl} weights. Remind that in Section 1.3.1, where the existence of ultrametricity is shown in a infinite range model (but using distances defined from the overlaps), Eq. (1.52) tells us that only equilateral and isosceles triangles are allowed (in fact some isosceles triangles are also forbidden, those that do not satisfy this relation, that is, assuming $q_1 < q_2 < q_3$, all weights p_{iij} vanish if $i > j$). Therefore, if the scalene terms, p_{ijl} with $i \neq j \neq l$ and the forbidden isosceles terms vanish, ultrametricity holds. In fact, after using the symmetry under permutations of the indices and relations from replica equivalence, only weights from scalene and forbidden isosceles are free parameters, the rest of the parameters can be expressed as a function of them and weights p_i. For a given k, there are $\binom{k}{3}$ scalene weights and $\binom{k}{2}$ forbidden isosceles parameters.

Now, we will study, as an example, the case when $k = 5$. Using Eqs. (3.35) and (3.36) with the overlaps q_4 and q_5, we get

$$\begin{aligned} 0 &= \frac{1}{4}p_5 p_4 + \frac{p_{541}^2}{p_1} + \frac{p_{542}^2}{p_2} + \frac{p_{543}^2}{p_3} + \frac{p_{544}^2}{p_4} + \frac{p_{554}^2}{p_5} \\ &- \left(\frac{p_{551}p_{441}}{p_1} + \frac{p_{552}p_{442}}{p_2} + \frac{p_{553}p_{443}}{p_3} + \frac{p_{554}p_{444}}{p_4} + \frac{p_{555}p_{544}}{p_5} \right) \end{aligned} \tag{3.40}$$

Using replica equivalence relations, the allowed isosceles parameter and the equilateral parameters of the previous relation can be written as a function of the forbidden isosceles and scalene parameters

$$p_{555} = \frac{1}{2}p_5 (1 + p_5) - p_{554} - p_{553} - p_{552} - p_{551} \tag{3.41}$$

$$\begin{aligned} p_{444} &= \frac{1}{2}p_4 (1 + p_4 - p_5) - p_{441} - p_{442} - p_{443} \\ &+ p_{541} + p_{542} + p_{543} + p_{554} \end{aligned} \tag{3.42}$$

$$p_{544} = \frac{1}{2}p_4 p_5 - p_{541} - p_{542} - p_{543} - p_{554} \tag{3.43}$$

Substituting Eqs. (3.41), (3.42) and (3.43) in Eq. (3.40) we find

$$\begin{aligned} 0 &= 2p_1p_2p_3p_4p_5E_0^{5,4} + [2p_1p_2p_3p_5p_{554} + p_1p_2p_3p_4\,(3p_5 - 2p_{555})]\,(p_{543} + p_{542} \\ &+ p_{541}) + 4p_1p_2p_3p_5\,(p_{543}p_{542} + p_{543}p_{541} + p_{542}p_{541}) + [2p_2p_3p_5\,(p_1 + p_4)]\,p_{541}^2 \\ &+ [2p_1p_3p_5\,(p_2 + p_4)]\,p_{542}^2 + [2p_1p_2p_5\,(p_3 + p_4)]\,p_{543}^2 \end{aligned} \tag{3.44}$$

where in $E_0^{5,4}$ we include all the terms independent of the scalene parameters. It can be written as

$$\begin{aligned} E_0^{5,4} &= \tfrac{p_1p_4p_5}{4}\left[\tfrac{2p_{551}}{p_1p_5}\left(1-\tfrac{2p_{554}}{p_4p_5}\right)\left(1-\tfrac{2p_{441}}{p_1p_4}\right)+\left(1-\tfrac{2p_{551}}{p_1p_5}\right)\tfrac{4p_{554}p_{441}}{p_1p_4^2p_5}\right] \\ &+\tfrac{p_2p_4p_5}{4}\left[\tfrac{2p_{552}}{p_2p_5}\left(1-\tfrac{2p_{554}}{p_4p_5}\right)\left(1-\tfrac{2p_{442}}{p_2p_4}\right)+\left(1-\tfrac{2p_{552}}{p_2p_5}\right)\tfrac{4p_{554}p_{442}}{p_2p_4^2p_5}\right] \\ &+\tfrac{p_3p_4p_5}{4}\left[\tfrac{2p_{553}}{p_3p_5}\left(1-\tfrac{2p_{554}}{p_4p_5}\right)\left(1-\tfrac{2p_{443}}{p_3p_4}\right)+\left(1-\tfrac{2p_{553}}{p_3p_5}\right)\tfrac{4p_{554}p_{443}}{p_32p_4^2p_5}\right] \end{aligned} \tag{3.45}$$

The terms with the form

$$\frac{2p_{iij}}{p_ip_j} \tag{3.46}$$

belong to $[0,1]$ due to the fact that all the weights are positive. Therefore, it is obvious that $E_0^{4,3}$ is non-negative. Thus, all of the terms of Eq. (3.44) are also non-negative, so in order to satisfy the equation, all the scalene parameters must vanish. Repeating this method with other pairs of overlaps, one finds that all the scalene parameters do vanish

$$p_{543} = p_{542} = p_{541} = p_{532} = p_{531} = p_{521} = p_{432} = p_{431} = p_{421} = p_{321} = 0 \tag{3.47}$$

The following step is to study the isosceles parameters (in this case in $k = 4$), although they are a bit more tricky. Using Eqs. (3.35) and (3.37) with the overlaps q_1, q_2 and q_3 (assuming $q_1 < q_2 < q_3 < q_4$), we get

$$0 = \tfrac{p_1p_2p_3}{4}\left[\tfrac{2p_{331}}{p_1p_3}\left(1-\tfrac{2p_{332}}{p_2p_3}\right)\left(1-\tfrac{2p_{221}}{p_1p_2}\right)+\left(1-\tfrac{2p_{331}}{p_1p_3}\right)\tfrac{2p_{332}}{p_2p_3}\tfrac{2p_{221}}{p_1p_2}\right] \tag{3.48}$$

Repeating this method one finds other three similar relations. All of them imply that three of the forbidden isosceles parameters vanish

$$p_{331} = p_{441} = p_{442} = 0 \tag{3.49}$$

and one of the rest p_{332}, p_{221} or p_{443} do also vanish. Therefore, two of the forbidden isosceles parameters do not vanish and ultrametricity is violated. Fortunately, for a general k there are $\binom{k}{2} \sim k^2$ forbidden isosceles parameters and $k/2$ of these parameters violate ultrametricity. As k grows proportion of isosceles parameters which violate ultrametricity decreases and in the limit $k \to$ tends to 0.

We can conclude that if one assumes that replica equivalence and overlap equivalence hold, all the scalene and forbidden isosceles parameters vanish and, thus, ultrametricity also holds.

3.1.4 Ultrametricity in short range models

Finally, in 1996 Íñiguez, Parisi and Ruiz-Lorenzo [75] demonstrated that if ultrametricity holds in a short range spin glass model, Eq. (1.52) of ultrametricity in mean field is recovered. Let $\mathcal{H}$ be this short range spin glass model

$$\mathcal{H} = -\sum_{\langle ij \rangle} J_{ij}\sigma_i\sigma_j \tag{3.50}$$

which is invariant under permutations of replicas. Then, the general expression of the joint probability $P^{12,13,23}$ is

$$\begin{aligned} P^{12,13,23}(q_{12},q_{13},q_{23}) &= A(q_{12})\delta(q_{12}-q_{13})\delta(q_{12}-q_{23}) \\ &+ B(q_{12},q_{13})\theta(q_{12}-q_{13})\delta(q_{13}-q_{23}) \\ &+ B(q_{13},q_{23})\theta(q_{13}-q_{23})\delta(q_{23}-q_{12}) \\ &+ B(q_{23},q_{12})\theta(q_{23}-q_{12})\delta(q_{12}-q_{13}) \end{aligned} \tag{3.51}$$

Moreover, the two replicas probability $P^{12,13}$ can be computed from Eq. (3.51) integrating over q_{23}, so

$$\begin{aligned} P^{12,13}(q_{12},q_{13}) &= \left[A(q_{12}) + \int_{q_{12}}^{\infty} dq_{23} B(q_{13},q_{23})\right]\delta(q_{12}-q_{13}) \\ &+ B(q_{12},q_{13}) \end{aligned} \tag{3.52}$$

Integrating again, now over q_{13}, the one replica probability distribution is computed

$$P(q_{12}) = A(q_{12}) + \int_{q_{12}}^{\infty} dq_{13} B(q_{12},q_{13}) + \int_{-\infty}^{\infty} dq_{13} B(q_{12}.q_{13}) \tag{3.53}$$

Using Eq. (3.17) and a little algebra, one finds that

$$A(q_{12}) = \int_{-\infty}^{q_{12}} dq_{13} B(q_{12},q_{13}) \tag{3.54}$$

$$B(q_{12},q_{13}) = 2\left(\int_{-\infty}^{\infty} dq_{23} B(q_{12},q_{23})\right)\left(\int_{-\infty}^{\infty} dq_{23} B(q_{13},q_{23})\right) \tag{3.55}$$

Besides, using Eqs. (3.53) and (3.54) one gets

$$P(q_{12}) = 2\int_{-\infty}^{\infty} dq_{23} B(q_{12},q_{23}) \tag{3.56}$$

Finally, taking into account Eqs. (3.56), (3.54) and (3.55) one finds

$$A(q_{12}) = \frac{1}{2}x(q_{12})P(q_{12}) \tag{3.57}$$

$$B(q_{12},q_{13}) = \frac{1}{2}P(q_{12})P(q_{13}) \tag{3.58}$$

Substituting them in Eq. (3.51), Eq. (1.52) is recovered. So, if ultrametricity holds in finite dimensional spin glasses, it will be the same kind of ultrametricity as obtained in mean field

Sample-to-sample fluctuations of the overlap distributions in the three-dimensional Edwards-Anderson spin glass

R. A. Baños, A. Cruz, L. A. Fernandez, J. M. Gil-Narvion, A. Gordillo-Guerrero, M. Guidetti, D. Iñiguez, A. Maiorano, F. Mantovani, E. Marinari, V. Martin-Mayor, J. Monforte-Garcia, A. Muñoz-Sudupe, D. Navarro, G. Parisi, S. Perez-Gaviro, F. Ricci-Tersenghi, J. J. Ruiz-Lorenzo, S. F. Schifano, B. Seoane, A. Tarancón, R. Tripiccione and D. Yllanes.

Published in *Phys. Rev. B* **84**, 174209 (2011).

3.2 Introduction

Spin glasses are model glassy systems which have been studied for decades and have become a paradigm for a broad class of scientific applications. They not only provide a mathematical model for disordered alloys and their striking low-temperature properties (slow dynamics, age-dependent response), but they have also been the test-ground for new ideas in the study of other complex systems, such as structural glasses, colloids, econophysics, and combinatorial optimization models. The non-trivial phase-space structure of the mean-field solution to spin glasses [76, 77, 78] encodes many properties of glassy behavior.

Whether the predictions of the mean-field solutions correctly describe the properties of finite-range spin-glass models (and of their experimental counterpart materials) is a long-debated question. The Droplet Model describes the spin glass phase in terms of a unique state (apart from a global inversion symmetry) and predicts a (super-universal) coarsening dynamics for the off-equilibrium regime. [79] Moreover, there is no spin glass transition in presence of any external magnetic field. On the other side, the Replica Symmetry Breaking scenario [78, 80], based on the mean field prediction, describes a complex free-energy landscape and a non-trivial order parameter distribution in the thermodynamic limit; the dynamics is critical at all temperatures in the spin-glass phase. The spin glass transition temperature is finite also in presence of small magnetic fields; the search for the de Almeida-Thouless line $T_c(h)$ is the purpose of many numerical experiments (see, for example, Ref. [81]).

From the theoretical perspective, the last decade has seen a strong advance in the understanding of the properties of the mean-field solution: its correctness has been rigorously proved thanks to the introduction of new concepts and tools, like stochastic stability or replica and overlap equivalence [82, 83, 84, 85, 86]. Besides, numerical simulation has been the methodology

of choice when investigating finite-range spin glasses, even if the computational approach is severely plagued by the intrinsic properties (slow convergence to equilibrium, slowly growing correlation lengths) of the simulated system's (thermo)dynamics. In this respect, a Moore-law-sustained improvement in performance of devices for numerical computation and new emerging technologies in the last years has allowed for very fast-running implementation of standard simulation techniques. By means of the non-conventional computer Janus [87] we have been able to collect high-quality statistics of equilibrium configurations of three-dimensional Edwards-Anderson spin glasses, well beyond what would have been possible on conventional PC clusters.

Theoretical predictions and Janus numerical data have been compared in detail in Refs. [88] and [89]. One of the main results presented therein is that equilibrium properties at a given finite length scale correspond to out-of-equilibrium properties at a given finite time scale. On experimentally accessible scales (order 10^4 seconds waiting times corresponding to order 10^2 lattice sizes) the Replica Symmetry Breaking picture turns out as the only relevant effective theory. Theories in which some of the fundamental ingredients of the mean-field solutions are lacking (overlap equivalence in the TNT model [90], ultrametricity in the Droplet Model) show inconsistencies when their predictions are compared to the observed behavior.

In this work we reconsider the analysis of the huge amount of data at our disposal, focusing on the sample-to-sample fluctuations of the distribution of the overlap order parameter. The assumptions of the mean-field theory allow us to make predictions on the joint probabilities of overlaps among many real replicas which can be tested against numerical data for the three-dimensional Edwards-Anderson model. The structure of the paper is as follows: in section 3.3 we give some details on the considered spin-glass model and the performed Monte Carlo simulations. In the subsequent section we first recall some fundamental concepts such as stochastic stability, ultrametricity, replica and overlap equivalence and some predictions on the joint overlap probability densities, and then present a detailed comparison with numerical data. In section 3.5 we show how finite-size numerical overlap distributions compare to the mean-field prediction in which finite-size effects are appropriately introduced. We finally present our conclusions in the last section.

3.3 Monte Carlo Simulations

3.3.1 The Model

We consider the Edwards-Anderson model [91] in three dimensions, with Ising spin variables $\sigma_i = \pm 1$ and binary random quenched couplings $J_{ij} = \pm 1$. Each spin, set on the nodes of a cubic lattice of size $V = L^3$ (L being the lattice size), interacts only with its nearest neighbors under periodic boundary conditions. The Hamiltonian is:

$$H = -\sum_{\langle i,j \rangle} J_{ij}\sigma_i\sigma_j \quad , \tag{3.59}$$

where the sum extends over nearest-neighbor lattice sites. In what follows we are dealing mainly with measures of the *spin overlap*

$$q_{ab} = \frac{1}{L^3}\sum_i \sigma_i^a \sigma_i^b \ , \tag{3.60}$$

where a and b are replica indices, and the sample-dependent frequencies $N_J(q_{ab})$ with which we estimate the overlap probability distribution $P_J(q)$ of each sample (we indicate one-sample quantities by the subscript J):

$$P_J(q_{ab}) = \left\langle \delta\left(q_{ab} - \frac{1}{L^3}\sum_i \sigma_i^a \sigma_i^b \right) \right\rangle \ , \tag{3.61}$$

where $\langle(\cdots)\rangle$ is a thermal average. In what follows $\overline{(\cdots)}$ denotes average over disorder.

3.3.2 Numerical Simulations

We present an analysis of overlap probability distributions computed on equilibrium configurations of the three-dimensional Edwards-Anderson model defined in Eq. (3.59). We computed the configurations by means of an intensive Monte Carlo simulation on the *Janus* supercomputer. Full details of these simulation can be found in Ref. [89].For easy reference, we summarize the parameters of our simulations in Table 3.1. In order to reach such low temperature values, it has been crucial to tailor the simulation time, on a sample-by-sample basis, through a careful study of the temperature random-walk dynamics along the parallel tempering simulation.

L	$T_{\min}$	$T_{\max}$	N_T	N_S
8	0.150	1.575	10	4000
16	0.479	1.575	16	4000
24	0.625	1.600	28	4000
32	0.703	1.549	34	1000

Table 3.1: A summary of parameters of the simulations we have used in this work. For each lattice size, L, we considered N_S samples, with four independent real replicas per sample. For the Parallel Tempering algorithm, N_T temperatures were used between $T_{\min}$ and $T_{\max}$, uniformly distributed in that range (except in the case of $L = 8$, in which we have 7 temperatures uniformly distributed between 0.435 and 1.575 plus the 3 temperatures 0.150, 0.245 and 0.340). Our MCS consisted of 10 Heat-Bath sweeps followed by 1 Parallel Tempering update. More detailed information regarding these simulations can be found in Ref. [89].

3.4 Replica equivalence and ultrametricity

The Sherrington-Kirkpatrick (SK) model [76] is the mean-field counterpart of model (3.59). It is defined by the Hamiltonian

$$H = \sum_{i \neq j} J_{ij} \sigma_i \sigma_j \ , \tag{3.62}$$

where the sum now extends to all pairs of N Ising spins and the couplings J_{ij} are independent and identically-distributed random variables extracted from a Gaussian or a bimodal distribution with variance $1/N$. The quenched average of the thermodynamic potential may be performed by rewriting the n-replicated partition function in terms of an $n \times n$ overlap matrix $Q_{a,b}$ for which the saddle-point approximation gives the self-consistency equation

$$Q_{ab} = \langle \sigma^a \sigma^b \rangle \ , \tag{3.63}$$

where the average $\langle (\cdots) \rangle$ involves an effective single-site Hamiltonian in which $Q_{a,b}$ couples the replicas. The thermodynamics of model (3.62) is recovered in the limit $n \to 0$, after averaging over all possible permutations of replicas.

The overlap probability distribution $P(q)$ is defined in terms of such an averaging procedure: for any function of the overlap $f(q)$, one has that

$$\int dq_{a,b} P(q_{a,b}) f(q_{a,b}) = \lim_{n \to 0} \frac{1}{n!} \sum_{p} f(Q_{p(a),p(b)}) \ , \tag{3.64}$$

the sum being over permutations p of the n replica indices. The assumption of the replica approach is that $P(q)$ defined in this way is the same as the large-volume limit of the disorder average $\overline{P_J(q)}$ of the probability distribution of the overlap defined in Eqs. (4.19) and (3.61).

The hierarchical solution [78] for Q_{ab} is based on two main assumptions: stochastic stability and ultrametricity. In what follows we are interested in the consequences of such assumptions when dealing with a generic random spin system defined by a Hamiltonian $H_J(\sigma)$, where the subscript J summarizes the dependence on a set of random quenched parameters, e.g., the random couplings in models (3.59) and (3.62).

Stochastic stability [82, 83] in the replica formalism is equivalent to replica equivalence [84, 85]: one-replica observables retain symmetry under replica permutation even when the replica symmetry is broken. This property implies that the $n \times n$ overlap matrix for an n-replicated system, satisfies

$$0 \equiv \sum_c \left[f(Q_{ac}) - f(Q_{bc}) \right] \tag{3.65}$$

for any function f and any indices a, b. In the framework of the solution to the mean-field model, this is necessary for having a well defined free energy [77, 85] in the limit $n \to 0$. A consequence of (3.65) is, given a set of n real replicas, the possibility of expressing joint probabilities of m among the $n(n-1)/2$ overlap variables to joint probabilities for overlaps among a set of up to m replicas. [85] The following relations hold, for instance, in the cases $n = 4, m = 2$ and $n = 6, m = 3$:

$$\begin{aligned} 3P\left(q_{12}, q_{34}\right) &= 2P\left(q_{12}\right) P\left(q_{34}\right) \\ &+ \delta\left(q_{12} - q_{34}\right) P\left(q_{12}\right) \ , \end{aligned} \tag{3.66}$$

$$\begin{aligned} 15P\left(q_{12}, q_{34}, q_{56}\right) &= 2P\left(q_{12}, q_{23}, q_{31}\right) \\ &+ 5P\left(q\right) P\left(q'\right) P\left(q''\right) \\ &+ 2\delta\left(q - q'\right) P\left(q'\right) P\left(q''\right) \\ &+ 2\delta\left(q' - q''\right) P\left(q\right) P\left(q'\right) \\ &+ 2\delta\left(q - q''\right) P\left(q\right) P\left(q'\right) \\ &+ 2\delta\left(q - q'\right) \delta\left(q' - q''\right) P\left(q\right) \ , \end{aligned} \tag{3.67}$$

where $q \equiv q_{12}$, $q' \equiv q_{34}$, $q'' \equiv q_{56}$.

Note that relation (3.66) quantifies the fluctuations of the overlap distribution: even in the limit of very large volumes, for the joint probability of two independent overlaps,

$$P(q_{12}, q'_{34}) \equiv \overline{P_J(q_{12}, q'_{34})} \neq \overline{P_J(q_{12})}\ \overline{P_J(q'_{34})} \ . \tag{3.68}$$

Ultrametricity is the other remarkable feature of the mean-field solution, stating that when picking up three equilibrium configurations, either their mutual overlaps are all equal or two are equal and smaller than the third. A distance can be defined in terms of the overlap so that all triangles among states are either equilateral or isosceles. In terms of overlaps probabilities, the property reads:

$$\begin{aligned} P(q_{12}, q_{23}, q_{31}) &= \delta(q_{12} - q_{23})\delta(q_{23} - q_{31})B(q_{12}) \\ &+ [\Theta(q_{12} - q_{23})A(q_{12}, q_{23})\delta(q_{23} - q_{31}) \\ &+ \text{two perm.}] \end{aligned} \tag{3.69}$$

where $\Theta(x)$ is the Heaviside step function. By replica equivalence, A and B can be expressed in terms of $P(q)$: [97]

$$A(q, q') = P(q)P(q') \ , \tag{3.70}$$

$$B(q) = x(q)P(q) \ , \tag{3.71}$$

$$x(q) = \int_{-q}^{q} P(q')dq' \ . \tag{3.72}$$

Ultrametricity implies that the joint probability of overlaps among n replicas, which in principle depends on $n(n-1)/2$ variables, is a function of only $n-1$ variables. Thus, using replica equivalence, it is reduced to a combination of joint probabilities of a smaller set of replicas. Note that $P(q_{12}, q_{23}, q_{31})$ is the only *non-single-overlap* quantity appearing in the r.h.s. of Eq. (3.67): by combining replica equivalence and ultrametricity, three-overlap probabilities reduce to combinations of single-overlap probabilities.

Stochastic stability, or equivalently replica equivalence, is a quite general property that should apply also to short-range models, in the hypothesis that the model is not unstable upon small random long-range perturbations [82]. Whether short-range models would feature ultrametricity is a long-debated question, for which direct inspection by numerical means is the methodology of choice. It has been shown [98] that, in the hypothesis that the overlap distribution is non-trivial and fluctuating in the thermodynamic limit, then ultrametricity is equivalent to the simpler assumption of *overlap equivalence*, in the sense that it is the unique possibility when both replica and overlap equivalence hold. Overlap equivalence states that, in the presence of replica symmetry breaking, given any local function $A_i(\sigma)$, the generalized overlap $q_A = N^{-1}\sum_i A_i(\sigma^a)A_i(\sigma^b)$, with a, b indices of real replicas, does not fluctuate when considering configurations at fixed spin-overlap [99]: all definitions of the overlap are equivalent. Assuming that stochastic stability is a very generic property, there may be violation of ultrametricity only in a situation

in which also overlap equivalence is violated. In this respect, evidence of overlap equivalence has been found in both equilibrium and off-equilibrium numerical simulations of the Edwards-Anderson model [89, 100, 88].

The aim of this work is a numerical study of the sample-to-sample fluctuations of the overlap distribution; we focus on the sample statistics of the cumulative overlap probability functions defined by

$$X_J(q) \equiv \int_{-q}^{q} P_J\left(q'\right) dq' \ . \tag{3.73}$$

This is a random variable, since it depends on the random disorder, and we denote by $\Pi_q(X_J)$ its probability distribution. We estimate the moments of the Π_q distribution as

$$\begin{aligned} X_k(q) &= \int x^k \Pi_q(x) dx = \overline{\left[X_J\left(q\right)\right]^k} \\ &= \overline{\left[\int_{-q}^{q} P_J\left(q'\right) dq'\right]^k} \ , \end{aligned} \tag{3.74}$$

where $P_J\left(q\right)$ are the Monte Carlo overlap frequencies for a given sample.

Given a set of three independent spin configurations we obtain also the probability for the three overlaps to be smaller than q:

$$X_{\mathrm{T}}(q) = \overline{\int_{-q}^{q} P_J(q_{12}, q_{23}, q_{31}) dq_{12} dq_{23} dq_{31}} \tag{3.75}$$

In the replica equivalence assumption $X_k(q)$ can be expressed in terms of $X_{\mathrm{T}}(q)$ and $X_1(q)$; integrating the Ghirlanda-Guerra relations (3.66,3.67) up to $k = 3$ we have:

$$X_2(q) = \frac{1}{3} X_1(q) + \frac{2}{3} X_1^2(q) \ , \tag{3.76}$$

$$\begin{aligned} X_3(q) &= \frac{1}{15}\left[2X_{\mathrm{T}}(q) + 2X_1(q)\right. \\ &+ \left. 6X_1^2(q) + 5X_1^3(q)\right] \ . \end{aligned} \tag{3.77}$$

Ultrametricity imposes a further constraint: from relations (3.69 - 3.72) it follows

$$X_{\mathrm{T}}(q) = \left[x(q)\right]^2 \equiv X_1^2(q) \ , \tag{3.78}$$

And the quantities (3.74) become polynomials in X_1 only. The above relation simply states that, if ultrametricity holds, the probability of finding three overlaps smaller than q factorizes to the probability of finding two overlaps

independently smaller than q, with the third bound to be equal to at least one of the previous two.

For models in which the overlap is not fluctuating in the large-volume limit (i.e., $P(q)$ is a delta function) the above relations are satisfied but reduce to trivial identities. If the replica symmetry is broken, then stochastic stability imposes strong constraints on the form of the overlap matrix and consequently on the overlap probability densities. Ultrametricity is a further simplification: lack of this property might indicate that more than one overlap might be needed to describe the equilibrium configurations [98].

We can extract further information from the distribution $\Pi_q(x)$. It has been found [101, 102, 103] that in mean-field theory the probability distribution $\pi(y)$ of the random variable $Y_J = 1 - X_J$ behaves as a power law for $Y_J \sim 1$. This implies that $\Pi_q(x)$ also follows a power law for small x values

$$\begin{aligned} \pi_q(y \to 1) &\sim (1-y)^{x(q)-1} \quad , \\ \Pi_q(s \to 0) &\sim s^{x(q)-1} \quad . \end{aligned} \tag{3.79}$$

Since for most samples the $P_J(q)$ is a superposition of narrow peaks around sample-dependent q values, separated by wide q intervals in which P_J is exactly zero, when dealing with data from simulations of finite-size systems, it is convenient to turn to the cumulative distribution of the X_J to improve the statistical signal, especially at small q values:

$$\Pi_q^C(s) = \int_0^s dx \Pi_q(x) \tag{3.80}$$

which should verify at small s

$$\Pi_q^C(s \to 0) \sim s^{x(q)} \; ; \tag{3.81}$$

the probability of finding a sample in which the overlap probability distribution $P_J(q)$ in the interval $[0, q]$ is small enough to verify $\int_{-q}^{q} P(q')dq' < s$ goes to zero as a power law of s.

3.4.1 Numerical results

We recall that in our simulations we tailored the temperature range for the parallel tempering implementation to improve its performance as discussed in Ref. [89]. This brought us to direct measurements of observables at temperature sets that were not perfectly overlapping at all lattice sizes. In what follows we compare data at temperatures that are slightly different for different lattice sizes. Considering that even if the simulations were performed

at exactly the same temperatures, tiny size-dependent critical effects may always affect the results, we preferred not to perform involved interpolations to correct for order 1% or less of temperature discrepancies. In what follows we will refer to the set of data at $T \sim 0.64T_c$ and $T \sim 0.75T_c$ for the sake of brevity; the precise values of the temperatures are summarized in Table 3.2. We also compare data at exactly $T = 0.625 = 0.57T_c$ for lattice sizes $L = 8, 16, 24$.

As our simulations were not optimized to study the critical region, we take the value $T_c = 1.109(10)$ from Refs. [104] and [105] (featuring many more samples and small sizes to control scaling corrections). Still, combining the critical exponents determination of these references with the Janus data used herein, we obtain a compatible value of 1.105(8). [106]

L	$T \sim 0.57T_c$	$T \sim 0.64T_c$	$T \sim 0.75T_c$
8	0.625	–	0.815
16	0.625	0.698	0.844
24	0.625	0.697	0.842
32	–	0.703	0.831

Table 3.2: Temperature values for each lattice size ($T_c = 1.109$ [104, 105]).

We simulated four independent real replicas per sample: thus we avoid any bias in computing $X_T(q)$, Eq. (3.75), by picking three configurations in three distinct replicas. We show the computed $X_T(q)$ for the largest lattices $L = 24$ and $L = 32$ in Fig. 3.1 i) considering only configurations for different replicas (data labeled as ABC); ii) picking two configurations out of three from the same replica (labeled AAB); iii) picking the three configurations in the same replica (labeled AAA) . To minimize the effect of bias due to *hard* samples, we picked up the same number of configurations per sample, spaced in time by an amount proportional to the exponential autocorrelation time τ_{exp} of that sample [89]. The three data sets (ABC, AAB, AAA) are equivalent and small deviations at low q values remain within error bars: this is a strong indication of the statistical quality of our data, as described in Ref. [89].

We now come to test the Ghirlanda-Guerra relations, Eqs. (3.76) and (3.77). Plotting the two sides of Eq. (3.76) parametrically in q, the data show a slight deviation from the theoretical prediction (see Fig. 3.2 top). It is interesting to compare the discrepancies for different lattice sizes. As the position and width of $P(q)$ are size-dependent, it seems more natural to compare functions of the moments X_k for different lattice sizes as functions

of the integrated probability $x(q) = X_1(q)$ (see Fig. 3.2 middle). It is evident from the third plot in Fig. 3.2 that the quantity

$$K_2 = \left[X_2 - (X_1 + 2X_1^2)/3\right]^2 \tag{3.82}$$

is definitely non-zero although very small in the entire range. However, the data are compatible with K_2 decreasing with lattice size and becoming null in the $L \to \infty$ limit.

We can reach similar conclusions regarding X_3 as a function of $X_{\rm T}$ and X_1, and the quantity

$$K_3 = \left[X_3 - (2X_{\rm T} + 2X_1 + 6X_1^2 + 5X_1^3)/15\right]^2 \tag{3.83}$$

(see Fig. 3.3). Even if the data for different lattice sizes stand within a couple of standard deviations, there is a clear improvement in the agreement between the prediction and the Monte Carlo data as the size increases.

The data plotted in Fig. 3.4 take into account the ultrametric relation (3.78). When comparing $X_{\rm T}$ and X_1^2 small deviations from the prediction arise. However, data for $L = 32$ have strong fluctuations, and do not hint at any clear tendency with the system size. The bottom plot in Fig. 3.4 shows data for the quantity

$$K_3^u = \left[X_3 - (2X_1 + 8X_1^2 + 5X_1^3)/15\right]^2, \tag{3.84}$$

which we obtain by substituting (3.78) in (3.83). The same considerations we made above apply here: the agreement with ultrametric relations (3.77) and (3.78) improves with increasing L.

We can compare the results above with those of Ref. [103], in which a good agreement between theoretical prediction of the kind of Eqs. (3.76), (3.77), (3.78) and Monte Carlo data on $3D$ Edwards-Anderson spin glass with Gaussian couplings was reported, but without clear evidence on whether the very small discrepancies could be controlled or not in the limit of large volume. In this respect, we have been able to thermalize systems of linear sizes up to twice the largest lattice studied in Ref. [103] and these larger sizes show a trend towards satisfying Eqs. (3.76), (3.77), (3.78) that was not clear in Ref. [103]. We also note that finite-size effects are stronger at low temperatures, and obtaining evidence of the correct trend requires data from simulations of larger systems than at higher temperature. We can also compare data at $T \sim 0.75 T_{\rm c}$ and $T = 0.57 T_{\rm c}$ (we have data at exactly $T = 0.625$ for lattice sizes $L = 8$, $L = 16$ and $L = 24$ but unfortunately not for $L = 32$). We see that at $T \sim 0.75 T_{\rm c}$ the data for the squared differences K_3^u and $\left[X_{\rm T} - X_1^2\right]^2$ are almost size-independent (this is actually true for $\left[X_{\rm T} - X_1^2\right]^2$ when $L > 8$, see Fig. 3.5, top). At $T \sim 0.64 T_{\rm c}$ (see Fig. 3.4),

such effects cannot be clearly told by comparing only the smallest lattices considered, $L = 16$ and $L = 24$. At $T = 0.57T_c$, size-dependent effects are strong even for $L = 16, 24$ (see Fig. 3.5, bottom).

Having data from four independent replicas per sample, we have access to the joint probability of two independent overlaps. According to Eq. (3.66) the quantity

$$\frac{P(q_{12}, q_{34})}{P(q_{34})} - \frac{2}{3}P(q_{12}) = P(q_{12}|q_{34}) - \frac{2}{3}P(q_{12}) \ , \tag{3.85}$$

(where $P(\cdot|\cdot)$ denotes conditional probability) when plotted versus q_{12}, should be a delta function in q_{34}. This quantity is shown for $L = 32$, $T \sim 0.64T_c$ and two values of q_{34} in the top plot of Fig. 3.6 and reveals a clear peak around q_{34}. At high q_{12} values there is a small excess in the probability $P(q_{12})\,P(q_{34})$, so the difference in Eq. (3.85) becomes negative. As one sees in Fig. 3.6 this happens at values $q_{12} \gtrsim q_{\rm EA}$, i.e., in a region of atypically large overlaps that should vanish in the thermodynamical limit. The size dependence for the quantity in Eq. (3.85) is not easy to quantify from the data: as one can see in Fig. 3.6 (bottom) for a particular choice of q_{34}, the peak height tends to increase with L (at least for $T \sim 0.75T_c$), but in a very slow way, making extrapolations in the $L \to \infty$ limit practically impossible. Despite this, we note that the negative peaks get narrower as the system size increases: we expect then that this effect will disappear at larger system sizes.

We conclude this section commenting the asymptotic behavior of the cumulative probability $\Pi_q^C(z)$, Eq. (3.81). The small-z decay is clearly a power law (see top plot in Fig. 3.7), but the best fit exponent is significantly different from the estimate obtained by integrating the overlap distribution $P(q)$. Fig. 3.7 shows a comparison of the exponent $x(q)$ obtained by the two methods, for some lattice sizes, many cut-off values q and two temperatures, $T \sim 0.64T_c$ and $T \sim 0.57T_c$. Although the differences seem to decrease by increasing the lattice size, the trend is very slow and even not in a clear direction for some values of the cutoff q. Again, the only conclusion that can be drawn is that the finite-size effects are large, even for $L = 32$, and safe extrapolations in the $L \to \infty$ limit cannot be done.

A closer inspection of the data reported in Fig. 3.7 reveals that the difference between the two data sets is roughly a constant, and this difference becomes extremely important in the limit of small q, where one would expect both measurements of $x(q)$ to approach zero. Contrary to expectations, the $x(q)$ estimated from the data of Π_q^C seems to remain non-zero even in the $q \to 0$ limit. A possible explanation for this observation comes from the fact that the delta peaks in the $P_J(q)$ get broader for systems of finite size. Indeed, in the thermodynamic limit, one would expect $P_J(q)$ to be the sum of

delta functions centered on overlap values extracted from the average distribution $P_\infty(q)$: if this expectation is true, then the value for $X_J(q)$ is nothing but the probability of having a peak at an overlap value smaller than q and this is exactly $x(q)$. However, if the delta peaks acquire a non-zero width Δ due to finite-size effects, then for $q < \Delta$ the overlap probability distribution close to the origin $P_J(0)$ may be affected by broad peaks centered on overlaps larger than q, which should not count in the thermodynamical limit. If this explanation is correct, then the limit $q \to 0$ for the data shown in Fig. 3.7 (bottom) obtained from Π_q^C should give a rough estimate, in the large L limit, for the peak width Δ (see data in Table 3.3 and discussion below).

3.5 The order parameter distribution

We now compare the $P(q)$ obtained in numerical simulations of the three-dimensional Edwards-Anderson model (3.59) to the prediction obtained by smoothly introducing controlled finite-size effects on a mean-field-like distribution consisting in a delta function centered in $q = q_{\rm EA}$ and a continuous tail down to $q = 0$ (a similar analysis has been carried out for long-range spin-glass models, see Ref. [107]). On the positive q axis one has

$$\begin{aligned} P_\infty(q) &= \widetilde{P}(q)\Theta(q_{\rm EA} - q) \\ &+ [1 - x_\infty(q_{\rm EA})]\delta(q - q_{\rm EA}) \,, \qquad (3.86) \\ x_\infty(q_{\rm EA}) &= \int_0^{q_{\rm EA}} dq\, \widetilde{P}(q) \,. \qquad (3.87) \end{aligned}$$

It is convenient to introduce the effective field h trough

$$q = \tanh(h) \qquad (3.88)$$

and consider its distribution

$$\begin{aligned} \mathcal{P}_\infty(h) &= P_\infty\big(q(h)\big)\frac{dq(h)}{dh} \\ &= \frac{dq(h)}{dh}\widetilde{P}\big(q(h)\big)\Theta(h_{\rm EA} - h) + \\ &\quad [1 - x_\infty(q_{\rm EA})]\delta(h - h_{\rm EA}) \,, \qquad (3.89) \\ x_\infty(q_{\rm EA}) &= \int_0^{h_{\rm EA}} dh\widetilde{\mathcal{P}}(h) \,, \qquad (3.90) \end{aligned}$$

being clear that $q_{\rm EA} = \tanh(h_{\rm EA})$. This change of variable smooths the constraint on the fluctuations of q near the extremes of the distribution.

L	T/T_c	q_{EA}	$x_\infty(q_{EA})$	Δ
32	0.75	0.663(19)	0.91(13)	0.0923(80)
	0.64	0.7319(30)	0.828(28)	0.1015(30)
24	0.75	0.69674(72)	1.0000(3)	0.10618(84)
	0.64	0.7625(27)	0.876(24)	0.1182(24)
	0.57	0.7954(24)	0.842(25)	0.1216(32)
16	0.75	0.73780(73)	1.000031(7)	0.1443(10)
	0.64	0.809(16)	1.00(14)	0.150(11)
	0.57	0.8210(41)	0.811(49)	0.1683(51)
8	0.75	0.8250(21)	1.000001(9)	0.2872(37)
	0.57	0.886(18)	0.95(18)	0.296(28)
L	T/T_c	α	γ	χ^2/d.o.f.
32	0.75	1.92(34)	11.2(1.2)	20/97
	0.64	0.93(44)	7.7(1.0)	38/103
24	0.75	2.04(21)	9.68(55)	45/101
	0.64	0.95(21)	6.88(41)	69/107
	0.57	0.75(17)	5.62(30)	88/110
16	0.75	1.76(16)	5.14(31)	77/107
	0.64	0.45(21)	4.50(52)	133/113
	0.57	0.53(19)	3.37(40)	161/115
8	0.75	0.73(22)	2.02(34)	501/121
	0.57	0.49(16)	1.36(17)	466/123

Table 3.3: Results of the fitting procedure of Eq. (3.94) on numerical $P(q)$ data, with kernel exponent $k = 2.5$ (see Eq. (3.91)). All errors on parameters are jackknife estimates. We used the symbol χ^2 in the table to denote the sum of squares of residuals, which is not a true chi-square estimator as the values of $P(q)$ at different q are mutually correlated.

In a finite-size system the thermodynamical distribution $\mathcal{P}_\infty(h)$ will be modified, mainly by the fact that delta functions become distributions with non-zero widths. Remember that, in the thermodynamical limit, we expect the distribution $\mathcal{P}_J(h)$ for any given sample to be the sum of delta functions. A simple way to take into account the spreading of the delta functions due to finite-size effects is to introduce a symmetric convolution kernel

$$G_\Delta^{(k)}(h - h') \equiv C \exp\left[- \left(|h - h'| / \Delta \right)^k \right] , \tag{3.91}$$

where C is a normalizing constant and the spreading parameter Δ is assumed

not to depend on h, [5] while it should have a clear dependence on the system size, such that $\lim_{L\to\infty}\Delta = 0$. The parameter k, to be varied in the interval $[2,3]$, is introduced in order to consider convolutions different from the Gaussian case ($k = 2$).

In order to obtain an analytic expression for the finite size distribution

$$\mathcal{P}_L(h) \equiv \int dh' \frac{\mathcal{P}_\infty(h') + \mathcal{P}_\infty(-h')}{2} G_\Delta^{(k)}(h - h') \;, \tag{3.92}$$

we assume the following form for the continuous part of the distribution

$$\widetilde{\mathcal{P}}(h) \equiv \widetilde{P}\big(q(h)\big)\frac{dq(h)}{dh} = \widetilde{P}(0)(1 + \alpha h^2 + \gamma h^4) \;, \tag{3.93}$$

where $\widetilde{\mathcal{P}}(0) = \widetilde{P}(0) = P_\infty(0)$, α and γ are free parameters to be inferred from the data. The final result is

$$\begin{aligned} \mathcal{P}_L(h) &= [1 - x_\infty(q_{\rm EA})]\frac{G_\Delta^{(k)}(h - h_{\rm EA}) + G_\Delta^{(k)}(h + h_{\rm EA})}{2} \\ &+ \widetilde{P}(0)\int_{-h_{\rm EA}}^{h_{\rm EA}} dz \, \left[1 + \alpha z^2 + \gamma z^4\right] G_\Delta^{(k)}(h - z) \end{aligned} \tag{3.94}$$

where $x_\infty(q_{\rm EA}) = 2\widetilde{P}(0)[h_{\rm EA} + \alpha h_{\rm EA}^2/3 + \gamma h_{\rm EA}^5/5]$.

We let α, γ, $q_{\rm EA}$ and Δ vary in a fitting procedure to $P(q)$ Monte Carlo data; values of $\widetilde{P}(0)$ are fixed to the Monte Carlo values $P_{MC}(0)$. The choice of the exponent k in the convolution kernel is crucial. We varied k in the interval $[2,3]$. The Gaussian convolution $k = 2$ turned out to be the worst choice in such interval, giving rise to unphysical negative weights for the delta function contributions, i.e., $1 - x_\infty(q_{\rm EA}) < 0$. We obtained very good results with the choice $k = 2.5$. Fit parameters are reported in Table 3.3 for some lattice sizes and temperatures, while Fig. 3.8 shows comparison between Monte Carlo $P(q)$ and the relative fitting curve. Although the fitting curves interpolate nicely the numerical $P(q)$, some of the fitting parameters may look strange: in particular $q_{\rm EA}$ is a bit larger than the peak location and $x_\infty(q_{\rm EA}) \simeq 1$ (for example, in the $L = 32$ data the difference is around 2%). It is worth remembering that in the solution of the SK model at low temperatures the continuous part $\mathcal{P}(q)$ has a divergence for $q \to q_{\rm EA}^-$, which can easily dominate the delta function in finite-size systems (where delta peaks are broadened). Indeed, by increasing the system size, $q_{\rm EA}$ seems

[5] This introduces a q-dependent spread, as the Jacobian of the transformation (3.88) stretches the distribution at high q values.

to move towards the location of the peak maximum and $x_\infty(q_{\rm EA})$ becomes smaller than 1.

In order to make a stronger test of the above fitting procedure, we have used the fit parameters in Table 3.3 to derive the finite-size conditional probability

$$P_L(q|q') = P_L(q,q')/P_L(q') \tag{3.95}$$

applying the convolution kernel $G_\Delta^{(k)}(h-h')$ to the $L=\infty$ joint probability given by the Ghirlanda-Guerra relation, r.h.s of Eq.(3.66). Fig. 3.8 shows a comparison between our extrapolated $P_L(q_{12}|q_{34}=q_0)$ and the Monte Carlo data for $L=32$, $T=0.64T_{\rm c}$ and three values of q_0: the agreement is very good at any value of q_0, especially considering that the fitting parameters were previously fixed by interpolating the unconditional overlap distribution $P_L(q)$.

3.6 Conclusions

We performed a direct inspection of stochastic stability and ultrametricity properties on the sample-to-sample fluctuations of the overlap probability densities obtained by large-scale Monte Carlo simulations of the three-dimensional Edwards-Anderson model. We found small but still sizeable deviations from the prediction of the Ghirlanda-Guerra relations but a clear tendency towards improvement of agreement with increasing system size.

Large fluctuations make it difficult to draw any definitive conclusion on the analysis of the ultrametric relation (3.78) when taking into account data for the largest lattice size. In addition, critical effects show up at $T\sim 0.75T_{\rm c}$. Considering that for a stochastically stable system overlap equivalence is enough to infer ultrametricity, the results presented here support and integrate the analyses and claims of Refs [88], [89] and [100], in which the authors reported strong evidence of overlap equivalence.

We also turned our attention to the shape of the overlap probability distribution, showing that finite-size $P_L(q)$ and $P_L(q,q')$ compare well with mean-field (infinite-size) predictions, modified by finite-size effects that only make delta functions broad.

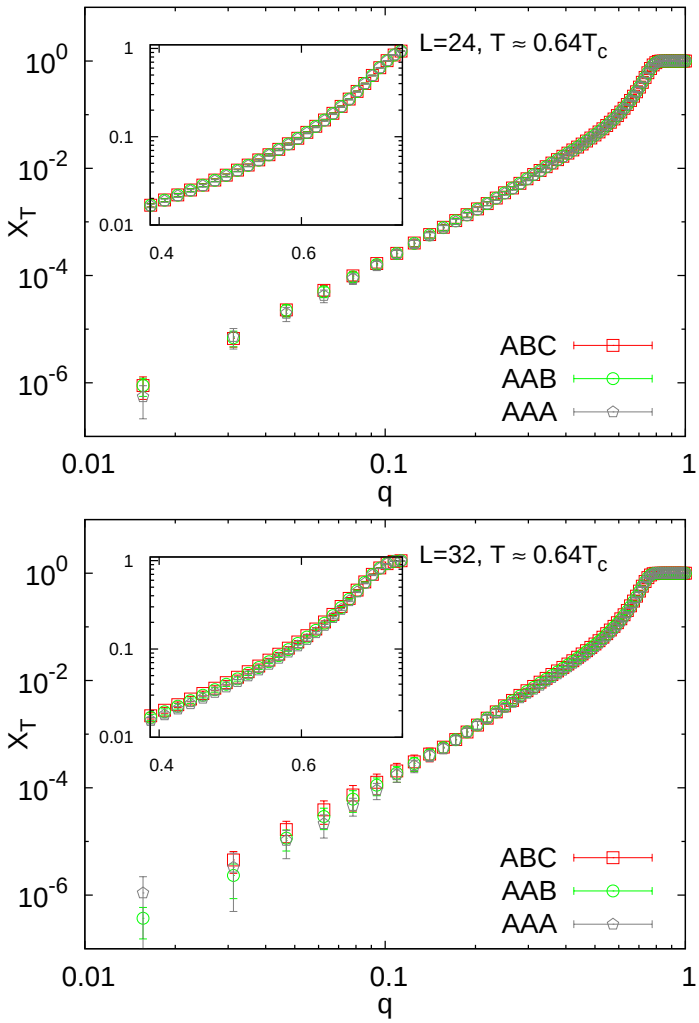

Figure 3.1: (Color online) The quantity $X_{\rm T}$ as defined in the text, as a function of q for lattice size $L = 24$ (top) and $L = 32$ (bottom) at temperature $T \simeq 0.64 T_{\rm c}$. Insets show a magnified view of the region $q \sim 0.6$ (log-log plot). Plots show data for $X_{\rm T}$ computed only with triplets of independent configurations (ABC), with triplets in which two configurations belong to the same Monte Carlo history (AAB), and triplets in which all configurations come from the same Monte Carlo history (AAA). No significant difference shows up as long as we take enough uncorrelated configurations from the same replica.

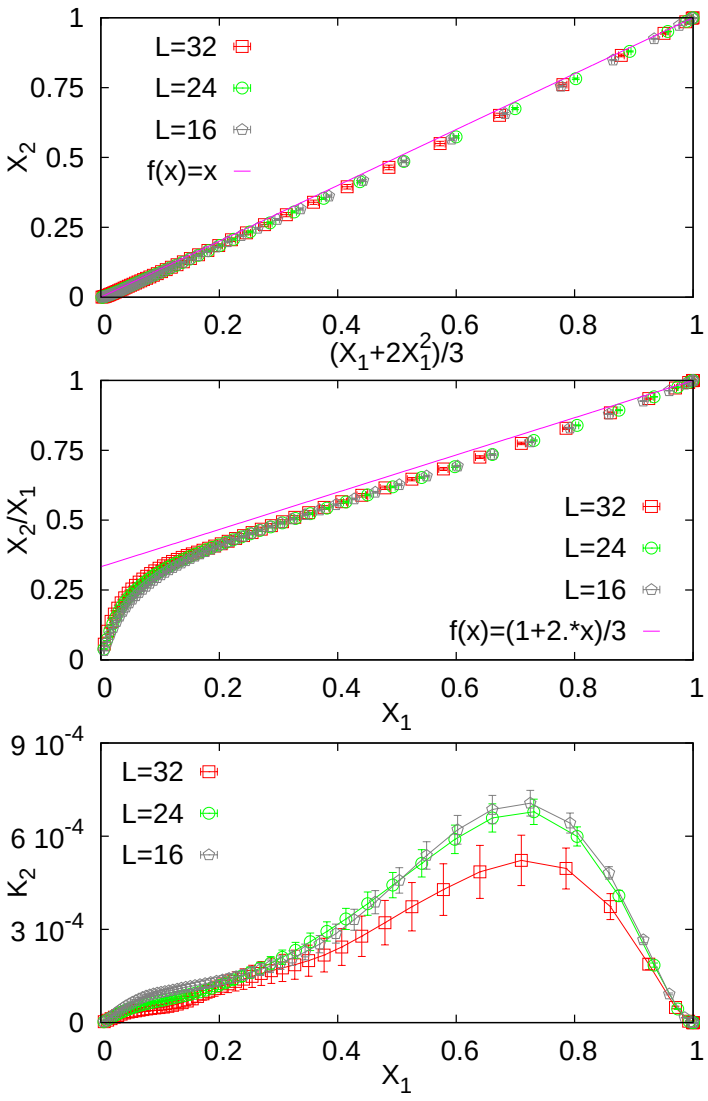

Figure 3.2: (Color online) Top: X_2 as a function of the corresponding polynomial in X_1 (Eq. (3.76)). The straight line is the theoretical prediction (unit slope). Center: the ratio X_2/X_1 as a function of X_1, where the straight line is the theoretical prediction. Bottom: the squared difference $K_2 = [X_2 - (X_1 + 2X_1^2)/3]^2$ as function of X_1. Data refer to $T \sim 0.64 T_c$

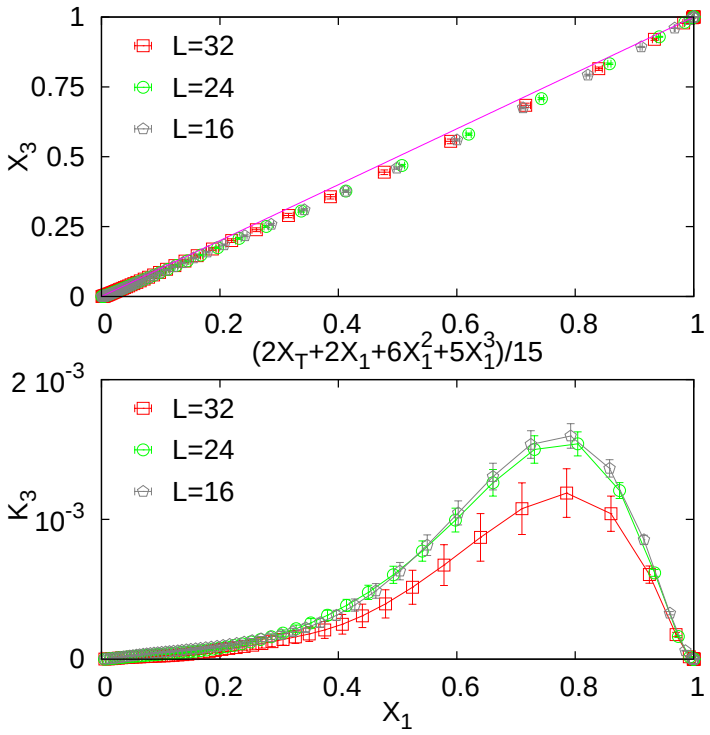

Figure 3.3: (Color online) Data at $T \sim 0.64T_c$. Top: X_3 as a function of the corresponding polynomial in X_1 and X_T (Eq. (3.77)). The straight line is the theoretical prediction (unit slope). Bottom: the squared difference $K_3 = [X_3 - (2X_T + 2X_1 + 6X_1^2 + 5X_1^3)/15]^2$ as function of X_1, $T = 0.64T_c$. Lines connecting points are only a guide to the eye.

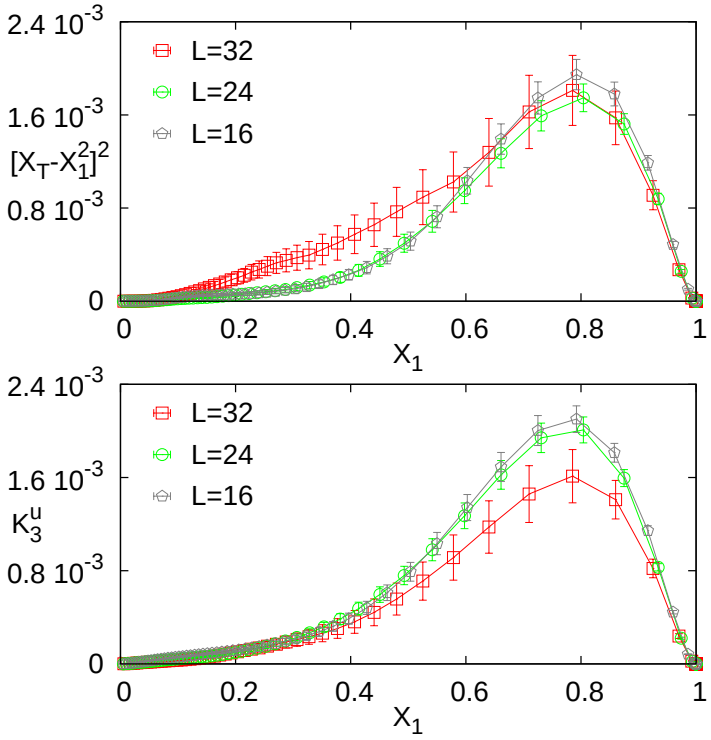

Figure 3.4: (Color online) Top: The squared difference $[X_{\rm T} - X_1^2]^2$ as a function of X_1. Bottom: the quantity $K_3^u = [X_3 - (2X_1 + 8X_1^2 + 5X_1^3)/15]^2$ as a function of X_1. All data for $T \sim 0.64 T_{\rm c}$ and for lattice sizes $L = 16, 24, 32$. The lines connecting the data points are only intended as a guide to the eye.

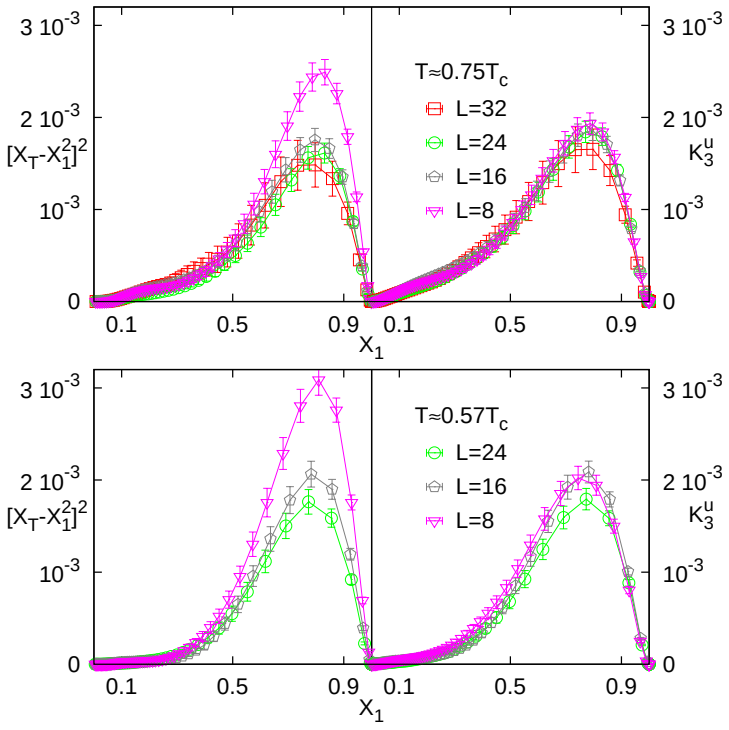

Figure 3.5: (Color online) Square difference $[X_{\rm T} - X_1^2]^2$ (left) and the quantity $K_3^u = [X_3 - (2X_1 + 8X_1^2 + 5X_1^3)/15]^2$ (right) as a function of X_1. Top: for $T = 0.75T_{\rm c}$ and $L = 8, 16, 24, 32$. Bottom: for $T = 0.57T_{\rm c}$ and $L = 8, 16, 24$.

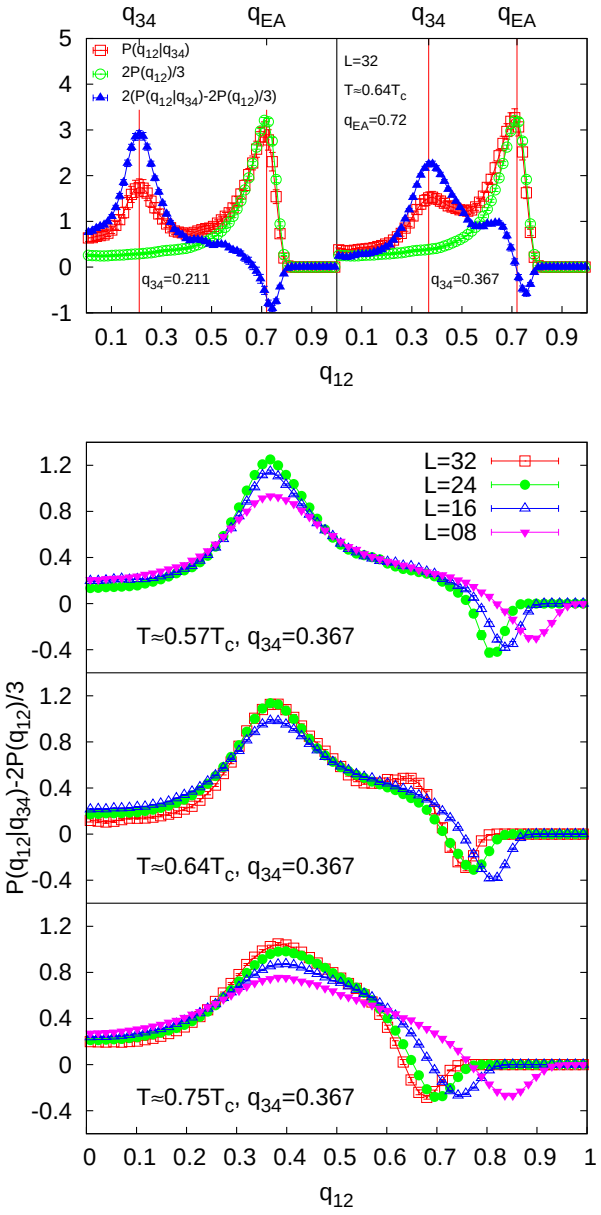

Figure 3.6: (Color online) Top: The conditioned probability $P(q_{12}|q_{34})$ (open squares) for $L = 32$ and $T \sim 0.64T_c$ and two values of $q_{34} = 0.211$ (left) and $q_{34} = 0.367$ (right). We also plot $2P(q_{12})/3$ (open circles) and the difference (full triangles) of the two above quantities (Eq. (3.85) in the text), scaled by a factor 2 for a better view. q_{34} and $q_{\rm EA}$ values are indicated by vertical lines for visual reference. We took the value $q_{EA}(L = 32, T = 0.64T_c) \sim 0.72$ as given in Ref. [89]. Bottom: The difference $P(q_{12}|q_{34}) - 2P(q_{12})/3$ with $q_{34} = 0.367$, for different lattice size compared at temperatures $T = 0.75T_{\rm c}$, $T = 0.64T_{\rm c}$, $T = 0.57T_{\rm c}$.

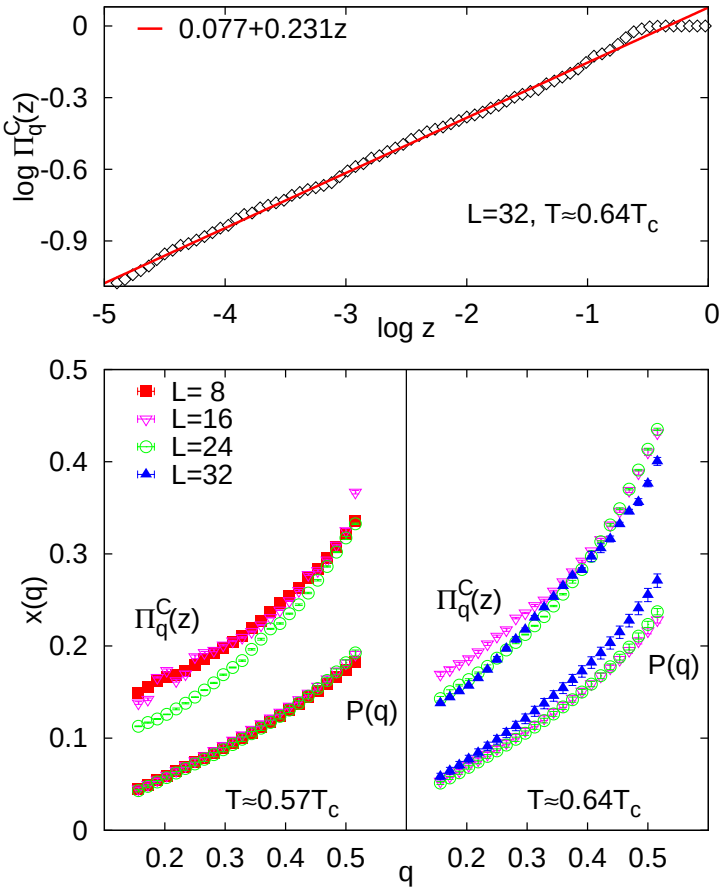

Figure 3.7: (Color online) Asymptotic behavior of the cumulative probability $\Pi_q^C(z)$ (Eq. (3.81)). Top: small-z decay for $L = 32$, $T = 0.64T_c$ and $q = 0.3125$. Bottom: comparison of the exponent $x(q)$ obtained by the two methods described in the text (uppermost data points represent values obtained by fitting $\Pi_q^C(z)$, lowermost data points come from integrating the $P(q)$), for some lattice sizes, many cut-off values q and temperatures $T \sim 0.57T_c$ (left) and $T \sim 0.64T_c$ (right).

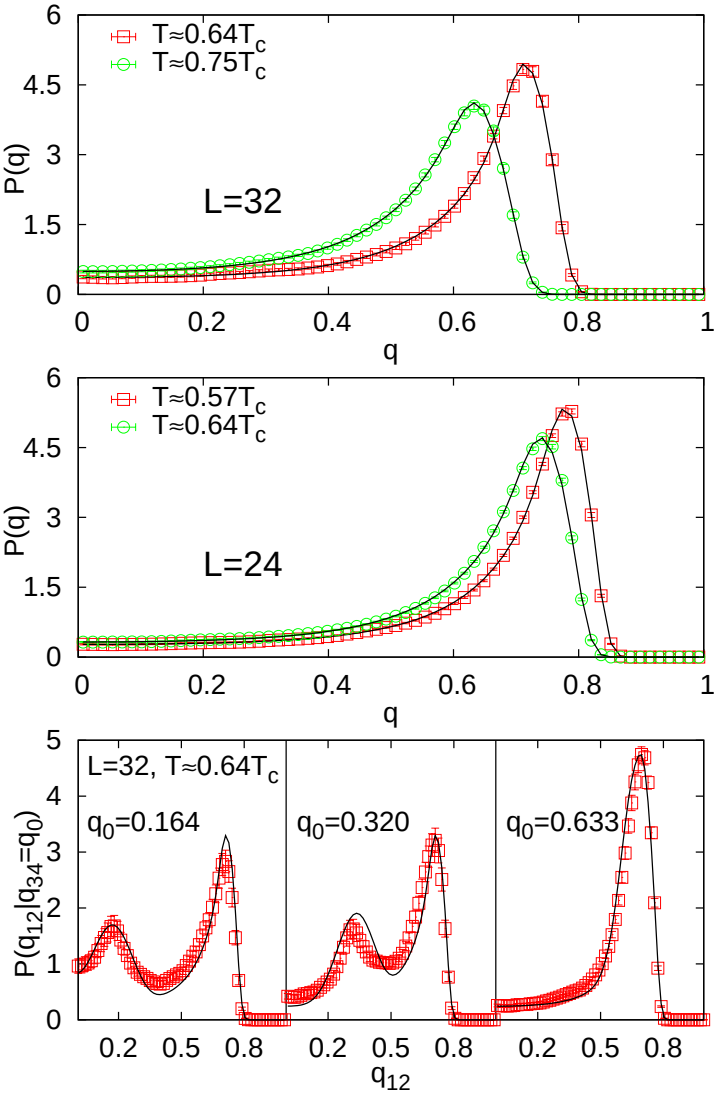

Figure 3.8: (Color online) Comparison between the Monte Carlo data of the $P(q)$ and the convolution computed as described in the text (solid lines). Top: $L = 32$, $T \sim 0.64T_c$ and $T \sim 0.75T_c$. Center: $L = 24$, $T \sim 0.57T_c$ and $T \sim 0.64T_c$. Bottom: the conditioned probability $P(q_{12}|q_{34} = q_0)$ for $L = 32$, $T \sim 0.64T_c$ and some values of q_0.

Chapter 4

Microscopic dynamics of the 3D Spin Glass in presence of a magnetic field

4.1 Preliminary study

In Section 1.3 we have explained two different scenarios which are approaches to real spin glasses with analytical solution. The first scenario, Replica Symmetry Breaking (RSB), is the mean field approach, which can be interpreted as a $D = \infty$ model. The second scenario, droplet, is exact at dimension $D = 1$. However, the behaviour that these two scenarios predict for a spin glass in presence of an external magnetic field, h, is completely different. RSB predicts that a phase transition to a spin glass phase happens even when $h > 0$, whereas Droplet predicts that the spin glass phase is destroyed in presence of a magnetic field (even for Heisenberg spin glasses).

Therefore, the existence of a phase transition in presence of an external magnetic field in a spin glass system of dimensionality $D = 3$ is still a controversial issue, both in experimental and theoretical physics. In RSB, the phase diagram in $T - h$ variables presents a line which indicates where the phase transition takes place. This line is the so-called the *de Almeida-Thouless* (AT) line (see figure 4.1). The *upper critical dimension is* $D_U = 6$ is the minimun dimensionality where it is shown that this scenario holds. Thus the behavior of the system between $D = 1$ (Droplet holds) and $D = 6$ (RSB holds) is not clear and clarifying this point has been the goal of many research works. The behavior of the overlap probability density function may help us to distinguish between these two scenarios. In Section 1.3, the probability distribution of q in both scenarios in absence of a magnetic field

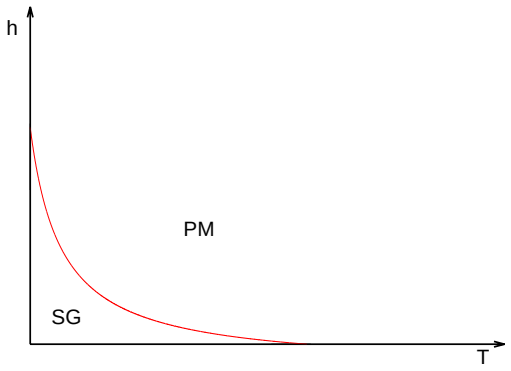

Figure 4.1: Phase diagram in $T - h$ variables in the RSB scenario. The de Almeida-Thouless line separates the paramagnetic and spin glass phases.

have been shown. If $h > 0$, the probability distribution changes, but the probability distribution of q in RSB scenario (see Figure 4.2) and in Droplet scenario (see Figure 4.3) are still completely different.

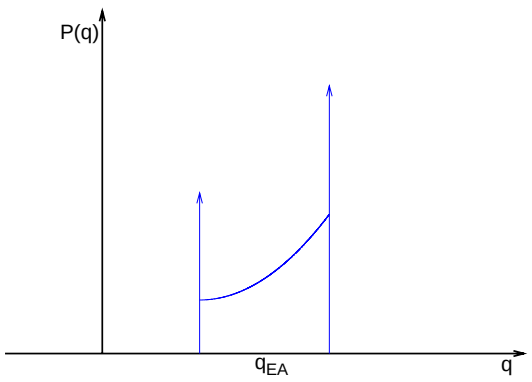

Figure 4.2: Probability distribution of q in presence of an external magnetic field in RSB scenario.

We will describe in the following sections the experimental situation and different analytical approaches to this problem.

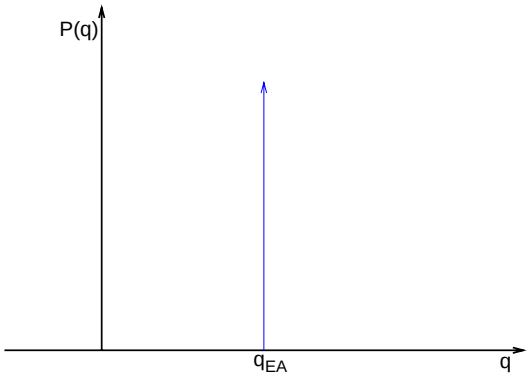

Figure 4.3: Probability distribution of q in presence of an external magnetic field in Droplet scenario.

4.1.1 Experimental results

Regarding experiments in spin glasses, we will focus on $Fe_{0.5}Mn_{0.5}TiO_3$ which is supposed to be a short range Ising spin glass[1]. This material was studied by Jönsson *et al* [108] in a large range of external magnetic fields, up to $h = 20000$ Oe and no phase transition was reported. They studied the decay of the overlap to control whether the phase transition happened. In figure 4.4, their results about this observable are shown.

From the classic Ogielski's paper [113], it is known that a decay like $q(t) \sim 1/t^x$ indicates the onset of a spin glass phase. For $h = 1000$ Oe in the Figure 4.4, one can observe that the behavior of $q(t)$ is almost a power law, and for $h = 300$ Oe this behavior is quite clear. Therefore this property suggests us that for a smaller external magnetic field, the spin glass phase transition might have been detected. Moreover, we will show the data of this experiment with those of a one dimensional long range model, KAC model [109, 110] with $\rho = 1.5$ [110] in Figure 4.5. This model roughly corresponds to the four dimensional short range model. In this figure, one can observe that the critical field in four dimensions is near $h = 1000$ Oe and critical field decrease with the dimensionality, which supports the previous deduction that experimentalist should try smaller magnetic fields ($h \leq 1000$ Oe) to detect a spin glass phase transition in real samples ($D = 3$).

Besides, an AT line was found in Heisenberg spin glasses [111] (remind that Droplet scenario states that this line should not exist even in Heisenberg

[1] $Fe_{0.5}Mn_{0.5}TiO_3$ is an Ising like spin glass whereas AgMn at 2.5% and $CdCr_{1.7}IN_{0.3}S_4$ are Heisenberg like spin glasses.

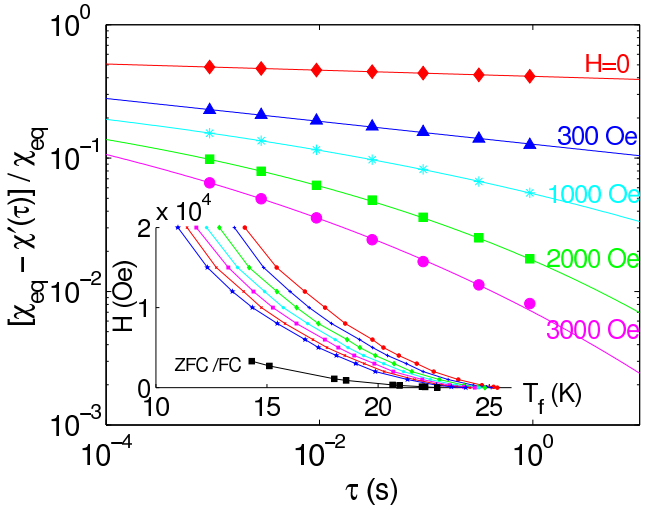

Figure 4.4: Behavior for the dynamical overlap, $q(\tau)$ (which is proportional to the quantity plotted in the y-axis), as a function of time for different magnetic fields. Figure from Ref. [108].

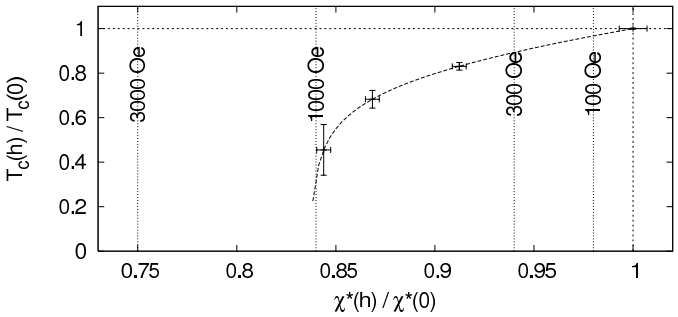

Figure 4.5: Relative decrease of $T_c(h)/T_c(0)$ with increase field for $\rho = 1.5$ and $h = 0$, 0.1, 0.15 and 0.2 versus the relative decrease of χ^* (ZFC susceptibility). Figure from Ref. [110]. Experimental data from $Fe_{0.5}Mn_{0.5}TiO_3$, see Ref. [108].

spin glasses). The same authors also studied Ising-like samples (FeNiPBAl) [112] and reached the same conclusion that we stated here, the magnetic fields used in experiments are too high to see a spin glass phase transition in Ising spin glasses.

To sum up, one can conclude that experimental data suggest us that the spin glass phase transition may take place for $h < 1000$ Oe for the Ising Universality class.

4.1.2 Analytical approaches

From the theoretical point of view, one can study the replicated Hamiltonian but only above the critical temperature, that is, in the paramagnetic phase. This Hamiltonian becomes [114], in terms of the original overlap field Q_{ab} (remind that $Q_{aa} = 0$),

$$\begin{aligned}\mathcal{H} &= \frac{1}{4}\sum(\nabla Q_{ab})^2 + \frac{1}{4}r\sum Q_{ab}^2 - \frac{1}{6}w\sum Q_{ab}Q_{bc}Q_{ca} \\ &- \frac{1}{8}u\sum Q_{ab}Q_{bc}Q_{cd}Q_{da} + \frac{1}{4}x\sum Q_{ab}^2Q_{ac}^2 - \frac{1}{8}y\sum Q_{ab}^4 \\ &- \frac{1}{2}h^2\sum Q_{ab} + O(Q^5, h^2Q^2)\,. \end{aligned} \tag{4.1}$$

where w, u, x, and y are positive couplings.

Let Q be the minima and q_{ab} the fluctuations around that minima, then one can write that $Q_{ab} = Q + q_{ab}$. In presence of a magnetic field, h, the minima must satisfy [114]

$$rQ + 2wQ^2 - 3uQ^3 + 2xQ^3 - yQ^3 = h^2 \tag{4.2}$$

Taking the limit $n \to 0$ and neglecting higher orders of q_{ab}, the Hamiltonian, Eq. (4.1), becomes in

$$\begin{aligned}\mathcal{H} &= \frac{1}{4}\sum(\nabla q_{ab})^2 + \frac{1}{4}\left(r + uQ^2 + 2xQ^2 - 3yQ^2\right)\sum q_{ab}^2 \\ &- \frac{1}{2}Q\left(w - uQ - 2xQ\right)\sum_{a\neq b} q_{ab}q_{ac} - \frac{1}{4}uQ^2\sum_{a\neq b\neq c\neq d} q_{ab}q_{cd} \\ &- \frac{1}{6}w\sum q_{ab}q_{bc}q_{ca} - \frac{1}{2}uQ^2\sum_{a\neq c} q_{ab}q_{bc}q_{cd} + xQ\sum q_{ab}q_{ac}^2 \\ &- \frac{1}{2}yQ\sum q_{ab}^3 + O(q^4) \end{aligned} \tag{4.3}$$

Therefore, the starting field theory is a ϕ^3 theory with an *upper critical dimension* $D_U = 6$. Hence, the external magnetic field does not change D_U. The critical exponents in six dimensions are $\nu = 1/2$, $\beta = 1$ and $\eta = 0$, so one has the same critical behavior as in the $h = 0$ case at $D \geq 6$.

Notice that we can recover the usual ϕ^3 field theory for an Ising spin glass in absence of a magnetic field by putting $Q = 0$:

$$\mathcal{H} = \frac{1}{4}\sum(\nabla q_{ab})^2 + \frac{1}{4}r\sum q_{ab}^2 - \frac{1}{6}w\sum q_{ab}q_{bc}q_{ca}\,. \tag{4.4}$$

In the case $h = 0$ (that is, $Q = 0$) only one propagator exists. However, in presence of an external magnetic field one has three different types of propagators: longitudinal (L), anomalous (A), and replicon (R). Diagonalizing the quadratic term in Eq. (4.3) for finite n, one obtains [115]

$$G_L = G_1 + 2(n-2)G_2 + \frac{1}{2}(n-2)(n-2)G_3 = \frac{1}{p^2 + r - 2wQ(n-2)}\,, \quad (4.5)$$

$$G_A = G_1 + (n-4)G_2 - (n-3)3G_3 = \frac{1}{p^2 + r - wQ(n-4)}\,, \quad (4.6)$$

$$G_R = G_1 - 2G_2 + G_3 = \frac{1}{p^2 + r + 2wQ}\,, \quad (4.7)$$

being n the number of replicas and p the momentum. In terms of the original spin variables, G_1, G_2 and G_3 can be written

$$G_1(x) = \overline{\langle s_i s_{i+x}\rangle^2}\,, \quad (4.8)$$

$$G_2(x) = \overline{\langle s_i s_{i+x}\rangle \langle s_i\rangle}\,, \quad (4.9)$$

$$G_3(x) = \overline{\langle s_i\rangle^2 \langle s_{i+x}\rangle^2}\,. \quad (4.10)$$

Notice that if one sets $n = 0$, Eqs. (4.5) and (4.6) are identical:

$$G_A(p) = G_L(p) = \frac{1}{p^2 + r + 4wQ}\,. \quad (4.11)$$

Therefore, one actually has the replicon mode and two degenerated modes (anomalous and longitudinal).

Of course, if one sets $Q = 0$, then the standard propagator is recovered:

$$G_A(p) = G_L(p) = G_R(p) = \frac{1}{p^2 + r}\,. \quad (4.12)$$

In the standard mean field picture, the de Almeida-Thouless line is defined by imposing that only the replicon mode is massless, that is $G_R^{-1}(p = 0) = 0$, but the other two degenerated modes are massive. In other words, $G_L^{-1}(p = 0) = G_A^{-1}(p = 0) > 0$. Bray and Roberts [114] projected the original theory, Eq. (4.3), into the replicon subspace, using the behavior of the propagators in Mean Field and the degeneration of L and A modes. This is equivalent to setting the longitudinal and anomalous masses to infinity (one can write

$m_L^2 \propto G_L^{-1}(p=0)$ and analogously for the other two modes). The final projected Hamiltonian is:

$$\mathcal{H} = \frac{1}{4}\sum(\nabla R_{ab})^2 + \frac{1}{4}\tilde{r}\sum R_{ab}^2 - \frac{1}{6}w_1\sum R_{ab}R_{bc}R_{ca} - \frac{1}{6}w_2\sum R_{ab}^3 \quad (4.13)$$

They studied this projected Hamiltonian using a perturbative renormalization group and, at the order of the perturbation theory they used, no fixed points were found. Therefore a new strategy has been developed:

- One needs to avoid the degeneration between the anomalous and longitudinal propagators (or masses). So we will work with non zero n and at the very end of the computation, n will be set to 0.
- Due to the fact that the degeneration between the modes L and A has been broken, one can try to explore more exotic scenarios for the Almeida-Thouless line, like $m_R = m_A = 0$ and $m_L > 0$.
- The starting Hamiltonian should be the most general cubic Hamiltonian compatible with symmetry, extending the interacting cubic Hamiltonian from four couplings (as in Bray and Roberts [114]).

This strategy has been devised and followed by De Dominicis and Temesvari in reference [116]. Their Hamiltonian ($\mathcal{H} = \mathcal{H}^{(2)} + \mathcal{H}^{(3)}$) reads

$$\mathcal{H}^{(2)} = \frac{1}{2}\sum_{\mathbf{p}}\left[\left(\frac{1}{2}p^2 + m_1\right)\sum_{\alpha\beta}\phi_{\mathbf{p}}^{\alpha\beta}\phi_{-\mathbf{p}}^{\alpha\beta} + m_2\sum_{\alpha\beta\gamma}\phi_{\mathbf{p}}^{\alpha\gamma}\phi_{-\mathbf{p}}^{\beta\gamma} + m_3\sum_{\alpha\beta\gamma\delta}\phi_{\mathbf{p}}^{\alpha\beta}\phi_{-\mathbf{p}}^{\gamma\delta}\right] \quad (4.14)$$

$$\begin{aligned}\mathcal{H}^{(3)} &= -\frac{1}{6\sqrt{N}}\sum_{\mathbf{p_1}\mathbf{p_2}\mathbf{p_3}}{}'\left[w_1\sum_{\alpha\beta\gamma}\phi_{\mathbf{p}_1}^{\alpha\beta}\phi_{\mathbf{p}_2}^{\beta\gamma}\phi_{\mathbf{p}_3}^{\gamma\alpha} + w_2\sum_{\alpha\beta}\phi_{\mathbf{p}_1}^{\alpha\beta}\phi_{\mathbf{p}_2}^{\alpha\beta}\phi_{\mathbf{p}_3}^{\alpha\beta}\right. \quad (4.15)\\ &+ w_3\sum_{\alpha\beta\gamma}\phi_{\mathbf{p}_1}^{\alpha\beta}\phi_{\mathbf{p}_2}^{\alpha\beta}\phi_{\mathbf{p}_3}^{\alpha\gamma} + w_4\sum_{\alpha\beta\gamma\delta}\phi_{\mathbf{p}_1}^{\alpha\beta}\phi_{\mathbf{p}_2}^{\alpha\beta}\phi_{\mathbf{p}_3}^{\gamma\delta} + w_5\sum_{\alpha\beta\gamma\delta}\phi_{\mathbf{p}_1}^{\alpha\beta}\phi_{\mathbf{p}_2}^{\alpha\gamma}\phi_{\mathbf{p}_3}^{\beta\delta}\\ &+ \left. w_6\sum_{\alpha\beta\gamma\delta}\phi_{\mathbf{p}_1}^{\alpha\beta}\phi_{\mathbf{p}_2}^{\alpha\gamma}\phi_{\mathbf{p}_3}^{\alpha\delta} + w_7\sum_{\alpha\beta\gamma\delta\mu}\phi_{\mathbf{p}_1}^{\alpha\gamma}\phi_{\mathbf{p}_2}^{\beta\gamma}\phi_{\mathbf{p}_3}^{\delta\mu} + w_8\sum_{\alpha\beta\gamma\delta\mu\nu}\phi_{\mathbf{p}_1}^{\alpha\beta}\phi_{\mathbf{p}_2}^{\gamma\delta}\phi_{\mathbf{p}_3}^{\mu\nu}\right]\end{aligned}$$

where $\sum_{\mathbf{p_1}\mathbf{p_2}\mathbf{p_3}}{}'$ means that the sum is restricted to $\mathbf{p_1} + \mathbf{p_2} + \mathbf{p_3} = 0$.

They found a non trivial fixed point below six dimensions. As a test, they recover the previous results of Bray and Roberts. They computed the critical exponent, ν, related with the A and R sectors. However they were unable to

relate these two ν exponents to the physical critical exponents, like γ of the spin-glass susceptibility and the standard ν of the correlation length. They stated that this identification is difficult since the system presents two mass scales.

Some years later [117], Temesvári, computed the value of the eight different cubic couplings as a function of the original ones which appear in the Edwards-Anderson Hamiltonian, completing the work started in Ref. [116]. A more recent paper by Bray and Moore [118] states that the de Almeida-Thouless line should disappeared just at six dimensions:

$$h_{AT}^2 \propto (6 - D) \text{ as } D \to 6\,. \tag{4.16}$$

They further argue that the break point, x_1, of $P(q)$ in the Parisi's solution should be zero below $D < 6$. Their final conclusion is that no Almeida-Thouless line can be found below or at six dimensions.

Finally, in a recent paper of the *Janus collaboration* [119], simulations on four dimensional Ising spin glass in presence of an external magnetic field have been developed, showing the presence of a phase transition (please, see Section 7.5 for more details).

Dynamics of the $D = 3$ spin glass in an external magnetic field

M. Baity-Jesi, R. Alvarez Baños, A. Cruz, L. A. Fernandez, J. M. Gil-Narvion, A. Gordillo-Guerrero, D. Iñiguez, A. Maiorano, F. Mantovani, E. Marinari, V. Martin-Mayor, J. Monforte-Garcia, A. Muñoz Sudupe, D. Navarro, G. Parisi, S. Perez-Gaviro, M. Pivanti, J. J. Ruiz-Lorenzo, S. F. Schifano, B. Seoane, A. Tarancon, R. Tripiccione and D. Yllanes.

To be published

4.2 Introduction

The glass transition is a ubiquitous but still mysterious phenomenon in condensed matter physics [120, 121, 122]. Indeed, many materials such as spin glasses, fragile molecular glasses, polymers or colloids display a dramatic increase of relaxation times when cooled down to their glass temperature, $T_{\rm g}$. However, the dynamic slowing down is not accompanied by dramatic changes on structural or thermodynamic properties. In spite of this, quite general arguments suggest that the sluggish dynamic must be correlated with an increasing length scale [123]. However, this putative length scale can be fairly difficult to identify. In fact, it was suggested long ago that the slowdown is caused by the collective movements of an increasing number of elements in the system, with a free energy barrier growing with the size of the cooperative regions [124]. These cooperative regions become larger as the temperature gets closer to $T_{\rm g}$. The rather recent experimental evidence for cooperative dynamics comes from dynamical heterogeneities [125] or non-linear susceptibilities [126]. The work of Ref. [127] suggests that characteristic length-scales will soon be investigated as well in non-equilibrium, aging materials.

It is clear that simple model systems can be a blessing for the study of such a difficult problem. To some extent, spin glasses (which are disordered magnetic alloys [128]) can be such a model system. Upon cooling, they undergo a dynamic slowdown without developing any recognizable magnetic ordering pattern. Their study offers experimental advantages. Time-dependent magnetic fields are a very flexible tool to probe their dynamic response, which can be very accurately measured with a SQUID (for instance, see Ref. [198]). On the theoretical side, they are simple to model, which greatly eases numerical simulation. In fact, special-purpose computers have been built for the simulation of spin glasses [130, 131, 202, 133]. It is then not surprising that the study of spin glasses is ahead in some respects:

- We know that the dynamic slowdown is due to a thermodynamic phase

transition at $T_c = T_g$ [134, 135, 136]. The issue is subtler for supercooled liquids, as we discuss below.

- Experiments can measure the size of the *glassy* magnetic domains, $\xi(t_w)$ [137, 138]. These domains are rather large, of the order of 100 lattice spacings [137], compared with any length scale identified for structural glasses [126].

- The Janus dedicated computer [139] allows us to simulate non-equilibrium dynamics from picoseconds to a tenth of a second [133, 199], and to compute equilibrium correlation functions for large lattices and low temperatures [200]. As a result we are able to relate non-equilibrium correlation functions (at finite *times*) with their equilibrium counterpart in systems of finite *sizes* [201] (see also Ref. [143]).

However, not all is well. We know that spin glasses differ from structural glasses in, at least, two significant respects. First, like all magnetic systems, spin glasses enjoy time-reversal symmetry in the absence of an applied magnetic field. And second, free-energy barriers grow logarithmically with $\xi(t_w)$ in spin glasses [199], rather than with a power law as in fragile glasses.

The correspondence between spin glasses and structural glasses is more accurate, specially in the mean-field approximation, if one considers instead a rather artificial spin-glass model, the p-spin glass model, with p-body interactions [144, 145]. For odd p, the time-reversal symmetry is broken. The odd-p models, at least in the mean-field approximation, display a dynamic phase transition *in their paramagnetic phase*. Reaching thermal equilibrium becomes impossible in the temperature range $T_c < T < T_g$. The dynamic transition at T_g is identical to the ideal Mode Coupling transition of supercooled liquids [146]. The thermodynamic phase transition at T_c is analogous to the ideal Kauzmann's thermodynamic glass-transition [122]. The thermodynamic transition is very peculiar: although it is of the second order (in the Eherenfest sense), the spin-glass order parameter jumps discontinuously at T_c from zero to a non-vanishing value.

However, the analogy between structural glasses and p-spin glasses was established only in the mean-field approximation. Mean-field is to be trusted only for spatial dimensions larger than the so-called upper critical dimension d_u. There is no doubt that $d_u > 3$, hence it is legitimate to wonder how much of the analogy carries out to our three-dimensional world. On the one hand, for supercooled liquids, the ideal Mode Coupling transition is actually a crossover. The power-law divergences predicted by Mode Coupling theory hold when the equilibration time lies in the range 10^{-13} s $< \tau < 10^{-5}$ s. Fitting to those power-laws, one obtains a Mode Coupling temperature T_{MC}.

However, τ is finite at $T_{\rm MC}$ (typically $T_{\rm MC}$ is a 10% larger than the glass temperature T_g where $\tau \sim 10^4$ seconds). A theory for a thermodynamic glass transition at $T_{\rm c} < T_g$ has been put forward [147, 148, 149, 150], but it has still not been validated (however, see Ref. [151]). On the other hand, little is known on the behaviour of the p-spin glass model for dimensions below $d_{\rm u}$.

A different route to a simple enough model system is quite obvious: break time-reversal symmetry by placing a standard (as opposed to p-spin) spin glass in an external magnetic field. According to mean field [152, 153], though, breaking time reversal is not enough. The mean-field prediction is that, for standard spin glasses on a field, $T_{\rm c} = T_{\rm g}$. Furthermore, the spin-glass order parameter would behave continuously when T crosses $T_{\rm c}$. However, these objections have been challenged for three-dimensional systems (recall that $d_{\rm u} = 6$ [154]). An effective field-theory computation predicts that the spin glass in a magnetic field *is* the physical realization of a p-spin glass model for spatial dimensions below $d_{\rm u}$ [155]. Furthermore, an effective spin glass Hamiltonian in a field has been recently derived for a binary liquid mixture [156].

In fact, whether spin glasses in a magnetic field undergo a phase transition has been a long-debated and still open question (see, e.g., Refs. [157, 158]). Yet, recent numerical simulations in three dimensions [159, 160] did not find the thermodynamic transition predicted by Mean-Field. Experimental studies have been conducted as well, with conflicting conclusions [161, 162, 163, 164]. Only in four dimensions (note that $4 < d_{\rm u} = 6$) clear signatures of the transition have been found up to now. This exploit required the introduction of special finite-size analysis techniques as well as the power of the Janus special-purpose computer [165].

Our scope here is to explore the dynamical behaviour of three-dimensional spin glasses in a field using the Janus computer. We shall study lattices of size $L = 80$, where we expect finite-size effects to be negligible [133]. Our time scales will range from 1 picosecond (i.e., one Monte Carlo full lattice sweep [128]) to 0.1 seconds. Hence, if the analogy with structural glasses put forward by Moore and Drossel [155] holds, we should be able of identifying the Mode Coupling crossover. A bonus of studying spin glasses rather than structural glasses is a rather deep theoretical knowledge of the relevant correlation functions [166]. Hence, we shall be able to correlate the equilibration time τ with the correlation length ξ.

4.3 Model and observables

4.3.1 Model

We studied a three dimensional cubic lattice system with volume $V = L^3$ (L being the linear size) and periodic boundary conditions. On every node of the lattice there is an Ising spin, $\sigma_{\boldsymbol{x}} = \pm 1$ and nearest neighbors are joined bye quenched bimodal couplings, $J_{\boldsymbol{xy}} = \pm 1$. We also include a local magnetic field, $h_{\boldsymbol{x}}$, on every node. The magnetic field is Gaussian distributed with zero mean and variance H. Instead of continuous values, we used discrete values for the field by using the Hermite integrals of its probability distribution [167] (see the Appendix for more details on the implementation). We made this transformation to use more efficiently the supercomputer Janus [139, 202, 203]. We checked the compatibility of our approach by comparing with real Gaussian fields simulated on PCs (see also the Appendix). The Hamiltonian of the model is

$$\mathcal{H} = -\sum_{\langle \boldsymbol{x},\boldsymbol{y}\rangle} J_{\boldsymbol{xy}}\sigma_{\boldsymbol{x}}\sigma_{\boldsymbol{y}} - \sum_{\boldsymbol{x}} h_{\boldsymbol{x}}\sigma_{\boldsymbol{x}}, \tag{4.17}$$

where $\langle \boldsymbol{x}, \boldsymbol{y}\rangle$ means sum over nearest neighbors. A given realization of couplings, $J_{\boldsymbol{xy}}$, and external field, $h_{\boldsymbol{x}}$, defines a *sample*. We have simulated four replicas in parallel with the same couplings and protocols (annealing and direct quench).

4.3.2 Observables

First, a couple of useful definitions of local quantities. On every node x of the lattice we have the local overlap:

$$q_{\boldsymbol{x}}(t) = \sigma^{(1)}_{\boldsymbol{x}}(t)\sigma^{(2)}_{\boldsymbol{x}}(t)\,, \tag{4.18}$$

where the superscripts are the replica indices. The total overlap is written as

$$q(t_w) = \frac{1}{V}\overline{\sum_{\boldsymbol{x}} q_{\boldsymbol{x}}(t_w)}\,, \tag{4.19}$$

where $\overline{(\cdots)}$ means sample average (over the J's and h's). Notice that

$$\lim_{t_w\to\infty} q(t_w) = q_{\min}\,, \tag{4.20}$$

where $q_{\min}$ is the minimum overlap allowed by the system.

In addition, we have focused in this work on the magnetic energy defined as

$$E_{\mathrm{mag}}(t_w) = \frac{1}{V}\overline{\sum_{\boldsymbol{x}} h_{\boldsymbol{x}}\sigma_{\boldsymbol{x}}(t_w)}\,. \tag{4.21}$$

and

$$W(t_w) = 1 - TE_{\rm mag}(t_w)/H^2\,. \tag{4.22}$$

By integrating by parts the Gaussian magnetic field, which is inside of $E_{\rm mag}$, one can obtain that at equilibrium

$$W = \overline{\langle q\rangle}\,. \tag{4.23}$$

From Eqs. (4.20) and (4.23) one can conclude:

$$\lim_{t_w\to\infty}\left(W(t_w) - q(t_w)\right) = \overline{\langle q\rangle} - q_{\rm min}\,. \tag{4.24}$$

In the droplet model, the rhs of the previous equation is just zero, while it is non-zero in a spin glass phase.

Finally, we have also computed the complete spin-spin correlation function:

$$C(\boldsymbol{r}, t_w) = \sum_{\boldsymbol{x}} \overline{\left(\langle\sigma_{\boldsymbol{x}}\sigma_{\boldsymbol{x}+\boldsymbol{r}}\rangle - \langle\sigma_{\boldsymbol{x}}\rangle\langle\sigma_{\boldsymbol{x}+\boldsymbol{r}}\rangle\right)^2}\,. \tag{4.25}$$

We need four replicas to define the latter quantity properly. Finally we can extract the correlation length using the integral estimators [199]

$$\xi_{k,k+1}(t_w) \equiv \frac{I_{k+1}(t_w)}{I_k(t_w)} \propto \xi(t_w)\,. \tag{4.26}$$

where

$$I_k(t_w) \equiv \int_0^{L/2} {\rm d}r\; r^k C(r, t_w)\,, \tag{4.27}$$

where r means $\boldsymbol{r} = (r, 0, 0)$ and permutations.

4.3.3 Strategy and Outlook of our main results

Our strategy will rely on the study of the difference between $W(t_w)$ and $q(t_w)$ as a function of time and will also be based on the classic paper by Ogielski [131] in its analysis. Our approach has been twofold:

- We have extrapolated this difference to large waiting times, eventually to infinite time. As cited in the previous subsection, a non-zero value of this difference, for $t_w \to \infty$ (equilibrium), will mark the onset of a low-temperature region clearly different of the high temperature one (a paramagnetic phase). We have been able to do that for very low temperatures. We have found that the following law (see [131]) works

very well in this regime (even in the presence of an external magnetic field H):

$$W(t) - q(t) = a(T, H) + \frac{b}{t^x} \,. \tag{4.28}$$

Eventually b and x could also depend on the temperature [131] and on the external magnetic field. We recall that $a(T_1(H)^-, H) = 0$ marks the onset of a spin glass phase with a critical temperature given by $T_1(H)$.

- In the high temperature region, the difference $W(t)-q(t)$ should vanish for large t. In this temperature region we have found (as happens for $q(t)$ in the three dimensional Ising spin glass in no magnetic field [131]), that:

$$W(t) - q(t) = \frac{a}{t^x} \exp\left[- \left(\frac{t}{\tau} \right)^{\beta} \right] \,, \tag{4.29}$$

which allows us to compute the relaxation time, τ, in the high temperature region. In this approach, we have studied, as was done numerically by Ogielski and in experimental studies (e.g. [169]), the dependence of τ with the temperature. To model this behavior we will use the following (and standard) functional (critical) dependence:

$$\tau = \tau_0 (T - T_2(H))^{-\nu z} \,, \tag{4.30}$$

where τ_0 is a microscopical time, $T_2(H)$ marks a "divergence" of τ (assuming an underlying thermodynamical phase transition at $T_2(H) = T_c(H)$), ν is the correlation length critical exponent and z is the dynamical critical exponent. We have found that our numerical data for τ are very well described by this law.

At this point of the paper we will discuss both temperatures ($T_1(H)$ and $T_2(H)$) and the possible explanations of our findings using different frameworks (a non-thermodynamical phase transition and a RSB phase transition).

4.4 Simulation details

We have performed two independent sets of simulations, one at a fixed temperature and another with an annealing algorithm. In both cases we have simulated four replicas for each sample with external fields $H = 0.1$, 0.2 and 0.3. The linear size of the system is $L = 80$.

In the simulations at a *fixed temperature* we took 462 samples for each external field. The length of our simulations is 10^{10} Monte Carlo steps (MCS)

and the fixed temperature is $T = 0.7$. We measured at times with the form $t = [2^{i/4}]$, where $[\cdots]$ means the integer part.

L	T	H	MCS	N
80	0.7	0.1	10^{10}	462
80	0.7	0.2	10^{10}	462
80	0.7	0.3	10^{10}	462

Table 4.1: Details of the simulations at fixed temperature. MCS means total Monte Carlo steps and N means the number of samples simulated.

The other set of simulations was performed with an *annealing algorithm*. We started the simulation from a high temperature. After a certain number of MCS (lets name it *base*), we change the temperature to a new one 0.1 cooler, i.e. $T_{\text{new}} = T_{\text{old}} - 0.1$, and we duplicated the number of MCS, i.e. $base_{\text{new}} = 2 \times base_{\text{old}}$. We repeated the procedure until we reached the lowest simulated temperature. Therefore, at a temperature T, we perform $base \cdot 2^{\left(\frac{T_{\text{init}}-T}{0.1}\right)}$ MCS, where T_{init} is the initial temperature of the run. We performed in every case the annealing from $T = 2.0$ till $T = 0.4$ taking several bases, 10^5, 10^4, 10^3, 10^2, 10^1 or 10^0. We took 1000 samples for each external field and base, performing a total of $1.3 \times 10^5 \times base$ MCS in each sample and replica.

4.5 Results

In this section we will compute the asymptotic values of $W(t)$ and $q(t)$. We recall that $W(t)$ should extrapolate to the mean value of the overlap $\overline{q}$ and $q(t)$, starting from a disordered configuration, to the minimum value of the overlap q_{min}. If these two extrapolated values are different, we would find evidence for RSB. If, however, they are equal the droplet model should hold.

4.5.1 Low Temperature Region

We have used two different numerical protocols to study the low temperature region:

- Sudden-quenched runs from infinite temperature to a fixed (low) temperature.
- Annealing runs, just described in the Simulation Details Section.

L	$[T_{\text{init}}, T_{\text{end}}]$	H	$base$	MCS	N
80	$[2.0, 0.4]$	0.02	10^4	$1.3 \cdot 10^9$	1000
80	$[2.0, 0.4]$	0.02	10^3	$1.3 \cdot 10^8$	1000
80	$[2.0, 0.4]$	0.02	10^2	$1.3 \cdot 10^7$	1000
80	$[2.0, 0.4]$	0.02	10^1	$1.3 \cdot 10^6$	1000
80	$[2.0, 0.4]$	0.02	10^0	$1.3 \cdot 10^5$	1000
80	$[2.0, 0.4]$	0.05	10^4	$1.3 \cdot 10^9$	1000
80	$[2.0, 0.4]$	0.05	10^3	$1.3 \cdot 10^8$	1000
80	$[2.0, 0.4]$	0.05	10^2	$1.3 \cdot 10^7$	1000
80	$[2.0, 0.4]$	0.05	10^1	$1.3 \cdot 10^6$	1000
80	$[2.0, 0.4]$	0.05	10^0	$1.3 \cdot 10^5$	1000
80	$[2.0, 0.4]$	0.1	10^5	$1.3 \cdot 10^{10}$	1000
80	$[2.0, 0.4]$	0.1	10^4	$1.3 \cdot 10^9$	1000
80	$[2.0, 0.4]$	0.1	10^3	$1.3 \cdot 10^8$	1000
80	$[2.0, 0.4]$	0.1	10^2	$1.3 \cdot 10^7$	1000
80	$[2.0, 0.4]$	0.1	10^1	$1.3 \cdot 10^6$	1000
80	$[2.0, 0.4]$	0.1	10^0	$1.3 \cdot 10^5$	1000
80	$[2.0, 0.4]$	0.2	10^5	$1.3 \cdot 10^{10}$	1000
80	$[2.0, 0.4]$	0.2	10^4	$1.3 \cdot 10^9$	1000
80	$[2.0, 0.4]$	0.2	10^3	$1.3 \cdot 10^8$	1000
80	$[2.0, 0.4]$	0.2	10^2	$1.3 \cdot 10^7$	1000
80	$[2.0, 0.4]$	0.2	10^1	$1.3 \cdot 10^6$	1000
80	$[2.0, 0.4]$	0.2	10^0	$1.3 \cdot 10^5$	1000
80	$[2.0, 0.4]$	0.3	10^5	$1.3 \cdot 10^{10}$	1000
80	$[2.0, 0.4]$	0.3	10^4	$1.3 \cdot 10^9$	1000
80	$[2.0, 0.4]$	0.3	10^3	$1.3 \cdot 10^8$	1000
80	$[2.0, 0.4]$	0.3	10^2	$1.3 \cdot 10^7$	1000
80	$[2.0, 0.4]$	0.3	10^1	$1.3 \cdot 10^6$	1000
80	$[2.0, 0.4]$	0.3	10^0	$1.3 \cdot 10^5$	1000

Table 4.2: Details of the simulations with the annealing algorithm. The same notation as in Table (4.1) and T_{init} and T_{end} mark the initial and final temperatures of the annealing procedure.

We will start with a qualitative description of our results using the sudden-quenched runs.

In Figs. (4.6) and (4.7) we show the behavior of $q(t)$ and $W(t)$ as a function of time for two values of the magnetic field ($H = 0.1$ and 0.3 respectively), both runs at temperature $T = 0.7$.

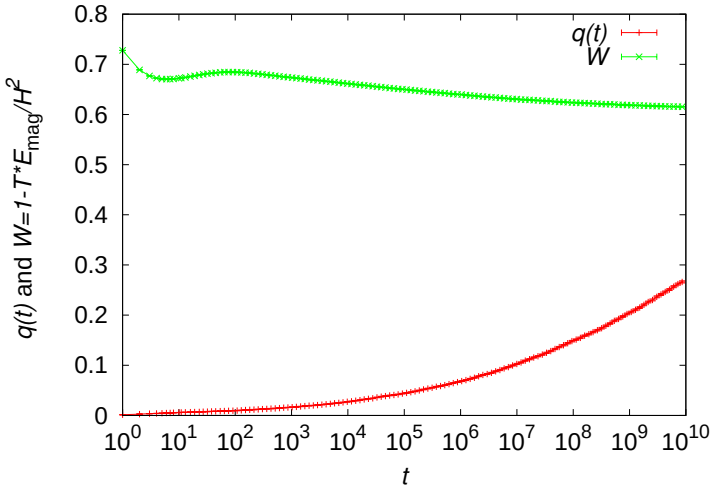

Figure 4.6: $q(t_w)$ and $W(t_w)$ at $T = 0.7$ and $H = 0.1$.

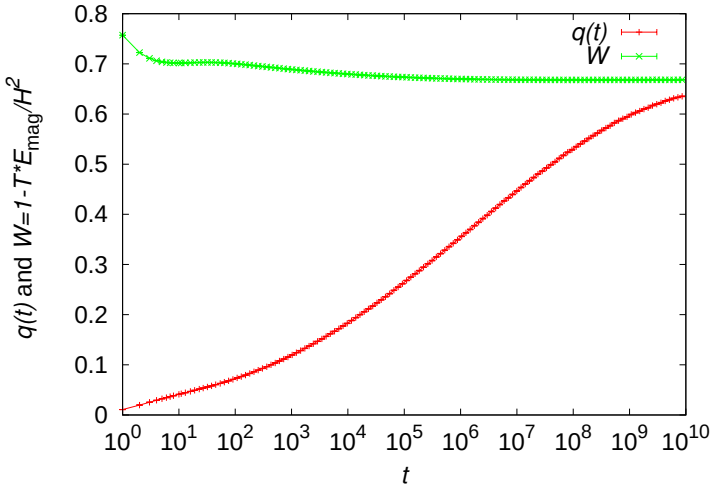

Figure 4.7: $q(t_w)$ and $W(t_w)$ at $T = 0.7$ and $H = 0.3$.

One can see that for $H = 0.1$ both curves are far away and that $q(t)$ has not reached the asymptotic behavior. However, the $H = 0.3$ data show a likely merging of the two curves, so we have obtained a clear signature of a paramagnetic phase for the pair $(T, H) = (0.7, 0.3)$.

From Figs. (4.6) and (4.7) it is clear that the sudden-quenched runs show us the onset of a paramagnetic phase ($T = 0.7$ and $H = 0.3$ case) but they cannot help us to affirm or discard the existence of a spin-glass phase since

the overlap is not yet in the asymptotic regime ($T = 0.7$ and $H = 0.1$ case). For this reason we have resort all our analysis to the annealing runs.

In Figs. (4.8) and (4.9) we show the behavior of two annealing runs with $base = 10^5$ for $H = 0.1$ and 0.3 respectively. It is clear from these two figures that the runs with annealing behave in a different way from those obtained at fixed temperatures. Notice that each step in the figures corresponds to a change in the temperature during the annealing procedure. In particular, the final overlap obtained in the runs is much larger than that obtained in the non-annealing runs. This fact has improved dramatically our results.

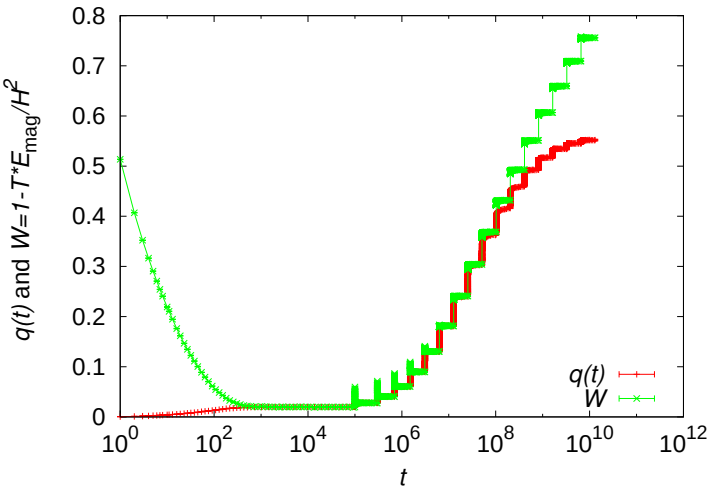

Figure 4.8: $q(t_w)$ and $W(t_w)$ for $H = 0.1$ and $base = 10^5$ (annealing run). Notice that every step in the figure corresponds with a change of the temperature.

We have observed that the difference between $W(t)$ and $q(t)$ follows with great precision a power law (see Eq. (4.28)) with an exponent essentially independent of the external magnetic field in the range of very low temperatures. This exponent seems to have a small dependence on the temperature and on the magnetic field. In the following we will take $x \simeq 0.22$, which describes extremely well the data at lower temperatures.

We show in Figs. (4.10), (4.11), (4.12), (4.13) and (4.14) our results for the following temperatures $T = 0.5$, 0.6, 0.7, 0.8 and 0.9 by plotting the difference $W(t) - q(t)$ as a function of $t^{-0.22}$ for the three simulated magnetic fields. Remember that if the difference between $q(t)$ and $W(t)$ extrapolates to a non-zero value, this is the onset of RSB. For the lowest temperature simulated, $T = 0.5$, one can see a non-zero extrapolated value of the difference

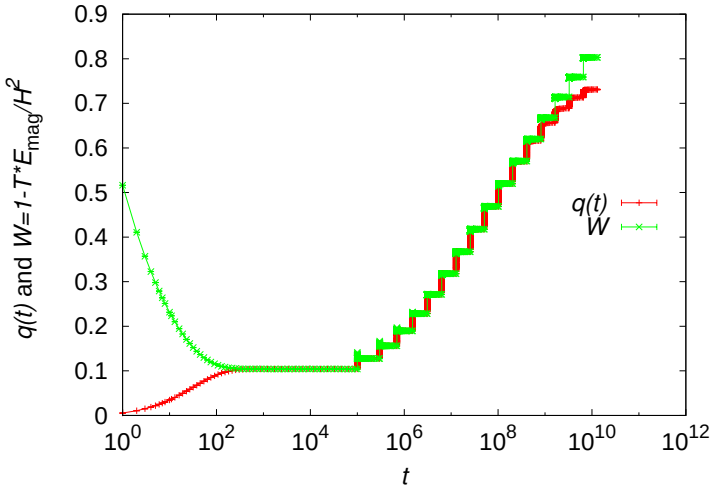

Figure 4.9: $q(t_w)$ and $W(t_w)$ for $H = 0.3$ and $base = 10^5$ (annealing run). Every step in the figure corresponds with a change of the temperature.

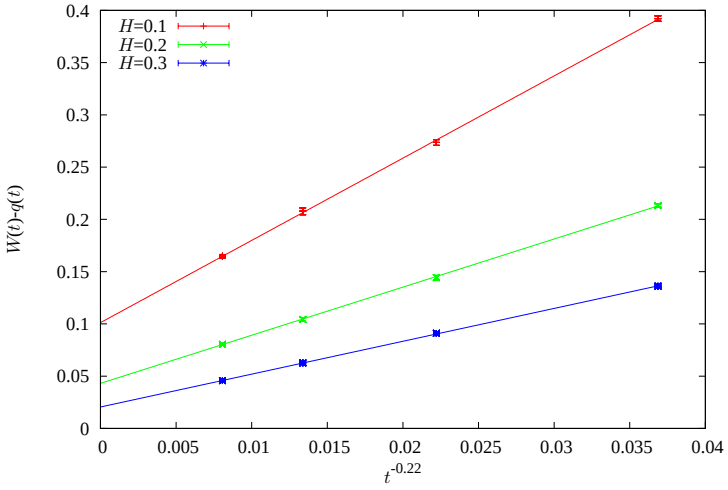

Figure 4.10: Extrapolation of the difference between $W(t)$ and $q(t)$ as a function of a power of time, for the three external magnetic fields simulated. Bottom to top: $H = 0.1$, 0.2 and 0.3. Temperature $T = 0.5$.

for the three magnetic fields, hence this temperature at these three magnetic fields behaves as driven by a spin glass phase. The dependence of the data plotted in these figures with the base parameter of the annealing procedure

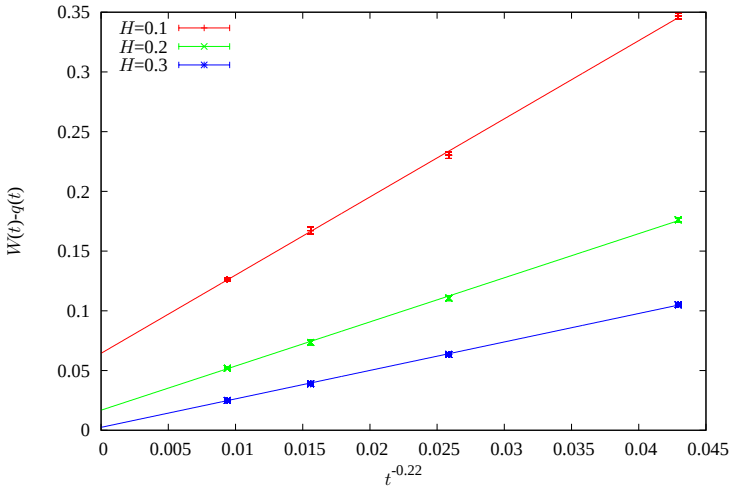

Figure 4.11: Extrapolation of the difference between $W(t)$ and $q(t)$ as a function of a power of time, for the three external magnetic fields simulated. Bottom to top: $H = 0.1$, 0.2 and 0.3. Temperature $T = 0.6$.

is inside the error bars.

If we examine the next higher temperature, $T = 0.6$, we can observe that the data corresponding to $H = 0.3$ extrapolate to zero, while the two lower magnetic fields, $H = 0.1$ and 0.2, still have a non-zero extrapolated value: we can conclude that the point $(T, H) = (0.6, 0.3)$ is just in the paramagnetic phase, whereas the pairs $(0.6, 0.2)$ and $(0.6, 0.1)$ are still in a spin glass phase.

In particular, we can state that the spin glass phase (the de Almeida-Thouless line) satisfies $T_1(H = 0.3) > 0.5$. For $T = 0.8$ (see Fig. (4.13)) only $H = 0.1$ extrapolates to a non-zero value, whereas at $T = 0.9$ (see Fig (4.14)) all three magnetic field extrapolates to a non positive value. One can roughly estimate that $T_1(H = 0.3) \simeq 0.6$, $T_1(H = 0.2) \simeq 0.7$ and $T_1(H = 0.1) \simeq 0.8$.

We can study in more detail the dependence of the power law exponent with the temperature. As it has been described above we have fitted the difference between $q(t)$ and $W(t)$ following the power law described by Eq. (4.28). This equation, with $a \geq 0$ should hold only deeply in the spin glass phase. If we approach the transition from below we would start to see the critical effects of the (thermodynamical) critical point, and the exponent x begin to be controlled by this critical point and not by the "critical" spin glass phase (Goldstone phase). So, in the critical region we should expect:

$$W(t) - q(t) = \frac{f}{t^{x_c}}\,, \tag{4.31}$$

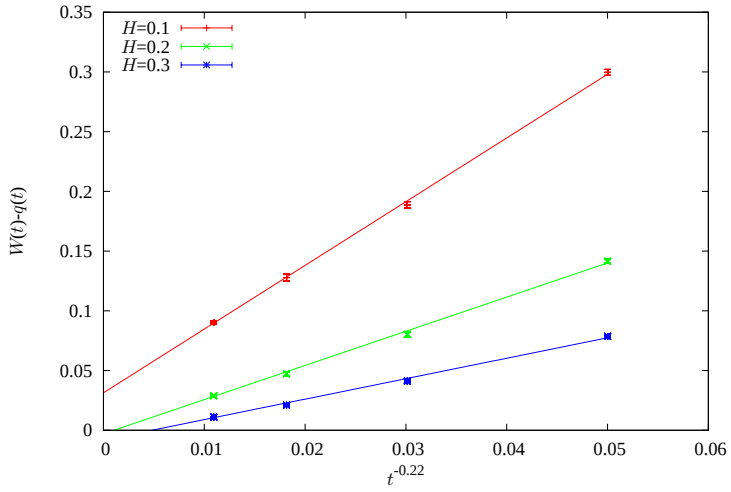

Figure 4.12: Extrapolation of the difference between $W(t)$ and $q(t)$ as a function of a power of time, for the three external magnetic fields simulated. Bottom to top: $H = 0.1$, 0.2 and 0.3. Temperature $T = 0.7$.

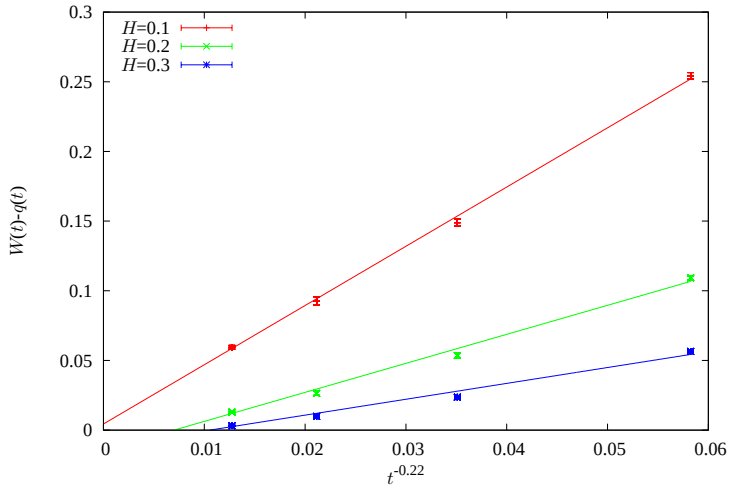

Figure 4.13: Extrapolation of the difference between $W(t)$ and $q(t)$ as a function of a power of time, for the three external magnetic fields simulated. Bottom to top: $H = 0.1$, 0.2 and 0.3. Temperature $T = 0.8$.

where in general x_c (driven by the critical point) should be different from x (driven by the spin glass phase, which is a critical one). Finally well above

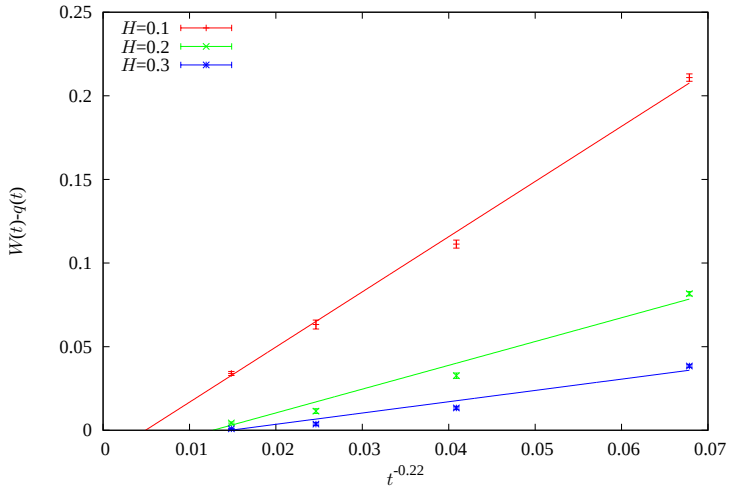

Figure 4.14: Extrapolation of the difference between $W(t)$ and $q(t)$ as a function of a power of time, for the three external magnetic fields simulated. Bottom to top: $H = 0.1$, 0.2 and 0.3. Temperature $T = 0.9$.

the critical region we should expect a stretched exponential behavior (see Eq. (4.29)).

From the previous discussion, and assuming the onset of a phase transition, it is clear that the x-exponent should take a constant value at lower temperatures (here we are assuming that the phase transition is Universal in the magnetic field), then change as we reach the critical region, and finally change again in the high temperature region since the pure power law is not longer valid (the behavior should switch to a stretched exponential). If we try to fit the high-temperature region with Eq. (4.28) with $a = 0$ or Eq. (4.31) instead of, for example Eq. (4.29), we will obtain a higher value of the x-exponent to compensate the lack of the exponential. This is just what happens in Fig. (4.15).

As an additional test we can monitor the behavior of the constant term in the power law fit (see Eq. (4.28). We present the dependence of a with temperature in Fig. (4.16), and we can observe that above a threshold (which depends on the magnetic field) the value of a starts to be negative. This conclusion reinforces the results obtained using a constant x-value in the fits. Notice that the values of x and a presented in figures (4.15) and (4.16) are obtained doing a three-parameter fit on our data, and that our choice for x (which is 0.22) is compatible with the x from the three-parameter fit in the low temperature region and for the three values of the magnetic fields.

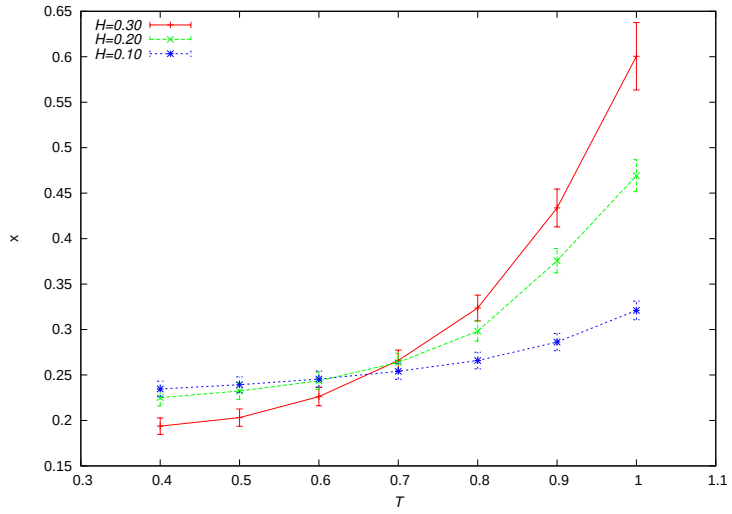

Figure 4.15: Exponent of the extrapolation of the difference between $W(t)$ and $q(t)$, x (see Eq. (4.28)), as a function of temperature, for the external magnetic fields simulated. Value computed from a three-parameter fit.

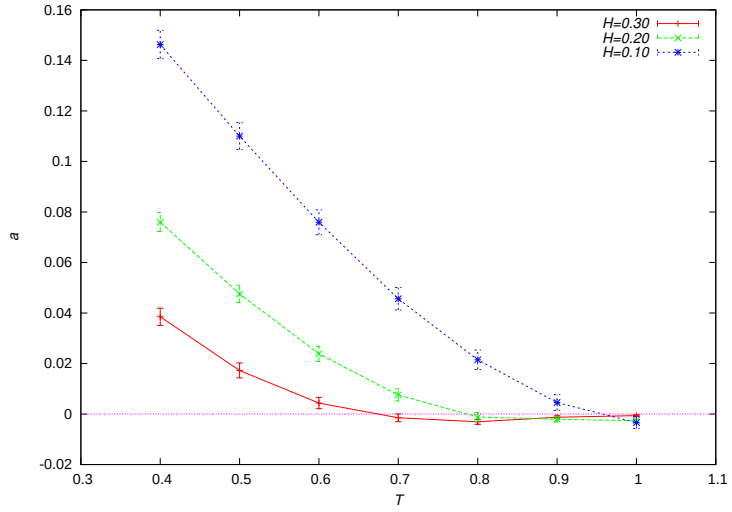

Figure 4.16: Asymptotic value of the extrapolation of the difference between $W(t)$ and $q(t)$, a (see Eq. (4.28)), as a function of temperature, for the external magnetic fields simulated. Value computed from a three-parameter fit.

We can use the temperature at which a becomes negative as our estimate of $T_1(H)$. From figure 4.16 we can estimate, now leaving vary the exponent

x, $T_1(H = 0.3) \simeq 0.65(5)$, $T_1(H = 0.2) \simeq 0.80(5)$, $T_1(H = 0.1) \simeq 0.96(5)$.

It is clear that we have found a spin glass region in field, nevertheless the method used cannot allow us to obtain a precise value of the de Almeida-Thouless line.

4.5.2 High temperature Region: Computation of the relaxation times

Once we have some estimates of $T_1(H)$ we can try to study the dynamical behavior of the system in the high temperature region. We have observed that our data for $W(t_w) - q(t_w)$ in this high temperature region follows very well the stretched exponential behavior (see Eq. (4.29)). This allows us to compute, using our annealing runs, the relaxation time as a function of the temperature. We should keep in mind that the computed time should be less than the maximum time the system is in a given temperature during the annealing process.

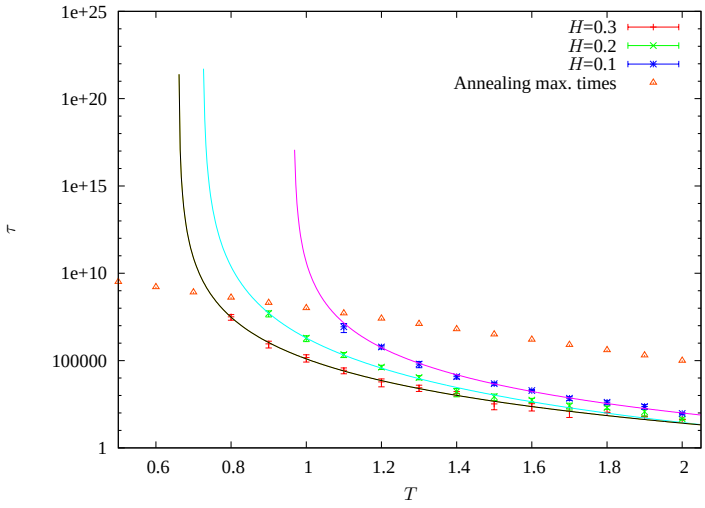

Figure 4.17: Behavior of the correlation time (τ) as a function of the temperature for the three magnetic fields simulated (see Eq. (4.30)). We also plot the best fits we have had using the critical law of τ, see the text for more details. Finally we have a discountinous line of triangles which marks the maximum times simulated during the annealing procedure at a given temperature, which marks a cutoff on our computation of the relaxation times.

Computing a fit to Eq. (4.29) is difficult due to the extreme correlation of our data, which prevents us from inverting its full covariance matrix (neces-

sary to define the χ^2 goodness-of-fit indicator). Therefore, we consider only the diagonal part of the matrix in order to minimize χ^2 and take correlations into account by repeating this procedure for each jackknife block in order to estimate the errors in the parameters. This is, of course, only an empirical procedure, but one that has been shown to work well under these circumstances (see, e.g., Ref. [199], especially sections 2.4 and 3.2).

In Fig. (4.17) we show the computed relaxation time as a function of the temperature and for the three simulated magnetic fields. In addition, we have plotted the maximum times the system spends at each temperatures (for our largest value of *base*).

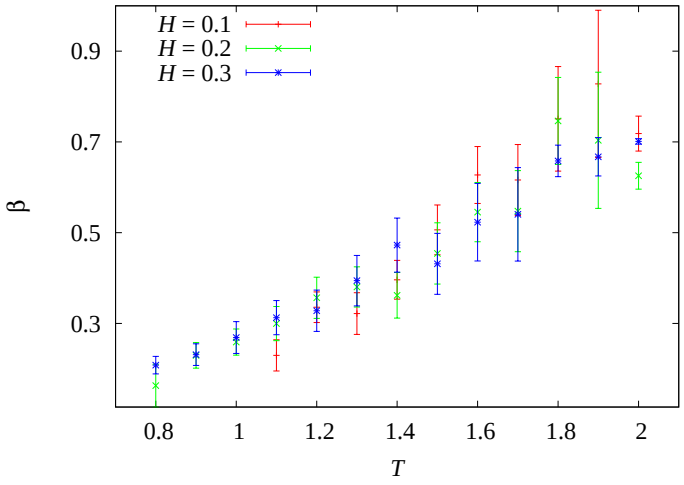

Figure 4.18: Behavior of the stretching exponent β (see Eq.(4.29)) as a function of T for our three simulated magnetic fields.

Let us mention, finally, that a possible additional source of uncertainty in our determination of τ is the depedence of the fit on the value of β. Indeed, for each T we are fitting simultaneously for x, A, τ and β in (4.29). However, a small variation in β can have a large effect on τ, which may lead us to think that the fit is unstable and unreliable. Fortunately (see Fig. 4.18), β is actually a very smooth monotonic function of T, which leads us to believe that our determination of τ is sound.

Fig. (4.17) shows us that the relaxation times are diverging very quickly, as a function of temperature, for the three magnetic field. One can examine in detail if this behavior is driven by a divergence at finite temperature. Again, and following Ref. ([131]) we try to fit the "divergence" of the relaxation time under the onset of a phase transition at finite temperature: e.g. by

using Eq. (4.30). The continuous lines in the fit correspond to this kind of fit (with very good χ^2/dof, dof being the number of degrees of freedom). We have obtained the following values:

- $H = 0.1$: $T_2 = 0.97(6)$ and $z\nu = 5.8(7)$. Using only $T \geq 1.2$ [$\chi^2/\text{dof} = 0.77$].
- $H = 0.2$: $T_2 = 0.72(6)$ and $z\nu = 7.3(1.0)$. Using only $0.9 \leq T \leq 1.7$ [$\chi^2/\text{dof} = 0.79$].
- $H = 0.3$: $T_2 = 0.66(8)$ and $z\nu = 6.2(1.6)$. Using only $0.8 \leq T \leq 1.7$ [$\chi^2/\text{dof} = 0.5$].

Since we have computed the correlation length in addition to the relaxation times, we can address the issue of the dependence of τ with ξ, which gives us useful information on the dynamics.

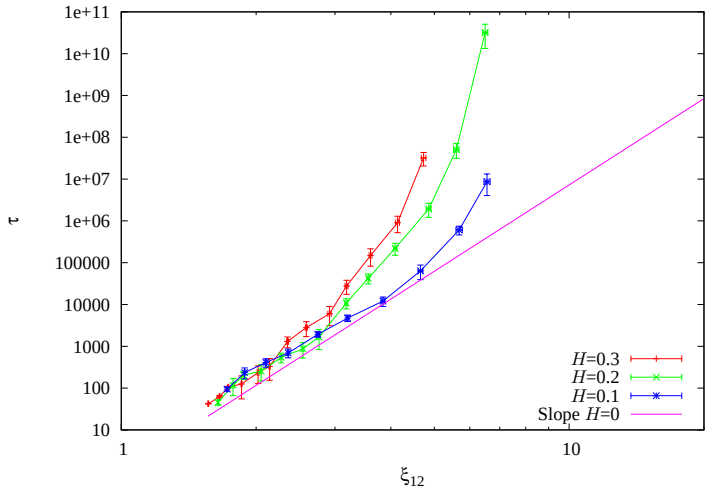

Figure 4.19: Behavior of τ against the correlation length (ξ_{12}) for the three magnetic fields simulated. We have also marked the $H = 0$ behavior: $\tau \simeq \xi^z$, with $z = 6.86$.

In Fig. (4.19) we plot τ against ξ_{12} (defined using Eq. (4.26)) for the three simulated magnetic fields. In addition, to control, we have plotted the $H = 0$ behavior ($\tau \propto \xi^z$, using the critical temperature value for the dynamical critical exponent $z \simeq 6.9$). From this figure, it is clear that the dependece of τ with ξ have changed when we have turned on the external magnetic field, however, we lack of accuracy in order to determine the analytical dependence.

4.6 Discussion of the Results

Since in our high-temperature study we have followed closely Ogielski's approach, we need to put the exponents and critical temperatures computed by Ogileski (remember at $H = 0$) in relation with the most accurate values found in the literature, in order to asses our own data.

- Ogileski provided as a critical temperature $T_g = 1.175(25)$ which should be compare with that computed in Ref. [170]: $T_c = 1.109(10)$: monitoring the relaxation times gives us an overestimated value (6%) of the critical temperature.
- He obtained $z\nu = 7.0(8)$ and $7.9(1)$. The most recent and accurate values for $\nu = 2.53(8)$ [170] and $z = 6.86(16)$[199], providing us $z\nu = 17.4(7)$. Hence, the computed value of $z\nu$ is off by a factor of two.
- Experimentalists have also followed this strategy since they are able to measure $q(t)$ in the high-temperature region. The experimental value for Ising spin glass can be quoted as: $z\nu \simeq 10.5(1.0)$ [169].

Summarizing, (at $H = 0$) one obtains an overestimated temperature (+6%) and a factor two off value for the product νz. Notice the robustness of the procedure even providing a wrong value of the product, essentially the same number (near 10) is obtained in real experiments. It is clear that the lack of corrections-to-scaling in the analysis of the relaxation times has strong effect in $z\nu$ but not so much in the critical temperature. With the available computational facilities we are unable to improve this procedure.

Once we have discussed the methodology (and some drawbacks) used to obtain our data, we can try to put a coherent physical picture. At this point, we have clearly three possibles scenarios:

NPT. No phase transition at all.

Both $T_1(H)$ and $T_2(H)$ should eventually drift to zero temperature or be the effect from a crossover from the $H = 0$ phase transition. The experiments in a field should give $T_2(H)$ (they can not access $T_1(H)$ in this way). They obtain a good dynamical scaling in field with $z\nu \simeq 9$, but this is usually interpreted as a crossover effect. In addition, the low-temperature behavior of the difference $(1/t^{0.22})$ could change if we simulate long waiting times (however, we remind the reader that we are already simulating up to the beginning of the experimental time scales). In addition, the value of $T_1(H = 0.1)$ is compatible with the critical temperature of the model n absence of magnetic field ($T_c(H = 0) \simeq 1.1$,

so our data for $H = 0.1$ coild be strongly affected by the $H = 0$ critical point. Yet, the values for $T_1(H = 0.2)$ and $T_1(H = 0.2)$ are not near to $T \simeq 1.1$, so, in principle, these two magnetic field should be avoided the crossover effect of the $H = 0$ critical point.

2PT. $T_1(H) < T_2(H)$ Scenario. This scenario is the most suggestive one from the point of view of the hypothetical correspondence beteween structural glasses and spin glasses on a magnetic field [155, 156]. The replica theory for structural glasses [147, 148, 149, 150] suggests that $T_2(H)$ would rather correspond to the Mode Coupling temperature (which is rather a crossover in three spatial dimensions), while a real thermodynamic phase transition would take place at $T_1(H)$. We note that the existence of a thermodynamic glass transition is being vigorously debated by the supercooled liquids community [122].

1PT. Only one thermodynamical phase transition. In this light, $T_1(H) = T_2(H)$, since the phase transition drives the divergence of the relaxation times and also the breakdown of the law given by Eq. (4.28). The main difference of this work regarding dynamical experimental studies is that we can also compute $T_1(H)$ in addition to $T_2(H)$. We note that this scenario is the one predicted by Mean Field theory.

Regarding the last two scenarios, our values of $T_1(H)$ and $T_2(H)$ are very similar, but they are not so accurate to fix the possible escenario. As cited in the fisrt scenario, we cannot even discard an eventual crossover of both T_1 and T_2 to zero (simulating larger values of *base*).

4.7 Conclusions

We have tried to characterize the behavior of the three-dimensional spin glass both in the high and low temperature regions, monitoring the behavior of the difference $W(t) - q(t)$.

These studies have allowed us to determine (at least in our range of simulated times) two changes of regime as a function of temperature: in the first one ($T_1(H)$), below that, the low temperature phase behaves as a spin glass one; in the second one ($T_2(H)$), we have obtained a divergence of the relaxation times. Numerically we have found that $T_s(H)$ is roughly similar to $T_1(H)$. We are simulating the beginning of the experimental times, so, we will have the same advantages and drawbacks as in real experiments: in particular, we cannot discard a change of the low-temperature exponent ($x \simeq 0.22$), which, eventually, can drive $T_1(H)$ to zero.

In order to grasp a better understaning of this problem, we have started to run equilibrium numerical simulations to complement the studies presented in this work.

4.8 Discretization of the Gaussian Magnetic Field

In this appendix we will describe the procedure we have used to discretize the Gaussian magnetic field in order to be able to simulate the Gaussian model in the Janus dedicated computer (which can no cope efficiently with non-integers numbers).

We have used the strategy, first introduced in Ref. [**?**], based on the use of Hermite polynomials. It is well known that a Gaussian integral can be done numerically as ($f(x)$ being an even function):

$$\int_{-\infty}^{\infty} dx f(x) e^{-x^2} \simeq \sum_{i=1}^{n} w_i f(x_i)\,, \tag{4.32}$$

where the weights w_i and the points x_i are tabulated (see, for instance, Ref. [167]). In particular, in this work we have used $n = 2$ and hence $x_1 = 0.524647623275$, $x_2 = 1.65068012389$, $w_1 = 0.804914090006$ and $w_2 = 0.0813128354472$. So, we can encode the Gaussian magnetic using only two bits.

Obviously, our $n = 2$ choice should fail for higher magnetic field and small lattice sizes. We have checked that our choice is valid at least for $H \leq 0.3$. In particular we have compared the data using $n = 2$ in the numerical simulation and that of a fully Gaussian one. In Fig. (4.20) we show the result of a test performed on a $L = 8$ by computing the overlap, thermal and magnetic energy (running on a PC-clusters). One can see in this figure data from $n = 2$ and $n = 5$ as well as Gaussian ones. The agreement is perfect.

Finally, we can cite that a strong test is that, in the paramagnetic phase, $q(t)$ and $W(t)$ should converge to the same value asymptotically, for example in Fig. (4.9).

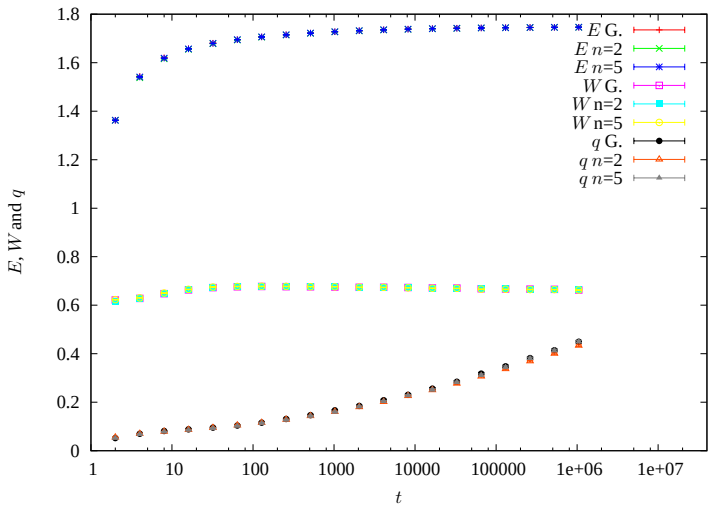

Figure 4.20: Thermal energy (E), magnetic energy ($W(t)$ and overlap ($q(t)$) as a function of time for $L = 8$, $T = 0.7$ and $H = 0.3$. We have plotted the results from a fully Gaussian (G.), $n = 2$ and $n = 5$ numerical simulations. Notice that all three simulations provided us with the same values of these three observables.

Chapter 5

Analysis of the zeros of the partition function in an Edwards-Anderson system

The characterization of phase transitions is an extremely important issue in statistical physics, in fact Chapters 2 and 4 of this thesis deal with this issue. In a first order phase transition, the first derivative of the free energy is discontinuous at the critical temperature in the thermodynamic limit and two different phases coexist. The behavior in a second order transition is different, because the quantities which diverges are the second derivative of the free energy and the correlation length, which can be characterized by the appropriate critical exponents. In fact, in finite size systems, which are the ones that can be simulated, these divergences smoothen. Many tools have been developed to study these phase transitions, but we will focus in this chapter in the one introduced by Lee and Yang [172, 173] in 1952. They studied the zeros of a lattice gas and found that the zeros live in the unit circle of the complex plane of the magnetic external field and condensed (as $V \to \infty$) onto the real axis when a phase transition happens (see appendix D for more details).

In 1965, Fisher started the study of the zeros in the complex plane of the temperature. However, there is not a theorem like the Lee-Yang one, so Fisher's zeros do not have to live in the unit circle. For example, in Figure 5.1 (taken from Ref. [177]), the locus of the Fisher's zeros of a two dimensional Ising model system, which do not lie on the unit circle.

Obviously, only simulations of finite size systems can be performed, so to study the properties in the $V \to \infty$ limit, one should simulate several lattice sizes and study the behavior of the system as a function of the size, the scaling. Besides, Janke and Kenna introduced in 2001 [174] a new tool

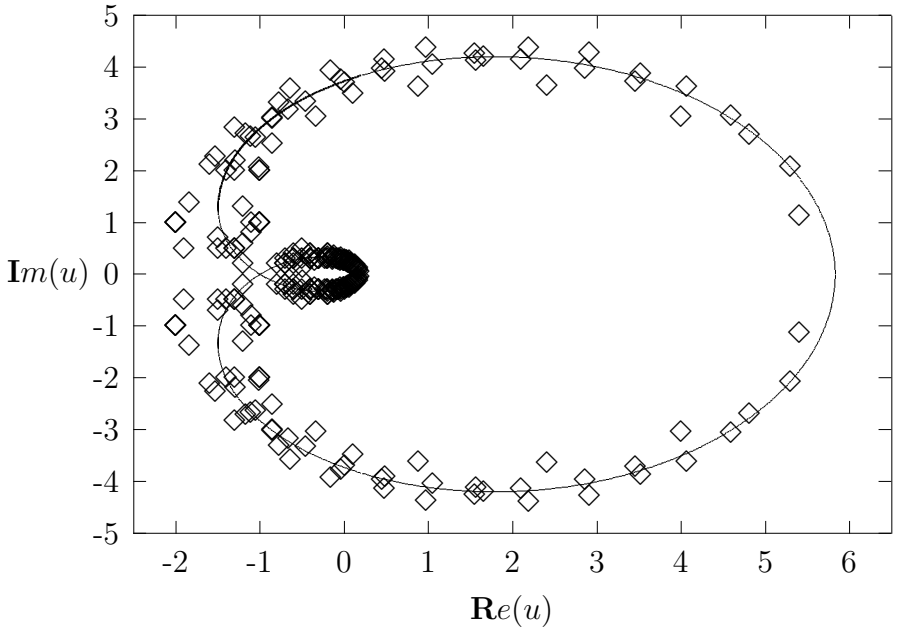

Figure 5.1: Locus of the Fisher zeros of a 2D Ising model, $L = 16$. Figure from Ref. [177]

using the density of the zeros (one can see its definition and a complete explanation in Section 5.3 of the paper attached) to determine the strength of the phase transition. This technique, has been used to study the phase transitions of several models, even though in some of them (like, for example, Potts models) where the Lee-Yang theorem does not actually hold, so the zeros do not lie on the unit circle. However, one can suppose that the zeros do condense onto the real axis when a phase transition happens. We will show some examples focused in spin models, firstly in pure models. In the two dimensional Ising model, the simplest pure spin system, it is well known that a second order phase transition happens and the specific heat presents a logarithmic singularity [176]. This technique is used in Ref. [174] to analyse the distribution of the Fisher's zeros in the two dimensional Ising model (determined in Ref. [177]) and the results are compatible with both, the existence of the phase transition and the logarithmic singularity of the specific heat.

Regarding Potts model, Janke and Kenna also studied it in reference [174], both the two dimensional and ten states Potts model (which is also studied in [178]) and the three dimensional three states Potts model. In the

first one a first order phase transition takes place, which is confirmed by the analysis of the density of zeros. Moreover, they managed to compute a latent heat $\Delta e = 0.698(2)$ while the exact value is 0.6961. Three dimensional and three states Potts model also has a first order phase transition but a weak one, so it is useful to check new algorithms to search phase transitions and characterized them. In the analysis of the density of the zeros done in the Ref. [174], the slope of the fit does not vanish near the origin, which shows the existence of a first order phase transition. Besides, they computed the latent heat $\Delta e = 0.247(5)$ which can be confronted with the value found in the literature 0.2421(5) [175].

In addition to the pure models, disordered systems have also been studied. In disorder systems one has to compute the zeros in every sample, average over the disorder before doing a similar analysis to the pure system. In Ref. [179] a two dimensional diluted Ising model is studied, supporting the strong universality hypothesis instead of the weak one, that is, the critical exponents do not change with the dilution and $\alpha = \hat{\alpha} = 0$. In Ref. [180] a four dimensional diluted Ising model is studied, and the existence of a phase transition is shown, even more clearly than using the standard numerical techniques.

Finally, in this thesis, we are really interested in the study of spin glasses, so we will apply this technique to study the three dimensional Ising spin glass model. Remind that in spin glasses the overlap is the order parameter, so we will use a parameter coupled with it to study the zeros of the partition function[1]. Therefore, one of the main goals of this work is to study how these zeros behave in a frustrated system like a spin glass. Moreover, we will be to study q_{EA}, which characterization has been attempted for long time.

[1]Overlap should play a similar role in spin glasses that magnetic field plays in Ising model, where it is the order parameter.

Numerical Study of the Overlap Lee-Yang Singularities in the Three-Dimensional Edwards-Anderson Model

R. A. Baños[1,2], J. M. Gil-Narvion[2], J. Monforte-Garcia[1,2], J. J. Ruiz-Lorenzo[3,2] and D. Yllanes[4,2]

[1] Departamento de Física Teórica, Universidad de Zaragoza, 50009 Zaragoza, Spain.
[2] Instituto de Biocomputación y Física de Sistemas Complejos (BIFI), 50018 Zaragoza, Spain.
[3] Departamento de Física, Universidad de Extremadura, 06071 Badajoz, Spain.
[4] Dipartimento di Fisica, La Sapienza Università di Roma, P.le A. Moro 2, 00185 Roma, Italy.

Published in *J. Stat. Mech.* P02031 (2013).

5.1 Introduction

In two seminal papers, T. D. Lee and C. N. Yang [181, 182] introduced a new tool to understand the origin of a phase transition by studying the complex singularities of the free energy, or, equivalently, the zeros of the partition function. In particular, they showed that all the zeros are located on the unit circumference on the complex activity plane (taking as variable $z = e^{-2h}$, where h is the external magnetic field). They also proved that if the zeros condense onto the real axis when $V \to \infty$ a phase transition takes place. Finally, they related, in the low-temperature phase, the density of zeros with the discontinuity in the order parameter (remember that the Ising model experiences a first-order phase transition when h changes at a fixed temperature below the critical one). This approach was subsequently extended to the temperature zeros by Fisher [183, 184, 185, 186].

We have Lee-Yang like theorems only for a limited class of non-disordered systems (such as Ising models). However, it is possible to develop a scaling theory by assuming that asymptotically the complex singularities (wherever they lie) touch the real axis (thus generating the phase transition). Hence, despite the lack of formal theorems it is still possible to apply Lee and Yang's main results to a wide class of systems (e.g., Potts models [187]). In this class of systems the zeros do not live on a circle as stated by the Lee-Yang theorem, but they still control the critical properties of the model. We will only assume this last fact irrespectively of the form of the locus of the zeros in the complex plane [187].

In Refs. [188, 189, 190] the analysis of complex singularities was applied successfully to diluted systems (in particular diluted Ising models in two and four dimensions). The key point for the applicability of the standard results, well tested in non-disordered systems, is to compute the complex singularities individually for each disorder realization (called sample) and then use the mean of the individual zeros (sample zeros) in order to test the scaling properties of the zeros and to study the properties of the integrated density of zeros. In this work we will also introduce the analysis of the median.

Nowadays we are interested in gaining a deeper understanding (from the point of view of the complex singularities) of the properties of an interesting frustrated and disordered system: the three-dimensional Ising spin glass. The magnetization, while very interesting in off-equilibrium dynamics and in experiments, plays no role in the critical behavior and in the understanding of the low-temperature properties in a finite-dimensional spin glass. The observable that controls this spin-glass phase is the overlap. Hence, in this work we have focused on the numerical study of the complex singularities linked with the overlap in order to study the phase transition and the properties of the spin-glass phase.

In the past, Lee-Yang and Fisher zeros were obtained in spin glasses by means of the numerical evaluation of the partition function on small lattices [191, 192, 193, 194]. This methodology was also applied to models defined on Bethe lattices [195]. Finally, some calculations were performed with the help of replicas [196].

More recently, the complex singularities linked with the external magnetic field were studied for the two and three-dimensional Ising spin glass model in the interesting reference [197], which focuses on the Griffiths singularity and computes all the zeros for small lattices.

In particular we are interested in characterizing the scaling of the individual zeros at the critical point (which will allow us to compute the anomalous dimension exponent) and checking the scaling in the spin-glass region. In addition, we want to study the properties of the density of zeros in the critical and spin-glass region: the behavior of this observable will clearly signal the phase transition. Finally, we will show how this density of zeros can be used to compute the Edwards-Anderson order parameter. However, the spin-glass susceptibility presents strong scaling corrections (even on an $L = 32$ lattice and $\beta = 1.4$), which induce strong corrections on the density of zeros allowing us (from the numerical point of view) only to test our density of zeros against the values of q_{EA} found in the literature, rather than attempting a direct numerical computation of the order parameter. We want to stress that in cases in which the spin glass susceptibility reaches the asymptotic value, the

method we propose will be able to provide directly the order parameter ($q_{\rm EA}$) giving an additional method to those used nowadays [198, 199, 200, 201].

Let us finally mention that we have obtained the data presented in this work from the analysis of the configurations produced in parallel tempering runs [200, 201] using the Janus computer [202, 203, 204].

5.2 Model and observables

We have studied the three-dimensional Edwards-Anderson model with dynamical variables σ_i. These variables are Ising spins and are placed on the nodes of a cubic lattice of linear dimension L and volume $V = L^3$. The Hamiltonian of the system is

$$\mathcal{H}_0 = -\sum_{\langle i,j\rangle} J_{ij}\sigma_i\sigma_j, \tag{5.1}$$

where $\langle ij\rangle$ indicates that the sum is over the nearest neighbouring sites. The couplings J_{ij} are random quenched constants with bimodal probability distribution, that is, $J = \pm 1$ with 50% probability. Every realization of the couplings is called a sample. Due to the fact that we have a random Hamiltonian, we have to deal with a double average: first the thermal average, which we will denote by $\langle(\cdots)\rangle$, and then the average over the samples, which we will denote by $\overline{(\cdots)}$.

We have simulated several real replicas of the system, so we can define the local overlap

$$q_i = \sigma_i^{(1)}\sigma_i^{(2)} \tag{5.2}$$

where $\sigma_x^{(1)}$ belongs to the first replica and $\sigma_x^{(2)}$ belongs to the second one. The spin overlap is defined from this local overlap as

$$Q = \sum_i q_i, \tag{5.3}$$

where the sum runs over the whole volume (V). In addition, we define $q \equiv Q/V$. These observables allow us to define some new quantities, for example the non-connected spin-glass susceptibility

$$\chi_{\rm SG} = \frac{1}{V}\overline{\langle Q^2\rangle}. \tag{5.4}$$

Let us now rewrite the Hamiltonian adding a new perturbation ϵQ and including the two replicas explicitly,

$$\begin{aligned}\mathcal{H}_\epsilon &= \mathcal{H}(\sigma_1) + \mathcal{H}(\sigma_2) + \epsilon Q \\ &= -\sum_{\langle i,j\rangle} J_{ij}\left(\sigma_i^{(1)}\sigma_j^{(1)} + \sigma_i^{(2)}\sigma_j^{(2)}\right) + \epsilon\sum_i \sigma_i^{(1)}\sigma_i^{(2)}.\end{aligned} \tag{5.5}$$

This Hamiltonian looks like that of the Ising model in a magnetic field

$$\mathcal{H}_h = \mathcal{H}_0 + h\mathcal{M}. \tag{5.6}$$

We can write the partition function, whose zeros we want to study, as

$$\begin{aligned} Z &= \sum_{[\sigma^{(1)}\sigma^{(2)}]} e^{-\beta\mathcal{H}_0+\beta i\epsilon Q} \\ &= \sum_{[\sigma^{(1)}\sigma^{(2)}]} \left(\cos(\beta\epsilon Q)e^{-\beta\mathcal{H}_0} + i\sin(\beta\epsilon Q)e^{-\beta\mathcal{H}_0}\right). \end{aligned} \tag{5.7}$$

Let Z_0 the partition function of the non-perturbed system, so

$$Z = Z_0\{\langle\cos(\beta\epsilon Q)\rangle + i\langle\sin(\beta\epsilon Q)\} \tag{5.8}$$

and we have to find the zeros of the function $\langle\cos(\beta\epsilon Q)\rangle$ since in absence of a magnetic field $\langle\sin(\beta\epsilon Q)\rangle$ is zero. The algorithm to find them is quite easy: we start from the list of individual measurements of Q for each sample (see Section 5.4) and evaluate the average $\langle\cos(\beta\epsilon Q)\rangle$, increasing ϵ in small steps $\Delta\epsilon$. When the function changes signs from one step to the next, we have found a zero in this interval. Obviously, the smaller $\Delta\epsilon$ the better the precision of the zero that we have found, but also the slower the analysis, so we have to be careful with the error estimates. We have analyzed the first four zeros of this function.

5.3 Finite-Size Scaling

One can obtain the expected behavior of the LY zeros by means of (see for example Ref. [187])

$$\epsilon \simeq \frac{1}{\sqrt{\chi_{\rm SG}V}} \tag{5.9}$$

therefore, the finite-size dependence, at the critical point, of the Yang-Lee zeros can be expressed as:

$$\epsilon_j(L) \sim L^{-x_1}, \tag{5.10}$$

where

$$x_1 = (D + 2 - \eta)/2, \tag{5.11}$$

and D is the dimensionality of the system, being $D = 3$ in this work. If corrections to scaling are taken into account, the above relation becomes

$$\epsilon_j(L) \sim L^{-x_1}\left(1 + \mathcal{O}(L^{-x_2})\right), \tag{5.12}$$

where x_2 is the leading correction-to-scaling exponent, $x_2 = \omega$.

In the broken symmetry phase, where the non-linear susceptibility diverges as the volume of the system, we expect the following behavior:

$$\epsilon_j(L) \sim \frac{1}{V}\,, \tag{5.13}$$

We can take scaling corrections into account, as in the critical point, and

$$\epsilon_j(L) \sim V^{-1}\left(1 + \mathcal{O}(L^{-x_3})\right)\,. \tag{5.14}$$

where x_3 is the leading correction-to-scaling exponent in the broken phase.[2].

In order to discuss the density of zeros we need to describe some known properties of the Hamiltonian defined in Eq. (5.5). This Hamiltonian was introduced in the past [205, 206]. In particular it experiences a first-order phase transition in ϵ, below the critical temperature of the uncoupled model. Hence, the overlap is discontinuous:

$$\lim_{\epsilon\to 0^{\pm}} \overline{\langle q\rangle}(\epsilon) = \pm q_{\rm EA}\,, \tag{5.15}$$

being the discontinuity at the transition just $2q_{\rm EA}$.

We can also introduce the density of zeros

$$\mu_\epsilon(\epsilon) = \sum_j \delta(\epsilon - \epsilon_j(L)) \tag{5.16}$$

and its integrated version

$$G(\epsilon) = \int_0^\epsilon dx \mu_\epsilon(x) \tag{5.17}$$

which takes the following value computed for a given zero:

$$G(\epsilon_j(L)) = \frac{2j-1}{2V}\,, \tag{5.18}$$

where j labels the j-th zero ($j = 1, 2, \ldots$). In order to deal with the discontinuous behavior of $G(\epsilon)$ at the zeros, we follow the recipe of references [207, 208]

[2]Both droplet and RSB predict algebraic decays for the connected correlation functions in the spin glass phase (the spin glass phase is critical in both models). In the droplet model the exponent of the decay is y (sometimes denoted as θ), so one can show that $x_3 = y$. In RSB depending of the value of q we have different decays (of the q-constrained correlation functions), denoting the decay exponents as $\theta(q)$. So the leading correction exponent can be shown to be the smallest of the different $\theta(q)$. See Refs. [200, 201] for a detailed discussion on $\theta(q)$.

and use the mean between two consecutive plateau values ($j-1$ and j). Anyhow, the asymptotic value of the integrated density computed in the j-th zero is j/V. We will discuss this point again in subsection 5.5.3.

This integrated density is very useful to characterize a phase transition. In general it behaves as

$$G(\epsilon) = a_1 \epsilon^{a_2} + a_3 \tag{5.19}$$

and we can extract a great amount of physical information from these three numbers (a_1, a_2 and a_3):

- In the symmetric phase $a_3 < 0$. In a broken phase $a_3 > 0$.
- In the onset of a first-order phase transition, varying ϵ as it is our case: $a_2 = 1$ and $a_3 = 0$. In addition we can extract the order parameter of the broken phase: $q_{\mathrm{EA}} = \pi a_1/\beta$.[3]
- At the critical point, $a_3 = 0$ and a_2 is related with the anomalous dimension η by means:

$$a_2 = \frac{2D}{D + 2 - \eta}\,. \tag{5.21}$$

5.4 Simulation details

We have run simulations for several lattice sizes on the Janus supercomputer [202, 203, 204] (for $L = 16, 24,$ and 32) and on conventional computers (for $L = 8$ and 12). These simulations were originally reported in [200], which gives full details on the chosen parameters and the thermalization protocol. In this section we give only a brief summary.

We have used the parallel tempering algorithm [209, 210], choosing the temperatures to maintain an acceptance around 20% in parallel tempering updates. Besides, since Janus needs far more time to do a parallel tempering

[3] In Lee and Yang's paper, the starting point is the Hamiltonian $\beta\mathcal{H}_h = \beta\mathcal{H}_{h=0} + hM$, where M is the total magnetization of the system. In terms of the fugacity $z = e^{-2h}$, they obtained the following result (valid below the critical temperature) for the density of zeros (in the fugacity variable that we will denote as $\mu_z(z)$): $\mu_z(0) = m_{\mathrm{sp}}/(2\pi)$, where m_{sp} is the spontaneous magnetization below the critical temperature. In order to transfer this result to our notation we remark that our "magnetic field" is $\beta\epsilon$, q_{EA} plays the role of m_{sp} and we need to use the standard law of the transformation of the probability densities ($\mu_z(z) = \mu_\epsilon(\epsilon)|d\epsilon/dz|$, where $z = \exp(-2\beta\epsilon)$), obtaining:

$$\mu_\epsilon(0) = \frac{q_{\mathrm{EA}}\beta}{\pi}\,. \tag{5.20}$$

Notice that near $\epsilon = 0$ we can identify a_1 with $\mu_\epsilon(0)$.

update than a heat-bath one, we have chosen to do one parallel tempering update every 10 heat-bath ones. In table 5.1 one can find a summary of the simulations parameters. In order to choose the simulation length, we have assessed thermalization on a sample-by-sample basis, using the temperature random walk technique [211, 200] (table 5.1 gives the average number of lattice updates for each L).

In general, each of the single processors (FPGAs) of Janus takes care of the simulation of one replica of the system. However, some samples have such a slow dynamics that even with this algorithm the simulation would be too long (more than six months of continuous running time), so we would need to accelerate it. For these few cases we have created a special low-level code that is in charge of the parallel tempering in the control FPGA of a board of Janus. This allows us to spread the simulation over several processors running only a subset of temperatures in each FPGA, thus accelerating the simulation by increasing the parallelism.

Table 5.1: Summary of the simulations. N_{T} is the number of simulated temperatures (evenly spaced between T_{min} and T_{max}); N_{mes} is the number of Monte Carlo steps (updates of the whole lattice) between measurements; $N_{\mathrm{HB}}^{\mathrm{med}}$ is the average simulation time (since we use the random-walk technique the simulation time depends on the sample); N_{sam} is the number of simulated samples. We have simulated four real replicas for each sample. Finally, $L = 8$ and $L = 12$ have been simulated on PCs and $L = 16$, $L = 24$ and $L = 32$ on Janus.

L	T_{min}	T_{max}	N_{T}	N_{mes}	$N_{\mathrm{HB}}^{\mathrm{med}}$	N_{sam}
8	0.150	1.575	10	10^3	7.82×10^6	4000
12	0.414	1.575	12	5×10^3	3.13×10^7	4000
16	0.479	1.575	16	10^5	9.71×10^8	4000
24	0.625	1.600	28	10^5	4.02×10^9	4000
32	0.703	1.549	34	2×10^5	1.90×10^{10}	1000

5.4.1 Data for the computation of the zeros

We have saved on disk every individual measurement of the overlap. Since we have simulated four real replicas of the system, for each sample we have a total of $6N_{\mathrm{HB}}/N_{\mathrm{mes}}$ values of Q. Given the variable N_{HB}, this ranges from 1.2×10^5 to 2×10^7 measurements for our largest lattices, so we have a very good precision for computing the zeros of the partition function. We have discarded the first half of the measurements for equilibration.

We want to study the behavior of the system in the critical temperature and in the low-temperature phase of the system, analyzing the scaling of the zeros. Therefore, we need to compute the zeros of different system linear sizes, L, but at the same temperature. Since we have not simulated the same temperatures for every lattice size, we have interpolated, using cubic splines, in order to estimate the zero at each of the chosen scaling temperatures.

5.5 Results

In this section we will study the behavior of the zeros as a function of the lattice size, both in the critical and in the spin-glass phase. Finally, we will compute the density of zeros and extract the η exponent from the analysis at the critical temperature and the Edwards-Anderson order parameter from the scaling in the low-temperature phase.

5.5.1 Scaling at the Critical Point

We first consider the scaling at the critical point and use it to determine the anomalous dimension, as in (5.10). Our simulations were optimized to investigate the low-temperature phase, for large system sizes, rather than to obtain the critical parameters. Therefore, we take the value of $\beta_c = 0.902(8)$ from [212], which features many more samples and small sizes to control scaling corrections but does not reach the low-temperature phase, and will also use this reference to check our value of η.[4]

Let us first consider a fit of the individual zeros, leaving aside corrections to scaling, i.e., following (5.10). For the j-th zero, we fit to

$$\epsilon_j(L) = A_j L^{-x_1}. \tag{5.22}$$

We report the results of these fits in table 5.2. We see that the first and second zeros follow (5.22) very well for $L \geq 8$, but for $j > 2$ we need to restrict the fit to $L \geq 12$. However, there is an inconsistency in the results: the value of x_1 should be the same for all zeros, but we see that it increases with j. Moreover, at least for the larger j, x_1 is incompatible with the expected value of $x_1 = 2.688(5)$, (taking $\eta = -0.375(10)$ from [212]) This hints that corrections to scaling should be taken into account, as in (5.12).

In order to do so, we consider all values of j at the same time and perform a global fit, enforcing data from different zeros to share the same x_1 and x_2.

[4] If we combine the critical exponents of [212] with the Janus simulations studied herein, we obtain a compatible value of $\beta_c = 0.905(7)$ [213].

Table 5.2: Fits of the zeros to $\epsilon_j(L) = A_j L^{-x_1}$, for $L \geq L_{\min}$. As we can see, with $L_{\min} = 8$ the χ^2 per degree of freedom is acceptable only for $j = 1, 2$, but with $L_{\min} = 12$ all the zeros have a reasonable fit. However, the value of x_1 grows with j, an indication that we have to consider corrections to scaling (see text).

j	$L_{\min}$	β	x_1	χ^2/d.o.f.
1	8	0.902	2.703(12)	1.78/3
2	8	0.902	2.712(6)	3.23/3
3	8	0.902	2.718(5)	8.12/3
4	8	0.902	2.725(5)	15.1/3
1	12	0.902	2.695(14)	1.27/2
2	12	0.902	2.715(8)	2.95/2
3	12	0.902	2.731(7)	2.19/2
4	12	0.902	2.745(7)	2.49/2

As points coming from a given L are correlated, the full covariance matrix has to be considered. We label our set of points $\{\epsilon_j(L_a)\}$ by their L and their j: we have data for $\mathcal{L} = 5$ different values of L ($L_1 = 8$, $L_2 = 12$, $L_3 = 16$, $L_4 = 24$, $L_5 = 32$) and for $j = 1, 2, 3, 4$. The appropriate goodness-of-fit estimator is, therefore,

$$\chi^2 = \sum_{i,j=1}^{4} \sum_{a,b=1}^{\mathcal{L}} [\epsilon_i(L_a) - A_i L_a^{-x_1}(1 + B_i L_a^{-x_2})] \sigma^{-1}_{(ia)(jb)} [\epsilon_j(L_b) - A_j L_b^{-x_1}(1 + B_j L_b^{-x_2})], \quad (5.23)$$

where $\sigma_{(ia)(jb)}$ is the covariance matrix of the set of zeros (which is block diagonal, since data for different L are uncorrelated).

Unfortunately, we do not have enough data to determine x_2 and x_1 at the same time (the resulting error in ω would be greater than 100%). Instead, we take $x_2 = \omega = 1.0(1)$ from [212] and fit only for x_1 and the amplitudes. The resulting fit for $L \geq 12$, shown in figure 5.2, gives

$$x_1 = 2.67(6)[1], \qquad \chi^2/\text{d.o.f.} = 5.88/7, \quad (5.24)$$

where the error in square brackets accounts for the uncertainty in ω. Our determination of x_1 is now compatible with the expected value of $x_1 = 2.688(5)$. Therefore, the scaling of the zeros is consistent at the critical point.

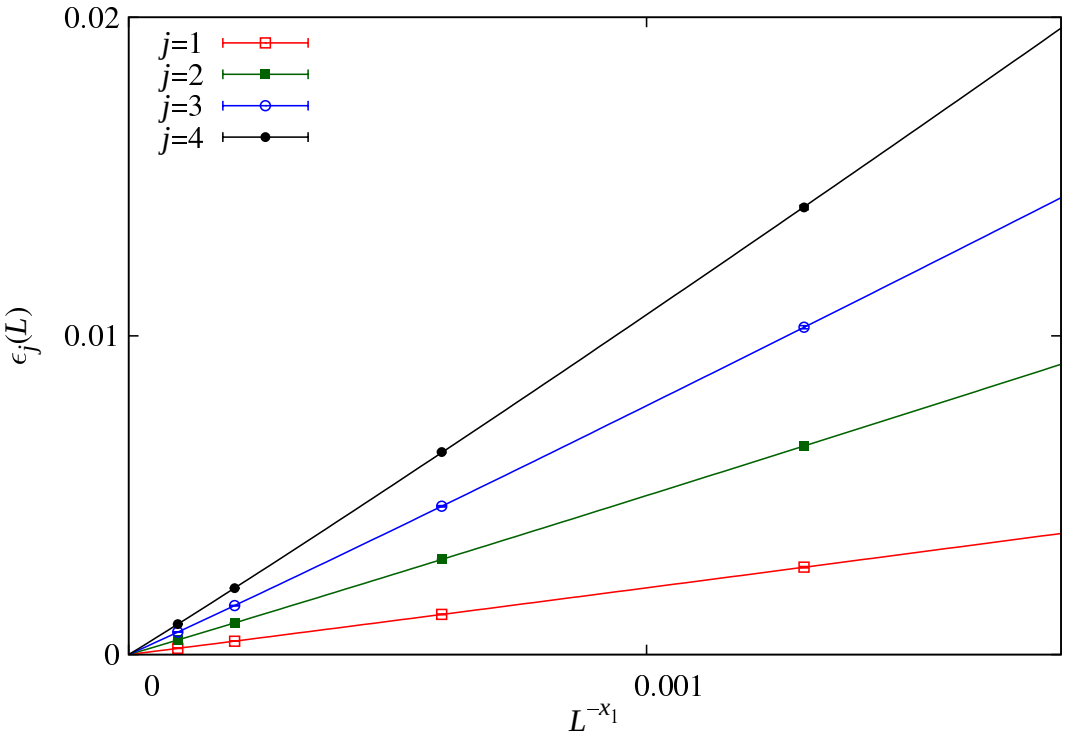

Figure 5.2: The four first zeros at $\beta = \beta_c$. In order to appreciate the scaling better, we show only the data for $L \geq 12$ and compare to equation (5.12), fixing $x_2 = \omega = 1.0(1)$ from [212] and performing a global fit for a common value of x_1 (see text). We obtain $x_1 = 2.67(6)[1]$, with a chi-square per degree of freedom of $\chi^2/\text{d.o.f.} = 5.88/7$.

5.5.2 Scaling in the low-temperature phase

Now we consider the scaling of $\epsilon_j(L)$ in the low-temperature phase. This time, we expect, from (5.13),

$$\epsilon_j(L) \simeq AL^{-x_1}, \tag{5.25}$$

with $x_1 = D$.

We have fitted the data for $\beta = 1.2$ (Figure 5.4) and $\beta = 1.4$ (Figure 5.3) to (5.25).[5] The results, in Table 5.3, show a value of x_1 incompatible with

[5]The crossover length L_c which marks the change between the criticality induced by the critical point at T_c ($L < L_c$) and that of the spin glass phase ($L > L_c$) has been computed for different values of β in reference [200]. In particular, we know that $L_c(\beta = 1.2) \simeq 6$ and $L_c(\beta_c = 1.4)) \simeq 2.5$. Hence all the data presented in this section belong to temperatures which lie deep into the spin glass phase. In other words, we can only see the critical effects induced by the spin-glass phase itself, which is critical, not those of the critical point at T_c.

Table 5.3: Scaling of the zeros in the low-temperature phase. For the two considered temperatures ($\beta = 1.2, 1.4$) we first show a fit without corrections to scaling for $L \geq 16$, that is $\epsilon_j(L) \simeq A_j L^{-x_1}$. As explained in Section 5.5.1, this is a global fit for the four zeros, considering their full covariance matrix. We then consider the same fit with corrections to scaling, trying different values for ω (see the text for more details). In all cases x_1 is smaller than the expected value $x_1 = D = 3$.

$L_{\min}$	β	ω	x_1	χ^2/d.o.f.
16	1.4	-	2.842(11)	7.34/7
12	1.4	1	2.57(12)	3.79/7
12	1.4	3	2.79(2)	4.18/7
12	1.4	0.255	2.75(10)	17.6/7
12	1.4	0.39	2.67(9)	14.7/7
12	1.4	0.65	2.55(11)	7.90/7
12	1.4	0.79	2.48(13)	5.03/7
16	1.2	-	2.844(10)	2.89/7
12	1.2	1	2.82(5)	10.5/7
12	1.2	3	2.84(2)	6.90/7
12	1.2	0.255	2.80(10)	12.3/7
12	1.2	0.39	2.80(12)	11.9/7
12	1.2	0.65	2.81(10)	11.3/7
12	1.2	0.78	2.81(8)	11.0/7

$x_1 = D = 3$. We have also included corrections to scaling, using both $\omega = 1$ (Goldstone-like correction) [214] and $\omega = 3$ (Ising ordered correction) [214], $\omega = y = 0.255$ (droplet) [215, 216, 217], $\omega = \theta(0) = 0.39$ (replicon and also $1/\hat{\nu}$ which controls the scaling correction of $q_{\rm EA}(L)$ [201]), $\omega = 0.79 = 2\theta(0)$ (twice the replicon [201]) and $\omega = 0.65 = \theta(q_{\rm EA})$ [201] but in neither case is the asymptotic $x_1 = D$ behavior recovered (see Table 5.3). In addition, we have forced the fits with $x_1 = 3$ and leaving free ω and the statistical quality of the fits was bad.

The origin of this discrepancy with the standard theory can be understood using Eq. 5.9. Notice from this equation that the scaling of the zeros depends strongly on the behavior of the non-connected spin glass susceptibility, so only with a divergence of this observable as the volume, we can recover $x_1 = 3$. However, for these two temperatures ($\beta = 1.2$ and 1.4) this is not the case (see Fig. 5.5). Notice that $\overline{\langle q^2 \rangle} = \chi/V$ has not reached the plateau asymptotic value[6]: Hence at these temperatures the spin-glass susceptibility

[6]In a spin glass phase, both the droplet as the RSB theory predict power law corrections

does not yet diverge as the volume.

5.5.3 Behavior of the integrated density of zeroes

We will start our analysis of the integrated density of zeros by plotting this density at the critical point in Fig.5.6. One can see that the largest lattices follow a pure power law as predicted by the theory. The slope, on a log-log scale, of this straight line should correspond with an exponent a_2. Fitting only the $L = 32$ points we obtain $a_2 = 1.16(2)$ in good agreement with the theory $a_2 = 1.116(2)$ (using Eq. 5.21 and $\eta = -0.375(10)$). To obtain this figure we have discarded in the fit the first zero.[7]

For large L we should expect a good collapse of all points in the same power law curve: the non collapsing part (small L in the figure) is due to the presence of scaling corrections (which we also found in the previous sections).

Now we will check the theoretical predictions for the integrated density of zeros in the broken phase, which predict a linear behavior in the perturbing parameter ϵ. Notice that in our case the margins between the critical point and the broken phase are tight since in the infinite volume limit we will see a behavior $\epsilon^{1.116}$ at the critical point which changes just below T_c to ϵ (of course, this is due to the value of the η exponent).

In Figs 5.7 and 5.8 we show that the data nearly follow a linear behavior of the integrated density deep in the spin glass phase (more concretely at $\beta = 1.2$ and $\beta = 1.4$), in particular for $L \geq 24$. The non-collapsing part of the curve is produced by the presence of scaling corrections as at the critical point.

However, it is easy to show that if the zeros do not follow (for the lattice sizes simulated), in the broken phase, a scaling as the inverse of the volume, then the integrated density of zeros does not follow exactly a linear behavior,

on the lattice size, so the approach to the infinite volume values is really slow.

[7] This phenomenon has been previously found in the literature. For example, the authors of [208] studied the anisotropic Ising model at the critical point and found a different behavior of the first zero in the study of the integrated density. This model shows a spreading distribution of the zeros in the fugacity complex plane. The authors suggest that the effect of this spreading distribution of the zeros is modifying the behavior of the first zero. We have not computed the complete distribution of the complex zeros (only in the straight line $i\epsilon$), nevertheless, we know from reference [197] that the zeros spread in the magnetic field complex plane, so it is quite natural to assume that we will have a similar (spreading) spatial distribution of the zeros in ϵ. Another possible explanation is that the behavior of the integrated density of zeros as j/L^3 is only asymptotic. These anomalies affect only the lower order zeros. Notice that this phenomenon affects only to the pre-factor of the power law of the smallest zeros. We have seen in subsection 5.5.1 that the first zero scales with the right power law. We thank R. Kenna for interesting comments regarding this behavior.

since $a_2 = D/x_1$. We have discussed at the end of Sec. 5.5.2 that this lack of $1/V$ behavior is related to a susceptibility that is not yet diverging as the volume.

In sec. 5.5.2 we have found an exponent $x_1 = 2.842(11)$ for $\beta = 1.2$ and $x_1 = 2.844(10)$ for $\beta = 1.4$, which implies that $a_2 = 1.056(4)$ and $a_2 = 1.055(3)$ for $\beta = 1.2$ and $\beta = 1.4$ respectively.

In Fig. 5.9 we show the behavior of the integrated density of zeros computed for our largest lattice ($L = 32$) and lowest temperature, ($\beta = 1.4$). Notice the points are not lying on a straight line. A fit to $a_1\epsilon^{a_2}$ works well, with a_2 consistent with the value computed from x_1 ($a_2 = 1.068(10)$). So we have obtained, numerically, $a_2 = 1.16(2)$, at the critical point which has changed to 1.068(10) in the broken phase.[8]

In this situation, we cannot compute the order parameter directly from the linear behavior of the integrated density since we are not observing a fully linear behavior. Hence, we confront our numerical data for $G(\epsilon)$ against the theoretical prediction for really small ϵ, which is $G(\epsilon) = (\beta q_{\rm EA}/\pi)\epsilon$. It is interesting to note (see Refs. [207] and [214]) that we can recover the exact slope for a given lattice size if we substitute the value of the order parameter computed for this lattice size. We have followed this advice, and we show in Figs. 5.11 and 5.12 our data for $G(\epsilon)$ at $\beta = 1.2$ and 1.4 showing $L = 32$ data. In addition we have plotted the asymptotic slope using the order parameter ($q_{\rm EA}$) computed for $L = 32$ lattices for these two temperatures in Ref. [200]. Notice that we have a slow approach to the right slope, but also that the overall picture seems to be correct.

In order to gain a better understanding of this effect, we have computed the density of zeros not with the average of the sample zeros but with the median of the probability distribution of the zeros.[9]

We show in Fig. 5.10 the histogram of the 1000 first zeros computed on the $L = 32$ lattice at $\beta = 1.4$. Notice from this figure the asymmetry of the histogram and the presence of events at large values of the zeros (which induces a large and strongly fluctuating value of the mean).

One can see in Figs. 5.11 and 5.12 that the median data produce an improved scaling, compared with those obtained from the mean, when comparing the data with the analytical prediction (slope provided by $q_{\rm EA}$).

For the sake of completeness, we can cite that the integrated density of

[8] We can do the same analysis with the x_1 exponent: we have obtained at the critical point $x_1 = 2.67(7)$, which should change in the broken phase to $x_1 = 3$, although we actually see with our numerical data $x_1 = 2.842(11)$.

[9] The probability distributions one usually finds in disordered systems present long tails due the presence of rare events, hence, the study of the median of this kind of distributions is also very useful (see for example [218, 213]).

zeros using the medians does not behave completely linearly but with a law $\epsilon^{1.06(2)}$ (for $\beta = 1.4$).

5.6 Conclusions

By studying the complex singularities linked with the overlap we have obtained a clear picture of the critical region and of the low temperature phase fully compatible with that obtained by other more standard approaches.

In particular, we have studied the behavior of the individual zeros as well as the integrated density at the critical point. In both cases we have obtained good values for the η exponent and we have seen that the data are compatible with the corrections to scaling published in the literature [212].

Finally, we have checked the scaling laws in the spin-glass phase, obtaining strong scaling corrections as found previously [200]. In addition we have obtained, by monitoring the behavior of the integrated density, a compatible picture using the zeros with that obtained from the order parameter of the model ($q_{\rm EA}$) computed in finite volumes with standard methods. We have also shown that the use of the median instead of the mean improves the overall picture.

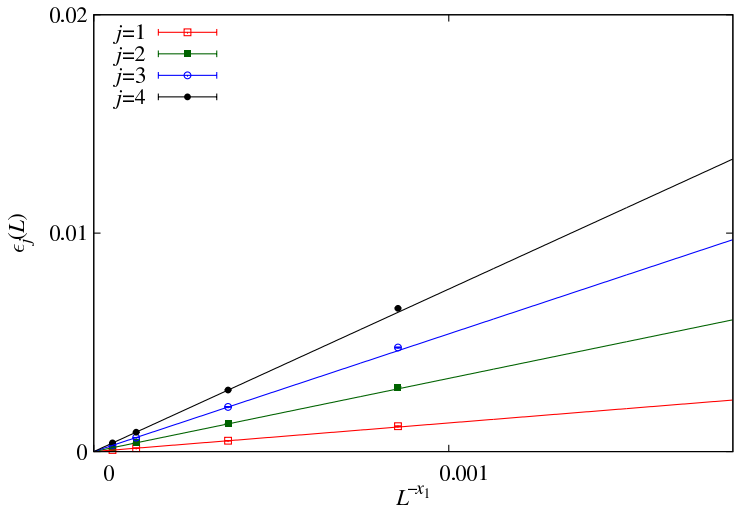

Figure 5.3: Scaling of the zeros at $\beta = 1.4$, with a best fit to (5.25) for $L \geq 16$. We obtain $x_1 = 2.842(11)$, with $\chi^2/\text{d.o.f.} = 7.34/7$.

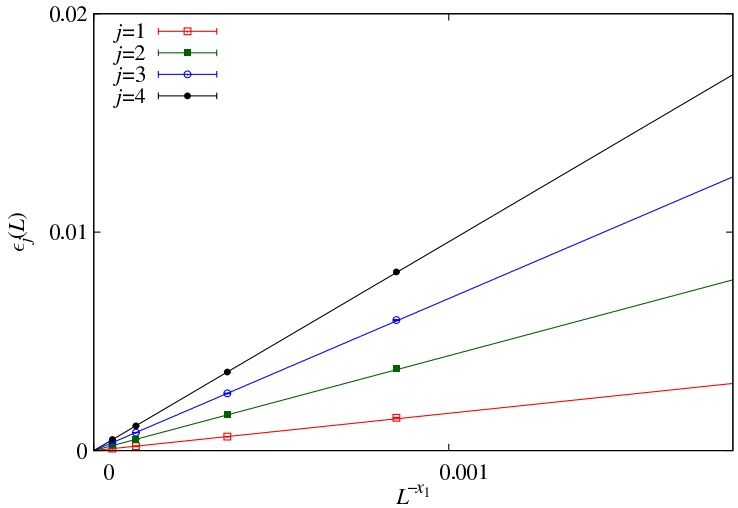

Figure 5.4: Scaling of the zeros at $\beta = 1.2$, with a best fit to (5.25) for $L \geq 16$. We obtain $x_1 = 2.844(10)$, with $\chi^2/\text{d.o.f.} = 2.89/7$.

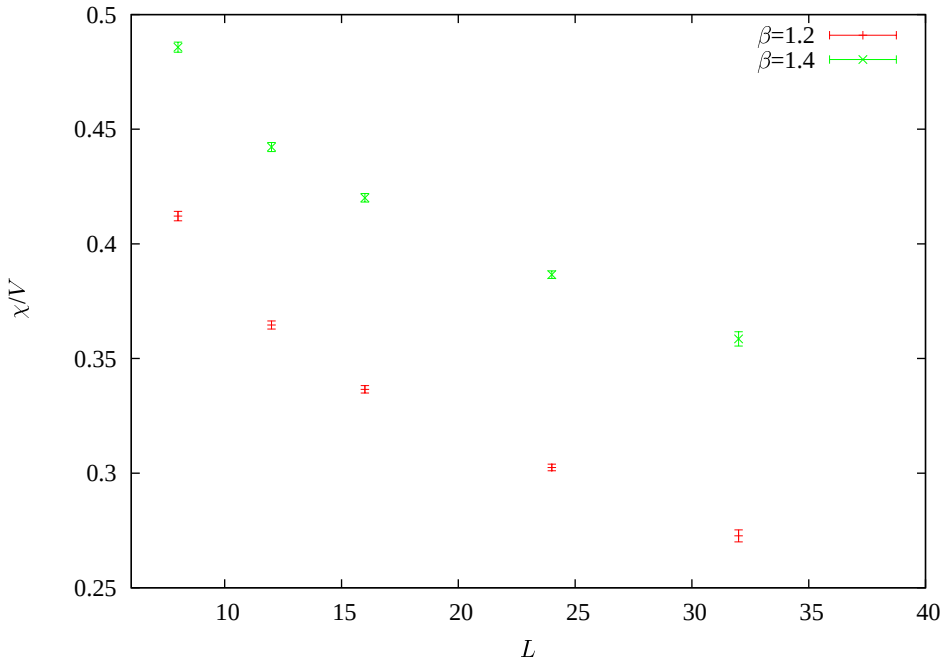

Figure 5.5: $\chi/V = \overline{\langle q^2 \rangle}$ versus the lattice size for $\beta = 1.2$ and 1.4. Notice that none of the temperatures have reached the plateau asymptotic value.

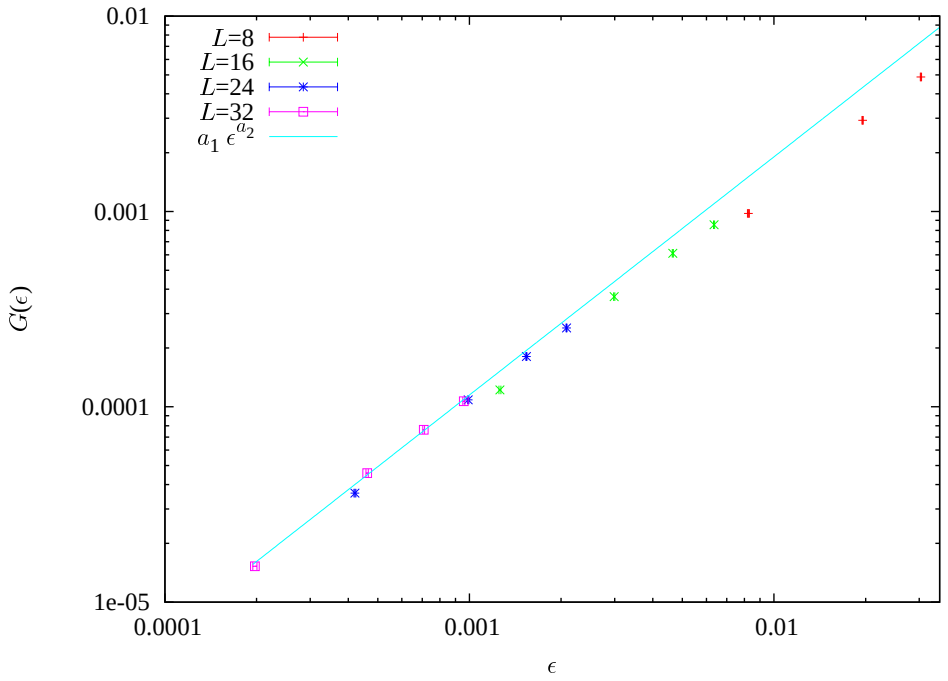

Figure 5.6: Integrated density of zeros versus the zeros at the critical point. $a_2 = 1.16(2)$.

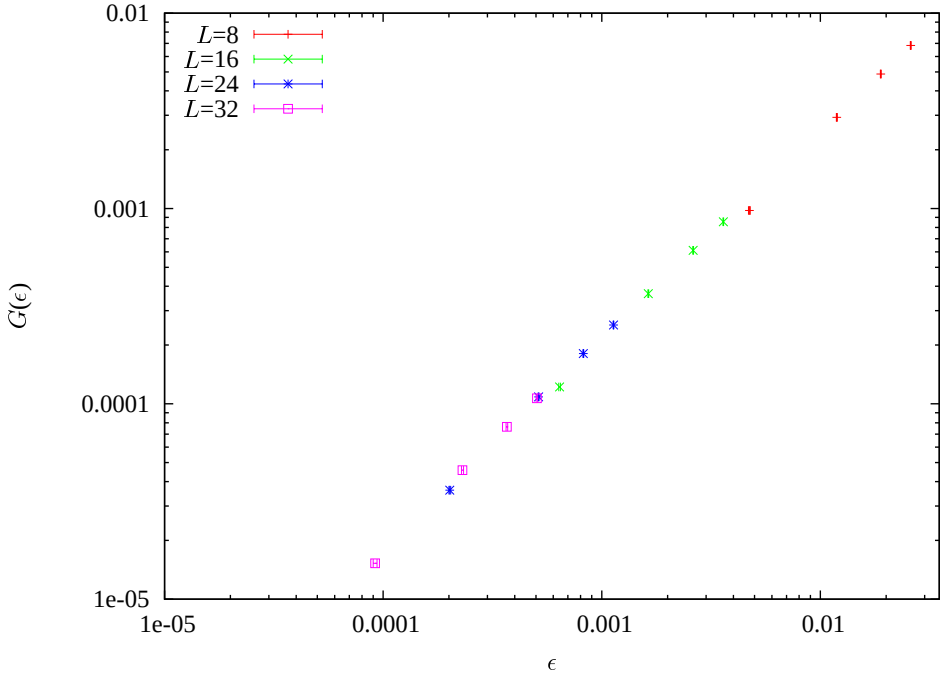

Figure 5.7: Integrated density of zeros versus the zeros for $\beta = 1.2$.

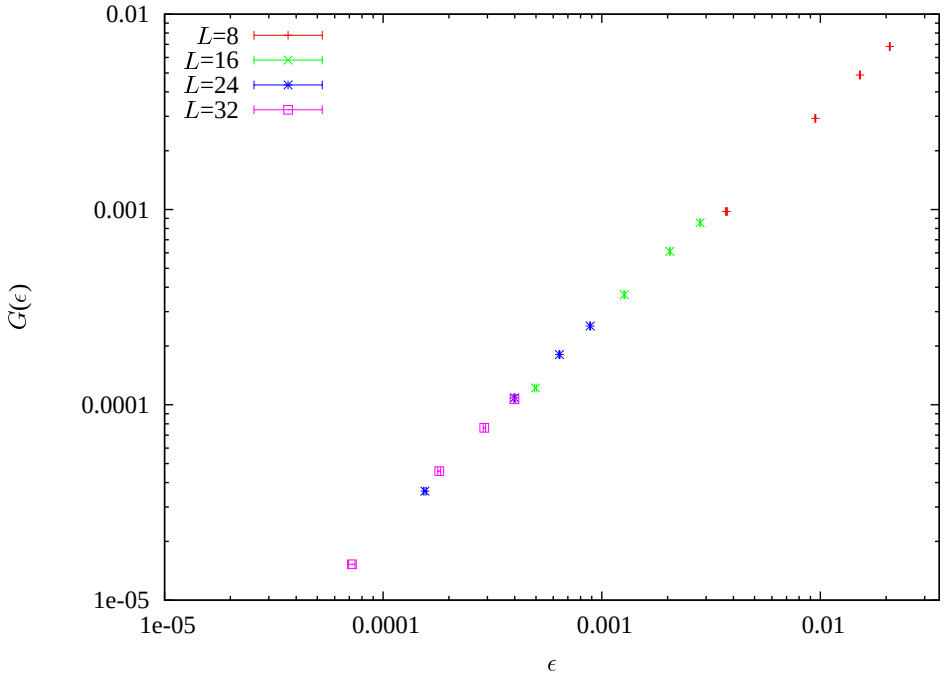

Figure 5.8: Integrated density of zeros versus the zeros at $\beta = 1.4$.

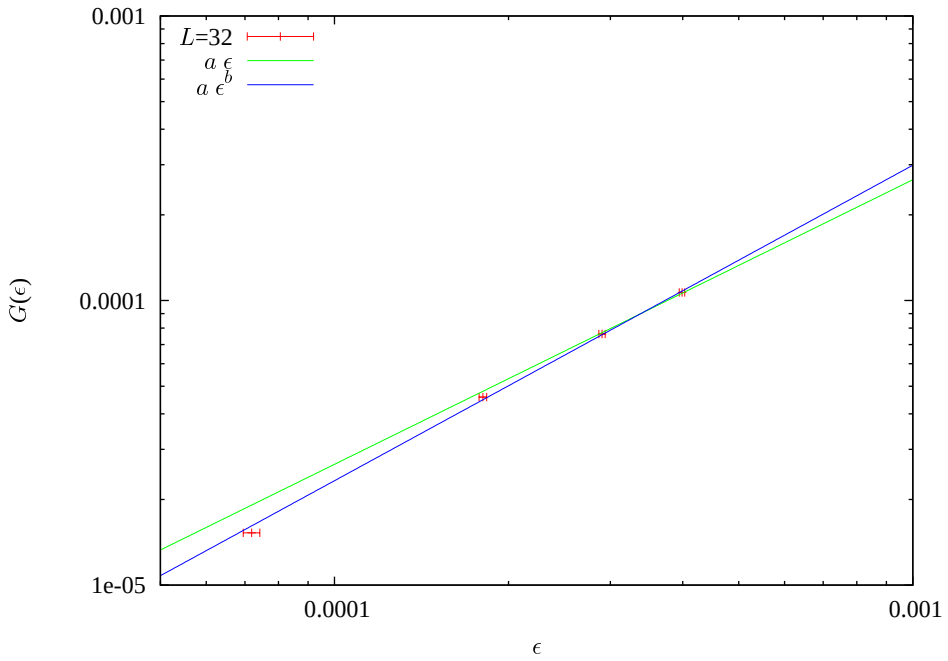

Figure 5.9: Integrated density of the zeros, for the largest lattice $L = 32$ and the lowest temperature $\beta = 1.4$. Notice that we are almost, but not in, the linear regime. The data are well fitted with $b = 1.068(10)$.

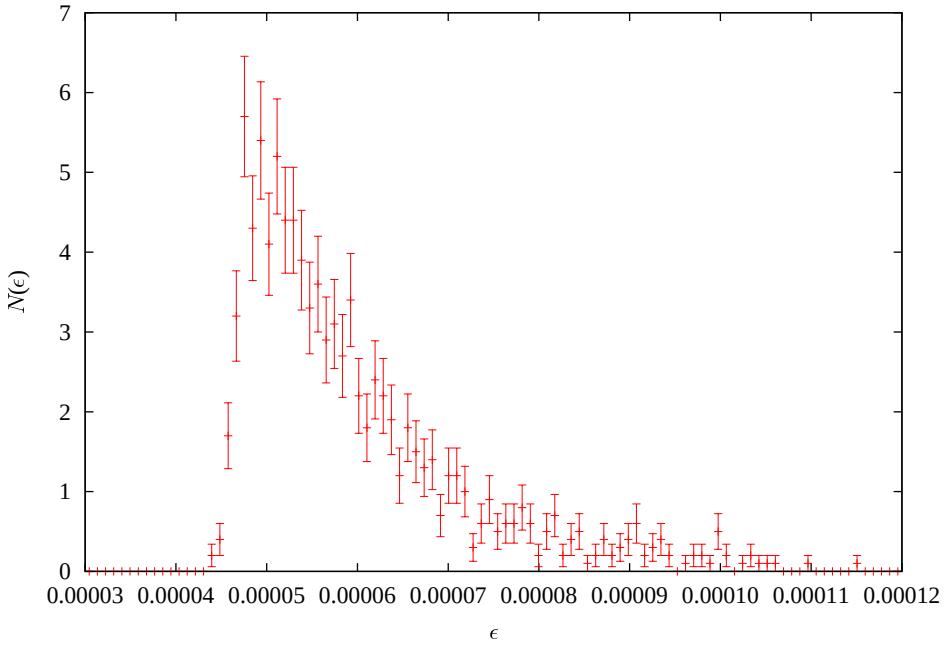

Figure 5.10: Histogram ($N(\epsilon)$ versus ϵ) for the 1000 first zeros computed for $L = 32$ and $\beta = 1.4$. Notice the lack of symmetry of the histogram and the presence of events for large values of the zeros.

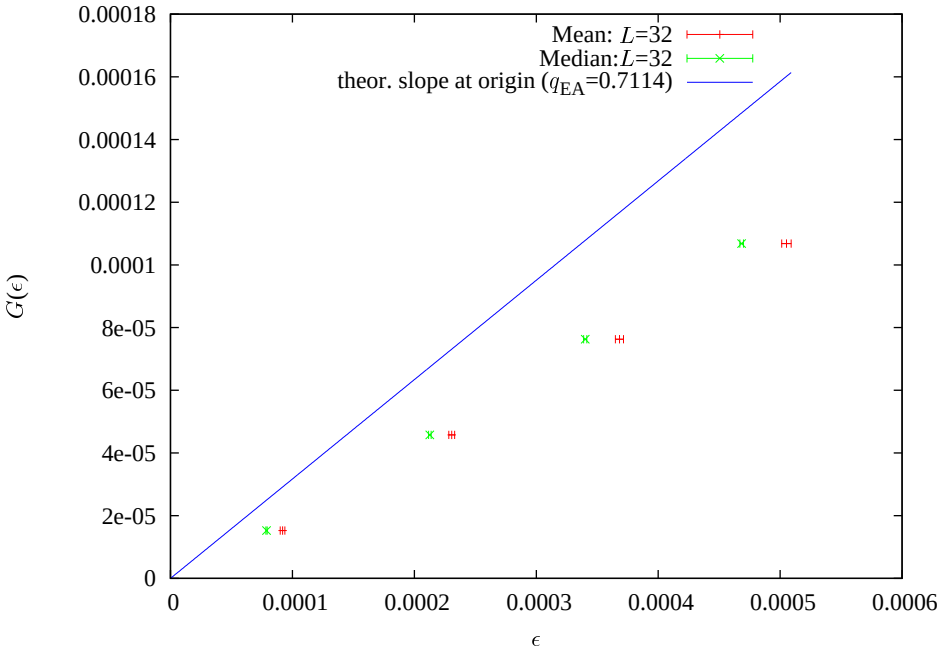

Figure 5.11: Integrated density of the zeros, for the largest lattice $L = 32$ and temperature $\beta = 1.2$ using the average of zeros. We have also plotted the median values. We have marked the expected slope at the origin, using the Edwards-Anderson order parameter computed in Ref. [200] for the $L = 32$ lattice.

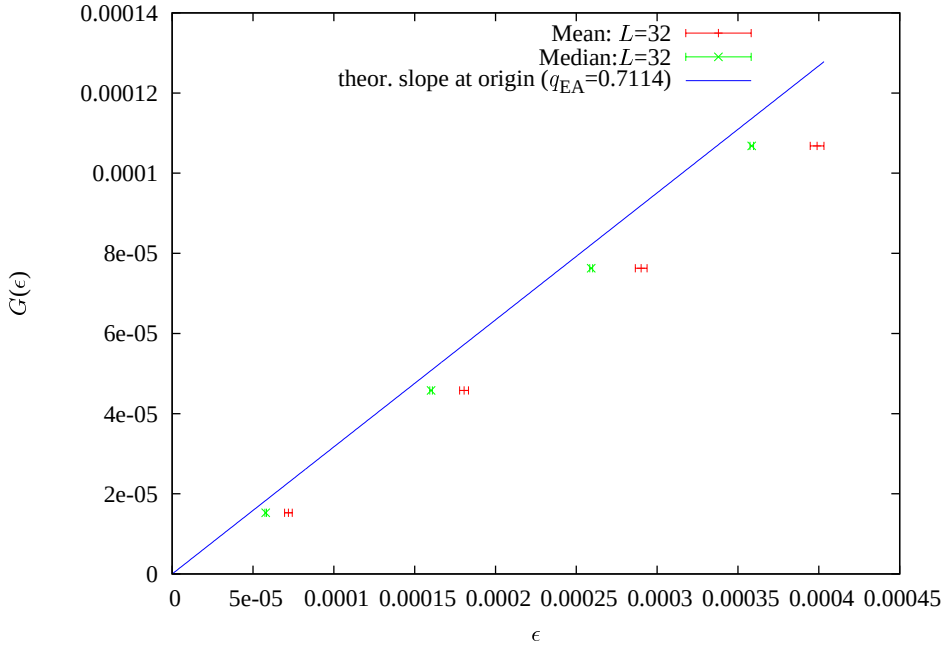

Figure 5.12: Integrated density of the zeros, for the largest lattice $L = 32$ and lowest temperature $\beta = 1.4$ using the average of zeros. We have also plotted the median values. We have marked the expected slope at the origin, using the Edwards-Anderson order parameter computed in Ref. [200] for the $L = 32$ lattice.

Chapter 6

Rejuvenation and memory

6.1 Introduction

One of the most interesting properties of the spin glasses is the aging, that is, the behavior of the system at low temperatures depends on the history of that system. Therefore, one can perform experiments where the temperature is kept constant or experiments where one changes the temperature. The aging at constant temperature arises in experiments that studies the thermoremanent magnetization (TRM) and the zero-cooled magnetization (ZFC) (see, for example, Refs. [10, 11, 12]). In experiments to study the TRM, one cools the spin glass up to a temperature, T, below its glass temperature, T_c, in presence of an external magnetic field, then one let the system evolves a time t_w and then one switches off the magnetic field. In experiments to study the ZFC the algorithm is different, one cools the system without an external magnetic field and switches it on after a time t_w at a temperature below its critical temperature.

However, in this chapter we will focus on experiments where the temperature is not kept constant. Then, rejuvenation and memory are the most relevant aging phenomena. To understand them, let us imagine the easiest experiment, a two temperatures (both below the glass temperature of the system) algorithm. Let be the system at temperature T_1 and, after a time t_s at this temperature, we change the temperature to a smaller one, T_2. Then, one can observe that the relaxation of some observables like the susceptibility, χ, is similar to the one that a system that had be cooled directly from a temperature higher than T_c to this T_2. This effect is the so-called rejuvenation. If one gets back the system to the temperature T_1, one does not observe this effect, but the susceptibility restart its relaxation where it left when the temperature was changed before. This effect is the memory. The

dip experiment shows these two effects very clear.

In the dip experiment, one decreases the temperature of the system at a constant rate but with several stops, that is, at several temperatures one spends a longer time. Then one increases the temperature at the same rate but without any stop. Experiments with this algorithm usually show spectacular evidences of rejuvenation and memory. For example, in references [219, 220] exp rformed and in Figures 6.1 mory effects.

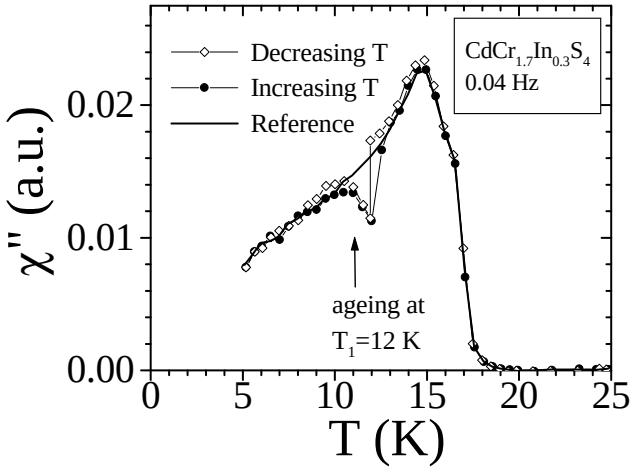

Figure 6.1: Susceptibility versus the temperature. Solid line is the reference one (without any stop). Open diamonds mark measurements while decreasing temperature with a stop at 12 K during 7h. Solid circles mark measurements increasing the temperature. The rate of the change of the temperature is 0.1 K/min. Figure from reference [219].

However, simulations have not been so successful so far perhaps due to the fact that simulation computers are not powerful enough.

6.2 Model, observables and simulation details

We performed simulations of Edwards-Anderson model

$$H = \sum_{<i,j>} J_{ij}\sigma_i\sigma_j \tag{6.1}$$

without an external magnetic field. J_{ij} are bimodal quenched random couplings.

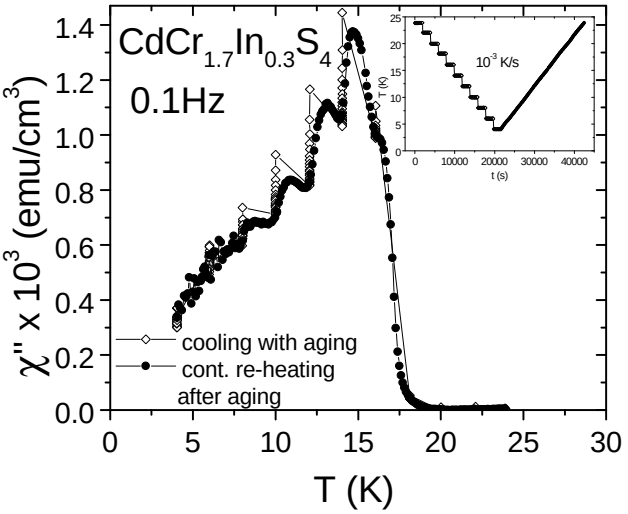

Figure 6.2: Susceptibility versus the temperature. In this figure, the stops are of 30 min. Figure from Ref. [220].

We measure the two times correlation function

$$C(t_w, t_w + t_0) = \frac{1}{V} \sum_i \langle \sigma_i(t_w) \sigma_i(t_w + t_0) \rangle \tag{6.2}$$

to calculate the real part of the susceptibility, which is, according to Fluctuation-Dissipation Theorem,

$$\chi(\omega = \frac{2\pi}{t_0}, t_w) \approx \frac{[1 - C(t_w, t_w + t_0)]}{T} \tag{6.3}$$

We also measure the coherence length, computed from the C_4 correlation function

$$C_4(\mathbf{r}, t_w) = \frac{1}{V} \overline{\sum_{\mathbf{x}} q_{\mathbf{x}}(t_w) q_{\mathbf{x}+\mathbf{r}}(t_w)} \tag{6.4}$$

$$\xi_{k,k+1}(t_w) \equiv \frac{I_{k+1}(t_w)}{I_k(t_w)} \propto \xi(t_w) \tag{6.5}$$

where

$$I_k(t_w) \equiv \int_0^{L/2} dr \; r^k C_4(r, t_w) \tag{6.6}$$

We have simulated three dimensional cubic lattices, with linear size $L = 256$ in the Janus dedicated computer (see appendix A), using parallel computation and a whole board of Janus for every sample. In the dip experiment we have simulated 64 samples with $T_{\max} = 2.015$, $T_{\min} = 0.575$ and only one

stop $T_{\text{stop}} = 0.775$. The system spent $781248 = (2 \cdot 5^8 - 2)$ MCS on every temperature but a 125 times longer time at T_{stop}. In the two temperatures experiment, we have performed simulations of 32 samples at $T = 0.9$ and $T = 0.8$.

6.3 Numerical results

6.3.1 Dip experiment

In Figures 6.3 and 6.4 one can observe the behavior of the susceptibility at a set value of t_0. However, rejuvenation and memory do not appear.

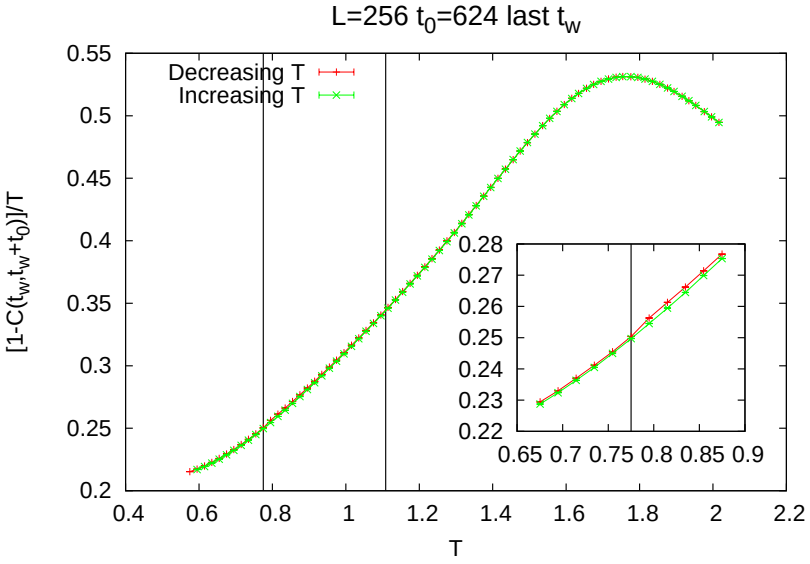

Figure 6.3: Susceptibility at $t_0 = 624$ and maximum t_w vs temperature.

We have also studied the coherence length, but the results are not better. In Figures 6.5 and 6.6 one can observe the coherence length of this experiment. It is quite clear that the system does not evolve enough to show up aging characteristics.

6.3.2 Two temperatures experiment

Finally, we have also studied the coherence length in a two temperatures protocol. Besides, references simulations at fixed temperatures have also been performed. The behaviour of the system, as can be observed in Figures 6.7 and 6.8, is the expected one: when the temperature is changed, the

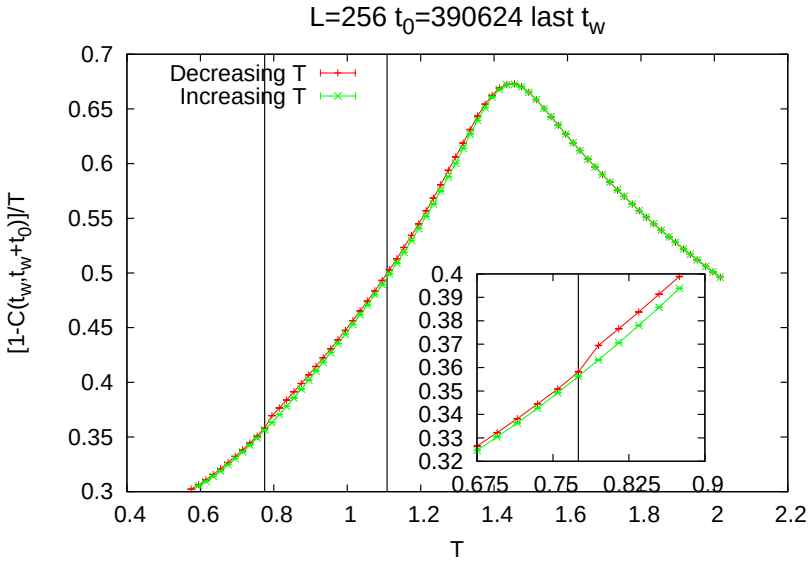

Figure 6.4: Susceptibility at $t_0 = 390624$ and maximum t_w vs temperature.

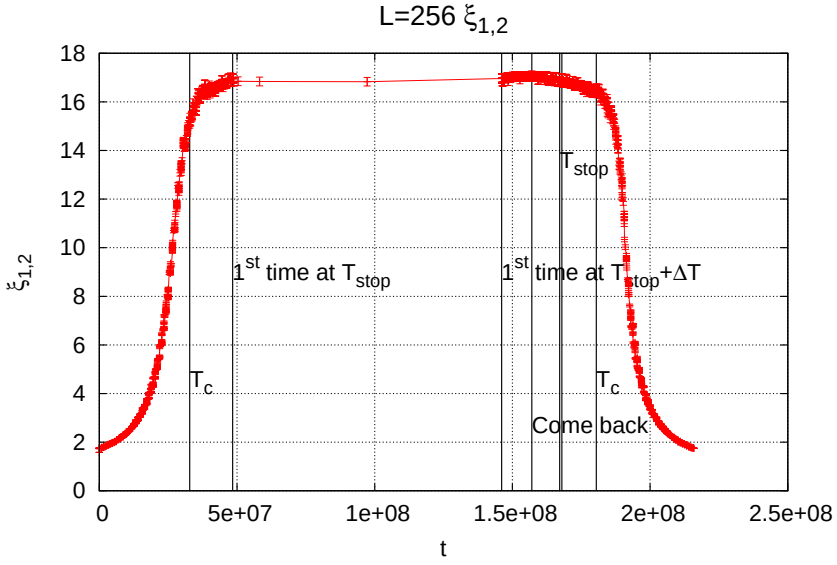

Figure 6.5: Coherence length versus t.

evolution of the coherence length tend to converge to the evolution at a fixed temperature. One also expect a decreasing of the coherence length when the temperature is changed due to chaos, which would indicate rejuvenation phenomenon. However, no evidence of a decreasing of the coherence length have been detected.

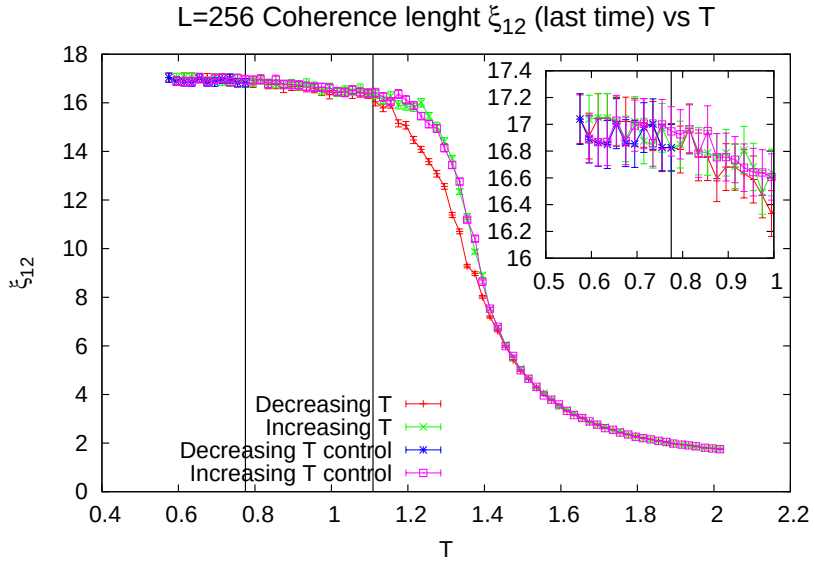

Figure 6.6: Coherence length (at the largest t_w in every temperature) versus temperature.

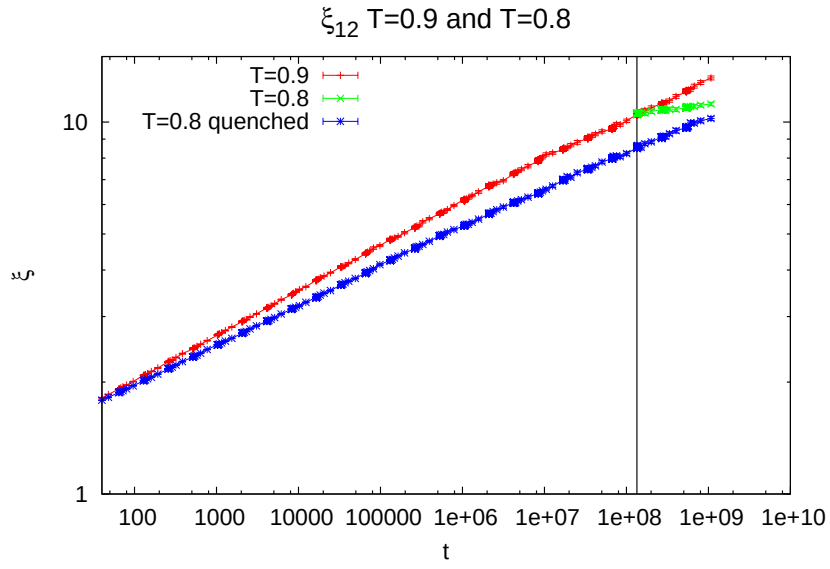

Figure 6.7: Coherence length versus t. Simulations of the same samples at fixed temperatures $T = 0.9$ and $T = 0.8$ are also plotted.

6.3.3 Conclusions

We have not manage to reproduce the dip experiment, even using the Janus machine and simulating lattices up to $L = 256$. Therefore, rejuvenation and

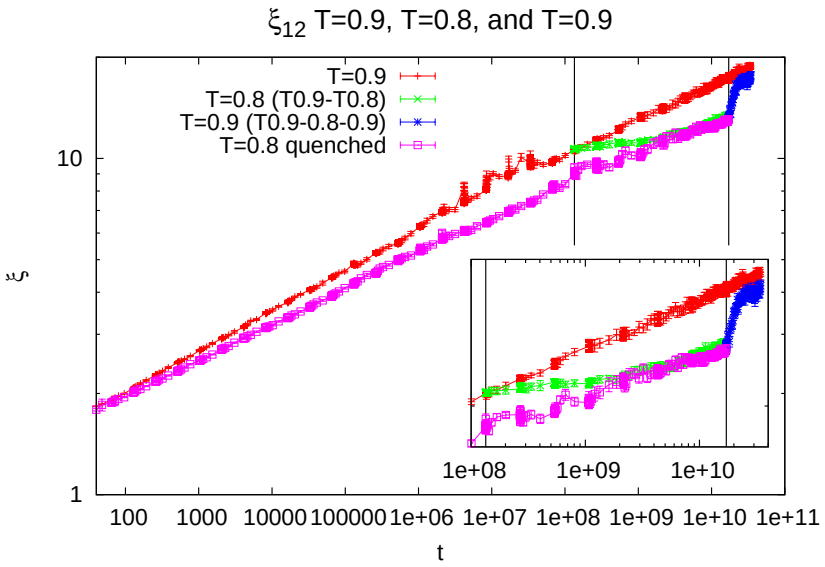

Figure 6.8: Coherence length versus t. Simulations of the same samples at fixed temperatures $T = 0.9$ and $T = 0.8$ are also plotted.

memory effects have not been detected in a protocol with several changes of temperature. The study of the coherence length has not shown better results, although it showed us that the system seemed to not evolve enough to show up aging effects, so it suggests us that we would need more powerful simulations to simulating dip experiment.

Chapter 7

Other researches in the Janus collaboration

7.1 Introduction

In the previous chapters are explained the works which form the main research task in this thesis. Besides, I have also worked in other researches of the Janus Collaboration since I joint the group in 2009. In the following, I will introduce a brief summary of these works:

- F. Belletti, A. Cruz, L. A. Fernandez, A. Gordillo-Guerrero, M. Guidetti, A. Maiorano, F. Mantovani, E. Marinari, V. Martin-Mayor, J. Monforte, A. Muñoz Sudupe, D. Navarro, G. Parisi, S. Perez-Gaviro, J. J. Ruiz-Lorenzo, S. F. Schifano, D. Sciretti, A. Tarancon, R. Tripiccione and D. Yllanes, *J. Stat. Phys.* **135**, 1121 (2009). Eprint: arXiv:0811.2864. *"An in-depth look at the microscopic dynamics of Ising spin glasses at fixed temperature"*.

- R. Álvarez Baños, A. Cruz, L. A. Fernandez, J. M. Gil-Narvion, A. Gordillo-Guerrero, M. Guidetti, A. Maiorano, F. Mantovani, E. Marinari, V. Martin-Mayor, J. Monforte-Garcia, A. Muñoz Sudupe, D. Navarro, G. Parisi, S. Perez-Gaviro, J. J. Ruiz-Lorenzo, S. F. Schifano, B. Seoane, A. Tarancon, R. Tripiccione and D. Yllanes, *J. Stat. Mech.* P06026 (2010). Eprint: arXiv:1003.2569. *"Nature of the spin-glass phase at experimental length scales"*.

- R. Álvarez Baños, A. Cruz, L. A. Fernandez, J. M. Gil-Narvion, A. Gordillo-Guerrero, M. Guidetti, A. Maiorano, F. Mantovani, E. Marinari, V. Martin-Mayor, J. Monforte-Garcia, A. Muñoz Sudupe, D.

Navarro, G. Parisi, S. Perez-Gaviro, J. J. Ruiz-Lorenzo, S. F. Schifano, B. Seoane, A. Tarancon, R. Tripiccione and D. Yllanes, *Phys. Rev. Lett.* **105**, 177202 (2010). Eprint: arXiv:1003.2943. *"Static versus dynamic heterogeneities in the $D = 3$ Edwards-Anderson-Ising spin glass"*.

- R. Álvarez Baños, A. Cruz, L. A. Fernandez, J. M. Gil-Narvion, A. Gordillo-Guerrero, M. Guidetti, D. Iñiguez, A. Maiorano, E. Marinari, V. Martin-Mayor, J. Monforte-Garcia, A. Muñoz Sudupe, D. Navarro, G. Parisi, S. Perez-Gaviro, J. J. Ruiz-Lorenzo, S. F. Schifano, B. Seoane, A. Tarancon, P. Tellez, R. Tripiccione and D. Yllanes, *PNAS* **109** 6452 (2012). Eprint: arxiv:1202.5593. *"Thermodynamic glass transition in a spin glass without time-reversal symmetry"*.

- M. Baity-Jesi, R. A. Baños, A. Cruz, L. A. Fernandez, J. M. Gil-Narvion, A. Gordillo-Guerrero, M. Guidetti, D. Iñiguez, A. Maiorano, F. Mantovani, E. Marinari, V. Martin-Mayor, J. Monforte-Garcia, A. Muñoz Sudupe, D. Navarro, G. Parisi, M. Pivanti, S. Perez-Gaviro, F. Ricci-Tersenghi, J. J. Ruiz-Lorenzo, S. F. Schifano, B. Seoane, A. Tarancon, P. Tellez, R. Tripiccione and D. Yllanes, *Eur. Phys. J. Special Topics* **210**, 33 (2012). *"Reconfigurable computing for Monte Carlo simulations: Results and prospects of the Janus project"*.

7.2 An In-Depth View of the Microscopic Dynamics of Ising Spin Glasses at Fixed Temperature

In this work (published in J. Stat. Phys **135**, 1121, 2009) a detailed study of the non-equilibrium dynamics of the three dimensional Ising spin glass model has been performed. Thanks to the use of Janus, simulations of up to 10^{11} MCS have been executed, which is an impressive value that approaches us to real experiments (remind that 1 MCS $\sim$ 1 ps, so 10^{11} MCS correspond to 0.1 seconds in real world). Simulations at different temperature have been performed and in table 7.1 is a summary of the simulation details of these simulations.

We will emphasize some of the observables studied in the work. Firstly, besides the usual correlation functions, we will define the two-time, two-site correlation function

$$C_{2+2}(\mathbf{r}, t, t_w) = \overline{\frac{1}{N}\sum_{\mathbf{x}} \left[c_{\mathbf{x}}(t, t_w) c_{\mathbf{x}+\mathbf{r}}(t, t_w) - C^2(t, t_w)\right]} \tag{7.1}$$

L	T	MC steps	N_s
80	0.6	10^{11}	96
80	0.7	10^{11}	63
80	0.8	10^{11}	96
80	0.9	2.8×10^{10}	32
80	1.1	4.2×10^{9}	32
80	1.15	2.8×10^{10}	32
80	0.7	10^{10}	768
40	0.8	2.2×10^{8}	2218

Table 7.1: Simulation details. N_S means the number of simulated samples.

With this function heterogeneous dynamics can be studied.

Moreover, bounds to q_{EA} are also computed with the stationary part, $C_\infty(t)$ of the two times correlation function $C(t, t_w)$:

$$0.62 \leq q_{\mathrm{EA}}(T = 0.6) \leq 0.733 \tag{7.2}$$

$$0.474 \leq q_{\mathrm{EA}}(T = 0.7) \leq 0.637 \tag{7.3}$$

$$0.368 \leq q_{\mathrm{EA}}(T = 0.8) \leq 0.556 \tag{7.4}$$

Finally, the thermoremanent magnetization can be studied with the two times correlation function, $C(t, t_w)$, in fact, when $t \gg t_w$ to a fixed value of t_w, then both can be identified. The results obtained are compatible with experimental ones.

7.3 Nature of the spin-glass phase at experimental length scales

In this work (published in J. Stat. Mech. P06026 (2010): [230]) a detailed study of the equilibrium spin glass phase is performed. Besides, in Ref. [229] and in this work the thermalization test explained in Section E.2.2 was developed.

The probability distribution of the overlap has been studied to distinguish whether the system behaves as a droplet or as in RSB solution. In Figures 7.1 and 7.2 this probability distribution of the overlap is plotted for several sizes. Notice that the curves near $q \sim 0$ have a plateau (different sizes curves converge in this region) where $P(q) > 0$. This result supports the RSB scenario.

With this quantity one can also compute q_{EA}. At temperature $T = 0.703$ one finds that $q_{\mathrm{EA}} = 0.538[11](6)$ and at temperature $T = 0.805$ one finds

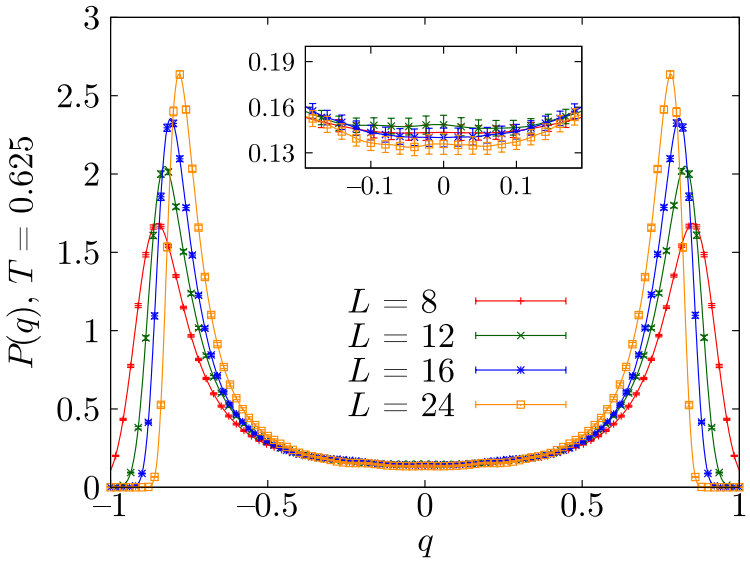

Figure 7.1: Probability distribution of the overlap at temperature T=0.625 Figure from J. Stat. Mech. P06026 (2010) [230].

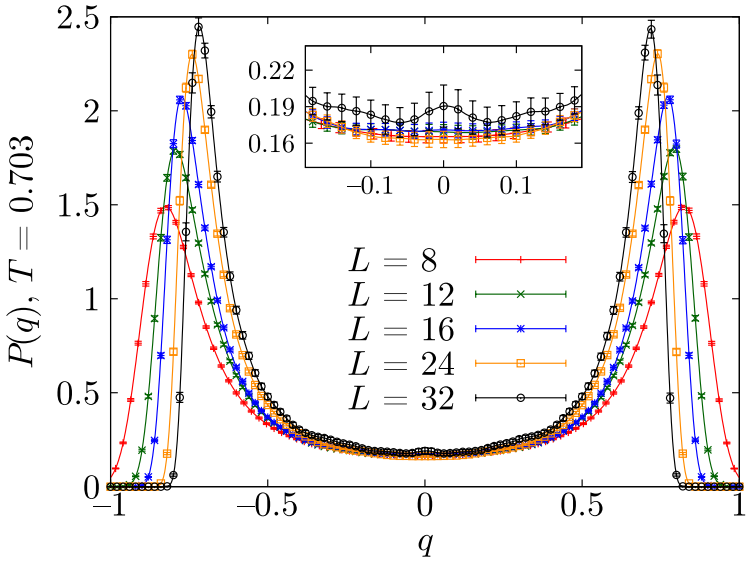

Figure 7.2: Probability distribution of the overlap at temperature T=0.703 Figure from J. Stat. Mech. P06026 (2010) [230].

that $q_{\mathrm{EA}} = 0.447[12](6)$. These values agree with the bounds from Eqs. (7.2), (7.3) and 7.4).

Another way to check which scenario holds in the spin glass phase is

studying the Binder cumulant

$$B(T) = \frac{\overline{\langle q^4 \rangle}}{\overline{\langle q^2 \rangle}^2} \tag{7.5}$$

In droplet scenario one expects that the Binder cumulant behaves like

$$B(T; L) = 1 + aL^{-\zeta} \tag{7.6}$$

whereas in the RSB scenario, one expects that it behaves like

$$B(T; L) = c + dL^{-1/\hat{\nu}} \tag{7.7}$$

Both fits are quite fine, although the value of ζ is smaller than droplet predicts. Finally, one can build a kind of dictionary to connect non-equilibrium and equilibrium simulations.

7.4 Static versus Dynamic Heterogeneities in the $D = 3$ Edwards-Anderson-Ising Spin Glass

In this work (published in Phys. Rev. Lett. **105** 177202 in 2010), the behavior of the heterogeneities (both static and dynamic ones) of a Ising spin glass with binary nearest-neighbour couplings and periodic boundary conditions at temperature $T = 0.64T_c$ is studied. These heterogeneities are studied using their characteristic length $\zeta(t, t_w)$, computed an integral estimator from the quantity $C_{2+2}(\mathbf{r}, t, t_w)$

The aging of the correlation length of the heterogeneities, $\zeta(t, t_w)$, suggests the existence of a phase transition. We will define the quantity F_q to study it

$$F_q = \hat{C}_4(\mathbf{k}_{\min}|q) \tag{7.8}$$

where $\hat{C}_4(\mathbf{k}_{\min}|q)$ is the Fourier transform at wave vector $\mathbf{k} \neq \mathbf{0}$ of the conditional correlation function C_4 at fixed overlap q. Using finite size scaling one can gets that

$$F_q = L^{D-\theta(q_{\mathrm{EA}})} G(L^{1/\hat{\nu}}(q - q_{\mathrm{EA}})) \tag{7.9}$$

Let be $y = C_4(\mathbf{k}_{\min}|q)$, the exponent of L. In the Figure 7.3, one can observe crossovers in F_q/L^y for a couple of values of y, which shows the existence of a phase transition. Let $q_{L,y}$ be the point where, fixed y, a pairs of curves of lattices (L,$2L$) cross. Computing $q_{L,y}$ for several values of y allows us to calculate $q_{\mathrm{EA}} = 0.52(3)$ and $1/\hat{\nu} = 0.39(5)$

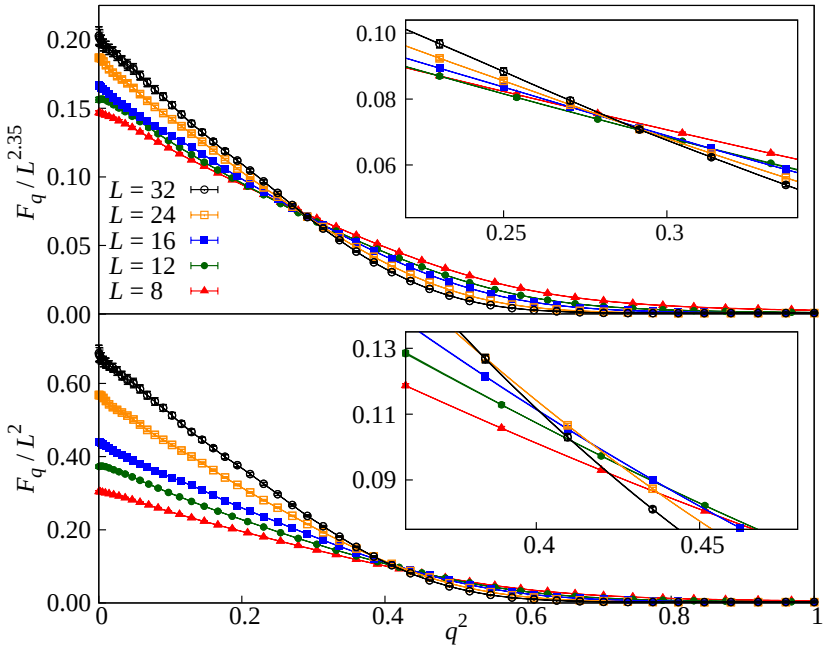

Figure 7.3: Crossovers of F_q/L^y for a couple of values of y: $y = 2.35$ (top) and $y = 2$ (bottom). The insets show in detail the crossing regions. Figure from Phys. Rev. Lett. **105** 177202.

7.5 Thermodynamic glass transition in a spin glass without time-reversal symmetry

One of the main goals in spin glasses is to determine whether the Almeida-Thouless line exists, because RSB scenario predicts that it does exist but droplet scenario does not. In this paper (published in PNAS **109** 6452-6456 in 2012 and in arxiv:1202.5593), a phase transition is searched and found in a four dimensional Ising spin glass in a field. In fact, the RSB scenario holds in the mean field approximation which is valid from infinite dimensions to the upper critical dimension D_U (remind that $D_U = 6$). In this paper, the existence of the phase transition in presence of a magnetic field is shown in four dimensions, which are below the upper critical dimension.

We will define $G(\mathbf{r})$ spatial autocorrelation function, $\hat{G}(\mathbf{k})$ the propagator in Fourier space and ξ_2 the second-moment correlation length computed from an Ornstein-Zernike expansion truncated in the quadratic term in k. The usual way to search phase consists in studying whether ξ_2/L has some intersections for different sizes L. In this case, any intersection takes place (as one can observe in the top panel of Figure 7.4), so it seems that the phase

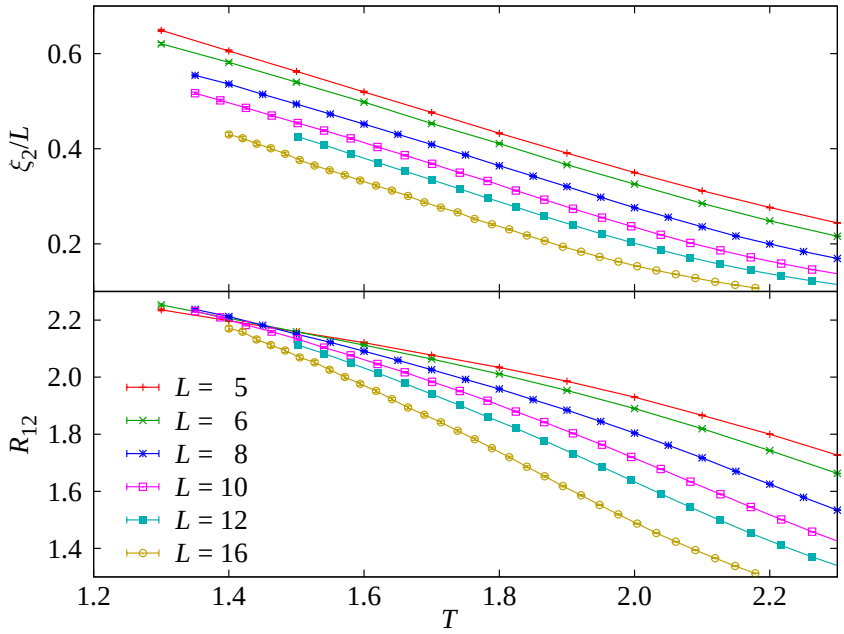

Figure 7.4: Top: plot of the ξ_2 correlation length versus temperature at $h = 0.15$. Any intersection is found. Bottom: plot of R_{12} versus temperature at $h = 0.15$. One can observe now intersections. Figure from PNAS **109** 6452-6456.

transition does not exist. However, this absence of intersections is due to the anomalous behaviour of the propagator in the $\mathbf{k} = 0$ mode (ξ_2 does depend of $\hat{G}(0)$). We will define a new quantity that avoid this $\mathbf{k} = 0$ problem:

$$R_{12} = \hat{G}(\boldsymbol{k}_1)/\hat{G}(\boldsymbol{k}_2), \tag{7.10}$$

where $\mathbf{k}_1 = (2\pi/L, 0, 0)$ and $\mathbf{k}_2 = (0, 2\pi/L, 0)$. Now, in the bottom panel of the figure 7.4 one can observe that intersections does exist, so a phase transition happens. To compute its critical parameters, one has to perform a bit technical analysis where one needs to assume that all the points of the Almeida-Thouless line belong to the same universality class. In the Table 7.2, the critical parameters of a couple of external magnetic fields are shown.

	$h = 0.3$	$h = 0.15$
$T_c(h)$	0.906(40)[3]	1.229(30)[2]
ν	1.46(7)[6]	
η	−0.30(4)[1]	

Table 7.2: Critical parameters for different values of external magnetic fields.

7.6 Reconfigurable computing for Monte Carlo simulations: Results and prospects of the Janus project

Janus is a supercomputer based on FGPA's that has been essential to develop this thesis. This paper (published in Eur. Phys. J. Special Topics **210**, 33 in 2012) is a kind of review of Janus with a brief summary of its scientific results. Using the Heat-Bath (HB) algorithm, one can compute the probability of one spin in the site k be $+1$. It depends only on its nearest neighbours because the difference between $E(\sigma_k = +1)$ and $E(\sigma_k = -1)$ is due to the interactions of the spin in the site k with its nearest neighbours whereas the rest of the sum to compute the energy, E, is exactly the same. Therefore, this probability is

$$P(\sigma_k = +1) = \frac{e^{-E(\sigma_k=+1)/T}}{e^{-E(\sigma_k=+1)/T} + e^{-E(\sigma_k=-1)/T}} = \frac{e^{\phi_k/T}}{e^{\phi_k/T} + e^{-\phi_k/T}} \tag{7.11}$$

which can be identify as a local field

$$\phi_k = \sum_m J_{km}\sigma_m \tag{7.12}$$

where m means the nearest neighbours of the site k. Therefore, to update a spin k using HB algorithm, one should compute this probability, generate a random number uniformly distributed in $[0, 1]$ and, then, choose the spin $\sigma_k = +1$ if the random number is smaller than $P(\sigma_k = +1)$ or $\sigma_k = -1$ if the random number is bigger than $P(\sigma_k = -1)$. Besides, one has to deal with all the spins of the whole lattice to complete a Monte Carlo Step (MCS). Fortunately, several characteristics of these operations (that one has to compute to perform a MCS) allow us to accelerate the simulation. The local field can only take several values, so one can compute them at the beginning of the simulation and store them in a look-up table (LUT) in the FPGA where the simulation is performed. Besides, one can deal with binary variables instead of the actual physical ones so one can compute magnitudes like ϕ_k using logical operations instead of arithmetic ones, which are quite faster. For example, let S_k and $\hat{J}_{km}$ be the binary variables of the spin σ_k and the coupling J_{km}. Then

$$S_k = \frac{1 - \sigma_k}{2} \tag{7.13}$$

$$\hat{J}_{km} = \frac{1 - J_{km}}{2} \tag{7.14}$$

$$F_k \equiv \sum_m \hat{J}_{km} \otimes S_m = \frac{(2D - \phi_k)}{2} \tag{7.15}$$

where $\otimes$ means the XOR operation and D is the dimension of the lattice.

Moreover, the simulation can be accelerated with parallelism. The easiest way to perform this parallelism is simulating different samples and replicas of the same sample in different FPGA's. However, parallelism is also useful in a single FPGA, for example, updating several spins at the same time. Let us imagine a chessboard scheme, if one wants to update a spin in a white site, one only needs spins in black sites. Therefore, one can store all the white sites of a lattice (an even the black sites of a replica) and update them parallely because all of them depends only on the black sites (on the white ones of the replica). In Janus, we have up to 800 update cells and every cell updates one spin every clock cycle. Every update cell receives the $2D$ nearest neighbour and couplings bit variables and one random number (generated by a 32 bits Parisi-Rapuano generator). Then it computes the local field, compares it with the random number and updates the spin. Therefore, we achieve up to 800 updates per second in every FPGA. For more details, please see Appendix A.

Chapter 8

Conclusions

In this thesis, Disordered Potts Model (DPM) and Edwards-Anderson Ising Spin Glass Model (ISGM) have been studied, both in three dimensions. In DPM (with the mean of the couplings $J_0 = 0$) we have found spin glass phase transitions for $p = 5$ and $p = 6$ states which take place at $\beta_c \sim p$. We also computed the critical exponents to characterize the phase transition, where, our main result in this model is found: as p increases, the phase transition tends to a first order one. However, we did not find any sign of a phase transition to a ferromagnetic phase at low temperatures, as predicted by mean field theory, in the whole range of temperatures studied, although this model allows its existence.

As far as ISGM is concerned, an in depth analysis have been performed. The behaviour of systems in equilibrium and non-equilibrium (this one even in presence of an external magnetic field) has been studied.

Firstly, we analysed the sample-to-sample fluctuations of the overlap distribution in order to check whether the system exhibits stochastic stability and ultrametricity. To check the first one, we tested whether Eq. (3.20) holds and we found a small discrepancy. Fortunately, it seems to be due to finite size effects and tends to disappear as L grows. Regarding ultrametricity, we did not manage to reach any clear conclusion about it, although it seems to improve as the size of the system grows.

Furthermore, the phase transition of ISGM has been also studied with the analysis of the zeros of the partition function. In fact, we have studied the zeros in ϵ of an ISGM with a small perturbation ϵQ, where Q is the overlap. At the critical temperature, the behavior of the zeros and the integrated density of zeros have been studied. The η exponents found in both studies are compatible with previous results of Ref. [212]. Moreover, we have checked the behaviour of the integrated density of zeros with the expected slope at the origin computed with the value of q_{EA} from the literature [200] with a

satisfactory result. Besides, the low temperature phase have also been analyzed and the results obtained are compatible with those from the literature achieved with more traditional techniques.

Regarding non-equilibrium behavior, we have found evidences of the existence of a glassy phase transition in three dimensions in presence of an external magnetic field. Although we cannot determine if a thermodynamic transition happens. The main evidence is the behavior of the autocorrelation time τ, which grows from several order of magnitude as temperature is decreased. This effect suggests the existence of two different phases and fitting its curve the critical temperature can be computed. Besides, fits of W and q from low temperatures support the hypothesis of this phase transition and even the expected critical temperatures are compatible.

Rejuvenation and memory have also been studied (in absence of an external magnetic field) using a quite large system $L = 256$. Unfortunately we have not been able to reproduce the dip experiment.

Capítulo 8

Conclusiones

En esta tesis se ha estudiado el Modelo de Potts Desordenado (DPM) y el Modelo de Vidrios de Espín de tipo Ising de Edwards-Anderson (ISGM), ambos en tres dimensiones. En el DPM (con valor medio de los acoplamientos $J_0 = 0$) hemos encontrado una transición a una fase de vidrio de espín para $p = 5$ y $p = 6$ estados que tiene lugar a $\beta_c \sim p$. También hemos calculado los exponentes críticos para caracterizar la transición de fase, donde hemos encontrado nuestro resultado más importante en este modelo: conforme crece p, la transición tiende hacia una de primer orden. Sin embargo, no hemos hallado signos de transición a una fase ferromagnética a bajas temperaturas, como predice la teoría de campo medio, en todo el rango de temperaturas estudiado, aunque este modelo permite su existencia.

En lo que respecta al ISGM, se ha llevado a cabo un profundo análisis de él. Se ha estudiado el comportamiento de sistemas en equilibrio y fuera del equilibrio (este último incluso en presencia de un campo magnético externo).

En primer lugar, analizamos las fluctuaciones entre muestras de la distribución del *overlap* para comprobar si el sistema exhibe estabilidad estocástica y ultrametricidad. Para comprobar la primera de ellas, comprobamos si se verificaba la Ec. (3.20) y hallamos una pequeña discrepancia. Afortunadamente, parece ser debida a efectos de tamaño finito y tiende a desaparecer conforme crece L. Respecto a la ultrametricidad, no hemos conseguido alcanzar ninguna conclusión clara, aunque parece que mejora conforme crece el tamaño del retículo.

Además, se ha estudiado la transición de fase del ISGM analizando los ceros de la función de partición. De hecho, hemos estudiado los ceros en ϵ de un ISGM con una pequeña perturbación ϵQ, donde Q es el *overlap*. En la temperatura crítica, se ha estudiado el comportamiento de los ceros y la densidad integrada de ceros. Los exponentes η hallados en ambos análisis son compatibles con los resultados previos de la Ref. [212]. Es más, hemos

contrastado el comportamiento de la densidad integrada de los ceros con la pendiente esperada en el origen calculada con el valor de q_{EA} obtenido de la literatura [200] con un resultado satisfactorio. Se ha analizado también la fase de baja temperatura y los resultados obtenidos son compatibles con los que se pueden encontrar en la literatura calculados con técnicas más tradicionales.

Respecto al comportamiento fuera del equilibrio, hemos hallado evidencias de una transición vítrea en tres dimensiones en presencia de un campo magnético externo. Aunque no hemos podido determinar si se lleva a cabo una transición termodinámica. La principal evidencia es el comportamiento del tiempo de autocorrelación τ, que crece varios órdenes de magnitud cuando se incrementa la temperatura. Este efecto sugiere la existencia de dos fases diferentes y ajustando su curva se puede calcular la temperatura crítica. Además, los ajustes realizados de W y q a bajas temperaturas apoyan la hipótesis de esta transición de fase e incluso las temperaturas críticas esperadas son compatibles.

También se ha estudiado el rejuvenecimiento y la memoria (en ausencia de campo magnético externo) usando un sistema bastante grande $L = 256$. Desafortunadamente no hemos conseguido reproducir el experimento *dip*.

Appendix A

Janus

Spin glasses are systems with a extremely slow dynamics, so one has to perform very long simulations to let the system reach the equilibrium. As a consequence, the computation power is extremely important. Even if one performs simulations out of equilibrium, one has to simulate a large amount of MCS (recall that one MCS is equivalent to 1 ps in real experimental time) and large lattices to avoid finite size effects, so these simulations are also very CPU time demanding. Therefore the design of a special purpose machine is a good option to deal with this problem. Besides, the characteristics of spin glasses simulations suggest that a special purpose computer may be even more interesting than in other traditional problems. For instance, the dynamical variables only take a small quantity of values (in Edwards-Anderson model, they only take two possible values) and many quantities can be computed with binary logical operations. Furthermore, these systems allows us to perform parallelization which may be optimized better in a special purpose computer.

Due to these advantages that a special purpose computer may present over traditional computer, designing of dedicated machines to this purpose is not new, in fact the present machine, *Janus*, is a kind of third generation of these dedicated computers. The first generation was *RTN*[222] which was built in Zaragoza in 1991 and was based on transputer processors. The second generation was *SUE*[223] which was built in Zaragoza in 2000. This machine was based on FPGAs (*Field Programmable Gate Array*) and the update speed was 217 ps/spin. Finally, *Janus* was built by a collaboration of the universities of Ferrara and Roma 1 *la Sapienza* in Italy and Extremadura, Complutense of Madrid and Zaragoza in Spain (this collaboration is the so-called *Janus collaboration*) in 2008. *Janus* is also based on FPGAs, although a more modern version than the one used in *SUE*. We will present a brief summary of the hardware architecture, how *Janus* is programmed and op-

timizations performed (if the reader wants a more exhaustive information, please see references [224, 225, 226]and, finally, the new generation of dedicated machine that the *Janus Collaboration* is developing, *Janus II*.

A.1 Hardware architecture

Janus is a dedicated computer based on FPGAs. The FPGAs used in *Janus* are Xilinx Virtex-4 LX200. Every board of *Janus* has 16 FPGA dedicated to simulations, called SP (from *Scientific Processor*) and 1 FPGA dedicated to data transfer and to control the SPs, called IOP (from *Input/Output processor*). Every node (SP or IOP) is housed in a small board plugged into the the main motherboard, so maintenance (for example, replacing nodes that are out of order) is quite easy. A PC host controls the board with a Gigabit-Ethernet connection (see Figure A.1 for a representation of this configuration and Figure A.2 for a actual picture of a Janus board). Every PC host controls two boards and *Janus* has 16 boards (8 PCs) in total, so one can use 256 SPs to simulate. The SPs of a board are connected each other with a nearest-neighbour toroidal network (see Figure A.3) and with the IOP. The main clock of *Janus* is 62.5 MHz, although several parts of the machine need faster clocks like the Gigabit-Ethernet interface in the IOP.

A.2 Programming in Janus. Optimizations

When one wants to perform a simulation in *Janus*, one has to develop a program in the PC host. Only the spin updates will be made on the SPs, so the rest of the simulation program like parallel tempering (although it may also be performed in a Janus board [230]) has to be implemented in the PC host. Besides, this program that runs in the PC must send to the SP parameters of the simulation like the number of MCS to simulate, the initial configuration of the spins if it is not randomly and so on. Obviously, it also reads the configuration after the MCS simulated to measures physical observables or just to store it. This program has to be made by the end user, but a set of C libraries has been developed to make easier this communication part of the program.

Furthermore, one must program the SPs themselves. FPGAs have a set of logical gates that can be connected, activated or disactivated, that is, one can program the hardware itself (using VHDL language, for example). This useful property allow us to simulate different models, sizes, etc. just choosing the suitable firmware of the SP. Once these firmwares are developed, the end

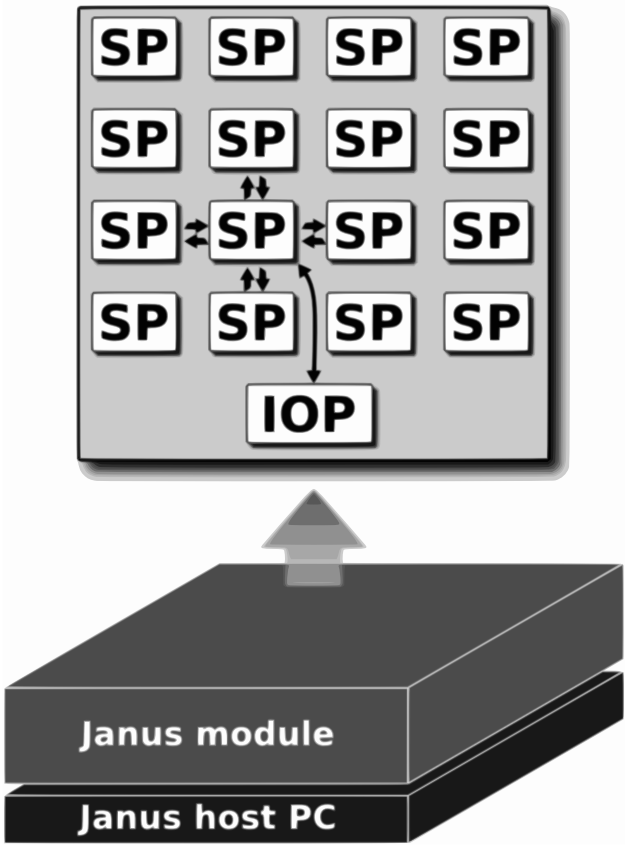

Figure A.1: Configuration of a Janus board

user has just to select which one he needs, using our C libraries to program the SPs with that firmware in a quite easy way again. Although the firmware developed for every model has different details implementation to the rest of models, we will comment some general details and optimizations of these firmwares. Perhaps, the main optimization one can achieve in spin glasses is parallelization. Let us imagine a chessboard where every square represents one site of the lattices, that is, one spin. To update a white spin, one only needs to know $2D$ (where D is the dimension of the system) black spins (see figure A.4) due to the fact that only nearest neighbours contribute in the Hamiltonian of these models. Therefore, to update the whole lattice one can make two steps, fist updating all the spins of one colour and later update all the spins of the other colour. Then, one can update parallely the spins in every step, in fact we have achieved up to 1024 parallel engine updates in *Janus*. A engine is a cell in the FPGA that updates one spin. It receives the data of the spins and couplings of the nearest neighbours (remind that

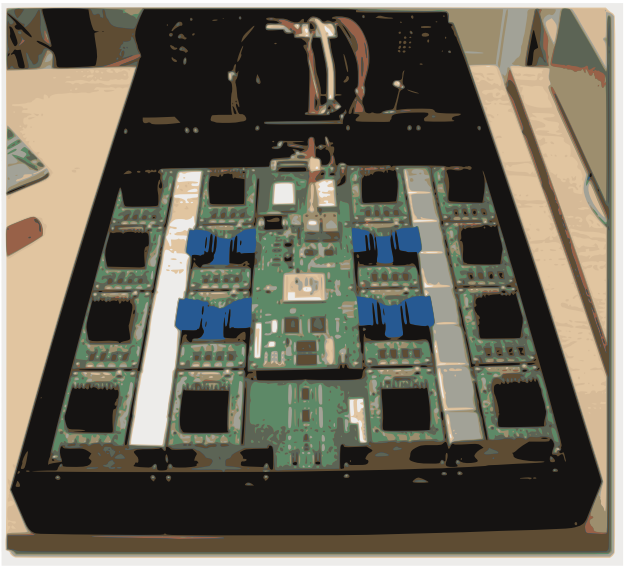

Figure A.2: A Janus board

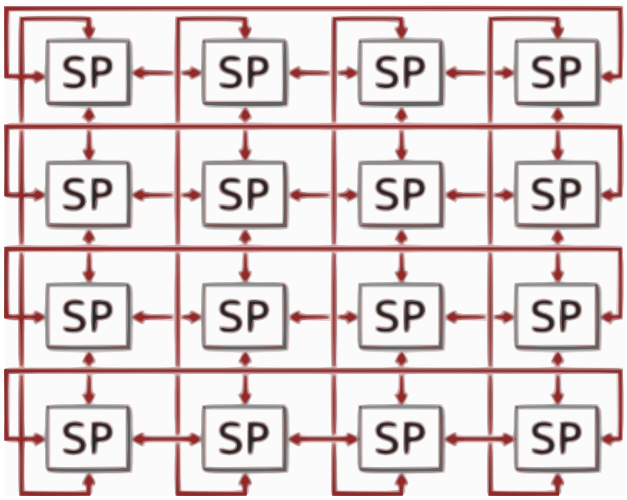

Figure A.3: Nearest-neighbour toroidal network of the SPs of a Janus board

they belong to the other *colour*) and a random number. However a new bottleneck appears, we need a new fresh random number in every update we do for every engine. We have used the Parisi-Rapuano [227] that is based on a so-called wheel (let I an element of this wheel) of at least 32 bits and the following operations

$$I(k) = I(k-24) + I(k-55) \quad \text{(A.1)}$$

$$R(k) = I(k) \otimes I(k-61) \quad \text{(A.2)}$$

where $R(k)$ is the random number generated. This algorithm to generate random numbers can be easily implemented in a logic circuit and, even one can obtain several random numbers at the same clock cycle, although the logical circuit gets more complicated. In spite of this parallel generation of random numbers, several different Parisi-Rapuano generators (with their own wheel) are necessary.

Janus	PC (2007-2008)	PC (2011-2012)
16	3000	170

Table A.1: Time necessary for update one spin in a 3D-Ising spin glass model (in ps/spin). Both PC simulations have been performed with SMSC strategy. For the test of 2007-2008, when Janus was being developed, a Intel Core2Duo (64 bits) 1.6 GHz processor was used. In the test of nowadays technology a dual socket quad-core eight core Intel Sandy Bridge board was used. In this case the time depends on the size of the lattice, we present here the time of a $L = 80$ lattice.

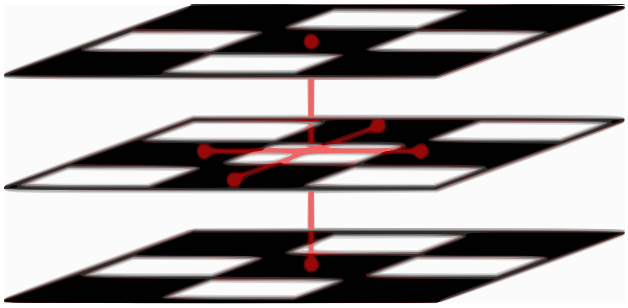

Figure A.4: Update of a white spin. One only needs black spins

As an example of the improve of the simulating speed achieved with *Janus* is shown in the table A.1 where the time to update in one spin in *Janus* is compared with traditional PC, both processors that were available when *Janus* were design and more modern ones. One can observe that even after 4 years, *Janus* is still one order of magnitude faster than multi-core processors. Simulating Potts model, situation was even better because *Janus* is three order of magnitude faster than processors available when it was designed, the time of update in *Janus* is 64 ps/spin while in a PC was 117 ns/spin in a four state 3D Potts glassy model.

A.3 Janus II

The next generation of dedicated computer is currently being designed by the *Janus Collaboration*. Several tests have been performed to decide the kind of processor that fits best to our purpose (GPU, FPGA, etc.). Finally, FPGAs have been chosen again, although a more recent version. Besides using a new version of FPGA, faster and with more memory than the one used in Janus I, several changes have been designed to improve the parallelization of simulations and to make easier that researches of different groups can use Janus II. Perhaps, the main improvement of Janus II is that the boards will be linked each other, so the two dimensional nearest neighbour toroidal network will become in a three dimensional one. Therefore, one can parallelize bigger lattices.

Appendix B

Finite Size Scaling and the Quotient Method

One of the more important problems that appears when one studies numerically a spin glass is that we are only able to simulate small lattices, but in nature we actually have far bigger system, in fact, we approximate a real system as $L \to \infty$, that is, the thermodynamic limit. We can deal with this problem using the finite size scaling. The finite size hypothesis tells us that the behavior of the system is determined by the ratio $L/\xi(\infty, t)$, where L is the linear size of the lattice, $\xi(\infty, t)$ is the correlation length of the infinite system, and $t = (T - T_c)/T_c$ is the so-called reduced temperature. If this quantity is large, we will be in the thermodynamic limit, and if it is small, we will be in the FSS regime.

If O is an observable that diverges in the thermodynamic limit as

$$\langle O(\infty, t)\rangle \propto |t|^{-x_0} \tag{B.1}$$

the finite size scaling Ansatz predicts that the mean value of the observable O behaves as

$$\frac{\langle O(L, t)\rangle}{\langle O(\infty, t)\rangle} = \hat{f}_0(L/\xi(\infty, t) + \mathcal{O}(\xi^{-\omega}, L^{-\omega})) \tag{B.2}$$

where $\hat{f}_0$ is a smooth function. One could use this equation with two different sizes of the system, L and sL and obtain

$$\frac{\langle O(sL, t)\rangle}{\langle O(L, t)\rangle} = \hat{\mathcal{F}}_0(L/\xi(L, t) + \mathcal{O}(\xi^{-\omega}, L^{-\omega})) \tag{B.3}$$

where $\hat{\mathcal{F}}_0$ is also a smooth function. As $\langle O(L, t)\rangle$ and $L/\xi(L, t)$ can be measured, one could fit the function $\hat{\mathcal{F}}_0$ and extrapolate $\langle O(\infty, t)\rangle$. However,

this quantity will have three sources of error, the error on the measure of $\langle O(L,t)\rangle$ and $L/\xi(L,t)$ and the error on the fit of $\hat{\mathcal{F}}_0$. Because of this problem, a different method may be used.

We will use the so-called quotient method. Firstly we will rewrite the finite size scaling Ansatz, Eq. (B.2), in a more useful way, using $\xi(\infty,t) \propto |t|^{-\nu}$ (that is, the exponent $x_\xi = \nu$) and Eq. (B.1)

$$\langle O(L,t)\rangle \propto \hat{f}_0(L/\xi(\infty,t))\,|t|^{-\frac{x_0\nu}{\nu}} = \hat{f}_0(L/\xi(\infty,t))\xi(\infty,t)^{\frac{x_0}{\nu}} \tag{B.4}$$

hence, one can rewrite the expression as

$$\langle O(L,t)\rangle = L^{\frac{x_0}{\nu}}\left[f_0(L/\xi(\infty,t)) + \mathcal{O}(\xi^{-\omega}, L^{-\omega}))\right] \tag{B.5}$$

Using this equation for the correlation length, one can find $\xi(\infty,t)$ as a function of $\xi(L,t)$, so finally the expression of the finite size scaling Ansatz is

$$\langle O(L,t)\rangle = L^{\frac{x_0}{\nu}}\left[F_0(L/\xi(L,t)) + \mathcal{O}(\xi^{-\omega}, L^{-\omega}))\right] \tag{B.6}$$

One can form the quotient of the mean of the observable O between two different sizes of the lattice, $L_1 = L$ and $L_2 = sL$ (where one usually chooses $s = 2$)

$$Q_0^L = \frac{\langle O(sL,t)\rangle}{\langle O(L,t)\rangle} \tag{B.7}$$

and evaluate it at the temperature β_c^L where

$$\frac{\xi(sL,t)}{sL} = \frac{\xi(L,t)}{L} \tag{B.8}$$

The result is

$$Q_0^L\big|_{\beta=\beta_c^L} = s^{x_0/\nu} + \mathcal{O}(L^{-\omega}) \tag{B.9}$$

from which we can compute the exponents ratios x_0/ν, but one has to be careful because β_c^L is not exactly β_c

$$\beta_c^L - \beta_c \propto \frac{1-s^{-\omega}}{s^{1/\nu}-1} L^{-\omega-\frac{1}{\nu}} \tag{B.10}$$

Appendix C

Gaussian magnetic fields

In a spin glass glass with quenched random couplings, the physical relevant information only depends on the first two moments of the distribution of the site-depending magnetic field. Despite that, using a Gaussian distribution of the magnetic fields is more realistic and allow us to simplify with analytic calculation some observables, in fact it allows us to simulate only two replicas of the system instead of four. Besides, some relations between the observables could be obtained. However a Gaussian magnetic field is more CPU-demanding than a binary one because we have to deal with real numbers instead of integer ones. As we performed our simulations mainly in JANUS (see A for more information about it), this difference is of huge importance, because we have to perform simulations with integer values of the magnetic fields. However, we can use the Gauss-Hermite quadrature, C.1, to approximate the behaviour of a system with Gaussian magnetic field with a system with a magnetic field that only can take some integer values.

C.1 Gauss-Hermite quadrature

One can approximate the result of a the integral that depends of the Gaussian distribution by using the Gauss-Hermite quadrature [167] that allows us to use a field that only takes some discrete values

$$\int e^{-x^2} f(x) dx \approx \sum_{i=1}^{n} \omega_i f(x_i) \tag{C.1}$$

where x_i are the roots of the Hermite polynomial, $H_n(x)$, the weights, w_i, are given by

$$w_i = \frac{2^{n-1} n! \sqrt{\pi}}{n^2 \left[H_{n-1}(x_i)\right]^2} \tag{C.2}$$

and n is the number of points used in the approximation. This approximation is useful because if we have a Gaussian magnetic field and we want to compute the average of some observable, $[O]_h$, we should calculate

$$[O]_h = \int P(h)O(h)dh = \int \frac{1}{\sqrt{2\pi}\sigma} e^{-h^2/2\sigma} O(h)dh \tag{C.3}$$

where $\sigma = H_{\text{ext}}$. If we can use C.1 approximation to calculate C.3, we could use a magnetic field that takes n integer values in our simulations with a probability distribution given by w_i. However, the integrals of C.1 and C.3 are different, so we have to do the easy change of variable $y^2 = \frac{x^2}{2\sigma^2}$. With this change of variable, C.1 becomes

$$\int \frac{1}{\sqrt{2}\sqrt{\pi}\sigma} \sqrt{2}\sigma e^{-y^2/2\sigma} f(\sqrt{2}\sigma y)dy \approx \sum_{i=1}^{n} \omega_i f(\sqrt{2}\sigma y_i) \tag{C.4}$$

hence, simplifying it, we obtain

$$\frac{1}{\pi} \int e^{-y^2/2\sigma^2} f(\sqrt{2}\sigma y)dy \approx \sum_{i=1}^{n} \omega_i f(\sqrt{2}\sigma y_i) \tag{C.5}$$

C.2 Simplification of χ_{SG}

With C.5 we are able to approximate a Gaussian magnetic field simulating just integer values. Besides, using a Gaussian magnetic field (or, in fact, this approximation) we can simplify the expression of some observables, for example the spin glass susceptibility, χ_{SG}. Let us write the naive expression of the susceptibility

$$\chi_{\text{SG}} = \frac{1}{V} \sum_{ij} \overline{\left[\langle \sigma_i \sigma_j \rangle - \langle \sigma_i \rangle \langle \sigma_j \rangle\right]^2} \tag{C.6}$$

expanding the square

$$\begin{aligned} \chi_{\text{SG}} &= \frac{1}{V} \sum_{ij} \overline{\langle \sigma_i \sigma_j \rangle_{\text{A}} \langle \sigma_i \sigma_j \rangle_{\text{B}} + \langle \sigma_i \rangle_{\text{A}} \langle \sigma_j \rangle_{\text{B}} \langle \sigma_i \rangle_{\text{C}} \langle \sigma_j \rangle_{\text{D}}} \\ &- \overline{2 \langle \sigma_i \sigma_j \rangle_{\text{A}} \langle \sigma_i \rangle_{\text{B}} \langle \sigma_j \rangle_{\text{C}}} \end{aligned} \tag{C.7}$$

where A, B, C and D are real replicas of the system. We will express C.7 in term of the overlap and one finally obtains that

$$\chi_{\text{SG}} = \sum_{ij} \overline{\langle q_i^{\text{AB}} q_j^{\text{AB}} \rangle + \langle q_i^{\text{AC}} q_j^{\text{BD}} \rangle - 2 \langle q_i^{\text{AB}} q_j^{\text{AC}} \rangle} \tag{C.8}$$

where $q^{\rm AB}$ means the overlap between the replicas A and B, $q^{\rm BD}$ the overlap between the replicas B and D, and so on. Therefore one would need to simulate four replicas to calculate this observable. However, thanks to a Gaussian (or its approximation) magnetic field, we are going to demonstrate that we will only need two replicas. We will define the following susceptibility

$$\chi_{\rm SG} = \frac{1}{3}A_6 + \frac{A_{10}}{2\beta h_0^2} + \frac{1}{6}\left\{\frac{A_{18}}{\beta^2 h_0^4} - 1 - \overline{q} - \frac{\delta_{{\rm x},0}\overline{[q]_{\rm h}}}{\beta^2 h_0^2}\right\} \tag{C.9}$$

where

$$A_6 = G_1 \tag{C.10}$$

$$A_{10} = \beta h_0^2 \left\{G_1 - 2G_2 + \overline{q}\right\} \tag{C.11}$$

and

$$A_{18} = \beta^2 h_0^4 \left\{G_1 - 6G_2 + 6G_3 + (1 - 2\overline{q})\right\} + \delta_{{\rm x},0} h_0^2 \overline{[q]_{\rm h}} \tag{C.12}$$

where

$$G_1 = \frac{1}{V}\overline{\sum_{ij}\langle\sigma_i\sigma_j\rangle^2} \tag{C.13}$$

$$G_2 = \frac{1}{V}\overline{\sum_{ij}\langle\sigma_i\sigma_j\rangle\langle\sigma_i\rangle\langle\sigma_j\rangle} \tag{C.14}$$

$$G_3 = \frac{1}{V}\overline{\sum_{ij}\langle\sigma_i\rangle^2\langle\sigma_j\rangle^2} \tag{C.15}$$

Firstly, we will demonstrate that C.9 is the same observable as C.7. Replacing C.10, C.11 and C.12 in C.9 one finds that

$$\begin{aligned}\chi_{\rm SG} &= \frac{1}{3}G_1 + \frac{1}{2}\frac{\beta h_0^2}{\beta h_0^2}\left\{G_1 - 2G_2 + \overline{q}\right\} + \frac{1}{6}\left\{\frac{\beta^2 h_0^4}{\beta^2 h_0^4}\left(G_1 - 6G_2 + 6G_3 + 1\right)\right. \\ &- \left. 2\overline{q} + \frac{1}{\beta^2 h_0^4}\delta_{{\rm x},0} h_0^2 \overline{[q]_{\rm h}} - 1 - \overline{q} - \frac{\delta_{{\rm x},0}\overline{[q]_{\rm h}}}{\beta^2 h_0^2}\right\}\end{aligned} \tag{C.16}$$

and operating

$$\begin{aligned}\chi_{\rm SG} &= \frac{1}{3}G_1 + \frac{1}{2}G_1 - G_2 + \frac{1}{2}\overline{q} + \frac{1}{6}G_1 - G_2 + g_3 + \frac{1}{6} - \frac{1}{3}\overline{q} + \frac{1}{\beta^2 h_0^2}\frac{1}{6}\delta_{{\rm x},0}\overline{[q]_{\rm h}} \\ &- \frac{1}{6} - \frac{1}{6}\overline{q} - \frac{1}{\beta^2 h_0^2}\frac{1}{6}\delta_{{\rm x},0}\overline{[q]_{\rm h}} = G_1 - 2G_2 + G_3\end{aligned} \tag{C.17}$$

Now, we will demonstrate that one can calculate those three quantities that appears in the expression C.9 of the $\chi_{\rm SG}$, A_6, A_{10}, and A_{18} simulating

only two replicas, thanks to the Gaussian magnetic field. As $A_6 = G_1$, it is obvious that it can be calculated with only two replicas, but A_{10} and A_{18} are not so trivial. We will assume that

$$A_{10} = \overline{[h_j \langle \sigma_i \sigma_j \rangle \langle \sigma_i \rangle]_h} \tag{C.18}$$

$$A_{18} = \overline{[h_i h_j \langle \sigma_i \sigma_j \rangle]_h} \tag{C.19}$$

then, one can calculate $\chi_{\rm SG}$ with only two replicas.
We will demonstrate C.18, that is, we will demonstrate that A_{10} defined as C.18 is the same quantity defined in C.11:

$$\begin{aligned} A_{10} &= \overline{\int dh_j e^{-h_j^2/2h_0^2} h_j \langle \sigma_i \sigma_j \rangle \langle \sigma_i \rangle} \\ &= \overline{\int (-h_0^2)\, dh_j \frac{d}{dh_j} \left(e^{-h_j^2/2h_0^2} \right) \langle \sigma_i \sigma_j \rangle \langle \sigma_i \rangle} \end{aligned} \tag{C.20}$$

Now, we will integrate by parts,

$$A_{10} = \overline{-h_0^2 e^{-h_j^2/2h_0^2} \langle \sigma_i \sigma_j \rangle \langle \sigma_i \rangle \Big|_{-\infty}^{\infty}} + \overline{h_0^2 \int dh_j e^{-h_j^2/2h_0^2} \frac{d}{dh_j} \langle \sigma_i \sigma_j \rangle \langle \sigma_i \rangle} \tag{C.21}$$

where the first term vanishes. It is easy to demonstrate that the derivative of the thermal average of every observable, O, that does not depend on h_j with respect to this magnetic field, h_i, is

$$\frac{d}{dh_j} \langle O \rangle = \beta \left(\langle O \sigma_j \rangle - \langle O \rangle \langle \sigma_j \rangle \right) \tag{C.22}$$

So, in our case

$$\frac{d}{dh_j} \left(\langle \sigma_i \sigma_j \rangle \langle \sigma_i \rangle \right) = \beta \left(\langle \sigma_i \sigma_j \rangle^2 - 2 \langle \sigma_i \sigma_j \rangle \langle \sigma_i \rangle \langle \sigma_j \rangle + \langle \sigma_i \rangle^2 \right) \tag{C.23}$$

where we have used that $\sigma_j^2 = 1$, so $\langle \sigma_i \sigma_j^2 \rangle = \langle \sigma_i \rangle$. Then,

$$\begin{aligned} A_{10} &= h_0^2 \overline{\int dh_j e^{-h_j^2/2h_0^2} \frac{d}{dh_j} \langle \sigma_i \sigma_j \rangle \langle \sigma_i \rangle} \\ &= h_0^2 \overline{\int dh_j e^{-h_j^2/2h_0^2} \beta \left(\langle \sigma_i \sigma_j \rangle^2 - 2 \langle \sigma_i \sigma_j \rangle \langle \sigma_i \rangle \langle \sigma_j \rangle + \langle \sigma_i \rangle^2 \right)} \\ &= \beta h_0 \left\{ G_1 - 2G_2 + \overline{[q]_{\rm h}} \right\} \end{aligned} \tag{C.24}$$

Finally, we have to demonstrate that A_{18} defined as in C.19 is the same quantity defined in C.12. Due to the fact that in C.12 we have a Kronecker delta, we will study two different cases, when $i \neq j$ and when $i = j$.

$$A_{18} = \overline{\int dh_i e^{-h_i^2/2h_0^2} \int dh_j e^{-h_j^2/2h_0^2} \langle\sigma_i\rangle\langle\sigma_j\rangle h_i h_j} \tag{C.25}$$

a) Case $i \neq j$:
Let us named

$$I_j = \int dh_j e^{-h_i^2/2h_0^2} \langle\sigma_j\rangle h_j \tag{C.26}$$

Rewriting C.25 one has

$$A_{18} = \overline{\int dh_i e^{-h_i^2/2h_0^2} I_j} \tag{C.27}$$

Now we integrate it by parts and the result of the integrate is

$$\begin{aligned} A_{18} &= \overline{-h_0^2 e^{-h_i^2/2h_0^2} \langle\sigma_i\rangle I_j \big|_{-\infty}^{\infty}} + \overline{h_0^2 \int e^{-h_i^2/2h_0^2} \frac{d}{dh_i} \langle\sigma_i\rangle I_j dh_i} \\ &= h_0^2 \overline{\int dh_i dh_j e^{-h_i^2/2h_0^2} \frac{d}{dh_i} \left(\langle\sigma_i\rangle\langle\sigma_j\rangle h_j\right)} \end{aligned} \tag{C.28}$$

since $i \neq j$,

$$A_{18} = h_0^2 \overline{\int dh_i dh_j e^{-h_i^2/2h_0^2} e^{-h_j^2/2h_0^2} h_j \frac{d}{dh_i} \left(\langle\sigma_i\rangle\langle\sigma_j\rangle\right)} \tag{C.29}$$

Now, we integrate by parts again and the result of the integrate is

$$\begin{aligned} A_{18} &= \overline{-h_0^4 e^{-h_j^2/2h_0^2} e^{-h_i^2/2h_0^2} \frac{d}{dh_j} \left(\langle\sigma_i\rangle\langle\sigma_j\rangle\right) \Big|_{-\infty}^{\infty}} \\ &+ \overline{h_0^4 \int dh_i dh_j e^{-h_j^2/2h_0^2} e^{-h_i^2/2h_0^2} \frac{d^2}{dh_i dh_j} \left(\langle\sigma_i\rangle\langle\sigma_j\rangle\right)} \end{aligned} \tag{C.30}$$

that is

$$A_{18} = \overline{h_0^4 \left[\frac{d^2}{dh_i dh_j} \left(\langle\sigma_i\rangle\langle\sigma_j\rangle\right)\right]_{\mathrm{h}}} \tag{C.31}$$

Now, we will calculate the second derivative by using twice the equation C.22

$$\begin{aligned} \frac{d^2}{dh_i dh_j} \left(\langle\sigma_i\rangle\langle\sigma_j\rangle\right) &= \beta^2 \left[\langle\sigma_i\sigma_j^2\rangle\langle\sigma_i\rangle + \langle\sigma_i^2\rangle\langle\sigma_j^2\rangle - 2\langle\sigma_i\rangle^2\langle\sigma_j^2\rangle\right. \\ &- 2\langle\sigma_i^2\rangle\langle\sigma_j^2\rangle + \langle\sigma_i^2\sigma_j\rangle\langle\sigma_j\rangle - 6\langle\sigma_i\sigma_j\rangle\langle\sigma_i\rangle\langle\sigma_j\rangle \\ &+ \left. 6\langle\sigma_i\rangle^2\langle\sigma_j\rangle^2 + \langle\sigma_i\sigma_j\rangle^2\right] \end{aligned} \tag{C.32}$$

Since $\sigma_i^2 = \sigma_j^2 = 1$

$$\begin{aligned} A_{18} &= \beta^2 h_0^4 \overline{[1 - \langle\sigma_i\rangle^2 - \langle\sigma_j\rangle^2 - 6\langle\sigma_i\sigma_j\rangle\langle\sigma_i\rangle\langle\sigma_j\rangle + 6\langle\sigma_i\rangle^2\langle\sigma_j\rangle^2 + \langle\sigma_i\sigma_j\rangle]_{\rm h}} \\ &= \beta^2 h_0^4 \left[1 - 2\overline{[q]_h} - 6G_2 + 6G_3 + G_1\right] \end{aligned} \tag{C.33}$$

b) Case $i = j$ In this case, the equation C.25 becomes

$$A_{18} = \overline{\int dh h^2 e^{-h^2/2h_0^2} \langle\sigma_i\rangle^2} \tag{C.34}$$

we will integrate by parts and the result is

$$\begin{aligned} A_{18} &= \overline{-h_0^2 e^{-h^2/2h_0^2} h \langle\sigma_i\rangle^2 \Big|_{-\infty}^{\infty}} + \overline{h_0^2 \int dh e^{-h^2/2h_0^2} \langle\sigma_i\rangle^2} \\ &+ \overline{h_0^2 \int dh e^{-h^2/2h_0^2} h \frac{d}{dh} \langle\sigma_i\rangle^2} \end{aligned} \tag{C.35}$$

The first of this integrals is trivial, it is the average of $\langle\sigma_i\rangle^2$ over the magnetic field. To compute the second one, we will integrate it by parts, so one has

$$\begin{aligned} A_{18} &= \overline{h_0^2 \left[\langle\sigma_i\rangle^2\right]_{\rm h}} - \overline{h_0^2 e^{-h^2/2h_0^2} \frac{d}{dh} \langle\sigma_i\rangle^2 \Big|_{-\infty}^{\infty}} \\ &+ \overline{h_0^4 \int dh e^{-h^2/2h_0^2} \frac{d^2}{dh^2} \langle\sigma_i\rangle^2} \\ &= \overline{h_0^2 \left[\langle\sigma_i\rangle^2\right]_{\rm h}} + \overline{h_0^4 \left[\frac{d^2}{dh^2} \langle\sigma_i\rangle^2\right]_{\rm h}} \end{aligned} \tag{C.36}$$

Now we have to calculate the second derivative of $\langle\sigma_i\rangle^2$ with respect to h using C.22 twice

$$\frac{d^2}{dh^2} \langle\sigma_i\rangle^2 = \beta^2 \left(2 - 8\langle\sigma_i\rangle^2 + 6\langle\sigma_i\rangle^4\right) \tag{C.37}$$

so, finally we have

$$\begin{aligned} A_{18} &= \overline{h_0^2 \left[\langle\sigma_i\rangle^2\right]_h} + \overline{h_0^4 \left[\beta^2 \left(2 - 8\langle\sigma_i\rangle^2 + 6\langle\sigma_i\rangle^4\right)\right]} = \overline{h_0^2 \left[q\right]_h} \\ &+ \beta^2 h_0^4 \left[2 - 6G_2(i=j) - 2\overline{[q]_h} + 6G_3(i=j)\right] \end{aligned} \tag{C.38}$$

where we have used that $G_1(i = j) = 1$. Therefore, for every i,j, the general expression of A_{18} is

$$A_{18} = \beta^2 h_0^4 \left(G_1 - 6G_2 + 6G_3 + 1 - 2\overline{[q]_{\rm h}}\right) + \delta_{ij} h_0^2 \overline{[q]_{\rm h}} \tag{C.39}$$

C.3 Relation between the overlap and the magnetic energy

As it is explained in section 4, one can define several observables like the overlap

$$q(t_w) = \frac{1}{V}\overline{\sum_i \sigma_i^{(1)}(t_w)\sigma_i^{(2)}(t_w)} \tag{C.40}$$

the magnetic energy

$$E_{\rm mag}(t_w) = \frac{1}{V}\overline{\sum_i h_i\sigma_i(t_w)} \tag{C.41}$$

and

$$W = 1 - \frac{TE_{\rm mag}}{h_0^2} \tag{C.42}$$

Besides, at the equilibrium W and q must satisfy

$$W = \overline{\langle q\rangle} \tag{C.43}$$

Now, we will demonstrate the relation C.43, integrating by parts. Firstly, one can rewrite C.42 using C.41. Besides, we will make explicit the average over the disorder due to couplings disorder (overline) and magnetic disorder ($[\cdots]_{\rm h}$).

$$W = 1 - \frac{T\overline{[\sum_i h_i\langle\sigma_i\rangle]_{\rm h}}}{Vh_0^2} = 1 - \frac{T\overline{\sum_i \int \frac{dh}{\sqrt{2\pi}h_0} h_i\langle\sigma_i\rangle e^{-h_i^2/2h_0^2}}}{Vh_0^2} \tag{C.44}$$

This integrate can be solved integrating by parts, so the result of the integrate in C.44 is

$$\begin{aligned}\int \frac{dh}{\sqrt{2\pi}h_0} h_i\langle\sigma_i\rangle e^{-h_i^2/2h_0^2} &= \frac{-h_0^2}{\sqrt{2\pi}h_0} e^{-h_i^2/2h_0^2}\langle\sigma_i\rangle\Big|_{-\infty}^{\infty} \\ &+ h_0^2\int \frac{dh}{\sqrt{2\pi}h_0}\frac{d}{dh}\left(\langle\sigma_i\rangle\right) e^{-h_i^2/2h_0^2}\end{aligned} \tag{C.45}$$

where the first term vanishes. One can compute the derivative using C.22

$$\frac{d}{dh}\left(\langle\sigma_i\rangle\right) = \beta\left(1 - \langle\sigma_i\rangle^2\right) \tag{C.46}$$

where we have used that $\sigma_i^2 = 1$. Therefore the integrate in C.44 can be expressed as

$$\int \frac{dh}{\sqrt{2\pi}h_0} h_i\langle\sigma_i\rangle e^{-h_i^2/2h_0^2} = h_0^2\beta\left(1 - \int \frac{dh}{\sqrt{2\pi}h_0}\beta\langle\sigma_i\rangle^2 e^{-h_i^2/2h_0^2}\right) \tag{C.47}$$

and replacing it in C.44

$$W = 1 - \frac{T\beta h_0^2 \overline{\sum_i \left(1 - \int \frac{dh}{\sqrt{2\pi}h_0} \beta \langle \sigma_i \rangle^2 e^{-h_i^2/2h_0^2}\right)}}{V h_0^2} = \overline{[\langle q \rangle]_{\mathrm{h}}} \tag{C.48}$$

so the relation C.43 at equilibrium is demonstrated.

Appendix D

Lee-Yang zeros

A new tool to study phase transitions was introduced in 1952 by T. D. Lee and C. N. Yang [172] [173] while they were studying the behavior of a lattice gas (although this model is equivalent to an Ising model in a magnetic field [4]). They demonstrated that the zeros of the partition function, Z, are located on the unit circle in the complex activity plane. Besides, the distribution of these zeros provides us with information about the existence of a phase transition. If the zeros do converge onto the real axis at a given β_c when the number of spins, N, tends to ∞, the free energy, F, will not remain analytic and the system undergoes a phase transition at β_c, whereas if the zeros do not converge onto the real axis, F will remain analytic and the phase transition does not exist.

We will use an Ising model on a graph of N sites and one link joining every pair of nodes (every site could have at most two links). Therefore, the number of nearest neighbours is $z = 2$, so one can compute the total number of links

$$L = \frac{Nz}{2} \tag{D.1}$$

The partition function is

$$Z = \frac{1}{2^N} \sum_{\sigma_i = \pm 1} \exp\left(\beta \sum_{(ij)} \sigma_i \sigma_j + \sum_i h_i \sigma_i \right) \tag{D.2}$$

where $\sum_{(ij)}$ denotes a sum over all links and h_i is the magnetic field at the site i. Defining two new variables

$$\rho_i = e^{-2h_i} \tag{D.3}$$

$$\tau = e^{-2\beta} \tag{D.4}$$

Notice that, due to the fact that $\beta \in (0, \infty)$, τ is real and $0 < \tau < 1$. One can rewrite the partition function as

$$Z = \frac{1}{2^N} \exp\left(\beta L + \sum_i h_i\right) P(\tau, \rho_i) \tag{D.5}$$

where P is

$$P = \sum_{\sigma_i \pm 1} \exp\left[\beta \sum_{(ij)} (\sigma_i \sigma_j - 1) + \sum_i h_i (\sigma_i - 1)\right] \tag{D.6}$$

One can realise that P is a polynomial in ρ_i and τ. Now, the problem of finding the zeros of the partition function has become a problem of finding the zeros of the polynomial P. If ρ and τ are both real and positive, P never vanishes, so we will assume that ρ is complex.

Now, we will report how to construct the polynomial P of a general graph. Firstly, we will construct it in the easiest cases: graphs with two and three sites. Later we will demonstrate that we can construct P of a general graph from these simple cases. Let P_{12} be the polynomial of a two sites graph, and P_{123} the one of a three sites graph. It is easy to compute that

$$P_{12} = 1 + \tau(\rho_1 + \rho_2) + (\rho_1 \rho_2) \tag{D.7}$$

$$P_{123} = (1 + \rho_1 \tau)(1 + \rho_3 \tau) + \rho_2(\tau + \rho_1)(\tau + \rho_3) \tag{D.8}$$

Now, we will demonstrate that we can calculate P_{123} just joining two graphs with two sites, that is, if one know P_{12}, one can compute P_{123} without using Eq. (D.6). Obviously, if we have two separate subsets of the graph, P factorizes, so one can write $P = P^{(1)} P^{(2)}$ and this property does not depend on the numbers of sites, $N^{(1)}$ and $N^{(2)}$ of every subset. Let a be a site of the first subset and b a site of the second one. It is trivial to write $P^{(1)}$ and $P^{(2)}$ as

$$\begin{aligned} P^{(1)} &= A_+ + \rho_a A_- \\ P^{(2)} &= B_+ + \rho_b B_- \end{aligned} \tag{D.9}$$

where A_+ and B_+ are the contributions when the spins are up, that is $\sigma_a = 1$ and $\sigma_b = 1$; and A_- and B_- are the contributions when the spins are down, that is $\sigma_a = -1$ and $\sigma_b = -1$. Therefore, one can compute the polynomial P as

$$P = P^{(1)} P^{(2)} = A_+ B_+ + \rho_a A_- B_+ + \rho_b A_+ B_- + \rho_a \rho_b A_- B_- \tag{D.10}$$

Now, one can identify the site a and the site b, so one will have just one connected graph, this process is called contraction process. Let ρ_{ab} be the new activity variable of the new site and $P^{(12)}$ the polynomial of the new contracted graph. Using Eq. (D.10), one can compute $P^{(12)}$, but, obviously, as now sites a and b are the same site, terms with factor A_+B_- or A_-B+ have no sense and Eq. (D.10) becomes

$$P^{(12)} = A_+B_+ + \rho_{ab}A_-B_- \tag{D.11}$$

One can check that, for instance, P_{123} can be computed using Eq. (D.11) and two graphs with two sites. The first graph has the sites 1 and 2_a and the second graph has the sites 2_b and 3. Using Eq. (D.7) one can write that

$$P_{12}^{(1)} = (1+\tau\rho_1) + (\tau+\rho_1)\rho_{2_a} \equiv A_+ + \rho_{2_a}A_- \tag{D.12}$$

$$P_{12}^{(2)} = (1+\tau\rho_3) + (\tau+\rho_3)\rho_{2_b} \equiv B_+ + \rho_{2_b}B_- \tag{D.13}$$

Identifying the sites 2_a and 2_b and calling the new activity variable ρ_2, one can use Eq. (D.11) and the result is the same that we calculated in Eq. (D.8).

Moreover, this contraction precess also works in a connected graph. Therefore, one can identify two different sites of the graph, a and b, as a unique site ab. Before identifying the two sites, the polynomial P is

$$P = A_{++} + A_{-+}\rho_a + A_{+-}\rho_b + A_{--}\rho_a\rho_b \tag{D.14}$$

but after identifying them, Eq. (D.14) becomes

$$P^{(ab)} = A_{++} + \rho_{ab}A_{--} \tag{D.15}$$

We will check this property computing the polynomial of a four nodes graph and using it to calculate the polynomial of a cyclic three nodes graph by identifying the extreme sites. Firstly, the polynomial P of a four sites graph is

$$\begin{aligned} P_{1234} &= 1 + \tau\left\{\rho_1\left[1+\rho_2\left(1+\rho_3\right)\right] + \rho_4\left[1+\rho_3\left(1+\rho_2\right)\right]\right\} \\ &+ \tau^2\left[\rho_1\rho_4\left(1+\rho_2+\rho_3\right) + \rho_2\left(1+\rho_3\right) + \rho_3\right] \\ &+ \tau^3\left(\rho_1\rho_3 + \rho_2\rho_4\right) + \rho_1\rho_2\rho_3\rho_4 \end{aligned} \tag{D.16}$$

so, identifying the two outer nodes, 1 and 4, one obtains

$$P_{\text{cyclic}} = 1 + \tau^2\left(\rho_1+\rho_2+\rho_3+\rho_1\rho_2+\rho_1\rho_3+\rho_2\rho_3\right) + \rho_1\rho_2\rho_3 \tag{D.17}$$

Therefore, we have demonstrated that one can construct every graph (with the only condition that every site must have at most two links) by joining

two sites graphs. Thus, we will study the zeros of the polynomial of a two sites graph and later we will generalize the result. As we defined P_{12} in Eq. (D.7), its roots have the form

$$\rho_1 = \frac{1 + \tau\rho_2}{\tau + \rho_2} \tag{D.18}$$

This expression defines a one to one relation between ρ_1 and ρ_2. As τ is real, the unite circle is invariant. And due to the fact that $0 < \tau < 1$, this relation exchanges the points inside the unit circle with the ones outside it. Then it is obvious that if $|\rho_1| < 1$ and $|\rho_2| < 1$ or both are smaller than 1, the polynomial does not vanish. This property can be generalize to every graph because it survives the contraction process. Let a and b be the sites that we will identify, and fixing all of the rest of ρ_i to be inside the unit circle. The polynomial P has the form

$$P = A_{++} + \rho\,(A_{+-} + A_{-+}) + \rho^2 A_{--}$$

since $P \neq 0$ if $|\rho_a| < 1$ and $|\rho_b| < 1$, $|A_{++}| \geq |A_{--}|$. Besides, Eq. (D.15) indicates that $P^{(ab)} = A_{++} + \rho_{ab}A_{--}$ so we realise that $P^{(ab)}$ can not vanish if all of the roots of the partition function are inside the unit circle. The system has a symmetry under inversion of the magnetic field of every site ($h \to -h \Rightarrow \rho \to \rho^{-1}$). We will sets now all ρ_i to the same value ($\rho_i \equiv \rho\ \forall i$), that is, we will have a uniform external magnetic field. Then the previous symmetry tells us $Z(h) = Z(-h)$, so from Eq. (D.5) we have that

$$e^{Nh}P(\tau,\rho) = e^{-Nh}P(\tau,\rho^{-1}) \Rightarrow P(\tau,\rho) = \rho^N P(\tau,\rho^{-1}) \tag{D.19}$$

Therefore if all the roots of the polynomial P lie inside the unit circle or all of them are outside it, the partition function can not vanish, so it only vanishes if the roots are in unit circle.

Now, we will write the free energy, F, using Eq. (D.5)

$$F = \frac{1}{N}\log(Z) = \frac{z\beta}{2} + h - \log(2) + \lim_{N\to\infty}\frac{1}{N}\log P(\tau,\rho) \tag{D.20}$$

The polynomial P can be factorized in its roots

$$P = \prod_{a=1}^{N}\left(1 - \frac{\rho}{\rho_a(\tau)}\right)$$

So, the free energy can be rewritten as

$$F = \frac{1}{N}\log(Z) = \frac{z\beta}{2} + h - \log(2) + \frac{1}{N}\sum_{a=1}^{N}\log\left(1 - \frac{\rho}{\rho_a(\tau)}\right)$$

One can define an angular density of the zeros $\mu(\varphi)$ with the properties

$$\mu(\varphi) = \mu(-\varphi) \geq 0 \tag{D.21}$$

$$\int_{-\pi}^{\pi} d\varphi \mu(\varphi) = 1 \tag{D.22}$$

where Eq. (D.21) is due to the symmetry of the system on h. Therefore, we finally find that the free energy is

$$F = \frac{1}{N}\log(Z) = \frac{z\beta}{2} + h - \log(2) + \int_{-\pi}^{\pi} d\varphi \mu(\varphi)\log\left(1 - \frac{\rho}{\rho_a(\varphi)}\right) \tag{D.23}$$

Now, we will study the magnetization, M, that is the first derivative of the free energy, when the external field $h \to 0$

$$M = \frac{\partial F}{\partial h} = 1 + \int_{-\pi}^{\pi} d\varphi \mu(\varphi)\frac{\partial}{\partial h}\left[\log\left(1 - \rho e^{-i\varphi}\right)\right] \tag{D.24}$$

as our expressions are in function of ρ instead of h, we will change the derivative

$$\frac{\partial}{\partial h} = \frac{\partial \rho}{\partial h}\frac{\partial}{\partial \rho} = -2\rho\frac{\partial}{\partial \rho} \tag{D.25}$$

and, using Eq. (D.21) we finally find that

$$\begin{aligned} M &= 1 + 2\int_{-\pi}^{\pi} d\varphi \mu(\varphi)\frac{\rho e^{-i\varphi}}{1 - \rho e^{-i\varphi}} = \int_{-\pi}^{\pi} d\varphi \mu(\varphi)\frac{1 + \rho e^{-i\varphi}}{1 - \rho e^{-i\varphi}} \\ &= \int_{-\pi}^{\pi} d\varphi \mu(\varphi)\frac{1 - \rho^2 - 2i\sin(\varphi)}{1 - 2\rho\cos(\varphi) + \rho^2} \\ &= \int_{-\pi}^{\pi} d\varphi \mu(\varphi)\frac{1 - \rho^2}{1 - 2\rho\cos(\varphi) + \rho^2} \end{aligned} \tag{D.26}$$

where the term with the $\sin(\varphi)$ vanishes because it is an odd function but we are integrating in an even interval. One can observe that when $h \to 0$, that is, $\rho \to 1$, the magnetization tends to 0 except when $\cos(\varphi) = 1$ which indicates us the existence of a phase transition.

As we present at the beginning of this appendix, a phase transition happens if $\cos(\varphi) = 1$, that is, if zeros converge onto the real positive axis when $N \to \infty$. Besides, with a contour integrate (applying residues), one can obtain that for $\tau < \tau_c$

$$M_{\pm} = \lim_{h \to \pm 0} M = \pm 2\mu(0) \tag{D.27}$$

Appendix E

Thermalization in disordered systems

When one simulates with statistical systems in the equilibrium, one has to be sure that the system has actually reached the equilibrium before analysing it, that is, if the system is thermalized. Therefore, one has two different problems, specially with systems with a so slow dynamics as spin glasses: the first is how one can accelerate the thermalization of the system to achieve that it reaches the equilibrium as faster as possible; and the second problem is how one can know if the system is really thermalized. There are several algorithms to help with the first problem, for example the parallel tempering algorithm which will be explained in this thesis, because is the algorithm that we have used in our simulations. Besides, one can deal with the second problem with several thermalization tests, in this thesis, logarithmic data binning and random-walk in temperatures will be explained.

E.1 Parallel Tempering Algorithm

Due to the fact that the free energy of a spin glass at low temperatures is extremely rugged, if you fix the system at a low temperature (smaller than the critical one) and let it evolve in a usual Monte Carlo simulation, its dynamics will be very slow because it may fall into the valley of a local minimum which the time that the system needs to escape is too large. Therefore, the simulating time need to reach the equilibrium is too long and makes the simulation impossible. To solve this problem, in parallel tempering algorithm [228] one simulate several copies of the system at different temperatures (low and high ones) and try to exchange its temperatures after a few MC steps. The higher temperature should be a temperature in the paramagnetic phase

where the system evolves quickly and the lowest temperature should be a temperature that we expect that gives us relevant information, because it is very time-demanding. This election is useful because when a configuration that is at a low temperature is changed to a high temperature, it will forget the local minimum where it stayed at the low temperature. Therefore, the algorithm works accurately if every configuration visits frequently temperatures up and below the critical one. For example, in Figure E.1, one can observe this behavior.

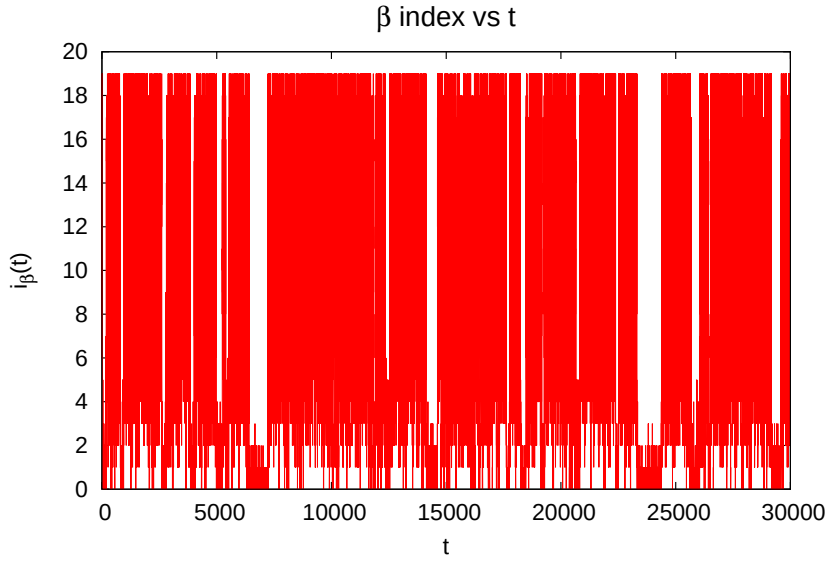

Figure E.1: Evolution of the index of the β where a given configuration stays. Notice that . Data from Potts (Section 2) simulations: a sample with $p = 5$ and $L = 12$.

Let N_T be the number of temperatures (or copies of every sample) that we are simulating and let $\{\beta_1, \cdots, \beta_i, \beta_{i+1}, \cdots, \beta_{N_T}\}$ be the set of actual inverse of the temperatures one has. In a parallel tempering update, one tries to exchange the configuration that are a certain temperature β_i and the configuration at the following β_{i+1} (sequentially from the lowest to the highest temperature), so a given configuration may change of temperature several times in a unique update. Let X and X' be the configurations, the probability with one accepts the exchange is

$$P = \min\left\{1, (\beta_i - \beta_{i+1})\left[E(X') - E(X)\right]\right\} \tag{E.1}$$

Therefore, one has to set the following parameters to perform a simulation with parallel tempering: the set of temperatures to simulate and the number

of MC steps between every parallel tempering update. To choose the set of temperatures (the highest and lowest one are chosen as it is explained before) the histograms of the energy at two neighbours temperatures should overlap to achieve that the acceptance of the exchange is large enough. The number of MC steps between parallel tempering updates is easier to set, because a few MC steps are usually enough in spin glasses to the system forgets. For example, in Janus, where a parallel tempering update is far more time-consuming than a MC step (because parallel tempering is usually perform in the PC that controls the simulation, so one has the typical delays due to the communications) the election 10 MC steps between parallel tempering has been frequently chosen.

E.2 Thermalization tests

E.2.1 Logarithmic Data Binning

When a statistical system is in equilibrium it may change its microstate, but the macrostate (the actual information one has) does not change, that is, if one measures an observable in a system in equilibrium, the value of the observable will not change although the system is in a different microstate (obviously, the value of the observable really changes due to statistical fluctuations within the error of our measures). This property can be used to determine whether or not the system is in the equilibrium. We will divide the total simulating time in blocks $b_n = \left(\frac{t_{\text{sim}}}{2^{n+1}}, \frac{t_{\text{sim}}}{2^n}\right)$ where t_{sim} is the total time of the simulation. Therefore in the first block b_0 one has the last half of the measurements, in the second block one has the last half of the rest of the measurements (that is, the second quarter of them) and so on. Then, one performs thermal average of an observable in every block and if a few of the first blocks have the same average (within the error), that is, if they are in a *plateau*, it indicates that the system is thermalized. If the system is not thermalized, one should extend the simulation (of all the samples) until the system satisfy this criterion.

E.2.2 Random Walk in Temperature

The previous method has the disadvantage that we have to extend the simulation of all the samples if the system is not thermalized although some of them may be actually thermalized but a few hard to thermalize sample are far to get the equilibrium. Therefore, one would like to determine if a single sample is thermalized to extend only those samples unthermalized and, then,

one can save computing time. This method, which was introduced in [229] and perfected in [230], allows us to detect the samples that must be extended. If one is using a parallel tempering algorithm (see section E.1), every configuration must cover the whole temperature range, changing several times from lowest to highest temperature. Let us consider the set of N_T inverse temperatures $\{\beta^{(0)}, \ldots, \beta^{(N_T-1)}\}$, so one has N_T configurations (in fact, one will have more systems because one usually needs to simulate several replicas) evolving in parallel with parallel tempering. Let $\beta^{(i)}(t)$ be the inverse temperature of the configuration i at time t. Now, one has to consider a function, $f(i)$, defined on the index of inverse temperatures $i \in (0, \ldots, N_T - 1)$ which should be monotonic and must change its sign in the critical temperature, that is, if $\beta_i > \beta_c > \beta_{i+1}$, the function $f(i)$ must change its sign between i and $i + 1$. The last condition that $f(i)$ must satisfy is that

$$\sum_{i=0}^{N_T-1} f(i) = 0 \tag{E.2}$$

which in equilibrium is equivalent to $\langle f \rangle = 0$, due to the fact that the probability that the configuration i is at a certain temperature of the set is uniform

$$P(\beta_i) = \frac{1}{N_T} \tag{E.3}$$

One is allowed to chose every arbitrary function that satisfies these conditions. If the set of temperatures is symmetrical, that is, one has the same number of temperatures higher and lower than the critical one, the simplest function is a linear one.

Now, one can define the correlation function

$$C(t) = \frac{1}{N - |t|} \sum_{s=1}^{N-|t|} f(i_s) f(i_{s+t}) \tag{E.4}$$

where N is the total simulation time. Besides, the normalized quantity can also be defined

$$\rho(t) = \frac{C(t)}{C(0)} \tag{E.5}$$

and with this quantity, one can compute the integrated autocorrelation time

$$\tau_{\text{int}} = \int_0^{\Lambda_{\text{int}}} dt \rho(t) \tag{E.6}$$

where $\Lambda_{\text{int}} = \omega t_{\text{int}}$ is a self-consistent window. Besides, one can average over the N_T configurations evolving in the parallel tempering.

This algorithm even allows us to compute the exponential autocorrelation time, which has more physical importance although it is usually far more complicated to compute. The correlation function can be extended on exponentially decaying modes

$$\rho(t) = \sum_j A_j e^{-t/\tau_{\exp,j}}, \text{ where } \sum_j A_j = 1 \tag{E.7}$$

Then, the exponential autocorrelation time, $\tau_{\exp}$ is the maximum of these $\tau_{\exp,j}$. To compute $\tau_{\exp}$ one has to fit the experimental data of $\rho(t)$ to a function like E.7. Since one has a large amount of different samples, one should make so many fits that an automatic algorithm must be developed. Firstly, one should choose a simply function $f(i)$ (the relative sizes of A_j depends on this choice) and average f over consecutive measures (this bins must be far shorter than τ) to remove the fast modes. Then, one can fit the experimental data to a function with only two modes, using the information of τ_{int} to set automatically the initial values of the parameters of the fit, because of the fact that $\tau_{\exp}$ and τ_{int} have usually the same order of magnitude (in fact, if E.7 has only one mode, $\tau_{\exp} = \tau_{\text{int}}$).

Appendix F

Behaviour of a disordered first order phase transition

In this appendix, the expected values of the "effective critical exponents" of a disordered first order phase transition will be computed [231]. In the following we will consider a diluted model with dilution p. Firstly, we will demonstrate an upper bond in the divergences of the specific heat and the connected susceptibilities. Let A be an observable, following Ref. [232], one can obtain

$$\frac{d\overline{\langle A\rangle}}{dp} \leq a\sqrt{\overline{\langle A^2\rangle}}L^{D/2} \tag{F.1}$$

where D is the dimension of the system. We will assume that $\sqrt{\overline{\langle A^2\rangle}}$ and $\overline{\langle A\rangle}$ are of the same order of magnitude. Then, it is easy to rewrite the Eq. (F.1) as

$$\frac{d\log\overline{\langle A\rangle}}{dp} \leq L^{D/2} \tag{F.2}$$

The logarithmic derivative contains information about the width of the critical region on a finite system. For example, in a susceptibility peak, the difference between the spin dilution and its thermodynamic limit is of the same order of magnitude of $L^{-D/2}$. Besides, one can define an effective exponent ν which tells us that this difference is of the same order of magnitude of $L^{-1/\nu}$, so one can write that

$$\nu \geq \frac{2}{D} \tag{F.3}$$

A similar argument is also valid for the derivative with respect to the magnetic field, so the logarithmic derivative of an observable A (in fact its mean value) with respect to the magnetic field diverges at most as fast as $L^{D/2}$, which is the upper bound of the specific heat and connected susceptibilities.

Now, we will compute the "effective exponents" for a first order phase transition on a finite size system in presence of disorder. In this kind of phase transition, two different phases coexist. We will assume that the lattice size is far larger than the correlation length of every phase. Let us label with the subscript $'+'$ quantities of the high temperature phase and with the subscript $'-'$ quantities of the low temperate one. Then, we will define some interesting quantities: let T^* be the temperature at which the correlation length divided by the lattice size is constant, that is

$$\frac{\xi(L_1,t)}{L_1} = \frac{\xi(L_2,t)}{L_2} \tag{F.4}$$

where $t \equiv (T - T^*)/T^*$; let Q be the latent heat, defined as $Q = E_+ - E_-$; let g_4^E be the binder cumulant of the energy defined as

$$g_4^E = \frac{1}{2}\left(3 - \frac{\overline{\langle E^4\rangle}}{\overline{\langle E^2\rangle}^2}\right) \tag{F.5}$$

and finally let C_v be the specific heat. Then, following Ref. [233] in a first order phase transition without disorder, one can get

$$T^*(L) - T_c = a(Q)L^{-D} \tag{F.6}$$
$$C_v(T^*) = c_1(C_{v+}, C_{v-}) + c_2(Q)L^D \tag{F.7}$$
$$1 - g_4^E(T^*) = g_1(E_+, E_-) + g_2(E_+, E_-, C_{v+}, C_{v-})L^{-D} \tag{F.8}$$

where $a(Q)$, $C_2(Q)$ and $g_1(E_+, E_-)$ vanish if $Q = 0$. However, we have demonstrated the existence of an upper bound for the divergences of the specific heat in presence of disorder, so in a disordered first order phase transition, Eq. (F.6) should be rewritten as

$$T^*(L) - T_c = b(Q)L^{-D/2} \tag{F.9}$$

Therefore, if one assumes that the observables diverges as fast as possible, one can get the following "effective critical" exponents.

$$\frac{1}{\nu} = \frac{D}{2} \tag{F.10}$$
$$\frac{\alpha}{\nu} = \frac{D}{2} \tag{F.11}$$
$$\frac{\gamma}{\nu} = \frac{D}{2} \tag{F.12}$$
$$\tag{F.13}$$

Finally, using

$$\eta = 2 - \frac{\gamma}{\nu} \tag{F.14}$$

one obtains that in $d = 3$, $\nu = 2/3$ and $\eta = 1/2$.

Bibliography

[1] D. J. Amit and V. Martín-Mayor, *Field Theory, the renormalization Group, and Critical Phenomena*, World Scientific (2005).

[2] K. H. Fisher and J. A. Hertz, *Spin Glasses*, Cambridge Studies in Magnetism (1991).

[3] V. Dotsenko, *Introduction to the Replica Theory of Disordered Statistical Systems*, Cambridge University Press (2001).

[4] J. J. Binney, N.J. Dowrick. A. J. Fisher and M. E. J. Newman, *The theory of critical phenomena*, Oxford Science Publications (1992).

[5] K. Binder and A. P. Young, *Rev. Mod. Phys.* **58**, 801 (1986) *"Spin glasses: Experimental facts, theoretical concepts, and open questions"*.

[6] M. A. Ruderman and C. Kittel, *Phys. Rev.* **96**, 99 (1954). *"Indirect Exchange Coupling of Nuclear Magnetic Moments by Conduction Electrons"*.

[7] T. Kasuya, *Prog. Theor. Phys.* **16**, 45 (1956). *"A Theory of Metallic Ferro- and Antiferromagnetism on Zener's Model"*.

[8] K. Yosida, *Phys. Rev.* **106**, 893 (1957). *"Magnetic Properties of Cu-Mn Alloys"*.

[9] S. Jimenez, V. Martin-Mayor, G. Parisi and A. Tarancon, *J. Phys.* A*: Math. Gen.* **36**, 10755 (2003). *"Aging in Spin Glasses in three, four and infinite dimensions"*.

[10] S. Nagata, P. H. Keesom and H. R. Harrison, *Phys. Rev.* B **19**, 1633 (1979). *"Low-dc-field susceptibility of CuMn spin glass"*.

[11] P. Granberg, P. Svedlindh, P. Nordblad, L. Lundgren and H. S. Chen, *Phys. Rev.* B **35** 2075 (1987). *"Time decay of the saturated remanent magnetization in a metallic spin glass"*.

[12] J. J. Prejean and J. Souletie, *Phys. Rev.* B **37** 577 (1988). *Comment on "Time decay of the saturated remanent magnetization in a metallic spin glass".*

[13] S. F. Edwards and P. W. Anderson *J. Phys.* F: *Met. Phys.* **5**, 965 (1975). *"Theory of spin glasses".*

[14] D. Elderfield and D. Sherrington, *J. Phys.* C: *Solid State Phys.* **16**, L497 (1983). *" The curious case of the Potts spin glass".*

[15] A. Erzan and E. J. S. Lage, *J. Phys.* C: *Solid State Phys.* **16**, L555 (1983). *"The infinite-ranged Potts spin glass model".*

[16] D. Sherrington and S. Kirkpatrick, *Phys. Rev. Lett.* **35**, 1792 (1975). *"Solvable Model of a Spin-Glass".*

[17] G. Parisi, J. Phys. A: Math. Gen. **13** 1101 (1980). *"The order parameter for spin glasses: A function on the interval 0-1".*

[18] G. Parisi, J. Phys. A: Math. Gen. **13** 1887 (1980). *"Magnetic properties of spin glasses in a new mean field theory".*

[19] G. Parisi, J. Phys. A: Math. Gen. **13** L115 (1980). *"A sequence of approximated solutions to the S-K model for spin glasses".*

[20] G. Parisi, Phys. Rev. Lett. **43** 1754 (1979). *"Infinite Number of Order Parameters for Spin-Glasses".*

[21] D. J. Thouless, J. R. L. Almeida and J. M. Kosterlitz, J. Phys. C **13** 3271 (1980). *"Stability and susceptibility in Parisi's solution of a spin glass model"*

[22] A. J. Bray and M. A. Moore, Phys. Rev. B **31**, 631 (1985). *"Critical behavior of the three-dimensional Ising spin glass".*

[23] M. A. Moore and A. J. Bray, J. Phys. C:Solid State Phys. **18** L699 (1985). *"The nature of the spin-glass phase and finite size effects"*

[24] A. A. Migdal, Zh. Eksp. Teor. Fiz **69** 1457 or Sov. Phys. JETP **42** 743 (1975). *"Infinite Number of Order Parameters for Spin-Glasses".*

[25] L. P. Kadanoff, Ann. Phys. **100** 359 (1976). *"Notes on Migdal's recursion formulas".*

[26] D. S. Fisher and D. A. Huse, Phys. Rev. Lett. **56** 1601 (1986). *"Ordered Phase of Short-Range Ising Spin-Glasses"*

[27] D. S. Fisher and D. A. Huse, Phys. Rev. B **38** 373 (1988) *"Nonequilibrium dynamics of spin glasses"*

[28] D. S. Fisher and D. A. Huse, Phys. Rev. B **38** 386 (1988) *"Equilibrium behavior of the spin-glass ordered phase"*

[29] G. Parisi, Phys. Rev. Lett. **50** 1946 (1983). *"Order Parameter for Spin-Glasses"*.

[30] K. Binder and J. D. Reger, Adv. Phys. **41** 547 (1992). *"Theory of orientational glasses models, concepts, simulations"*

[31] N. S. Sullivan, M. Devoret and D. Estève, Phys. Rev. B **30** 4935 (1984). *"Correlation functions in the quadrupolar glass phase of solid hydrogen"*

[32] K. H. Michel and J. M. Rowe, Phys. Rev. B **22** 1417 (1980). *"Existence of an orientational glass state in* $(\mathrm{KCN})_x\,(\mathrm{KBr})_{1-x}$ *mixed crystals"*

[33] A. Loidl, K. Knorr, R. Feile and J. K. Kjems, Phys. Rev. Lett. **51** 1054 (1983). *"Inelastic Neutron Scattering Study of the Structural Glass Transition in a K(Br,CN) Mixed Crystal"*

[34] D. J. Gross, I. Kanter and H. Sompolinsky, Phys. Rev. Lett. **55** 304 (1985) *"Mean-Field Theory of the Potts Glass"*

[35] G. Cwilich and T. R. Kirkpatrick, J. Phys. A: Math. Gen. **22** 4971 (1989). *"Mean-field theory and fluctuations in Potts spin glasses. I"*

[36] E. De Santis, G. Parisi and F. Ritort, J. Phys. A: Math. Gen. **28** 3025 (1995). *"On the static and dynamical transition in the mean-field Potts glass"*

[37] P. G. Debenedetti and F. H. Stillinger, Nature **410** 259 (2001). *"Supercooled liquids and the glass transition"*

[38] A. Cavagna, Phys. Rep. **476** 51 (2009). *"Supercooled liquids for pedestrians"*

[39] D. J. Gross and M. Mezard, Nuclear Phys B **240** 431 (1984). *"The simplest spin glass"*

[40] T. R. Kirkpatrick and P. G. Wolynes, Phys. Rev. A **35** 3072 (1987). *"Connections between some kinetic and equilibrium theories of the glass transition"*

[41] T. R. Kirkpatrick and P. G. Wolynes, Phys. Rev. B **36** 8552 (1987). *"Stable and metastable states in mean-field Potts and structural glasses"*

[42] T. R. Kirkpatrick and D. Thirumalai, Phys Rev. B **37** 5342 (1988). *"Mean-field soft-spin Potts glass model: Statics and dynamics"*

[43] T. R. Kirkpatrick and D. Thirumalai, Phys Rev. A **37** 4439 (1988). *"Comparision between dynamical theories and metastable states in regular and glassy mean-field spin models with underlying first-order-like phase transitions"*

[44] D. Thirumalai and T. R. Kirkpatrick, Phys Rev. B **38** 4881 (1988). *"Mean-field Potts glass model: Initial-condition effects on dynamics and properties of metastable states"*

[45] C. A. Angell, Science **267**, 1924 (1995). *"Formation of Glasses from Liquids and Biopolymers"*.

[46] C. Brangian, W. Kob and K. Binder, Europhys. Lett. **53** 756 (2001) *"Finite-size scaling at the dynamical transition of the mean-field 10-state Potts glass"*

[47] C. Brangian, W. Kob and K. Binder, J. Phys. A: Math. Gen. **35** 191 (2002) *"Statics and dynamics of the ten-state mean-field Potts glass model: a Monte Carlo study"*

[48] C. Brangian, W. Kob and K. Binder, Phil. Mag. B **82** 663 (2002) or arXiv:cond-mat/0104355 *"The High Temperature Dynamics of a mean field Potts glass"*

[49] C. Brangian, W. Kob and K. Binder, Europhys. Lett. **59** 546 (2002) *"Evidence against a glass transition in the 10-state short-range Potts glass"*

[50] C. Brangian, W. Kob and K. Binder, J. Phys. A: Math. Gen. **36** 10847 (2003) *"Statics and dynamics of the ten-state nearest-neighbour Potts glass on the simple-cubic lattice"*

[51] C. Brangian, W. Kob and K. Binder, Europhys. Lett. **53**, 756-761 (2001), preprint arXiv:cond-mat/0009475 *"Finite-size scaling at the dynamical transition of the mean-field 10-state Potts glass"*; Phil. Mag. B **82**, 663 (2002), preprint arXiv:cond-mat/0104355 *"Finite-size scaling at the dynamical transition of the mean-field 10-state Potts glass*

"; J. Phys. A : Math. Gen. **35**, 191 (2002), preprint arXiv:cond-mat/0106314 *"Statics and dynamics of the ten-state mean-field Potts glass model: a Monte Carlo study"*; Europhys. Lett. **59**, 546 (2002), preprint arXiv:cond-mat/0202232 *"Evidence against a glass transition in the 10-state short-range Potts glass"*; J. Phys. A: Math. Gen. **36**, (2003) 10847, preprint arXiv:cond-mat/0211195 *"Statics and dynamics of the ten-state nearest-neighbour Potts glass on the simple-cubic lattice "*.

[52] F. Belletti, M. Cotallo, A. Cruz, L. A. Fernández, A. Gordillo, A. Maiorano, F. Mantovani, E. Marinari, V. Martin-Mayor, A. Muñoz-Sudupe, D. Navarro, S. Perez-Gaviro, J. J. Ruiz-Lorenzo, S. F. Schifano, D. Sciretti, A. Tarancón, R. Tripiccione and J. L. Velasco, Comp. Phys. Comm. **178**, 208 (2008). *"Simulating spin systems on IANUS, an FPGA-based computer"*.

[53] F. Belletti, M. Cotallo, A. Cruz, L. A. Fernández, A. Gordillo-Guerrero, A. Maiorano, F. Mantovani, E. Marinari, V. Martin-Mayor, A. Muñoz-Sudupe, D. Navarro, S. Perez-Gaviro, M. Rossi, J. J. Ruiz-Lorenzo, S. F. Schifano, D. Sciretti, A. Tarancón, R. Tripiccione, J. L. Velasco, G. Zanier and D. Yllanes, Computing in Science & Engineering **11**, Issue 1, 48 (2009). *"Janus: An FPGA-Based System for High-Performance Scientific Computing"*.

[54] H. Nishimori and M. J. Stefen, Phys. Rev. B, **27**, 5644 (1983) *"Gauge-invariant frustrated Potts spin-glass"*. E. Marinari, S. Mossa and G. Parisi, Phys. Rev. B **59** 8401 (1999) *"Glassy Potts model: A disordered Potts model without a ferromagnetic phase"*; L. A. Fernández, A. Maiorano, V. Martin-Mayor, D. Navarro, D. Sciretti, A. Tarancón and J. L. Velasco, Phys. Rev. B **77**, 104432 (2008) *"Critical properties of the four-state commutative random permutation glassy Potts model in three and four dimensions"*. D. M. Carlucci, Phys. Rev. B **60**, 9862 (1999) *Comment on "Glassy Potts model: A disordered Potts model without a ferromagnetic phase"*. J.L. Jacobsen and M. Picco, Phys. Rev. E **65**, 026113 (2002) *"Phase diagram and critical exponents of a Potts gauge glass"*.

[55] L. W. Lee, H. G. Katzgraber and A. P. Young, Phys Rev. B **74**, 104416 (2006). *"Critical behavior of the three- and ten-state short-range Potts glass: A Monte Carlo study"*

[56] See for example D. J. Amit and V. Martin-Mayor, *Field Theory, the Renormalization Group and Critical Phenomena,* (World-Scientific, Singapore, third edition, 2005).

[57] D. Elderfield and D. Sherrington, J. Phys.C **16**, L497 (1983) *"The curious case of the Potts spin glass"*. D. Elderfield and D. Sherrington, J. Phys.C **16**, L971 (1983) *"Spin glass, ferromagnetic and mixed phases in the disordered Potts model"*. D. J. Gross, I. Kanter and H. Sompolinsky, Phys. Rev. Lett. **55**, 304 (1985) *"Mean-field theory of the Potts glass"*.

[58] G. Parisi and F. Rapuano, Phys. Lett. B **157**, 301 (1985). *"Effects of the random number generator on computer simulations"*.

[59] M. Tesi, E. Janse van Resburg, E. Orlandini and S. G. Whillington, J. Stat. Phys. **82**, 155 (1996) *"Monte carlo study of the interacting self-avoiding walk model in three dimensions"*; K. Hukushima and K. Nemoto, J. Phys. Soc. Jpn. **65**, 1604 (1996) *"Exchange Monte Carlo Method and Application to Spin Glass Simulations"*; E. Marinari, *Optimized Monte Carlo Methods*, in *Advances in Computer Simulation*, edited by J. Kertész and Imre Kondor (Springer-Verlag, Berlin 1998), preprint arXiv:cond-mat/9612010; E. Marinari, G. Parisi and J. J. Ruiz-Lorenzo, *Numerical Simulations of Spin Glass Systems* in *Spin Glasses and Random Fields*, edited by A. P. Young (World Scientific, Singapore, 1997).

[60] L.A. Fernandez, V. Martin-Mayor, S. Perez-Gaviro, A. Tarancon and A.P. Young Phys. Rev. B 80, 024422 (2009). *"Phase transition in the three dimensional Heisenberg spin glass: Finite-size scaling analysis"*.

[61] A. D. Sokal, *Functional Integration. Basis and Applications*, lectures given at the 1996 Cargèse Summer School, edited by C. DeWitt-Morette, P. Cartier and A. Folacci (Plenum, New York, USA 1997).

[62] H. G. Ballesteros, L. A. Fernández, V. Martín-Mayor and A. Muñoz Sudupe, Phys. Lett. B **378**, 207 (1996). *"New universality class in three dimensions?: the antiferromagnetic RP^2 mode"*.

[63] A. Cruz, L. A. Fernández, A. Gordillo-Guerrero, M. Guidetti, A. Maiorano, F. Mantovani, E. Marinari, V. Martín-Mayor, A. Muñoz Sudupe, D. Navarro, G. Parisi, S. Pérez Gaviro, J. J. Ruiz Lorenzo, S. F. Schifano, D. Sciretti, A. Tarancón, R. Tripiccione, J. L. Velasco, D. Yllanes

and A. P. Young, Phys. Rev. B **79**, 184408 (2009). *"Spin Glass phase in the four-state three-dimensional Potts model"*

[64] A. Maiorano, V. Martin-Mayor, J. J. Ruiz-Lorenzo and A. Tarancon, Phys. Rev. B **76**, 064435 (2007). *"Weak first-order transition in the three-dimensional site-diluted Ising antiferromagnet in a magnetic field"*.

[65] H. G. Katzgraber, M. Körner and A. P. Young , Phys. Rev. B **73**, 224432 (2006). *"Universality in three-dimensional Ising spin glasses: A Monte Carlo study"*.

[66] M. Hasenbusch, A. Pelissetto and E. Vicari, Phys. Rev. B **78**, (2008) 214205. *"Critical behavior of three-dimensional Ising spin glass models"*.

[67] T. R. Kirkpatrick and P. G. Wolynes. Phys. Rev. B **36**, 8552 (1987). *"Stable and metastable states in mean-field Potts and structural glasses"*.

[68] B. Lobe, W. Janke and K. Binder. Eur. Phys. J. B **7**, 283 (1999). *"High-temperature series analysis of the p-state Potts glass model on d-dimensional hypercubic lattices"*.

[69] J. Detrey and F. de Dinechin, Microprocessors and Microsystems **31**, 537 (2007). *"Parameterized floating-point logarithm and exponential functions for FPGAs"*.

[70] F. Guerra and F. L. Toninelli, Comm. Math. Phys. **230** 71 (2002). *"The Thermodynamic Limit in Mean Field Spin Glass Models"*

[71] F. Guerra, Comm. Math. Phys. **233** 1 (2003). *"Broken Replica Symmetry Bounds in the Mean Field Spin Glass Model"*

[72] M. Talagrand, C. R. Acad. Sci. Paris, Ser. I **337** 111 (2003). *"The generalized Parisi formula"*

[73] P. Contucci, C. Giardina, C. Giberti and C. Vernia, Phys. Rev. Lett. **96** 217204 (2006) *"Overlap Equivalence in the Edwards-Anderson Model."*

[74] G. Parisi and F. Ricci-Tersenghi, J. Phys. A: Math. Gen., **33** 113 (2000). *"On the origin of ultrametriciy"*

[75] D. Iñiguez, G. Parisi and J. J. Ruiz-Lorenzo, J. Phys. A: Math. Gen., **29** 4337 (1996). *"Simulation of three-dimensional Ising spin glass model using three replicas: study of Binder cumulants."*

[76] D. Sherrington and S. Kirkpatrick, *Phys. Rev. Lett.* **35** 1792 , (1975). *"Solvable Model of a Spin-Glass"*.

[77] G. Parisi, *J.Phys.A: Math. Gen.*, **13**, 1101 (1980). *"The order parameter for spin glasses: a function on the interval 0-1 "*.

[78] M. Mézard, G. Parisi and M.A. Virasoro, *Spin Glass Theory and Beyond* 1987 World Scientific, Singapore.

[79] D.S. Fisher and D.A. Huse, *Phys. Rev. Lett.* **56** 1601 (1986) *"Ordered Phase of Short-Range Ising Spin-Glasses"*; *Phys. Rev. B* **38** 373 (1988) *"Nonequilibrium dynamics of spin glasses"*; *Phys. Rev. B* **38** 386 (1988) *"Equilibrium behavior of the spin-glass ordered phase"*.

[80] E. Marinari, G. Parisi, F. Ricci-Tersenghi, J.J. Ruiz-Lorenzo and F. Zuliani *J. Stat. Phys.* **98**, 973 (2000). *"Replica Symmetry Breaking in Short-Range Spin Glasses: Theoretical Foundations and Numerical Evidences"*.

[81] Auditya Sharma and A.P. Young, *Phys. Rev. B* **84**, 014428 (2011). *"de Almeida–Thouless line studied using one-dimensional power-law diluted Heisenberg spin glasses"*.

[82] F. Guerra, *Int. J. Mod. Phys. B* **10**, 1675 (1997). *"About the overlap distribution in mean field spin glass models"*.

[83] M. Aizenman and P. Contucci, *J. Stat. Phys.* **92**, 765 (1998). *"On the Stability of the Quenched State in Mean-Field Spin-Glass Models"*.

[84] S. Ghirlanda and F. Guerra, *J. Phys. A: Math. Gen.* **31** 9149 (1998). *"General properties of overlap probability distributions in disordered spin systems. Towards Parisi ultrametricity "*.

[85] G. Parisi, available as preprint `cond-mat/9801081`. *"On the probabilistic formulation of the replica approach to spin glasses"*.

[86] M. Talagrand, *Ann. Math.* **163**, 221 (2006). *"The Parisi formula"*.

[87] The Janus Collaboration: F. Belletti, M. Cotallo, A. Cruz, L. A. Fernandez, A. Gordillo, A. Maiorano, F. Mantovani, E. Marinari, V. Martin-Mayor, A. Muñoz-Sudupe, D. Navarro, S. Perez-Gaviro, J. J.

Ruiz-Lorenzo, S. F. Schifano, D. Sciretti, A. Tarancon, R. Tripiccione and J. L. Velasco, *Comp. Phys. Comm.* **178**, 208 (2008). *"Simulating spin systems on IANUS, an FPGA-based computer"*.

[88] F. Belletti, M. Cotallo, A. Cruz, L.A. Fernandez, A. Gordillo-Guerrero, M. Guidetti, A. Maiorano, F. Mantovani, E. Marinari, V. Martin-Mayor, A. Munoz Sudupe, D. Navarro, G. Parisi, S. Perez-Gaviro, J.J. Ruiz-Lorenzo, S.F. Schifano, D. Sciretti, A. Tarancon, R. Tripiccione, J.L. Velasco, and D. Yllanes, *Phys. Rev. Lett.* **101**, 157201 (2008) *"Nonequilibrium Spin-Glass Dynamics from Picoseconds to a Tenth of a Second"*; F. Belletti, A. Cruz, L.A. Fernandez, A. Gordillo-Guerrero, M. Guidetti, A. Maiorano, F. Mantovani, E. Marinari, V. Martin-Mayor, J. Monforte, A. Muñoz-Sudupe, D. Navarro, G. Parisi, S. Perez-Gaviro, J.J. Ruiz-Lorenzo, S.F. Schifano, D. Sciretti, A. Tarancon, R. Tripiccione and D. Yllanes, *J. Stat. Phys.*, **135**, 1121 (2009) *"An In-Depth View of the Microscopic Dynamics of Ising Spin Glasses at Fixed Temperature"*.

[89] Janus Collaboration: R. Alvarez Banos, A. Cruz, L.A. Fernandez, J. M. Gil-Narvion, A. Gordillo-Guerrero, M. Guidetti, A. Maiorano, F. Mantovani, E. Marinari, V. Martin-Mayor, J. Monforte-Garcia, A. Munoz Sudupe, D. Navarro, G. Parisi, S. Perez-Gaviro, J. J. Ruiz-Lorenzo, S.F. Schifano, B. Seoane, A. Tarancon, R. Tripiccione, D. Yllanes, *J. Stat. Mech.* P06026 (2010). *"Nature of the spin-glass phase at experimental length scales"*.

[90] F. Krzakala and O.C. Martin, *Phys. Rev. Lett.* **85**, 3013 (2000). *"Spin and Link Overlaps in Three-Dimensional Spin Glasses"*.

[91] F. S. Edwards and P. W. Anderson, *J. Phys. F* **5** 965, (1975) *"Theory of spin glasses"*; *J. Phys. F.* **6,** 1927, (1976) *"Theory of spin glasses. II"*.

[92] K. Hukushima and K. Nemoto, *J. Phys. Soc. Japan,* **65,** 1604 (1996). *"Exchange Monte Carlo Method and Application to Spin Glass Simulations"*.

[93] E. Marinari, Optimized Monte Carlo Methods, in *Advances in Computer Simulation*, Ed. J. Kerstesz and I. Kondor, (Springer-Verlag, 1998).

[94] L.A. Fernandez, V. Martin-Mayor, S. Perez-Gaviro, A. Tarancon, A.P. Young, Phys. Rev. B **80** 024422 (2009). *"Phase transition in the three dimensional Heisenberg spin glass: Finite-size scaling analysis"*.

[95] D. Amit and V. Martin-Mayor, *Field Theory, the Renormalization Group and Critical Phenomena*, World Scientific, Singapore (2005).

[96] A. Sokal, *Functional Integration: Basics and Applications*, edited by C. DeWitt-Morette, P. Cartier, and A. Folacci, Plenum, New York (1997).

[97] D. Iñiguez, G. Parisi and J.J. Ruiz-Lorenzo, *J. Phys. A.: Math. Gen*, **29**, 4337 (1996). *" Simulation of three-dimensional Ising spin glass model using three replicas: study of Binder cumulants "*.

[98] G. Parisi and F. Ricci-Tersenghi, *J. Phys. A: Math. Gen.* **33**, 113 (2000). *"On the origin of ultrametricity"*.

[99] G.G. Athanasiu, C.P. Bachas and W.F. Wolff, *Phys. Rev. B* **35**, 1965 (1987). *"Invariant geometry of spin-glass states"*.

[100] P Contucci, C. Giardinà, C. Giberti, G. Parisi, and C. Vernia, *Phys. Rev. Lett.* **99**, 057206 (2007). *"Ultrametricity in the Edwards-Anderson Model"*.

[101] M. Mézard, G. Parisi, N. Sourlas, G. Toulouse, and M. Virasoro, *Phys. Rev. Lett.* **52**, 1156 (1984) *"Nature of the Spin-Glass Phase"*.

[102] M. Mézard, G. Parisi and M.A. Virasoro, *J. Physique Lett.* **46**, 217 (1985). *"Random free energies in spin glasses"*.

[103] E. Marinari, G. Parisi and J.J. Ruiz-Lorenzo, *Phys. Rev. B.* **58**, 14852 (1998). *"Phase structure of the three-dimensional Edwards-Anderson spin glass"*.

[104] M. Hasenbusch, A. Pelissetto and E. Vicari, *J. Stat. Mech* L02001 (2008). *"The critical behavior of 3D Ising spin glass models: universality and scaling corrections"*.

[105] M. Hasenbusch, A. Pelissetto and E. Vicari, *Phys. Rev. B* **78**, 214205 (2008). *"Critical behavior of three-dimensional Ising spin glass models"*.

[106] A. Billoire, L. A. Fernandez, A. Maiorano, E. Marinari, V. Martin-Mayor, D. Yllanes, *J. Stat. Mech.* P10019 (2011). *"Finite-size scaling analysis of the distributions of pseudo-critical temperatures in spin glasses"*.

[107] L. Leuzzi, G. Parisi, F. Ricci-Tersenghi and J.J. Ruiz-Lorenzo, *Phys. Rev. Lett.* **101**, 107203 (2008). *"Dilute One-Dimensional Spin Glasses with Power Law Decaying Interactions"*.

[108] P. E. Jönsson, H. Takayama, H. Aruga Katori and A. Ito, Phys. Rev. B **71**, 180412(R) (2005). *"Dynamical breakdown of the Ising spin-glass order under a magnetic field"*.

[109] L. Leuzzi, G. Parisi, F. Ricci-Tersenghi and J. J. Ruiz-Lorenzo, Phys. Rev. Lett. **101**, 107203 (2008). *"Dilute One-Dimensional Spin Glasses with Power Law Decaying Interactions"*.

[110] L. Leuzzi, G. Parisi, F. Ricci-Tersenghi and J. J. Ruiz-Lorenzo, Phys. Rev. Lett. **103**, 267201 (2009). *"Ising Spin-Glass Transition in a Magnetic Field Outside the Limit of Validity of Mean-Field Theory"*.

[111] D. Petit, L. Fruchter and I.A. Campbell, Phys. Rev. Lett. **83**, 5130 (1999). *"Ordering In A Spin Glass under Applied Magnetic Field"*.

[112] D. Petit, L. Fruchter and I.A. Campbell, Phys. Rev. Lett. Phys. Rev. Lett. **88**, 207206 (2002). *"Ordering in Heisenberg Spin Glasses"*.

[113] A. T. Ogielski, Phys. Rev. B **32** 7384 (1985). *"Dynamics of the three-dimensional Ising spin glasses in thermal equilibrium"*.

[114] A. Bray and S. A. Roberts, J. Phys. C **13**, 5405 (1980). *"Renormalisation-group approach to the spin glass transition in finite magnetic fields "*.

[115] A. Bray and M. A. Moore, J. Phys. C: Solid State Phys., **12**, 79 (1979). *"Replica symmetry and massless modes in the Ising spin glass"*.

[116] C. De Dominicis and T. Temesvári, Phys. Rev. Lett. 89, 097204 (2002). *"Replica Field Theory and Renormalization Group for the Ising Spin Glass in an External Magnetic Field"*.

[117] T. Temesvári, Phys. Rev. B 78, 220401(R) (2008). *"Almeida-Thouless transition below six dimensions"*.

[118] A. Bray and M. A. Moore, Phys. Rev. B 83, 224408 (2011). *"Disappearance of the de Almeida-Thouless line in six dimensions"*.

[119] Janus collaboration: R. Alvarez Baños, A. Cruz, L. A. Fernandez, J. M. Gil-Narvion, A. Gordillo-Guerrero, M. Guidetti, D. Iñiguez, A. Maiorano, E. Marinari, V. Martin-Mayor, J. Monforte-Garcia, A. Muñoz Sudupe, D. Navarro, G. Parisi, S. Perez-Gaviro, J. J. Ruiz-Lorenzo, S. F. Schifano, B. Seoane, A. Tarancon, P. Tellez, R. Tripiccione, and D. Yllanes, PNAS **109** 6452 (2012). *"Thermodynamic glass transition in a spin glass without time-reversal symmetry"*.

[120] P. G. Debenedetti, *Metastable Liquids*, Princeton University Press, Princeton (1997).

[121] P. G. Debenedetti and F. H. Stillinger, *Nature* **410**, 259 (2001). *"Supercooled liquids and the glass transition"*.

[122] A. Cavagna, *Physics Reports* **476**, 51 (2009). Eprint: arXiv:0903.4264. *"Supercooled liquids for pedestrians"*.

[123] A. Montanari and G. Semerjian, *J. Stat. Phys.* **125**, 23 (2006). Eprint: arXiv:cond-mat/0201107. *"p-Spin Model in Finite Dimensions and Its Relation to Structural Glasses"*.

[124] G. Adam and J. H. Gibbs, *J. Chem. Phys.* **43**, 139 (1965).

[125] E. R. Weeks, J. C. Crocker, A. C. Levitt, A. Schofield and D. A. Weitz, *Science* **287**, 627 (2000).

[126] L. Berthier, G. Biroli, J. P. Bouchaud, L. Cipelletti, D. El Masri, D. L'Hôte, F. Ladieu and M. Pierno, *Science* **310**, 1797 (2005).

[127] H. Oukris and N. E. Israeloff, *Nature Physics* **06**, 135 (2010).

[128] J. A. Mydosh, *Spin Glasses: an Experimental Introduction*, Taylor and Francis, London (1993).

[129] D. Hérisson and M. Ocio, *Phys. Rev. Lett.* **88**, 257202 (2002). Eprint: arXiv:cond-mat/0112378. *"Fluctuation-dissipation ratio of a spin glass in the aging regime"*.

[130] A. Cruz, J. Pech, A. Tarancon, P. Tellez, C. L. Ullod and C. Ungil, *Comp. Phys. Comm* **133**, 165 (2001). Eprint: arXiv:cond-mat/0004080. *"SUE: A special purpose computer for spin glass models"*.

[131] A. Ogielski, *Phys. Rev.* B **32**, 7384 (1985). *"Dynamics of three-dimensional Ising spin glasses in thermal equilibrium"*.

[132] F. Belletti, M. Cotallo, A. Cruz, L. A. Fernandez, A. Gordillo, A. Maiorano, F. Mantovani, E. Marinari, V. Martin-Mayor, J. Monforte, A. Muñoz Sudupe, D. Navarro, S. Perez-Gaviro, J. J. Ruiz-Lorenzo, S. F. Schifano, D. Sciretti, A. Tarancon, R. Tripiccione and J. L. Velasco (Janus Collaboration), *Comp. Phys. Comm.* **178** 208 (2008). Eprint: arXiv:0704.3573. *"Simulating spin systems on IANUS, an FPGA-based computer"*.

[133] F. Belletti, M. Cotallo, A. Cruz, L. A. Fernandez, A. Gordillo-Guerrero, M. Guidetti, A. Maiorano, F. Mantovani, E. Marinari, V. Martin-Mayor, A. Muñoz Sudupe, D. Navarro, G. Parisi, S. Perez-Gaviro, J. J. Ruiz-Lorenzo, S. F. Schifano, D. Sciretti, A. Tarancon, R. Tripiccione, J. L. Velasco and D. Yllanes (Janus Collaboration), *Phys. Rev. Lett.* **101**, 157201 (2008). Eprint: arXiv:0804.1471. *"Nonequilibrium spin-glass dynamics from picoseconds to one tenth of a second"*.

[134] K. Gunnarsson, P. Svendlindh, P. Nordblad, L. Lundgren, H. Aruga and A. Ito, *Phys. Rev.* B **43**, 8199 (1991). *"Static scaling in a short-range Ising spin glass"*.

[135] M. Palassini and S. Caracciolo, *Phys. Rev. Lett.* **82**, 5128 (1999). Eprint: arXiv:cond-mat/9904246. *"Universal finite-size scaling functions in the 3D Ising spin glass"*.

[136] H. G. Ballesteros, A. Cruz, L. A. Fernandez, V. Martin-Mayor, J. Pech, J. J. Ruiz-Lorenzo, A. Tarancon, P. Tellez, C. L. Ullod and C. Ungil, *Phys. Rev.* B **62**, 14237 (2000). Eprint: arXiv:cond-mat/0006211. *"Critical behavior of the three-dimensional Ising spin glass"*.

[137] Y. G. Joh, R. Orbach, G. G. Wood, J. Hammann, E. Vincent, *Phys. Rev. Lett.* **82**, 438 (1999).

[138] F. Bert, V. Dupuis, E. Vincent, J. Hammann and J. P. Bouchaud, *Phys. Rev. Lett.* **92**, 167203 (2004)

[139] F. Belletti, F. Mantovani, G. Poli, S. F. Schifano, R. Tripiccione, I. Campos, A. Cruz, D. Navarro, S. Perez-Gaviro, D. Sciretti, A. Tarancon, J. L. Velasco, P. Tellez, L. A. Fernandez, V. Martin-Mayor, A. Muñoz Sudupe, S. Jimenez, A. Maiorano, E. Marinari and J. J. Ruiz-Lorenzo (Janus Collaboration), *Computing in Science and Engineering* **8**, 41 (2006). *"Ianus: And Adaptive FPGA Computer"*.

[140] F. Belletti, A. Cruz, L. A. Fernandez, A. Gordillo-Guerrero, M. Guidetti, A. Maiorano, F. Mantovani, E. Marinari, V. Martin-Mayor, J. Monforte, A. Muñoz Sudupe, D. Navarro, G. Parisi, S. Perez-Gaviro, J. J. Ruiz-Lorenzo, S. F. Schifano, D. Sciretti, A. Tarancon, R. Tripiccione and D. Yllanes (Janus Collaboration), *J. Stat. Phys.* **135**, 1121 (2009). Eprint: arXiv:0811.2864. *"An in-depth look at the microscopic dynamics of Ising spin glasses at fixed temperature"*.

[141] R. Álvarez Baños, A. Cruz, L. A. Fernandez, J. M. Gil-Narvion, A. Gordillo-Guerrero, M. Guidetti, A. Maiorano, F. Mantovani, E. Marinari, V. Martin-Mayor, J. Monforte-Garcia, A. Muñoz Sudupe, D. Navarro, G. Parisi, S. Perez-Gaviro, J. J. Ruiz-Lorenzo, S. F. Schifano, B. Seoane, A. Tarancon, R. Tripiccione and D. Yllanes (Janus Collaboration), *J. Stat. Mech.* P06026 (2010). Eprint: arXiv:1003.2569. *"Nature of the spin-glass phase at experimental length scales"*.

[142] R. Álvarez Baños, A. Cruz, L. A. Fernandez, J. M. Gil-Narvion, A. Gordillo-Guerrero, M. Guidetti, A. Maiorano, F. Mantovani, E. Marinari, V. Martin-Mayor, J. Monforte-Garcia, A. Muñoz Sudupe, D. Navarro, G. Parisi, S. Perez-Gaviro, J. J. Ruiz-Lorenzo, S. F. Schifano, B. Seoane, A. Tarancon, R. Tripiccione and D. Yllanes (Janus Collaboration), *Phys. Rev. Lett.* **105**, 177202 (2010). Eprint: arXiv:1003.2943. *"Static versus dynamic heterogeneities in the $D = 3$ Edwards-Anderson-Ising spin glass"*.

[143] S. Franz, M. Mézard, G. Parisi, L. Peliti, *Phys. Rev. Lett.* **81**, 1758 (1998).

[144] T. R. Kirkpatrick and D. Thirumalai, *Phys. Rev.* B **36**, 5388 (1987).

[145] T. R. Kirkpatrick, D. Thirumalai and P. G. Wolynes, *Phys. Rev.* A **40**, 1045 (1989)

[146] W. Götze and T. F. Sjögren, *Rep. Prog. Phys.* **55**, 241 (1992).

[147] M. Mézard and G. Parisi, *Phys. Rev. Lett.* **82**, 747 (1999).

[148] M. Mézard and G. Parisi, *J. Chem. Phys.* **111**, 1076 (1999).

[149] B. Coluzzi, G. Parisi and P. Verrocchio, *Phys. Rev. Lett.* **84**, 3006 (2000).

[150] G. Parisi and T. Rizzo, *J. Phys.* A **43**, 235003 (2010).

[151] S. Singh, M. Ediger and J. de Pablo, *Nature Mater.* **12**, 139 (2013).

[152] J. R. L. de Almeida and D. J. Thouless, *J. Phys.* A **11**, 983 (1978). *"Stability of the Sherrington-Kirkpatrick solution of a spin glass model"*.

[153] M. Mézard, G. Parisi and M. Virasoro, *Spin-Glass Theory and Beyond* World Scientific, Singapore (1987).

[154] A. J. Bray and S. A. Roberts, *J. Phys.* C*: Solid St. Phys.* **13**, 5405 (1980). *"Renormalisation-group approach to the spin glass transition in finite magnetic fields"*.

[155] M. Moore and B. Drossel, *Phys. Rev. Lett.* **89**, 217202 (2002). Eprint: arXiv:cond-mat/0201107. *"p-Spin Model in Finite Dimensions and Its Relation to Structural Glasses"*.

[156] C. J. Fullerton and M. A. Moore (2013). Eprint: arXiv:1304.4420. *"The Growing Correlation Length in Glasess"*.

[157] A. J. Bray and M. A. Moore, *Phys. Rev.* B **83**, 224408 (2011). Eprint: arXiv:1102.1675. *"Disappearance of the de Almeida-Thouless line in six dimensions"*.

[158] G. Parisi and T. Temesvári, *Nucl. Phys.* B **858**, 293 (2012). Eprint: arXiv:1111.3313. *"Replica symmetry breaking in and around six dimensions"*.

[159] A. P. Young and H. G. Katzgraber, *Phys. Rev. Lett.* **93**, 207203 (2004). Eprint: arXiv:cond-mat/0407031. *"Absence of an Almeida-Thouless line in three-dimensional spin glasses"*.

[160] T. Jörg, H. Katzgraber and F. Krzakala, *Phys. Rev. Lett.* **100**, 197202 (2008). Eprint: arXiv:0712.2009. *"Behavior of Ising Spin Glasses in a Magnetic Field"*.

[161] P. E. Jönsson, H. Takayama H. Aruga Jatori and A. Ito, *Phys. Rev.* B **71**, 180412(R) (2005). Eprint: arXiv:cond-mat/0411291. *"Dynamical breakdown of the Ising spin-glass order under a magnetic field"*.

[162] D. Petit, L. Fruchter and I. Campbell, *Phys. Rev. Lett* **83**, 5130 (1999). Eprint: arXiv:cond-mat/9910353. *"Ordering In A Spin Glass under Applied Magnetic Field"*.

[163] D. Petit, L. Fruchter and I. Campbell, *Phys. Rev. Lett* **88**, 207206 (2002). Eprint: arXiv:cond-mat/011112. *"Ordering in Heisenberg Spin Glasses"*.

[164] Y. Tabata, K. Matsuda, S. Kanada, T. Yamazaki, T. Waki, H. Nakamura, K. Sato and K. Kindo, *Journal of Physical Society of Japan* **79**, 123704 (2010). Eprint: arXiv:1009.6115. *"Existence of a Phase Transition under Finite Magnetic Field in the Long-Range RKKY Ising Spin Glass $Dy_x Y_{1-x} Ru_2 Si_2$"*.

[165] R. A. Banos, A. Cruz, L. A. Fernandez, J. M. Gil-Narvion, A. Gordillo-Guerrero, M. Guidetti, D. Iniguez, A. Maiorano, E. Marinari, V. Martin-Mayor, J. Monforte-Garcia, A. Munoz Sudupe, D. Navarro, G. Parisi, S. Perez-Gaviro, J. J. Ruiz-Lorenzo, S. F. Schifano, B. Seoane, A. Tarancon, P. Tellez, R. Tripiccione and D. Yllanes, *Proc. Natl. Acad. Sci. USA* **109**, 6452, (2012). Eprint: arXiv:1202.5593. *"Thermodynamic glass transition in a spin glass without time-reversal symmetry"*.

[166] C. de Dominicis and I. Giardina, *Random Fields and Spin Glasses*, Cambridge University Press, Cambridge, England (2006).

[167] M. Abramowitz and I. A. Stegun, *Handbook of Mathematical Functions: with Formulas, Graphs, and Mathematical Tables.*, Dover Publications, ninth edition, New York (1972).

[168] F. Belletti, M. Guidetti, A. Maiorano, F. Mantovani, S. F. Schifano, R. Tripiccione, M. Cotallo, S. Perez-Gaviro, D. Sciretti, J. L. Velasco, A. Cruz, D. Navarro, A. Tarancon, L. A. Fernandez, V. Martin-Mayor, A. Muñoz-Sudupe, D. Yllanes, A. Gordillo-Guerrero, J. J. Ruiz-Lorenzo, E. Marinari, G. Parisi, M. Rossi and G. Zanier (Janus Collaboration), *Computing in Science and Engineering* **11**, 48 (2009). *"Janus: An FPGA-based system for high-performance scientific computing"*.

[169] T. Jonson, K. Jonason, P. E. Jönsson and P. Nordblad, *Phys. Rev.* B **59**, 8770 (1999).

[170] M. Hasenbusch, A. Pelissetto and E. Vicari, *J. Stat. Mech.* L02001 (2008).

[171] L. Leuzzi, G. Parisi, F. Ricci-Tersenghi and J. J. Ruiz-Lorenzo, *Phys. Rev. Lett.* **103** 267201 (2009). Eprint: arXiv:0811.3435. *"Ising Spin-Glass Transition in a Magnetic Field Outside the Limit of Validity of Mean-Field Theory"*.

[172] C. N. Yand and T. D. Lee, Phys. Rev. Lett. **87**, 404 (1952). *"Statistical Theory of Equations of State and Phase Transitions. I. Theory of Condensation"*

[173] T. D. Lee and C. N. Yang, Phys. Rev. Lett. **87**, 410 (1952). *"Statistical Theory of Equations of State and Phase Transitions. II. Lattice Gas and Ising Model"*

[174] W. Janke and R. Kenna, J. Stat. Phys, **102**, 1211 (2001). *"The Strength of the First and Second Order Phase Transitions from Partition Function Zeroes"*

[175] W. Janke and R. Villanoca, Nucl. Phys. B **489** 679 (1997). *""*.

[176] R. Abe, Prog. Theor. Phys, **37**, 1070 (1967). *"Logarithmic Singularity of Specific Heat near the Transition Pont in the Ising Model"*

[177] N. A. Alves, J.R. Drugowich de Felicio and U. H. E.Hansmann, Int. J. Mod. Phys. C **8**, 1063 (1997). *"A new look at the 2D Ising model from exact partition function zeros for large lattice sizes"*

[178] W. Janke and R. Kenna, Comp. Phys. Comm. **147**, 443 (2002). *"Density of partition function zeroes and phase transition strength"*

[179] R. Kenna and J. J. Ruiz-Lorenzo, Phys. Rev. E **78**, 031134 (2008). *"Scaling analysis of the site-diluted Ising model in two dimensions"*

[180] A. Gordillo-Guerrero, R. Kenna and J. J. Ruiz-Lorenzo, Phys. Rev. E **80**, 031135 (2009). *"Site-diluted Ising model in four dimensions"*

[181] Yang C N and Lee T D 1952 *Phys. Rev. Lett.* **87** 410

[182] Lee T D and Yang C N 1952 *Phys. Rev. Lett.* **87** 410

[183] Fisher M, in lectures in theoretical physics, vol 12, p 1. (University of Colorado Press, Boulder, 1965).

[184] One S, Karaki Y, Suzuki M and Kawabata C 1968 *J. Phys. Soc. Japan* 54.

[185] Falcioni M, Marinari E, Paciello M L, Parisi G and Taglienti B 1982 *Phys. Lett.* **108B** 331

[186] Marinari E 1984 *Nucl. Phys.* **B235** 123

[187] Kenna R, Johnston DA and Janke W 2006 *Phys. Rev. Lett.* **96** 115701

[188] Ruiz-Lorenzo J J 1997 *J. Phys.* A **30** 485

[189] Kenna R and Ruiz-Lorenzo J J 2008 *Phys. Rev. E* **78** 031134

[190] Gordillo-Guerrero A, Kenna R and Ruiz-Lorenzo J J 2009 *Phys. Rev. E* **80** 031135

[191] Ozeki Y and Nishimori H 1988 *J. Phys. Soc. Jpn.* **57** 1087

[192] Damgaard P H and Lacki J 1995 *Int. J. Mod. Phys.* **6** 819

[193] Bhanot G and Lacki J 1993 *J. Stat. Phys.* **71** 259

[194] Saul L and Kardar M 1993 *Phys. Rev. E* **48** R3221

[195] Matsuda Y, Müller M, Nishimori H, Obuchi T and Scardicchio A 2010 *J. Phys. A: Math. and Theor.* **43** 285002

[196] Takahashi K 2011 *J. Phys.Math. and Theor.* **44** 235001

[197] Matsuda Y, Nishimori H and Hukushima K 2008 *J. Phys. A: Math. Theor.* **41** 324012

[198] Hérisson D and Ocio M 2002 *Phys. Rev. Lett.* **88** 257202 (*Preprint* arXiv:cond-mat/0112378)

[199] Belletti F, Cruz A, Fernandez L A, Gordillo-Guerrero A, Guidetti M, Maiorano A, Mantovani F, Marinari E, Martin-Mayor V, Monforte J, Muñoz Sudupe A, Navarro D, Parisi G, Perez-Gaviro S, Ruiz-Lorenzo J J, Schifano S F, Sciretti D, Tarancon A, Tripiccione R and Yllanes D (Janus Collaboration) 2009 *J. Stat. Phys.* **135** 1121

[200] Baños R A, Cruz A, Fernandez L A, Gil-Narvion J M, Gordillo-Guerrero A, Guidetti M, Maiorano A, Mantovani F, Marinari E, Martin-Mayor V, Monforte-Garcia J, Muñoz Sudupe A, Navarro D, Parisi G, Perez-Gaviro S, Ruiz-Lorenzo J, Schifano S F, Seoane B, Tarancon A, Tripiccione R and Yllanes D (Janus Collaboration) 2010 *J. Stat. Mech.* P06026 (*Preprint* arXiv:1003.2569)

[201] Baños R A, Cruz A, Fernandez L A, Gil-Narvion J M, Gordillo-Guerrero A, Guidetti M, Maiorano A, Mantovani F, Marinari E, Martin-Mayor V, Monforte-Garcia J, Muñoz Sudupe A, Navarro D, Parisi G, Perez-Gaviro S, Ruiz-Lorenzo J, Schifano S F, Seoane B, Tarancon A, Tripiccione R and Yllanes D (Janus Collaboration) 2010 *Phys. Rev. Lett.* **105** 177202 (*Preprint* arXiv:1003.2943)

[202] Belletti F, Cotallo M, Cruz A, Fernandez L A, Gordillo A, Maiorano A, Mantovani F, Marinari E, Martin-Mayor V, Monforte J, Muñoz Sudupe A, Navarro D, Perez-Gaviro S, Ruiz-Lorenzo J J, Schifano S F, Sciretti D, Tarancon A, Tripiccione R and Velasco J L (Janus Collaboration) 2008 *Comp. Phys. Comm.* **178** 208–216 (*Preprint* arXiv:0704.3573)

[203] Belletti F, Guidetti M, Maiorano A, Mantovani F Schifano S F, Tripiccione R, Cotallo M, Perez-Gaviro S, Sciretti D, Velasco J L, Cruz A, Navarro D, Tarancon A, Fernandez L A, Martin-Mayor V, Muñoz-Sudupe A, Yllanes D, Gordillo-Guerrero A, Ruiz-Lorenzo J J, Marinari E, Parisi G, Rossi M and Zanier G (Janus Collaboration) 2009 *Computing in Science and Engineering* **11** 48

[204] Baity-Jesi M, Banos R A, Cruz A, Fernandez L A, Gil-Narvion J M, Gordillo-Guerrero A, Guidetti M, Iniguez D, Maiorano A, Mantovani F, Marinari E, Martin-Mayor V, Monforte-Garcia J, Munoz Sudupe A, Navarro D, Parisi G, Pivanti M, Perez-Gaviro S, Ricci-Tersenghi F, Ruiz-Lorenzo J J, Schifano S F, Seoane B, Tarancon A, Tellez P, Tripiccione R and Yllanes D 2012 *Eur. Phys. J. Special Topics* **210** 33 (*Preprint* arXiv:1204.4134)

[205] Parisi G and Virasoro M 1989 *J. Phys. I France* **50** 3317

[206] Franz S, Parisi G and Virasoro M 1992 *J. Phys. I France* **2** 1869

[207] Janke W and Kenna R 2001 *J. Stat. Phys.* **102** 1211

[208] Janke W, Johnston D A and Kenna R 2004 *Nucl. Phys.* B **682** 618

[209] Hukushima K and Nemoto K 1996 *J. Phys. Soc. Japan* **65** 1604 (*Preprint* arXiv:cond-mat/9512035)

[210] Marinari E 1998 Optimized Monte Carlo methods *Advances in Computer Simulation* ed Kerstész J and Kondor I (Springer-Berlag)

[211] Fernandez L A, Martin-Mayor V, Perez-Gaviro S, Tarancon A and Young A P 2009 *Phys. Rev.* B **80** 024422

[212] Hasenbusch M, Pelissetto A and Vicari E 2008 *Phys. Rev.* B **78** 214205

[213] Billoire A, Fernandez L A, Maiorano A, Marinari E, Martin-Mayor V and Yllanes D 2011 *J. Stat. Mech.* P10019 (*Preprint* arXiv:1108.1336)

[214] Gordillo-Guerrero A, Kenna R and Ruiz-Lorenzo JJ (in preparation)

[215] Carter A, Bray A J and Moore M A 2002 *Phys. Rev. Lett.* **88** 077201

[216] Boettcher S 2004 *Europhys. Lett.* **67** 453

[217] Boettcher S 2005 *Phys. Rev. Lett.* **95** 197205

[218] Fernandez L A, Gordillo-Guerrero A, Martin-Mayor V and Ruiz-Lorenzo J J 2008 *Phys. Rev. Lett.* **100** 057201

[219] K. Jonason, E. Vincent, J. Hammannn, J. P. Bouchaud and P. Nordblad, Phys. Rev. Lett. **81**, 3243 (1998) *"Memory and Chaos Effects in Spin Glasses"*

[220] V. Dupuis, F. Bert, J.-P. Bouchaud, J. Hammann, F. Ladieu, D. Parker and E. Vincent, cond-mat/0406721v2 *"Aging, rejuvenation and memory phenomena in spin glasses"*

[221] S. Jimenez, V. Martin-Mayor and S. Perez-Gaviro, Phys. Rev. B **72** 054417 (2005) *"Rejuvenation and memory in model Spin Glasses in 3 and 4 dimensions"*

[222] The RTN collaboration, Procc. of CHEP 92, CERN 92-07.

[223] A. Cruz, J. Pech, A. Tarancón, P. Téllez, C. L. Ullod and C. Ungil, Comp. Phys. Comm. **133**, 165 (2001). *"SUE: A special purpose computer for spin glass models"*.

[224] F. Belletti, F. Mantovani, G. Poli, S. F. Schifano, R. Tripiccione, I. Campos, A. Cruz, D. Navarro, S. Perez-Gaviro, D. Sciretti, A. Tarancon,J. L. Velasco, P. Tellez, L. A. Fernandez, V. Martin-Mayor, A. Muñoz Sudupe, S. Jimenez, A. Maiorano, E. Marinari and J. J. Ruiz-Lorenzo, Computing in Science and Engineering, **8**, 41 (2006). *"IANUS: An adaptive FPGA Computer"*.

[225] F. Belleti, M. Cotallo, A. Cruz, L. A. Fernandez, A. Gordillo, A. Maiorano, F. Mantovani, E. Marinari, V. Martín-Mayor, A. Muñoz-Sudupe, D. Navarro, S. Pérez-Gaviro, J. J. Ruiz-Lorenzo, S. F. Schifano, D. Sciretti, A. Tarancón, R. Tripiccione and J. L. Velasco, Computer Physics Communications **478**, 208 (2008). *"Simulating spin systems on IANUS, an FPGA-based computer"*.

[226] F. Belletti, M. Guidetti, A. Maiorano, S. F. Mantovani, F. Schifano, R. Tripiccione, M. Cotallo, S. Perez-Gaviro, D. Sciretti, J. L. Velasco, A. Cruz, D. Navarro, A. Tarancon, L. A. Fernandez, V. Martin-Mayor, A. Muñoz Sudupe, D. Yllanes, A. Gordillo-Guerrero, J. J. Ruiz-Lorenzo, E. Marinari, G. Parisi, M. Rossi and G. Zanier, Computing in Science and Engineering **11**, 48, issue 1 (2009). *"Janus: An FPGA-Based System for High-Performance Scientific Computing"*.

[227] G. Parisi and F. Rapuano, Phys. Lett. B **157**, 301 (1985) *"Effects of the random number generator on computer simulations"*.

[228] K. Hukishima and K. Nemoto, J. Phys. Soc. Japan **65**, 1604 (1995). *"Exchange Monte Carlo Method and Application to Spin Glass Simulations"*.

[229] L. A. Fernandez, V. Martin-Mayor, S. Perez-Gaviro, A. Tarancon and A. P. Young, Phys. Rev. B **80**, 024422 (2009). *"Phase transition in the three dimensional Heisenberg spin glass: Finite-size scaling analysis"*.

[230] R. Alvarez Baños, A. Cruz, L. A. Fernandez, J. M. Gil-Narvion, A. Gordillo-Guerrero, M. Guidetti, A. Maiorano, F. Mantovani, E. Marinari, V. Martin-Mayor, J. Monforte-Garcia, A. Muñoz Sudupe, D. Navarro, G. Parisi, S. Perez-Gaviro, J. J. Ruiz-Lorenzo, S. F. Schifano, B. Seoane, A. Tarancon, R. Tripiccione and D. Yllanes, J. Stat. Mech. P06026 (2010). *"Nature of the spin-glass phase at experimental lenght scales"*.

[231] A. Maiorano, V. Martin-Mayor, J. J. Ruiz-Lorenzo and A. Tarancon, Phys. Rev. B **76**, 064435 (2007). *"Weak first-order transition in the three-dimensional site-diluted Ising antiferromagnet in a magnetic field"*.

[232] J. T. Chayes, L. Chayes, D.S. Fisher and T. Spencer, Phys. Rev. Lett. **57**, 2999 (1986). *"Finite-Size Scaling and Correlation Lengths for Disordered Systems"*.

[233] M. S. S. Challa, D. P. Landau and K. Binder, Phys. Rev. B **34**, 1841 (1986), *"Finite-size effects at temperature-driven first-order transitions"*.

List of Figures

List of Tables